Applications of Automation Technology to Fatigue and Fracture Testing and Analysis

THIRD Volume

A. A. Braun and
L. N. Gilbertson, editors

ASTM STP 1303

STP 1303

Applications of Automation Technology to Fatigue and Fracture Testing and Analysis: Third Volume

A. A. Braun and L. N. Gilbertson, Editors

ASTM Publication Code Number (PCN): 04-013030-30

ASTM
100 Barr Harbor Drive
West Conshohocken, PA 19428-2959

ISBN: 0-8031-2416-3
ASTM Publication Code Number (PCN): 04-013030-30

Peer Review Policy

Each paper published in this volume was evaluated by two peer reviewers and at least one editor. The authors addressed all of the reviewers' comments to the satisfaction of both the technical editor(s) and the ASTM Committee on Publications.

The quality of the papers in this publication reflects not only the obvious efforts of the authors and the technical editor(s), but also the work of these peer reviewers. The ASTM Committee on Publications acknowledges with appreciation their dedication and contribution of time and effort on behalf of ASTM.

Printed in Scranton, PA
October 1997

Foreword

The Third Symposium on Applications of Automation Technology to Fatigue and Fracture Testing and Analysis was presented in Norfolk, Virginia on 14 November, 1995. The symposium was held in conjunction with the 13–16 November 1995 meeting of ASTM Committee E8 on Fatigue and Fracture, which sponsored the symposium. Arthur A. Braun, MTS Systems Corporation, and Leslie N. Gilbertson, Zimmer, Inc., served as chairmen of the symposium and editors of the resulting publication.

Contents

Overview

This is the third symposium on Applications of Automation Technology to Fatigue and Fracture Testing and Analysis. The papers in this book exemplify the typical evolution of computers and their applications. The simpler applications of past years are becoming more sophisticated, the hardware is becoming smaller and more powerful, and computers are doing things now that weren't even considered previously.

Data acquisition was a natural application of computers, even before the invention of the microprocessor. The microprocessor has made data acquisition application in fatigue applications ubiquitous. The paper "Networked Data Acquisition Systems for Strain Data Collection," by G. McLean, B. Prescott, and M. Ellens, brings computer networking to the field of portable fatigue data acquisition. With an innovative application of networking technology they have created a very small modular expandable data acquisition, which can collect field strain data, pre-process it, and forward it for further analysis and storage. This permits use of the system on applications where previous larger systems would have inhibited the natural use of the device under study. In the paper "Fatigue and Reliability Assessment Incorporating Computer Strain Gage Network Data," by M. Ellens, J. Provan, G. McLean, and M. Sanders, the authors made use of the system to make fatigue life prediction on the unique application of racing mountain bicycles.

The paper "Cycle-by-Cycle Compliance Based Crack Length Measurement," by R. Sunder, points up one of the problems related to the ubiquitous nature of computer data acquisition. There is a natural tendency to assume that newer and faster computers and computer hardware will always give better information. This paper clearly points out that computer hardware is a tool. A tool that must be intelligently and appropriately applied, and verified.

Robert Tregoning highlights, in the paper "Feasibility Study of Alternating Current Potential Drop Techniques for Elastic-Plastic Fracture Toughness Testing," the capability of computer systems to combine more than one sensory input and previously developed calibration data to calculate a near real time data output.

Another major category of computer use in Fatigue is in simulation. The paper "Fatigue Life Contours from Elastic FEM Considering Multiaxial Plasticity" by T. Langlais, J. Vogel, D. Socie, and T. Cordes, combines multiaxial fatigue damage rules with finite element analysis to predict fatigue damage. The authors then take it one step further by using high-quality computer graphics to help designers more easily understand the damage analysis.

The paper "Computer Modeling and Simulation in a Full-Scale Aircraft Structural Test Laboratory," by R. Hewitt and J. Albright, presents a new idea for using computers to improve the economics of fatigue testing itself. They have adapted a commercially-available personal computer program to modeling complex structural tests. This enables them to predict the behavior of the complex test control systems and optimize allowing more rapid startup and completion of these complex tests without the danger of damaging one of a kind structures.

The advent of microprocessors has had a large effect on the control capabilities of fatigue test equipment. The control schemes have ranged from hybrid designs where a computer is integrated with an analog controller system to full digital systems where computers replace the analog control circuitry. The paper "Computer-Controlled High Strain Rate Compression Test System," by C. Venkatesh, T. Prakash, and R. Sunder takes a specialized hybrid approach to a control problem. The computer controls the servo-valve gain on a dual servovalve system in order to get the response speed required for the application.

Another similar hybrid control application is covered in the paper "Adaptive PID Control of Dynamic Materials-Testing Machines Using Remembered Stiffness," by C. Hinton. In this application a computer is used to optimize gain for the current stiffness of the test sample. For applications such as low cycle fatigue it can be set up to use results of the previous cycle where insufficient immediate information is available.

The paper "Characteristics and Automated Control of a Dual-Frequency Servohydraulic Test System," by K. Reifsnider, S. Case, and L. Mosiman contains a discussion of a mostly digital hybrid control system. The system controls two in line actuators to superimpose two independent and widely separated load frequencies on a single sample.

The large increases in the speed and power of microprocessors has enabled the use of calculated control variables in full digital control fatigue test systems. The paper "Materials Characterization Using Calculated Control," by J. Christiansen, R. Oehmke, and A. Schwarzkopf contains a review of requirements for calculating control variables and suggestions for some variables suitable for calculated control.

The final paper, entitled "Control of a Biaxial Test Using Calculated Input Signals and Cascade Control," by F. Albright and L. Johnson, uses calculated control variables to solve a problem in planar biaxial testing. The authors use calculated feedback signals and a hierarchical processing algorithm on multiple inputs in a digital controller to prioritize the effects of the input signals on the resultant output loads. All this to prevent irrelevant movement in the planar test region.

A. A. Braun

MTS Systems Corp., Eden Prairie, MN; symposium co-chairman and co-editor.

L. N. Gilbertson

Zimmer Inc., Warsaw, IN; symposium co-chairman and co-editor.

Data Acquisition

G. McLean,[1] B. Prescott,[1] and M. Ellens[1]

Networked Data Acquisition Systems for Strain Data Collection

REFERENCE: McLean, G., Prescott, B., and Ellens, M., "**Networked Data Acquisition Systems for Strain Data Collection,**" *Applications of Automation Technology to Fatigue and Fracture Testing and Analysis: Third Volume, ASTM STP 1303,* A. A. Braun and L. N. Gilbertson, Eds., American Society for Testing and Materials, 1997, pp. 5–18.

ABSTRACT: Issues surrounding the implementation of fast, effective, and accurate strain measurement systems continue to make strain measurement a difficult instrumentation problem. Difficulties in constructing effective systems for strain measurement are particularly felt in fatigue testing, large-scale testing, or in the testing of mobile vehicles. A brief analysis of the difficulties encountered in these applications provides a motivation for the design of new system architectures for strain measurement based on a paradigm of networks and information processing. The design of a networked data acquisition system for strain measurement is described. The system involves a dedicated data acquisition system installed at each gage or rosette that performs bridge excitation and completion, regular sampling, and monitors trend information. A digital communications network is used to allow each gage to be configured as a client in a stateless client-server network application. Together, the components form a new architecture for strain data acquisition based on a network of intelligent devices that can be controlled by any general purpose computer. The proposed system architecture addresses many of the problems associated with conventional strain measurements by minimizing its reliance on analog signal manipulation. The paper discusses the design of a prototype system designed in this manner and discusses the performance that can be achieved using this approach.

KEYWORDS: strain gage, data acquisition, smart transducer

Since the discovery by Lord Kelvin in 1856 that the electrical resistance of certain metals changes in proportion to mechanical strain, the resistive strain gage has emerged as a useful and enduring technology for the measurement of strain [*1*]. To this day, the resistive strain gage is ubiquitous in fatigue and fracture measurement systems, serving first as the primary transducer for determining the response of materials under load and more recently as a calibration standard for evaluating the performance of more modern methods of measuring deformation. As a direct result of the proven performance of the resistive strain gage, it continues to be integrated into measurement systems. In this paper we discuss the systems aspects of strain gage measurement based on typical fatigue measurement applications. The fruit of this discussion is the development of a new architecture for strain measurement systems that improves performance, reduces errors, and simplifies strain gage system implementation.

The apparent simplicity of the strain gage transducer belies the difficulty associated with actually obtaining useful measurements from it. Figure 1 shows the basic components of an analog strain measurement system that consists of a strain gage or gages, a precision excitation voltage, completion resistors to form a Wheatstone bridge, and a display device. This is the basic configuration that has been in use for the better part of this century [2]. While advances

[1] Dept. of Mechanical Engineering, University of Victoria, P.O. 3055, Victoria, British Columbia, Canada V8W-3P6.

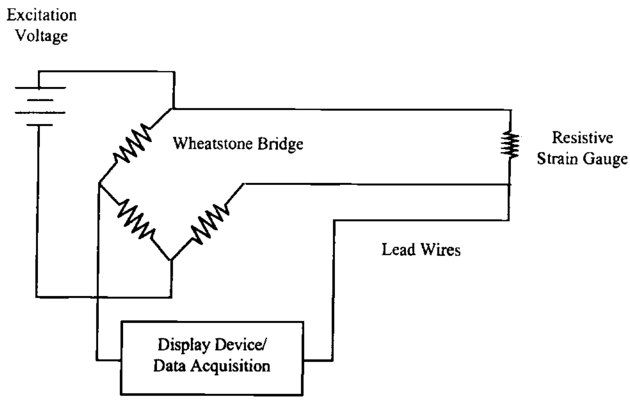

FIG. 1—*Simple strain measurement system.*

in data acquisition technology have tended to improve what can be done with the output of the Wheatstone bridge, the transducer itself has not changed appreciably. The excitation voltage must be low to ensure that gage self-heating does not induce an apparent strain, and the percentage change in resistance must also be fairly small so that linear approximations to the bridge equations can be assumed (for less than full bridge configurations). These considerations produce voltage outputs on the order of millivolts for full-scale response, making the strain measurement signal susceptible to degradation from electrical noise, or even from the effects of variations in the resistance of the lead wires that connect the gage, bridge, and display device. While these unwanted effects can be carefully assessed and eliminated by a variety of means, the integration of strain gage measurements in modern measurement systems present problems that are not easily solved by manual means [*3–5*].

The strain gage continues to be used in many modern measurement systems for determining strains, determining loads via some strain to load relationships, and for monitoring fatigue damage accumulation. It is therefore surprising that relatively little has been done to evolve measurement systems that are particularly well-suited to the rigors of strain measurement. Instead, strain measurement systems continue to be developed as analog measurement systems, albeit with the replacement of the traditional display device with some form of computerized data acquisition. The result is that we are able to digitally record strain values, but must still contend with the problems of the strain measurement system. Furthermore, this lack of specialized measurement system prevents the acquisition of useful data in many circumstances where it would be beneficial to obtain strain measurements, as we will discuss in following sections.

It is our contention that practical strain measurement systems can be improved by separating the instrumentation from the communication, display, and storage elements. The basic philosophy of this new approach is presented in the section "Limitations of Strain Data Acquisition Systems." In the section "Networked Strain Data Acquisition Systems," we present the design of a networked data acquisition system for strain measurement and illustrate how this system removes certain barriers that have hitherto made strain data acquisition a difficult task.

The development of "intelligent" strain gages described in this paper follows a general trend within the design of instrumentation systems toward "smart" transducers [*6*]. While for many specialized applications development has focused on transducers embedded within a chip, here we concentrate on the development of very small and lightweight data acquisition systems that are embedded in the object under test. Located in proximity to the gages, the system provides information-processing capability directly at the measurement site. This system architecture opens the door for new avenues in strain measurement that are not feasible using conventional means.

Strain Measurement System Integration

To illustrate the pertinent issues in the design of strain measurement systems for fatigue testing, we present two hypothetical case studies. In the first, we will discuss the issues surrounding the integration of many strain measurements into a single data acquisition system as would be demanded when testing large structures. In the second, we discuss the requirements for the design of a system that would be capable of measuring strain from a few sites on a very small, mobile structure. By considering the issues surrounding system integration at these two extremes we show the limitations of the present strain measurement system architecture and develop design requirements for the new architectures.

Large-Scale Strain Measurement Systems

The first application to be considered consists of applying many strain measurements that are spatially distributed over a large object. This case study is representative of what might be performed for aircraft testing [7] in a laboratory setting: The object under test is stationary but subject to known cyclic loading and the response to these applied loads is measured throughout the object.

The primary issue involved in implementing and maintaining a strain measurement system for such applications revolves around the proper installation of the many gage sites and integration of data from these sites into a single centralized data-gathering facility. The information processing issues will be discussed in the next section. Here we discuss the issues associated with physically installing the system.

These scenarios may involve several dozen to several hundred strain measurement sites. Existing data acquisition systems that would be suitable for interfacing to the strain measurements are commonly available and are based upon general purpose analog to digital (A/D) converters. The general strategy requires that the gages be connected in an analog fashion via long lead wires to the data collection site as illustrated in Fig. 2. The issue for the large-scale system is that each gage must be integrated into some form of Wheatstone bridge circuit before

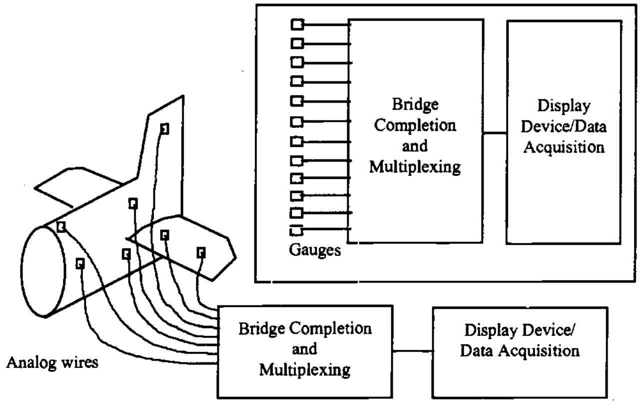

FIG. 2—*Conventional large-scale strain measurement systems.*

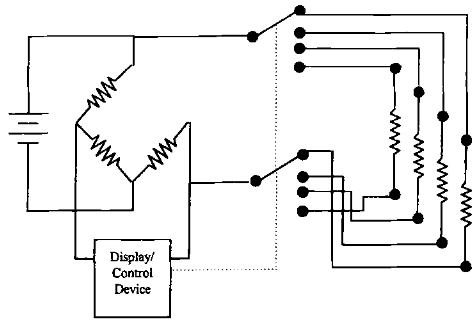

FIG. 3—*Conventional gage switching arrangement.*

voltage measurements can be made. Typically this is done by independent excitation and completion of a bridge for each gage and then multiplexing each gage/bridge to the data acquisition system as shown in Fig. 3. Therefore, the overall system incorporates a tree structure with the computer at the root, branching to control some form of relay multiplexer which then branches to connect to individual gages as illustrated in Fig. 2.

The physical realization of this tree-structured architecture is problematic since it requires that active switching elements be included in the analog measurement loop. The problems associated with switching can be minimized through careful deployment of the system components, but it is nonetheless a constant source of concern. Various strategies can be considered for multiplexing the measurements into the single system, beginning with the idea of multiplexing all measurements into a single A/D converter, or considering the use of multiple A/D converters within the measurement system. Whatever approach is taken, it must be understood that measurements will be taken in a round-robin fashion. The time required to switch to a new bridge/gage and allow the measurement to settle governs the maximum throughput of the system.

Issues with lead wires will become a major concern in such an application since the measurement sites are, by definition, distributed over a reasonably large area and then connected to the data-gathering facility. Typically, three to six wire connections will be required between the multiplexer and each gage/gage pair. For the hypothetical 100 measurement test under consideration, this results in an umbilical of 500 conductors connected to the computer. The physical installation and maintenance of the interconnection between the gages and the data acquisition system thus represents a significant (though hard to assess) cost.

Mobile/Portable Strain Measurement

The difficulties associated with integrating measurements from multiple sites into a single measurement system described in the previous section are exacerbated when small, mobile structures must be monitored. The need for fast, accurate measurement of strains *in-situ* is great. While rough estimates of loading spectra can be established through observation of use and failure, the opportunity for gathering precise strain information is attractive. Through gathering such data it becomes possible to characterize actual loads on an object and thus obtain a close tailoring of testing loads to actual service loads. Examples of applications involving this approach can be found in [*8*].

The requirements for such *in-situ* measurements are stringent. The measurement system used must be unobtrusive (in terms of volume and mass) to the point that the measurement system does not interfere with the normal operation of the object. For instance, measurement of strains on a large ship would not normally preclude the installation of a normal data acquisition system based on personal computer technology. The situation becomes somewhat more difficult as the application is changed to a road vehicle or aircraft and becomes extremely difficult when even smaller objects must be monitored.

While dedicated systems for mobile strain measurement *have* been developed, the realm of mobile instrumentation is dominated by the advent of the laptop computer, aided by the recent development of the PCMCIA card systems [9]. It is important to point out that the vehicular measurement system is topologically identical to the large-scale, static, strain measurement system—a central data collection capability is installed from which multiple strain measurement sites are connected. The interconnection remains analog and the limitations are primarily as before (multiplexing, sampling rate, storage issues, etc.), but now with the added limitation imposed because the system is not expandable beyond a small number of input channels.

The installation of a dedicated data acquisition system on a moving vehicle puts the measurement system totally into the use environment. This has several implications for gathering data since the data acquisition can only be controlled from the moving vehicle; the system must be capable of operating in the vehicle's environment (not a problem for A/D conversion, but devices that store data tend to be sensitive to temperature, humidity, air quality, and vibration), and the vehicle must be taken out of service in order for the collected data to be retrieved.

These limitations are not serious if a dedicated vehicle is assigned to be used for data collection. However, the expense involved in doing this makes it difficult to collect sufficient data to make it representative of typical service loads. For example, in an ongoing study of helicopter landing gear the high cost of paying for test time, and the associated costs of installing a laptop-based data acquisition system for each test period precluded the opportunity for collecting data over a long period, during bad weather, and during actual service missions. Paradoxically, it was the operation of the landing gear in these situations which was of interest, so the data acquisition system, while perfectly adequate for taking measurements on the ground, was too unwieldy to allow the gathering of the required data. Ideally, the data acquisition system would be left on board a test helicopter for very long periods of time so a state of constant readiness for interesting events would be maintained.

As the scale of objects under study decreases, the problem of strain measurement increases. In the extreme, small radio telemetry systems can be used to provide a wireless means of acquiring strain data, but such systems typically employ a voltage to frequency converter and hence accommodate only a single channel of analog strain measurement. Given the nature of analysis and modeling that presently accompanies the data acquisition effort, it is unreasonable to expect that single-channel measurements will suffice. Small objects, or vehicles, such as bicycles, skis, figure skates or various sorts of portable machinery are constrained to the point that it is impossible to install a traditional data acquisition system without seriously impeding the use of the object, thus making the measurement exercise rather pointless. These points are expanded upon in Ref. *8*.

Information Processing

In both cases considered in the previous section the gage/lead wire is considered to be the instrument and the computer/multiplexer is the recording device. Viewed this way, the computer strain gage monitoring system is directly equivalent to the traditional strain measurement system and it is implicitly understood that the computer system must record the data as it is generated. However, from an information processing perspective it is important to understand what the data will be used for before the system requirements can be fully comprehended.

In order to capture significant events in the data, a sufficiently high sampling rate is required. This rate will, of course, vary depending upon the application, but for a high-performance strain

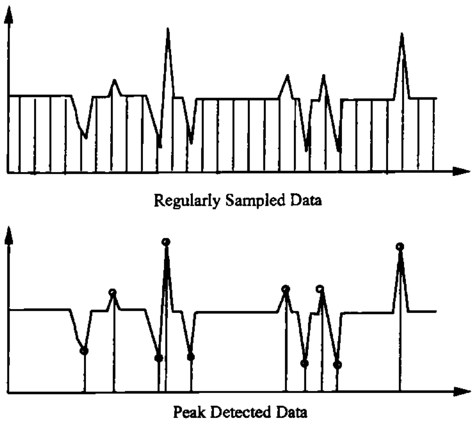

FIG. 4—*Regular sampling versus peak detection.*

measurement system a typical sampling rate of 1 kHz is required. This means that any data acquisition system must be capable of sampling each gage output at this rate and storing the results in real time.

For the large-scale system (100 gages), a net sampling rate of 100 kHz is required. This is easily feasible with present A/D converter technology. However, it is not clear that any single system will be capable of switching gages into a bridge and obtaining useful bridge measurements at this rate. Furthermore, even if the external equipment were able to be controlled at this rate, the internal data transfer requirements for sampling, timestamping, and storing data imply a rate of approximately 3 to 5 megabit/s. This represents a significant data transfer rate.

A review of the data requirements for fatigue measurements leads to the conclusion that streams of regularly sampled data are in fact not well used by the analysis process [*10*]. In fact, it is primarily peak information that is of use in fatigue analysis. Rapid sampling is required to ensure that peaks are not lost, but fatigue analysis would normally proceed by extracting peaks from the sampled data and discarding the remaining non-peak samples. Therefore, since only peaks are informative, it makes sense to build the peak detection capability directly into the data acquisition system. Returning to the large-scale example, if peaks are expected to occur 50 times/s for each channel, then the data transfer rate is reduced from 3 to 5 megabit/s to about 150 kilobit/s. This comparison is shown schematically in Fig. 4.

The peak detection example serves to distinguish between data rate and useful information rate within the system. Other feature patterns can be envisioned, such as simple statistical summaries of strain over time, or particular events such as overloads, pre-triggering to capture high sample rate data before and after events, etc. Knowledge of the type of event that actually conveys information serves to enable the designer to reduce data rates without sacrificing useful measurement performance.

Limitations of Strain Data Acquisition Systems

The preceding sections have discussed the nature of the data acquisition systems typically used for strain measurement. The relative extremes of very large-scale strain measurement (large number of measurement sites) and mobile strain measurement (fewer sites, but limited space) serve to identify weaknesses with the dominant approach to measurement system design.

The problems inherent in maintaining this dominant paradigm have been illustrated in the previous sections:

- Problems arise because the entire system is "measurement." There is no distinction between the measurement aspects of a system and the communication/control aspects of a system. Lead wire effects are dominant, but so are the effects of multiplexers, relays, and other switching elements required to integrate many strain measurements into a single data collection device.
- To the extent that multiple strain measurements share the same bridge, the measurements are not electrically independent of each other. In large-scale applications, the connection between the strain measurement site and the central data collection system must be complete before testing can occur. A failure of one strain measurement may easily introduce errors that will corrupt other strain measurements.
- The existing paradigm has no way of distinguishing between data and *useful* data (in other words, information) before the data has been collected and stored. As described in detail previously, this unnecessarily increases the requirements for both data acquisition and data storage.

It is our contention that strain measurement systems are unnecessarily complicated by the foregoing problems. Many of these issues can be addressed by recognizing strain measurement systems as a particularly specialized class of information processing system, and can therefore exploit advances in information technology. The following two points are key to establishing an information processing view of strain measurement system configurations:

(1) The resistive strain gage and Wheatstone bridge constitute the strain measurement device being used. All other system components (lead wires, multiplexers, etc.) serve as communications components to provide a means of connecting the measurement device to the storage or display device. It is important to realize that the major complexity of strain measurement systems lies not so much in the difficulty associated with obtaining strain measurements, but with the problems inherent in communicating these measurements within a rather archaic network of analog interconnection.

(2) As computational means are inevitably present in the acquisition and storage of strain data, there is no need to continue with the idea that *all* data must be stored. In fact, the information rate associated with a measurement is likely to be significantly lower than the actual data rate implied by the sampling frequency. This argument can be applied from two points of view. The first argument is from information theory, based on measurements of the entropy of signals. The success of data compression in other forms of communication can be used to great advantage within strain measurements as well [*11*]. The second argument states that most strain data analysis involves only a small portion of the sampled data, as discussed previously. Generally, the volume of data is too great, and the sampling rates are high only to ensure that important, short-term events such as excursions to peaks are recorded. Therefore, if the strain measurement system is capable of distinguishing between events and non-events then very efficient use of the communication channels can be made.

The new paradigm for strain measurement is based upon adopting the ideas of communications systems. Information must be communicated efficiently within the system. In the following sections we present the implications of this shift in system design and discuss issues for the implementation of such a system.

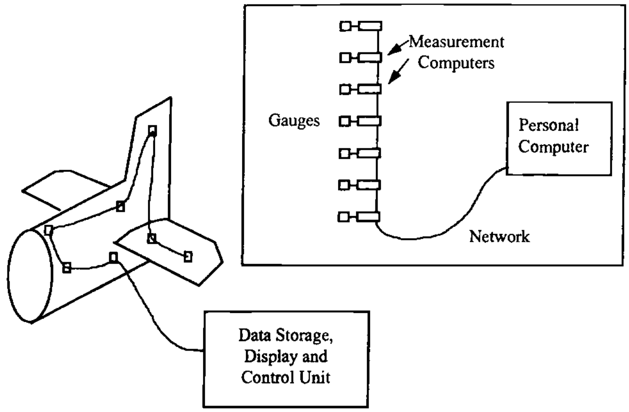

FIG. 5—*Networked data acquisition system.*

Networked Strain Data Acquisition Systems

If the move toward a measurement system based upon the manipulation of symbols (information) rather than the transmission of signals (analog data) is to be achieved, then the general approach to system design outlined in the previous section must be mapped to a particular technology for implementation. The system must now be seen as being composed of a collection of independent sources of strain information connected to an information-gathering device. Thus all measurements may be observed, monitored, and evaluated from a central location and each individual measurement site may be altered from that same central location. The three components that comprise this system (data sources, network, and computer) are shown schematically in Fig. 5, which can be compared to Fig. 2 to obtain a visual assessment of the difference in approach between the two systems. In this section, each major component of the system will be discussed separately.

The Strain Gage Data Source

At the outset, the move toward an information-processing system requires that the traditional lead wires used to connect strain gages to display or storage devices be replaced with a communications network. This in turn implies that the strain data be converted from continuous analog signal to digital value *at the measurement site* and that the decision about what part of the data to communicate is made at the site. In short, the movement to a communication-based paradigm for strain measurement systems requires that each strain gage be equipped with some rudimentary level of "intelligence" to perform the following functions:

1. High sampling rate local A/D conversion for a single measurement site,
2. Local data compression by automated feature detection and coding, and
3. Control of interface-to-communications system.

A system that performs these functions would also provide benefits from a purely instrumental point of view:

1. A dedicated bridge would be installed for each measurement site,
2. Lead wires would be of minimum length,

3. Bridge excitation could be controlled locally, thus making all strain measurements independent, and
4. Failure of any particular instrument would have no effect upon the operation of the overall system.

While the installation of a dedicated data acquisition system at each gage site may at first seem like overkill, it must be pointed out that since this system would handle the interface between analog and digital communications for a single measurement site only, the computing requirements become quite modest. For example, a typical system may seek to achieve a 1 kHz sampling rate for a single channel of strain data, would include a precision voltage reference, instrumentation grade amplifier and precision A/D converter, and may include a local temperature measurement for compensation. Electronic components to achieve these functions are commonly available and in particular can be constructed into functional systems built around any of a variety of available microcontrollers. These microcontrollers can be programmed to control an analog input channel and in addition contain sufficient computing resources to perform any required data compression or feature extraction. Finally, the microcontroller acts as an interface to the digital communication system.

In short, the installation of a computer at each strain measurement site provides the necessary technology to implement the shift in systems design from analog measurement to digital communications and by so doing minimizes the problems associated with the traditional paradigm. The strain measurement system now becomes an *embedded system* and as such becomes a cousin to the burgeoning number of embedded control systems that are being used for everything from shop floor automation to building controls [*12*]. The strain measurement system becomes a system of smart strain gages that communicate their data in an efficient manner when it is appropriate for them to do so. They are not "controlled," they "report."

Communications Network

Provided that the smart strain gage can be built, the system now becomes a collection of many independent measurement sites that are each serviced by some sort of microcontroller. Therefore, all measured data now exist in digital form and it becomes the task of the communications network to provide a means of allowing all of the smart strain gages to communicate their data to the central data-gathering facility. This system is no longer specialized as a particular type of instrumentation; it is a generic local area network and thus allows the system designer to take advantage of the very rapid technological advances that have taken place in this area over the past decade.

One of the various open network protocols such as I^2C, CANNet, ARCnet or ethernet provides a suitable architecture from which the overall system can be constructed [*13,14*].

Central Data-Gathering Facility

The task of gathering data from a network of independent data acquisition devices (smart strain gages) becomes comparatively simple if the network protocol has been adequately specified and if the smart strain gages themselves have been designed specifically to suit this network protocol.

Using a client/server protocol, each smart strain gage can be instructed to report its summary data according to one of a number of predefined scenarios. Gages can be configured to operate very differently, while still sharing the same communications network. Once the smart strain gages are properly configured, all data originates from the smart strain gages so the central data-gathering facility need do no more than passively receive data, decode its origin, and then display or store the data in the appropriate location. No specialized hardware is required to do this so long as the central data-gathering system has access to the communications network. This means that virtually any computer can be utilized as the central data-gathering facility, particularly if the network and communications protocol are chosen to conform to general standards.

Practical Considerations

While the new paradigm for strain measurement appears to provide some distinct advantages to traditional strain measurement systems, the components described in the previous sections combine to create a considerably sophisticated system that could easily become expensive, large, and unreliable. There are also certain considerations that must be met in order to provide a system that has the theoretical advantages described and that is also workable from a practical point of view:

- The smart strain gages must be small enough so that many of them can be installed in a reasonably constricted area. They must allow for local testing of the measurement as well as being capable of integration into the overall network.
- The communications network must be no more difficult to install than the network of lead wires that would be required for a traditional system.
- Adding or removing a measurement site must not have adverse effects on the operation of the rest of the system.
- Software and user interface issues must not dominate the implementation of the overall system.

In other words, for the new design to be accepted it must have all of the flexibility of the traditional system design while simultaneously providing the new capabilities described herein.

At the intersection between the idealized goals of a new measurement system methodology and the practical requirements for a successful strain measurement system lies a very rich space in which to design a solution to this problem. The simple network of analog strain gages is not sufficiently complex to provide the required functionality; it is too limited by the problems of extending analog measurements over long distances. On the other hand, a local area network of personal computers would easily provide the sort of flexibility and computing power to provide incredible functionality; but cost, physical size, and power requirements point to the obvious conclusion that a network of personal computers *does not* define a satisfactory solution either. Between these two extremes, however, represents an area of technological development that has progressed rapidly over the past decade. The technologies associated with "Embedded Controllers" allows for large networks of comparatively simple computing elements to be connected easily, cheaply, and extensively [*15*]. While no off-the-shelf solution is presently available to address the need presented for networked strain data acquisition, the components required to construct such a system *are* commonly available.

In 1993 a pilot project was initiated at the University of Victoria to determine the feasibility of constructing small computer networks for strain data acquisition. The resulting system comprises a stateless client/server network of data servers that connect via a bus system to a central data gathering facility which, in turn, communicates with a general purpose computer (for data gathering and analysis) via an RS-232 port.

The data servers include a complete precision analog to digital converter system with a nominal sampling rate of 1 kHz and 12 bit resolution. Since each data server services a single measurement site, it is possible to implement any bridge configuration and to offset the bridge as necessary in order to maximize the measurement range. The data servers are programmed with a variety of operating modes that allow a user to specify the sampling rate, the amount of digital low pass filtering to use, the reporting rate and a variety of feature extraction modes. For purposes of data acquisition for fatigue measurements, local peak detection provides an important method of maintaining a high sampling rate while communicating only important events. All sampling is timed locally, and there is an overall synchronization of time within the system that is conducted on a regular basis. Thus events are time-stamped to better than millisecond accuracy when they occur, ensuring accurate timing of data even in the event of delays in communication and storage because of heavy network traffic.

Data servers connect via press fit connections to the local area network thus allowing the network to be physically adapted as needed. Each data server is pre-configured with a unique address and all network communication is asynchronous, meaning that no precise timing or synchronization between data servers is required. Data servers can be physically added and removed from the network without taking the system off line.

A proprietary data bus is used as the interconnecting network, employing a pseudo-random collision handling methodology that allows the multiple data servers to communicate their data over the bus without the requirement for any explicit bus master or token passing arrangement. The bus runs through the installation as a ribbon and thus greatly reduces the amount of wiring required to configure the overall system. Of course, since timestamped digital data are being communicated over the network, the problems associated with long lead wires have been eliminated. Our prototype system allows the bus to be extended to lengths of up to 40 ft and longer bus extensions are under investigation.

An interface between the bus and general purpose computing devices has been developed that mediates between the instrumentation network and a standard RS-232 port. This allows any general purpose computer or even a dumb terminal to interface to the system, providing a means of acquiring data from the system and supplying control commands to the system. Using the communications server device, the entire data acquisition network is interfaced to any computer via a single serial port. In addition, it becomes possible to use modem technology and wireless modem technology to locate the data acquisition network remotely from the control and data storage computer.

The final component of the prototype system consists of a software package running on a generic computing platform that allows a user to specify the operating parameters desired for each data server independently, receives data from the network and stores it in independent data files. The data are stored in a manner that allows easy interfacing to a simple spreadsheet program for analysis. The goal in the design of this aspect of the system has been to eliminate the need for specialized computer knowledge so that noncomputer experts can configure the system and extract useful, meaningful data from it.

A schematic of the overall structure of this prototype system is shown in Fig. 6. A picture of the prototype data servers are shown in Fig. 7, including an early version, the working version, and an advanced pre-production version which employs surface mount component. The individual data servers are very small, measuring approximately 1 by 2 in. and weighing about 1 oz. This small size, combined with the relative ease of installation, provides a simple system that is easy to install.

The prototype system is capable of identifying up to 100 unique data servers on one network. Each data server maintains a nominal sampling rate of 1 kHz and the communication protocol running on the network has a bandwidth of approximately 500 samples/s. This latter unit of performance is important, since it represents the rate of information transfer rather than the simple data rate that the network can achieve. At 500 samples/s, we mean that the network is capable of communicating 500 time-stamped, addressed measurements per second. The exact composition of these measurements depends upon the system activity and the current mode of operation. For example, a single data server could regularly be sampling and reporting its data,

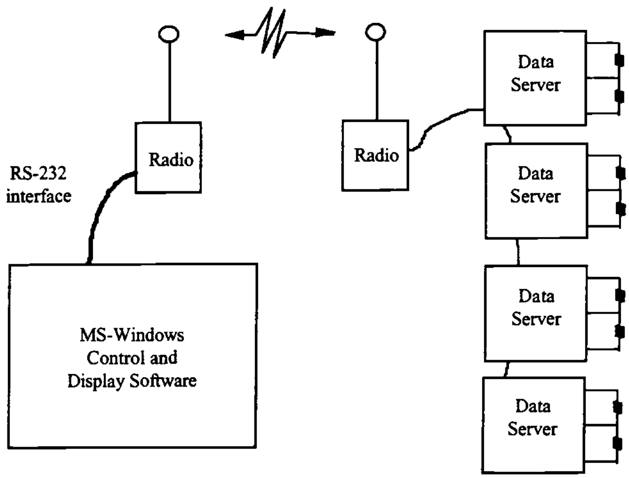

FIG. 6—*Prototype system schematic.*

or 100 data servers could be configured to sample and report at a rate of 5 Hz each. More realistically for the context of fatigue research, a relatively large number of measurement sites (on the order of 20 to 50) could be configured in peak detection mode and reporting extreme values in strain as they occur. The data servers contain small buffers that can store several dozen peak values if necessary before communicating the data. Therefore, even if every data server experiences a short duration burst of peak strains, no data will be lost, but will merely be queued up and communicated when the network resource becomes available. Since time stamping is performed within the data server when the event occurs, this operating strategy and a communications bandwidth of 500 samples/s provides an effective bandwidth that is much higher than 500 baud. Note that each data server samples its strain gage at the maximum 1 kHz rate at all times.

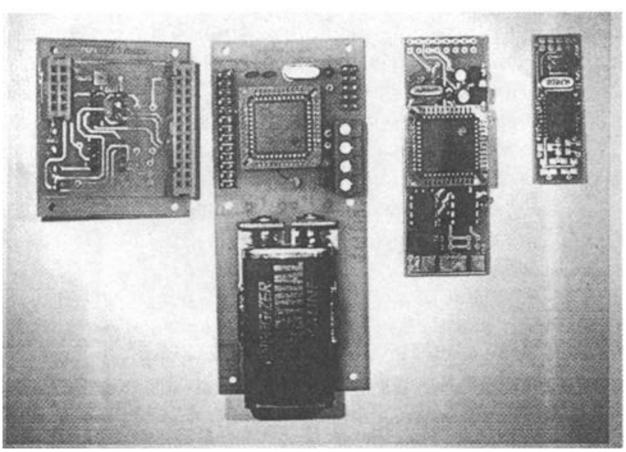

FIG. 7—*Prototype revisions. From left: stackable analog and digital circuit boards for first revision, integrated production version, and surface mount concept board.*

The system has been designed using standard microcontroller technology. Even so, the system described represents the third generation of this concept. The fourth generation system, employing surface mount technology, is presently being evaluated and the fifth generation, which employs 16 bit A/D conversion and a network communication rate of up to 5 kilo-samples/s, is being designed.

Even though the system has not been developed as a commercial product, the cost of the hardware for the system is competitive with the cost of data acquisition cards for personal computers. The data server boards include all necessary equipment to set up a strain gage measurement and so in fact provide increased convenience at a significantly lower cost than conventional data acquisition systems even at this prototype stage.

Discussion and Conclusion

The development of the networked data acquisition concept was motivated by considering the difficulties associated with performing strain measurement on large-scale applications in which many strain measurements are required and in mobile applications where there is a requirement for unobtrusive systems to allow strain measurements to be made *in-situ*. The strain measurement network that we have described and built addresses the problems identified with making effective strain measurements in these settings.

Application to large-scale strain measurement applications provides benefits both pragmatically and in terms of overall system performance. The installation of a data server at each strain measurement site immediately eliminates all of the considerations required to integrate multiple strain measurements into a single system. The effects of long lead wires and the difficulty with controlling multiplexers and bridge excitation over a distance are no longer a consideration. Instead, each gage site is serviced with an independent, lightweight, data acquisition system that provides a precision voltage reference and bridge completion circuit and also minimizes the analog signal path length. In short, each gage site is serviced with an optimal data acquisition system.

The overall system is now connected via a single data bus that connects the data servers in a daisy chain fashion so that no large umbilical cords of analog signals are required. The network is connected to a data gathering computer via a single RS-232 port to the communications server. It is possible to vary the network topology to include multiple communication servers on a single network loop, or multiple networks on a single RS-232 communication port. For very large applications, it may be desirable to run several independent networks that are distributed around the object under test.

By virtue of the independence of the multiple data servers, each gage site is sampled independently at a reasonably high sampling rate. Therefore, the equivalent sampling rate of this system for a 100-measurement site application is 100 kHz. Since preliminary data analysis and pattern feature extraction (such as peaks for fatigue analysis) are performed within each data server, no data will be lost provided the total information rate is below the network limitations. This is approximately 500 events/s on the present prototype and will be many times higher than this on future revisions of the system.

The networked data acquisition system described herein is very well suited to large-scale applications due to the independence of the measurements and the linear expansibility of the overall system. Any computer can now act as the central data repository and there needs to be no provision for any sort of expansion system since the computer requirements are not a function of the number of strain gage sites.

In the smaller scale, mobile application of the networked data acquisition system once again proves to be superior to traditional approaches to strain measurement. The lightweight and small size of the data servers allow them to be mounted in very tight quarters. By using wireless modem technology as a virtual wire between the communication server and the host computer, it becomes possible to remotely collect data from and reconfigure the data acquisition system without physically interfering with the system operation. Therefore, the networked approach to data acquisition makes the goal of *in-situ* strain measurement achievable. The prototype system is presently being used for strain data collection on mountain bicycles, speedboats, and helicopters and in all cases is providing data that have not been possible to obtain with traditional systems [9].

In both cases considered in this paper, the networked approach to strain data acquisition provides advantages over traditional techniques. Even at its present prototype stage of development, the networked data acquisition system is proving to provide superior performance at a lower cost than conventional measurement systems. As a result of this success, the development and refinement of networked data acquisition systems for strain measurement will continue.

References

[1] Wright, C. P., *Applied Measurement Engineering,* Prentice Hall, Englewood Cliffs, NJ, 1995.
[2] Sheingold, D. H., *Transducer Interfacing Handbook,* Analog Devices, Norwood, MA, 1980.
[3] Hewlett Packard Corp., "Practical Strain Gauge Measurements," *Application Note 290-1*
[4] Doebelin, E. C., *Measurement Systems,* McGraw Hill, New York, 1990.
[5] Dalley, J. W., Riley, W. F., McConnell, K. C., *Instrumentation for Engineering Measurement,* John Wiley and Sons, New York, 1994.
[6] Bryzek, J., "The Evolution of Smart Sensor and Transducer Design," *Sensors,* October, 1993.
[7] Goranson, U. G., "Damage Tolerance Facts and Fiction," *17 Symposium of International Committee on Aeronautical Fatigue,* 1993.
[8] Ellens, M., Provan, J., and McLean, G. F., "Application of a Computer Strain Gauge Network to In-Situ Stress and Fatigue Analysis," *Applications of Automation Technology to Fatigue and Fracture Testing,* American Society for Testing and Materials, Philadelphia, 1995.
[9] National Instruments, *Instrumentation Reference Catalogue,* 1995.
[10] Provan, J. W., "An Introduction to Fatigue," *Journal of Materials Education,* Vol. 11, Nos. 1, 2, 1989, pp. 1–104.
[11] Jayant, N. S. and Noll, P., *Digital Coding of Waveforms,* Prentice Hall, Englewood Cliffs, NJ, 1984.
[12] Goldschmidt, I. G., "A Data Communications Introduction to BACnet," *ASHRAE Journal,* November, 1994, pp. 22–28.
[13] Garrison, D., "Network Architectures for Embedded Control," *Technical Report,* University of Victoria Dept. of Mechanical Engineering, 1994.
[14] Stallings, W. *Handbook of Computer-Communications Standards, Vol. 1. The OSI Model and OSI-Related Standards,* MacMillan, New York, 1987.
[15] Raji, R. S., "Smart Networks for Control," *IEEE Spectrum,* June, 1994.

M. Ellens,[1] J. Provan,[1] G. McLean,[1] and M. Sanders[1]

Fatigue and Reliability Assessment Incorporating Computer Strain Gage Network Data

REFERENCE: Ellens, M., Provan, J., McLean, G., and Sanders, M., **"Fatigue and Reliability Assessment Incorporating Computer Strain Gage Network Data,"** *Applications of Automation Technology to Fatigue and Fracture Testing and Analysis: Third Volume, ASTM STP 1303,* A. A. Braun and L. N. Gilbertson, Eds., American Society for Testing and Materials, 1997, pp. 19–32.

ABSTRACT: This paper details a procedure by which reliable engineering components may be designed and produced to withstand specified fatigue loading situations. The procedure is a modification of the current aircraft industry's damage tolerance approach as outlined, among others, by Goranson [*1*]. For the design and manufacture of a specific component, the procedure incorporates a knowledge or specification of: (1) a typical fatigue loading history; (2) the determination of the stress time history at a location or locations of most concern; (3) typical fatigue crack geometries; (4) the mechanical properties, including the fatigue crack growth and closure characteristics, of the material from which the component is or will be manufactured; and, (5) in stochastic process terms, a time or cycle dependent description of the inherent statistical scatter that always accompanies fatigue crack growth.

While the procedure is quite general, its applicability is illustrated by an application to the improved design of mountain bicycle frames and components. Specifically and as an equivalent to standard aircraft flight-load histories such as TWIST, Mini-TWIST or FALSTAFF, the projected use of the results generated by the specialized data acquisition system whose development is described in a companion paper [2], is illustrated by estimating the fatigue crack growth characteristics and reliability of a mountain bicycle crank-arm. The procedure utilizes the loading history generated by "smart" strain gages situated on a mountain bicycle while the bicycle and rider are traversing a demanding mountainous trail. The acquisition system samples and captures strain data at 1 kHz with 12-bit resolution; performs peak detection and averaging calculations; transfers via digital radio the data to a Windows-based PC station at the trailhead; and analyzes these data both to determine stress profiles and to develop typical fatigue loading time-histories. Using this information, crack growth rate estimates based upon these load spectra, crack geometries typical of those found in mountain bicycle crank-arms, the crack closure concept, and the *da/dN* versus ΔK_{eff} for Al7075-T6 may be obtained. Coupling this information with a stochastic process interpretation of the scatter in these crack growth estimates leads to a meaningful description of component reliability.

KEYWORDS: load monitoring, stresses, fatigue, crack growth, stochastic processes, reliability

It is acknowledged that most industrial failures involve fatigue in one form or another. The assessment, however, of the fatigue reliability of industrial components being subjected to various fatigue loading situations remains one of the most difficult engineering problems still to be resolved. Furthermore, as both fracture and fatigue failures become more critical in higher

[1] Mechanical Engineering, University of Victoria, PO Box 3055, Victoria, BC V8W 3P6 Canada.

performance and complex structures and components, the need for more detailed information becomes more important.

Briefly, for fatigue processes and based upon Elber's [3] observation that fatigue-crack surfaces contact each other even during tension-tension cyclic loading, an understanding of various closure mechanisms and the influence of the plastic wake on the local crack-tip strain field have greatly enhanced the characterization of the fatigue-crack growth and fracture behavior of metallic materials, under, as exemplified in this paper, variable amplitude loading. Furthermore, most fatigue design requirements based on damage tolerance concepts assume the existence of flaws in a component. Such flaws detected by in-service inspections may either exist in the delivered component or develop as a result of fatigue during its service life. Acknowledging this and in order to improve reliability estimates, Provan and coworkers [4,5] have derived and experimentally investigated new reliability laws based on Markov and lognormal stochastic fatigue crack growth processes.

This paper systematically elaborates on these topics. General fatigue loading situations leading to an actual mountain bicycle loading history are detailed in the next section along with an illustration of the corresponding stress patterns and typical crack geometries encountered in mountain bicycle crank-arms. The fatigue crack growth characteristics of Al7075-T6 are listed in the subsequent section, prior to the presentation of an estimation of the fatigue crack growth rates for a typical crank-arm crack. Finally, the methodology behind the determination of the reliability of components, in general, and mountain bicycle crank-arms, in particular, closes this paper.

Fatigue Loading, Applied Stress Histories, and Cracks

In any study of the fatigue damage and reliability of engineering components, the loading patterns, or an estimation of their characteristics, must be determined. This paper highlights how the results generated by a new smart strain gage and data acquisition technique, described in [2], may be incorporated into investigations that lead to estimations of the fatigue crack growth and reliability characteristics of the component under review.

Mountain Bicycle Fatigue Loading Histories and Crank-arm Stresses

The approach to designing bicycle cranks and other bicycle components is similar to that of the aircraft industry. In-situ strain data are collected and standard load spectra are defined. Testing facilities capable of reproducing these standard spectra are then used to fatigue test, in this case, bicycle cranks to determine crack nucleation properties, failure mechanisms, and the cycles to failure. Simultaneously, stress analysis is performed and the results are used to develop accurate finite element models which can in turn be run through design optimization routines and included in reliability algorithms.

While it is recognized that the determination of the time-dependent stress field in bicycle cranks is an ongoing investigation, this section describes the approach, outlines the work completed and the work-in-progress. The work-to-date includes constant amplitude fatigue testing, preliminary 2-D finite element modeling of the press fit region, and preliminary in-situ load spectrum determination from a typical bicycle frame.

Modern mountain bicycle cranks are warm-forged, heat-treated, CNC machined, broached, and anodized Al7075-T6. The loading conditions and the stress distributions are complicated and in-situ data acquisition is difficult since the crank is rotating with respect to the rider and the bicycle frame. Typically, loading conditions range from pedaling loads of 2000 N during

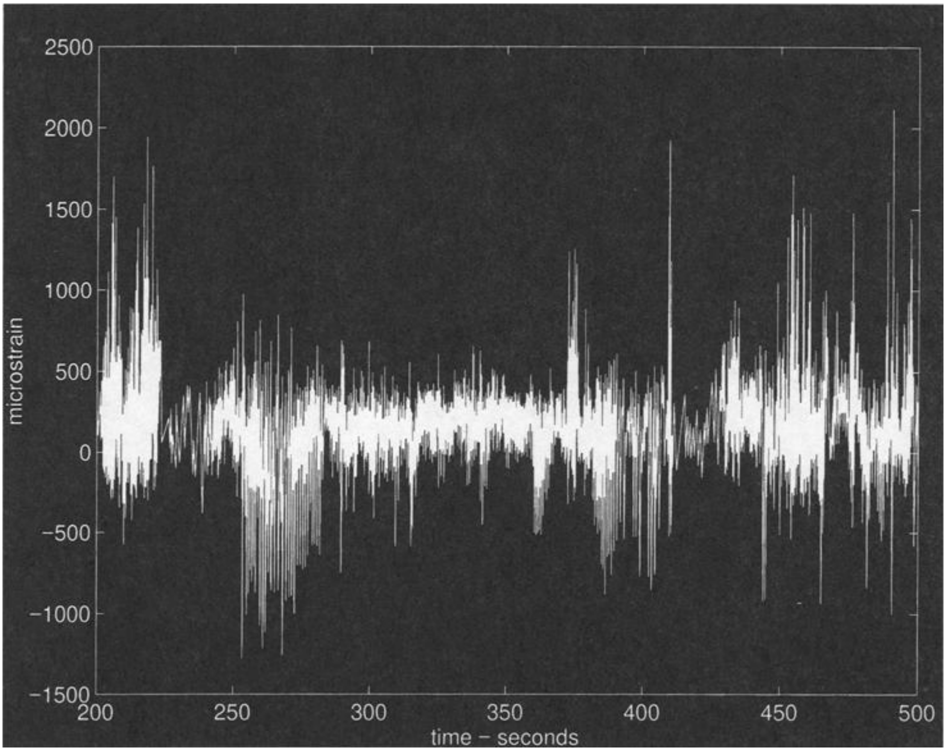

FIG. 1—*A typical 5-min loading pattern.*

hill climbing and sprinting [*6*] to impact G-forces of 3 to 5 Gs when landing from high jumps [*7*]. The stress distributions are generated by bending, torsion, and press fit conditions at the bottom bracket spindle.

The loading spectrum from the frame for a 5-min block is shown in Fig. 1 and for 4 s in Fig. 2. These suggest that the fatigue loading cycles may easily occur at a rate of 10 Hz. While these are representative spectra, they were generated by a smart strain gage situated near the center of the down-tube on a bicycle frame instrumented for the purpose of acquisition system testing (see the companion paper [*2*] for more details).

The results and geometry of a preliminary FEM modeling and analysis of the press fit region are shown in Fig. 3. Although in this example the stress levels are nonspecific, the stress distributions are representative. As expected, the high stress regions are near the corners of the press fit region of the crank-arm. The adopted FEM approach modeled the press fit region of the bottom bracket spindle and of the crank-arm. The same loads were applied to each model and varied until they deformed enough to allow for the press fit condition. The loads in this particular model were 800 MPa, tapering to 100 MPa.

Constant amplitude fatigue testing was performed on numerous crank-arms. The primary cause for the initiation of cracks, which eventually led to failure of the press fit region of these crank-arms, was fretting. Fretting failure occurred at the edges of the contact regions with the highest stresses and the black fretting residue from the aluminum was present as illustrated

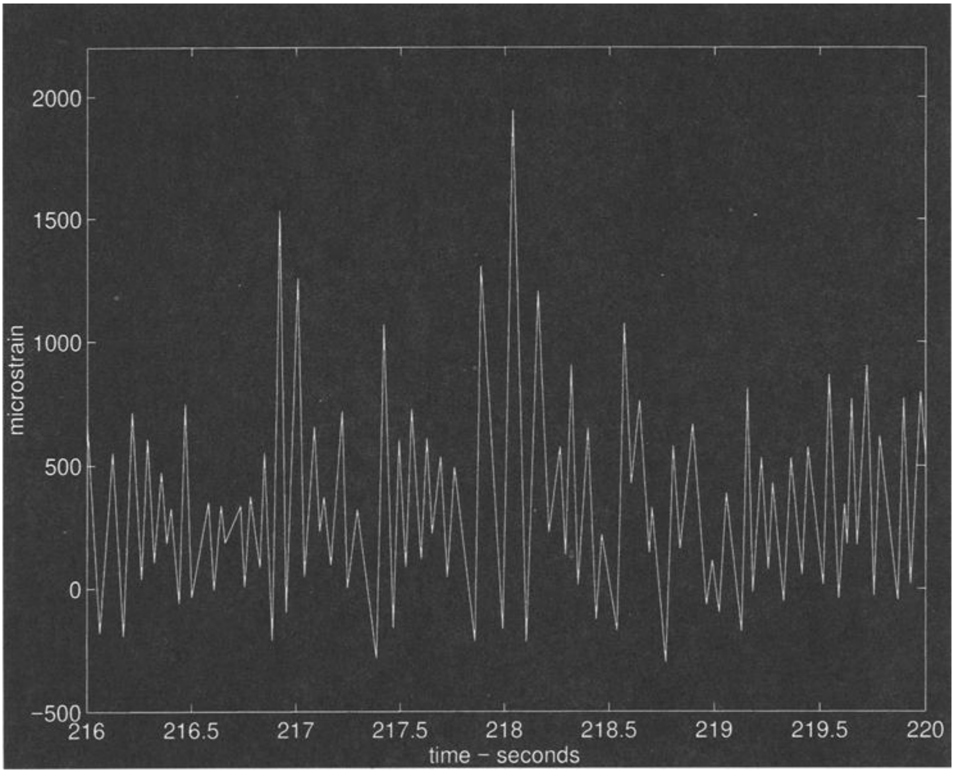

FIG. 2—*A typical 4-s loading history.*

in Fig. 4. In some cases, large sections of the surface broke free, indicating that coalescence of multiple cracks took place.[2]

The work-in-progress includes the development of a fatigue testing facility capable of reproducing in-situ load spectra, the design of a system to measure the in-situ pedaling loads, the experimentation with and testing of various methods outlined [*8,9*] to reduce the fretting problem, and the definition of load spectra for the frame, handlebars, and stems.

The precise nature of the fatigue induced cracks in this region of crank-arms is illustrated in Figs. 4 and 5. Figure 4 highlights a typical fracture surface, on which the fretting residue is clearly visible, while Fig. 5 illustrates scanning electron micrographs of one of the fracture surfaces. The latter clearly show both the region where the fatigue crack initiated and the fatigue striations caused by the crack penetrating into the material.

Fatigue Crack Growth Characteristics

This section deals with an implementation of fatigue crack growth and reliability assessment techniques first fully described in [*4*] and later presented in a modified form in [*5*]. These techniques have been compiled into the PRORAM© [10], software package.

[2] One of the first recommendations emanating from this investigation is that the fretting problem must be significantly reduced or eliminated in order to increase the reliability of this particular component.

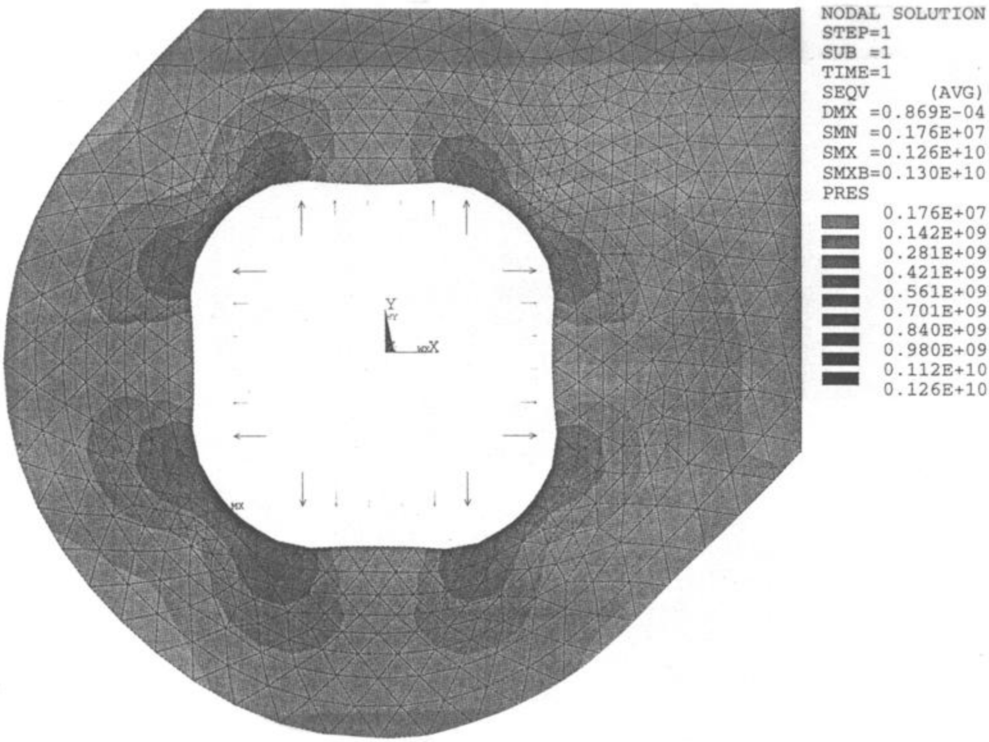

FIG. 3—*A FEM stress field in the press fit region of a crank-arm.*

PRORAM incorporates the fatigue crack closure concept. As discussed in [*5*], the opening stress intensity factor, K_{op}, associated with a quantitative knowledge of the crack opening load, P_{op}, is required for the determination of the effective stress intensity range factor, ΔK_{eff} defined by

$$\Delta K_{eff} = K_{max} - K_{op} \tag{1}$$

ΔK_{eff} is an important parameter for estimating the crack growth rate through, for example, a suitably modified Paris-Erdogan relationship [*11*]

$$\frac{da(t)}{dN} = c(\Delta K_{eff})^m \tag{2}$$

where $da(t)/dN$ represents the rate at which a crack of dimension $a(t)$ grows, and c and m are material characteristics. For the mountain bicycle crank-arm's Al7075-T6, the Paris-Erodgan parameters of Eq 2 were determined from those presented in [*12*] by a fit of $\log(da/dN)$ versus $\log(\Delta K_{eff})$ to the data and found to be:

Paris-Erdogan Parameters	c	m
Crank-arm Al7075-T6	4.45×10^{-6}	2.87

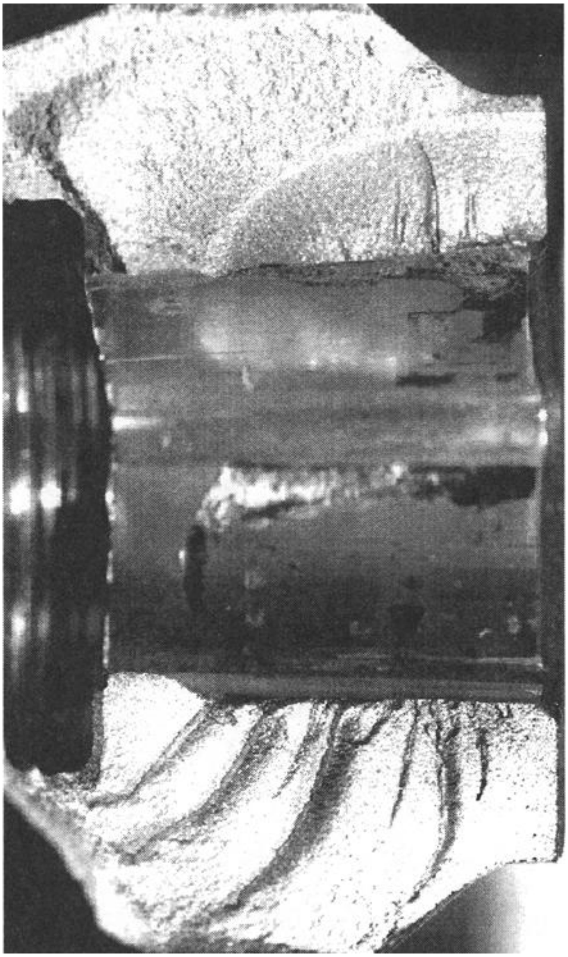

FIG. 4—*Fatigue fracture surfaces of a typical crank-arm which failed in the region of the press fit.*

Simulation of Fatigue Crack Growth in Crank-arms

From material fatigue crack growth characteristics similar to those presented above, an estimation of the anticipated crack growth and its statistical variation for actual industrial situations may be generated. The simulation technique, based upon the fast Fourier transform numerical technique [*4*] and incorporated into PRORAM, is designed specifically to give estimates of the reliability, availability and maintainability (RAM) of engineering components being subjected to fatigue degradation processes. The simulation requires the specification of two closure-lognormal stochastic parameters. The validity of lognormal crack growth rate models, including lognormal random processes, white noise, and random variable models, has been investigated using extensive fatigue crack growth data gathered from fastener hole specimens by Yang and his coworkers [*13*]. Hence, since the data do not as yet exist for Al7075-T6 and

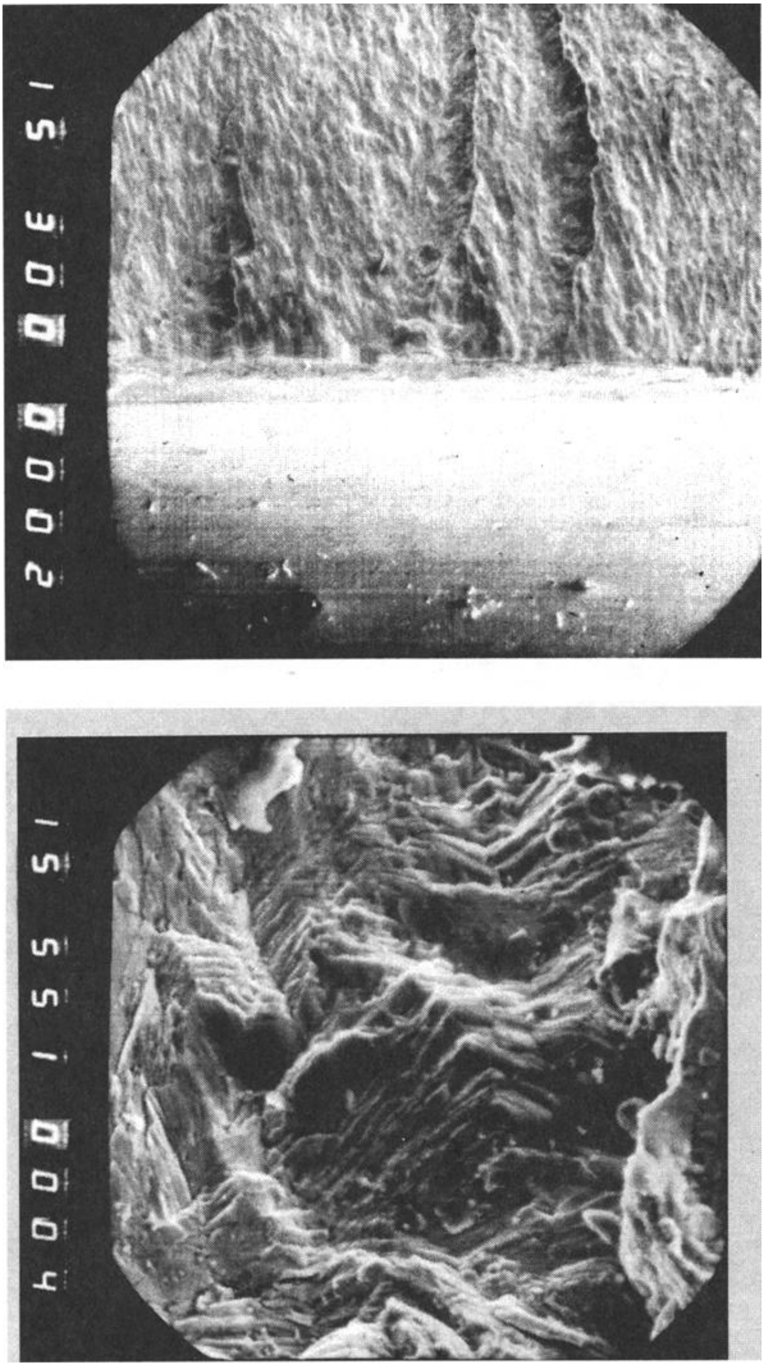

FIG. 5—*Electron micrographs of the fatigue fracture surfaces of a typical crank-arm which failed in the region of the press fit (original magnification 30× and 550×).*

the objective of this paper is to illustrate the general procedure, the same closure-lognormal stochastic parameters as those presented in [*4*], were assumed.

Closure-lognormal Parameters	σ^2	ξ
Crank-arm Al7075-T6	0.0047	0.00014

The simulation procedure also requires a method of transferring the previously presented standardized crack growth information into an estimation of crack propagation as it occurs in actual components and under specified loading situations. While it would have been preferable to choose a crack geometry similar to that illustrated in Fig. 4, there existed a significant variation in the crank-arm crack geometries to warrant some concern as to whether one crack could be selected as being the most representative. For this reason and in order to illustrate the procedure, a straight line crack propagating in a standard C(T) specimen, [*14*], was eventually selected. For an Al7075-T6 C(T) specimen with B = 2.5 mm and W = 50.8 mm, the growth of cracks with a load range ΔP = 2.5 kN, crack increment da = 0.2 mm, cycle increment dN = 1000 cycles was simulated 100 times. From this information both the mean and variance of the stochastic crack growth were obtained and are presented in Fig. 6. With this knowledge,

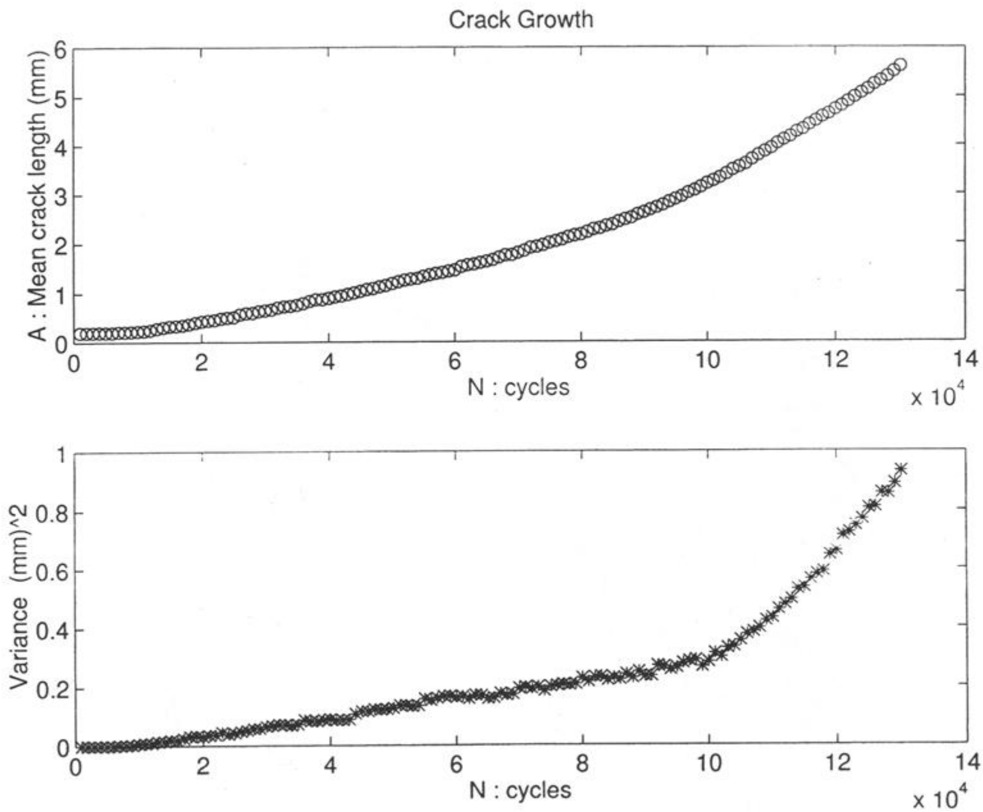

FIG. 6—*Simulated crack propagation for a typical crack in Al7075-T6.*

a complete reliability analysis of crank-arms can be carried out as illustrated in the following section.

Reliability

General Discussion

Stochastic processes describe random phenomena which have a multitude of possible outcomes. As detailed [*4,5*], by considering fatigue crack growth as a random phenomenon, a modified Markov process, namely the McGill-Markov process, was derived to determine the statistical regularity of the crack growth. Specifically, the crack propagation process is assumed to be a discrete-state, continuous-parameter and nonhomogeneous Markov process. By doing so, the transition probability density

$$P\{a(t) = j|a(\tau) = i\} = p_{ij}(\tau, t), \quad 0 \leq \tau < t, \tag{3}$$

where i and j are integer states and τ and t are times, becomes a variable which depends only on the time difference. Hence, if any time, t_n, the distribution, $P_i\{a(t_n)\}$, is known, then this distribution, in addition to a knowledge of the transition density function, p_{ij}, gives a procedure by which, at any future time of interest, the fatigue crack penetration distribution may be obtained by simply repeating the process as many times as is necessary.

In order to solve the (Chapman-)Kolmogorov differential equations which govern p_{ij}, an infinitesimal transition scheme must be specified [*15*]. In 1989, Provan and his coworkers, through examination of a variety of processes, developed a new form of intensity function which adequately describes the time evolution of material property degradation processes [*16*]. The intensity functions for this "McGill-Markov" process are:

$$q_j(t) = j\lambda(t),\ q_{kj}(t) = \begin{cases} (j - 1)\lambda(t) & \text{for } k = j - i, \\ 0 & \text{otherwise,} \end{cases} \qquad \text{for } t > 0; j = 1, 2, \ldots, \tag{4}$$

with the two degree of freedom $\lambda(t)$ for the McGill-Markov process being given by

$$\lambda(t) = \frac{\lambda(1 + \lambda t)}{1 + \lambda t^{\kappa}} \tag{5}$$

where λ and κ are positive empirical system parameters which are determined by a fit to either experimental or simulated data similar to that generated in the previous section. When these parameters are found, the material degradation response of components operating in a specified fatigue situation may be modeled. If the fatigue situation is changed, new system parameters must be determined.

The solution of the governing (Chapman-)Kolmogorov forward differential equation is well known [*15*]. For this linear, nonhomogeneous birth process it is given by

$$p_{ij}(\tau, t) = \binom{j - 1}{j - i} q^i (1 - q)^{j-1} \tag{6}$$

where, for the McGill-Markov process

$$q = e^{-\Lambda(\tau,t)}, \ \Lambda(\tau, t) = \int_{\tau}^{t} \lambda(t')\, dt' \tag{7}$$

Finally, in order to determine the entire history of the crack propagation distribution, the total probability may be continuously monitored via the fundamental *absolute probability relation*

$$P_j(t) = \sum_{i=1}^{j} p_{ij}(\tau, t)P_i(\tau), \tag{8}$$

where $P_j(t)$ is the probability of being in the jth (later) state at time t; $P_i(\tau)$ is the probability of being in the ith (earlier) state at time τ; and $p_{ij}(\tau, t)$ are the transition probabilities of a Markov process. Hence, for a McGill-Markov process it is necessary to specify the initial state and the transition probabilities in terms of λ and κ in order to describe the evolution of the entire process. This procedure has been fully implemented in PRORAM.

Reliability Analysis

Reliability maintenance and inspection/correction procedures via PRORAM and the McGill-Markov interpretation of material property degradation may now be undertaken. The reliability can be found if the critical crack size is known—it is the probability that the crack does not exceed this critical size. This quantity can be obtained by summing up the probability of a crack being of subcritical size.

A maintenance engineer ensuring the safe operation of a large number or fleet of similar structures specifies a desired level of reliability for each component (in this case the crank-arm) in the structure (in this case the mountain bicycle). Once this level has been determined, it becomes necessary to specify the schedule of the maintenance procedures that correspond to this desired level of component reliability. This may be accomplished by employing the McGill-Markov model to predict when the probability of component failure will reach the desired limit and then calling for an inspection/correction procedure. In this paper, inspection/correction processes are summarized as: stopping the degradation process for the entire fleet, identifying specific components that pose a risk to structural integrity, and carrying out the necessary maintenance procedures.

Analytically, as a result of the removal and replacement of these specific components during a single fleet inspection/correction procedure, there results two distinct populations. Population I, consists of the remaining components from the initial group, and Population II, is the group of replacement components. The reason for this distinction is that the McGill-Markov process is time-dependent or non-homogeneous. As shown [5], this implies that for an inspection/correction at time T_{inspect} the fatigue process continues for Population I, while for Population II it starts at time $T = 0$ and ends at time $T = T_{\text{final}} - T_{\text{inspect}}$. As long as the fatigue loading spectrum remains the same, the system parameters λ and κ for the specific component in question, can be used for Populations I and II. This process can easily be extended to include as many inspection/correction procedures as desired.

Another useful form of component reliability analysis is the optimization of fleet inspection times. As an example, suppose it is desired to minimize the total probability of component failure under the condition that there can be only one inspection/correction procedure carried out during the life expectancy of the components. Hence, the question, "what is the optimum time for this procedure?" may be posed. An inspection too early in the service life will remove few components that may subsequently fail, while a later inspection may be too late to remove components that will have failed. The optimum time for inspection will depend on several variables such as: critical crack size, repair size, inspection process, and the quality of replacement components.

Hence, the McGill-Markov model used in conjunction with a failure control methodology, PRORAM, can be a useful tool for obtaining valuable reliability information.

Mountain Bicycle Crank-arm Crack Propagation

This section presents, for a C(T) type crack in a mountain bicycle crack-arm being subjected to constant amplitude loading, the McGill-Markov stochastic fatigue crack growth properties of Al7075-T6. As described earlier, the two constant parameters λ and κ in the intensity functions $q_i(t)$ and $q_{kj}(t)$, defined in Eqs 4 and 5, are related to the stochastic properties of the material in question. Accordingly, the probability of the crack tip being in state i is increased, state by state, as the process progresses. Comparing the number of failed components to the totality of similar components, implies that there is a probability of the damage state becoming greater than a prescribed critical state at which failure occurs. Hence, λ and κ are the two system parameters which control this component's failure and play a significant role in both reliability assessment and in inspection/correction procedures. Applying the McGill-Markov model to the crank-arm data is an appropriate way to illustrate the capabilities of this approach.

These parameters are determined by a fit to fatigue crack growth data presented earlier. Several steps, however, must be taken before starting this iterative process. The first step is the normalization of data to an initial crack length of a_0 at time $t = 0$. This is done to eliminate the crack initiation stage. In the next step, the data are discretized into states of width Δa. Using the λ and κ, the probability histograms at future times are generated and the mean and variance calculated from $\mu_j(t) = \Sigma_j j p_j(t)$, and $\tilde{\sigma}_j^2(t) = \Sigma_j (j - \mu_j(t))^2 p_j(t)$. λ and κ, as system parameters, are thus determined by an iterative process of fitting the model predictions to those already available. In this way the following system parameters were determined.

System parameters	λ	κ
Crank-arm Al7075	6.9×10^{-5}	1.1

A plot of both the Markov and closure-lognormal simulation is shown in Fig. 7. The mean for the Markov simulation is shown as plus signs (+) and the initial simulation as circles (○). For the variance, the Markov is shown as a dotted line, and the closure-lognormal as *. Note that the mean for the McGill-Markov generated data closely reflect that of the closure-lognormal simulation, but that the variances are substantially different.

This comparison between the closure-lognormal simulated and the McGill-Markov model predictions, shows that the concept of describing fatigue crack growth in terms of stochastic processes, has the potential of being a flexible method of predicting the crack propagation statistics for industrially significant materials and situations.

Reliability Analysis of Al7075-T6 Crack-arms

The combination of the failure control system with the McGill-Markov model of PRORAM can be a very powerful tool for practical engineering reliability calculations. While two specific uses are highlighted in this section, others may be formulated without difficulty.

Reliability is defined as the probability a component will perform satisfactorily for a specified period of time. For determining reliability, the first step is to generate the crack size probability

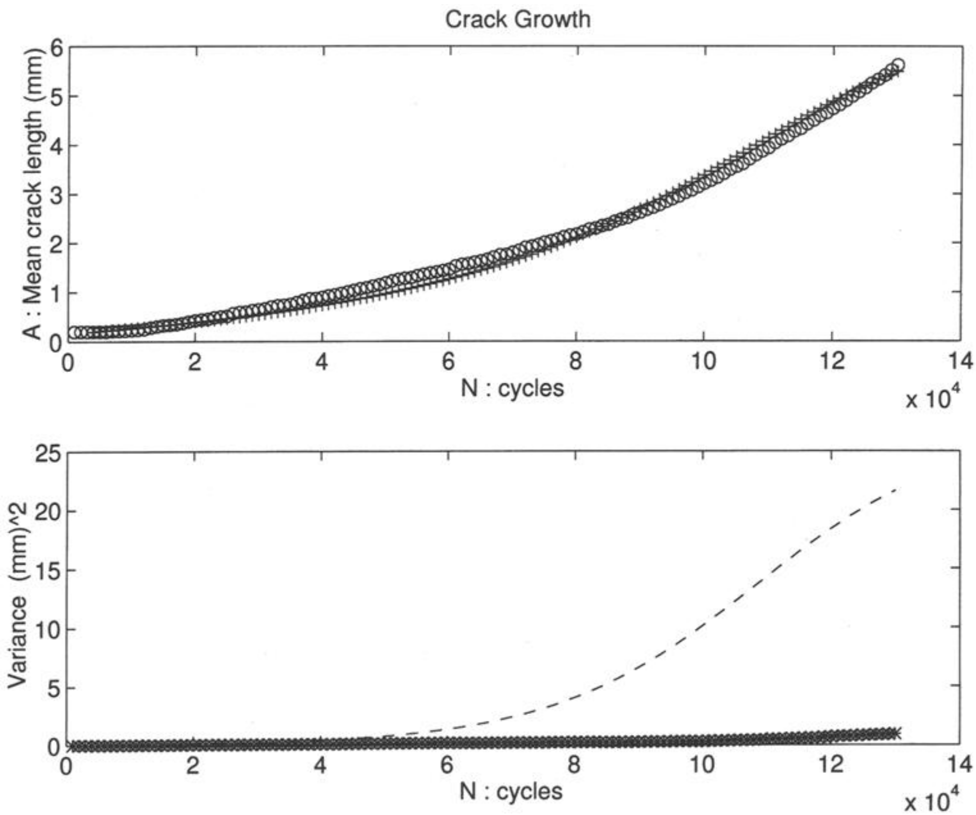

FIG. 7—*Mean and variance of the simulated closure-lognormal and McGill-Markov crack growths in Al7075-T6.*

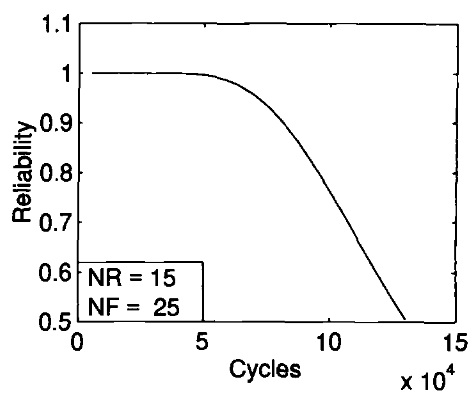

FIG. 8—*Reliability versus time for Al7075-T6 crack-arm, with* NF = *25, (a_{cr} = 5 mm).*

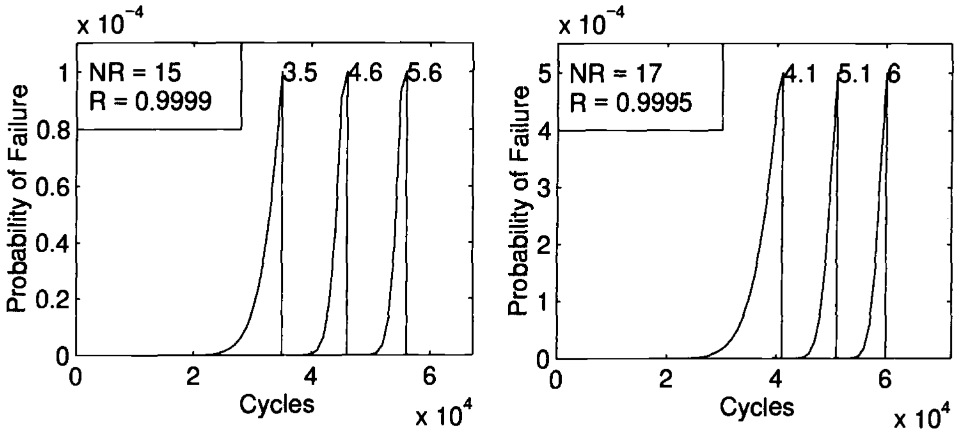

FIG. 9—*Inspection schedule for crank-arm at: (a) 0.9999, and (b) 0.9995 reliability levels.*

distributions, illustrated in the form of histograms, for given future times. The reliability can then be found if the critical crack size is known; it is the probability that the crack does not exceed this critical length. An implementation of this procedure is illustrated in Fig. 8 with the failure state (size) of $NF = 25$, ($a_{cr} = 5$ mm).

With reference to the section on reliability analysis, consider the determination of the appropriate inspection/correction intervals as a first illustration of the power of the McGill-Markov approach to improving reliability. By defining the replacement state (size), $NR = 15$, ($a_r = 3.0$ mm), and the desired reliability to be 0.9999, or $P_{fTOTAL}(t) = 1.0E{-}04$, the total probabilities of failure for times 0 to 6.5 E+04 cycles were obtained as illustrated in Fig. 9*a*. As can be seen, the inspection times for the appropriate inspection/correction procedures were determined as: 3.5 E+04, 4.6 E+04, and 5.6 E+04 cycles.

Alternatively, the results of a change in acceptable reliability level from 0.9999 to 0.9995 for a repair size, $NR = 17$ ($a_r = 3.4$ mm) are presented in Fig. 9*b*. As expected the repairs occur later than in the previous case.

As a second illustration of this approach, consider a specific inspection optimization analysis.

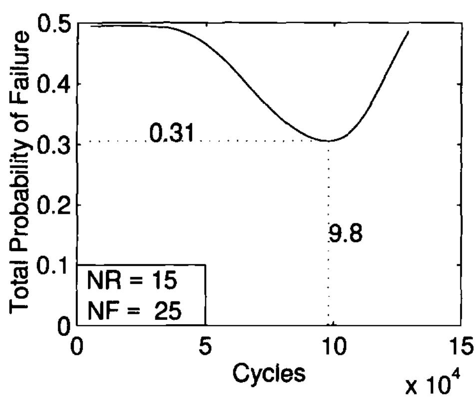

FIG. 10—*Optimum inspection time for mountain bicycle crank-arms.*

Suppose a design engineer is asked to optimize the time for a single inspection/correction operation during the life expectancy of an ensemble of components being subjected to similar fatigue loading situations. By specifying $NF = 25$ and $NR = 15$ for the failure and replacement states for this inspection, Fig. 10 is obtained. From this figure it is apparent that the optimum time for the single permissible inspection/correction is at 9.8 E+04 cycles and that the total probability of failure is decreased significantly by this single inspection.

These illustrations highlight the power of this procedure which combines a knowledge of the loading history acting on a component, the crack growth and closure characteristics of the material from which it is manufactured, typical crack geometries, and stochastic simulations of the actual crack growth rates and their inherent scatter.

References

[1] Goranson, U. G., "Damage Tolerance Facts and Fiction," 14th Plantema Memorial Lecture, *Proceedings,* 17th Symposium of International Committee on Aeronautical Fatigue, Boeing Commercial Aircraft Group, 1993.

[2] McLean, G., Prescott, B., and Ellens, M., "Network Data Acquisition Systems for Strain Data Collection," *Applications of Automation Technology to Fatigue and Fracture Testing and Analysis: Third Volume, ASTM STP 1303,* American Society for Testing and Materials, 1997.

[3] Elber, W., *Engineering Fracture Mechanics,* Vol. 2, 1970, p. 37.

[4] Farhangdoost, K. and Provan, J. W., "A Stochastic Systems Approach to Fatigue Reliability—An Application to Ti-6Al-4V," *Special Issue of Engineering Fracture Mechanics on Reliability of Structural and Mechanical Components under Fatigue,* G. I. Schuller, Guest Ed., 1995.

[5] Provan, J. W. and Farhangdoost, K., "A New Stochastic Systems Approach to Structural Integrity," *Proceedings,* FAA/NASA International Symposium on Advanced Structural Integrity Methods for Airframe Durability and Damage Tolerance, E. Harris, Ed., NASA Conference Publication 3274, 1994, pp. 603–619.

[6] Jim Martin MA, RPE, University of Texas, private communication.

[7] Hennig, E. and Goldman, D., "Effects of Shock and Vibration on Man," *Shock and Vibration Handbook 3rd ed.,* C. Harris, Ed., McGraw-Hill, New York, 1988, p. 44–54.

[8] Hattori, T., et al, "Fretting Fatigue Analysis of Strength Improvement Models with Grooving or Knurling on a Contact Surface," *Standardization of Fretting Fatigue Test Methods and Equipment, ASTM STP 1159,* M. Helmi Attia and F. B. Waterhouse, Eds., American Society for Testing and Materials, 1992, pp. 101–114.

[9] Waterhouse, R. B. and Trowsdale, A. J., "Residual Stress and Surface Roughness in Fretting Fatigue," *Proceedings,* International Conference on Frontiers of Tribology, A. Hilger, Bristol, April 1991.

[10] PRORAM©, Provan, J. W. and Sanders, M., *Fatigue Crack Growth and Mechanical Reliability Assessment,* Department of Mechanical Engineering, University of Victoria, Victoria, BC, Canada, 1996.

[11] Paris, P. C. and Erdogan, F., "A Critical Analysis of Crack Propagation Laws," *Journal of Basic Engineering, Transactions ASME,* Series D, Vol. 85, 1963, pp. 528–534.

[12] *Atlas of Fatigue Curves,* H. E. Boyer, Ed., American Society of Metals, 1986. Source: Meyers, M.-A. and Chawla, K. K., *Mechanical Metallurgy: Principles and Applications,* Prentice-Hall Inc., Englewood Cliffs, NJ, 1984, p. 716.

[13] Yang, J. N., Hsi, W. H., and Manning, S. D., "Stochastic Crack Growth Models for Application to Aircraft Structures," *Probabilistic Fracture Mechanics and Reliability,* J. W. Provan, Ed., Martinus Nijhoff, 1987, pp. 171–212.

[14] *Annual Book of ASTM Standards,* Section 3, Volume 3.01, American Society for Testing and Materials, 1995.

[15] Parzen, E., *Stochastic Processes,* Holden-Day, 1962.

[16] Provan, J. W. and Rodriguez III, E. S., "Part I: Development of a Markov Description of Pitting Corrosion," *Corrosion,* Vol. 45, 1989, pp. 178–192.

R. Sunder[1]

Cycle-by-Cycle Compliance Based Crack Length Measurement

REFERENCE: Sunder, R., "**Cycle-by-Cycle Compliance Based Crack Length Measurement,**" *Applications of Automation Technology to Fatigue and Fracture Testing and Analysis: Third Volume, ASTM STP 1303,* A. A. Braun and L. N. Gilbertson, Eds., American Society for Testing and Materials, 1977, pp. 33–42.

ABSTRACT: An attempt is made to track fatigue crack growth through cycle-by-cycle compliance estimates. The measurements are performed using continuous 16-bit data acquisition with multi-sample data averaging to reduce the influence of signal noise. With appropriate transducer ranging and data averaging, standard deviation in cycle-to-cycle estimates of crack size can be as low as one micron. Introduction of data smoothing techniques and further improvements in the quality of data acquisition hold the potential for cycle-by-cycle crack growth tracking over a wide range of growth rates.

KEYWORDS: compliance, fatigue crack growth, cycle-by-cycle estimates, data acquisition, data filtering, averaging

Advances in computer technology over the past three decades have consistently introduced the element of automation, repeatability, and organization into the process of mechanical testing [*1–3*]. Data acquisition determines the quality of test results and has benefited greatly from the steady drop in component costs. Twelve-bit analogue-to-digital converters (ADC) remained dominant for more than 20 years. But over the past five years, 16-bit ADCs have become inexpensive. More recently, a new type of low-speed, low-cost ADC called the sigma-delta converter was introduced, with 24-bit data resolution, that provides better than one part per million capability [*4*].

The jump in ADC resolution from 12 to 24 bits corresponds to an improvement by a factor of 4000. However, the quality of data acquisition can only be as good as the quality of acquired signals, and reducing signal noise below a certain extent is not an easy task. Real-time control and data acquisition boards contain a variety of digital and hybrid integrated chips, which generate noise or are susceptible to the influence of noise from other sources. Twelve-bit resolution corresponds to 5 mV over ± 10 V signal range. While engineering analogue electronics to restrict noise within this margin is by itself a demanding task, 16-bit resolution A-to-D conversions will be sensitive to noise even in the ± 1 mV level. Analogue signal filtering down to such levels appears to be impractical in a real-time fatigue test environment, where signal frequency can vary between 0.001 to 100 Hz. The 24-bit sigma-delta convertors incorporate digital filtering schemes to match required resolution, but these also restrict sampling rates to well below 100 Hz as resolution increases.

While the extent to which analogue signal filtering can be implemented is restricted, digital filtering of acquired data can considerably improve the quality of measurements [*5,6*]. As shown by Donald in [*5*], simple averaging of successively acquired data can dramatically reduce the adverse effects of signal noise.

[1] BiSS Research, 99, 14A Cross, Malleswaram, Bangalore 560003 India.

Unloading compliance is often used to track fatigue crack extension in laboratory testing of standard test coupons. Most application programs for automated testing employ periodic compliance measurements, assuming that crack growth in the interim would be negligible or of the same order as the resolution of crack length estimates. This study was aimed at evaluating the extent to which fatigue crack growth can be tracked on a cycle-by-cycle basis, taking advantage of improvements in the quality of data acquisition.

The next section describes how resolution of data acquisition can affect crack length estimates. This is followed by a description of two experiments employing cycle-by-cycle crack length estimates. The experiments were performed using an Intelligent Mechanical Test Controller (IMTC) with firmware for continuous data acquisition [7]. The IMTC is connected to a host PC-compatible computer for test automation.

Effect of Quality of Data Acquisition on Crack Length Measurement

The ASTM Test Method for Measurement of Fatigue Crack Growth Rates (ASTM E 647) describes procedures for crack length measurement from compliance in fatigue crack propagation (FCP) testing down to 10^{-7} mm/cycle. The results of such tests serve as inputs to determine the relationship between crack growth rate, *da/dN*, and stress intensity range, ΔK. ASTM E 647 recommends crack length estimates with a resolution of at least 0.1 mm or 0.2% of specimen width, whichever is greater.

Figure 1 shows how compliance resolution affects crack size resolution in the case of CT specimens with load line compliance measurement. Compliance resolution was simulated by assuming that both load range and crack opening displacement (COD) are estimated with the same resolution (bits). Crack size resolution was computed by assuming the worst case of a one bit loss in measured load range with one bit gain in COD or vice versa.

It may be noted that resolution is determined by the less of the two data ranges covered (load

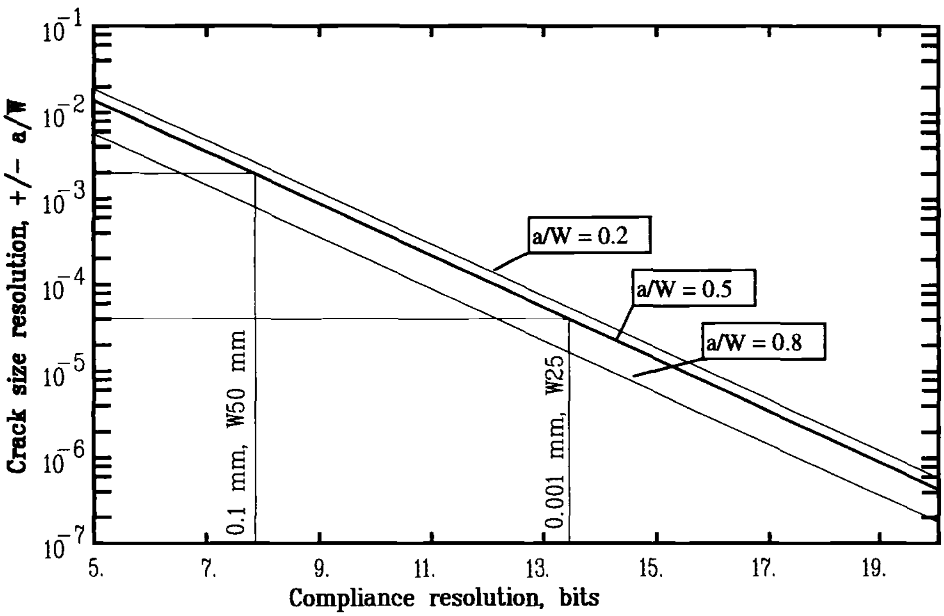

FIG. 1—*Effect of compliance resolution on crack size resolution.*

or COD) in a single compliance estimate. Thus, in 12-bit data acquisition, if load variation over a compliance data window is one-eighth of transducer range and COD variation is one-half of full range, compliance resolution would come down to nine bits.

It would appear that resolution requirements of ASTM E 647 can be met by 0.5% or 8-bit resolution in compliance estimates (see marker corresponding to 0.1 mm resolution for 50 mm wide CT specimen). This requirement is usually satisfied by 12-bit data acquisition, since measured load and COD data windows in the course of a test may not fall below 5 to 10% of selected transducer. Procedures for automated FCP testing incorporate periodic measurements of compliance from a burst of load and COD data collected over a single or multiple fatigue cycles. The periodicity of measurement is usually adequate to ensure that crack extension in the interim does not exceed specified resolution of crack length estimate.

Advances in cost effective data acquisition now permit better quality of compliance estimates than was possible a few years ago. 16-bit data acquisition makes it possible to make compliance estimates with 12-bit resolution or better. As shown in Fig. 1, this translates to an order of one micron on a 25-mm wide CT specimen. With the resolution of crack size estimates approaching the order of crack growth rate, *da/dN*, the potential of FCP test applications widens:

1. Cycle-by-cycle crack extension can be tracked at growth rates of the order of 10^{-4} mm/cycle and greater.
2. Transient phenomena associated with microstructure, overloads, etc., can be tracked more precisely, as smaller crack growth intervals are detected.
3. FCP testing can be extended to smaller specimen sizes, to enable fracture mechanics studies on miniature coupons cut from components.
4. Fatigue crack retardation and arrest can be detected more easily. Requirements for sustained crack growth at near threshold conditions could be relaxed to permit accelerated estimates of threshold conditions.

Cycle-by-cycle crack length monitoring requires continuous data acquisition and analysis by the host computer.

Scheme for Continuous Data Acquisition

Continuous data acquisition was implemented on the IMTC along with an on-line data averaging scheme, designed to reduce the influence of random signal noise. The data acquisition and averaging scheme works with user programmable parameters: selected channels, scan rate, sample size, and skip count. The last two are described schematically in Fig. 2. The parameters are preset for the entire data acquisition session that can then continue indefinitely, restricted only by disk space on the host computer. By suitably selecting sample size and skip count, the desired degree of averaging as well as data overlap is obtained.

When real-time data logging is initiated on the IMTC, data are continuously collected in a 256-byte ring buffer by an interrupt service routine (ISR) driven by a real-time clock pro-

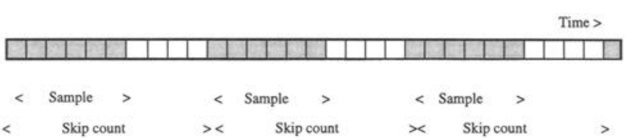

FIG. 2—*Strip chart settings in continuous data acquisition. Raw data are scanned at preset frequency. Sample size (grayed) determines extent of averaging. Skip count determines overlap in averaged data. The above schematic corresponds to sample size of six and skip count ten.*

grammed to deliver the required scan rate. Another ISR plucks the required sample of data points across the selected data acquisition channels, computes their sum and deposits the results into a second 16 kilobyte ring buffer. The sum when divided by sample size gives average. However, if the sample size is a power of two, the sum represents the average with additional pseudo resolution. Thus, the sum of 16 12-bit samples would give pseudo 16-bit resolution, while 16 16-bit points would yield pseudo 20-bit resolution. Elimination of the additional pseudo bits gives the average. In this study, a sample size of 16 was chosen with a skip count of 16. Under constant input signal conditions, these sampling parameters provided standard deviation less than one bit.

During the test, the PC-host computer continuously monitors the status of the IMTC ring buffer containing the growing stream of averaged data. These are periodically milked by the PC for storage and analysis. This process is asynchronous in that there may be a delay of a few seconds between the moment data are acquired from the test coupon and the moment they reach the PC. However, as data acquisition into the primary and secondary data buffers is strictly clock driven, the PC is in a position to establish the associated time tagging with individual data points. In the course of analysis, software on the PC proceeds to identify turning points in the incoming data stream to separate data from individual cycles. These are then processed to determine specimen response including compliance over a specified data window.

Experimental Procedure and Test Results

The quality of continuous data acquisition was evaluated by testing two different specimens on different servohydraulic testing machines, both controlled by an IMTC and the same application software. Test A was on a large capacity testing machine, with load and COD variation occurring over a small fraction of transducer range. Test B was on a small capacity testing machine, better suited to meet specific test requirement. The results from the two tests accentuate the significance of tailoring transducer ranges to suit specific tests.

In Test A, a 25-mm thick, 51-mm wide Al-alloy L77 C(T) specimen was tested with a 120 kN load cell and 4 mm range COD gage. The test coupon was precracked to 6.25 mm at P_{max} = 15 kN and R = 0.1. The test was then continued at P_{max} = 27 kN and R = 0.1 using a triangular wave form at 0.2 Hz. Continuous data acquisition on the PC was initiated from the very first cycle after precracking. The scan rate on IMTC was 1.6 kHz with a sample size and skip count of 16. This gives an effective data logging frequency of 100 Hz, yielding 500 load versus CMOD points per cycle.

In Test B, a 10-mm thick 40-mm wide Al-alloy 7075-T6 C(T) specimen was tested with a 10 kN load cell and 0.4 mm range COD gage. The specimen was precracked to 8 mm at P_{max} = 2 kN, R = 0.1, then tested at P_{max} = 4 kN, R = 0.1. Test wave form was triangular at a frequency of 0.5 Hz. Data scan rate on the IMTC was set to 3200 Hz with sample size and skip count of 16, giving an effective data logging frequency of 200 Hz or 400 load versus CMOD points per cycle.

The clevis grips in both tests were designed in accordance with ASTM E 647 requirements. In the course of the test, data were continuously acquired and logged into computer storage for post processing. 3 000 000 readings from over 6 000 cycles were collected in Test A. 15 000 000 readings from over 30 000 cycles were collected in Test B.

During post processing, unloading compliance was computed over a 65% data window from 95% down to 30% of maximum load. Crack length was computed using expressions in ASTM E 647. Effective modulus for plane strain was assumed. In case of Test A, observed crack length was 0.5 mm longer than estimated value at the end of the test. In Test B, no perceivable difference could be noticed between observed and estimated crack length at the conclusion of the test.

Figure 3 shows estimated crack size from cycle-by-cycle compliance measurements without

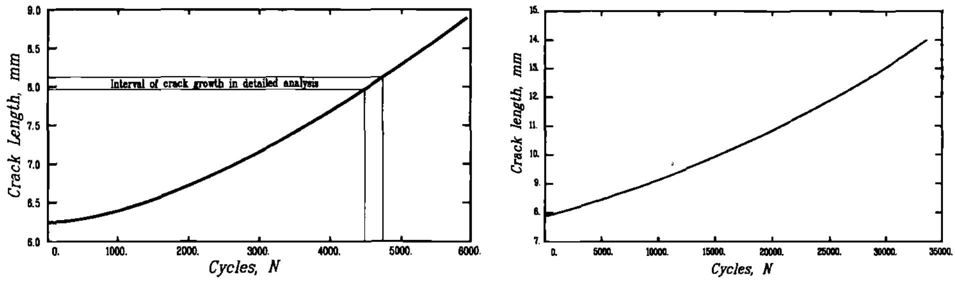

FIG. 3—*Cycle-by-cycle estimates of crack length in Test A (left) and Test B (right).*

any smoothing of data. When viewed in small segments, the estimates reveal the scatter observed in the experiments.

Compliance records for the first 500 cycles in Test A and 1 000 cycles in Test B appear in Fig. 4. There appeared to be a settling period over the first 150 cycles. This cannot be attributed to electronic equipment warm up, because the system had been switched *On* several hours

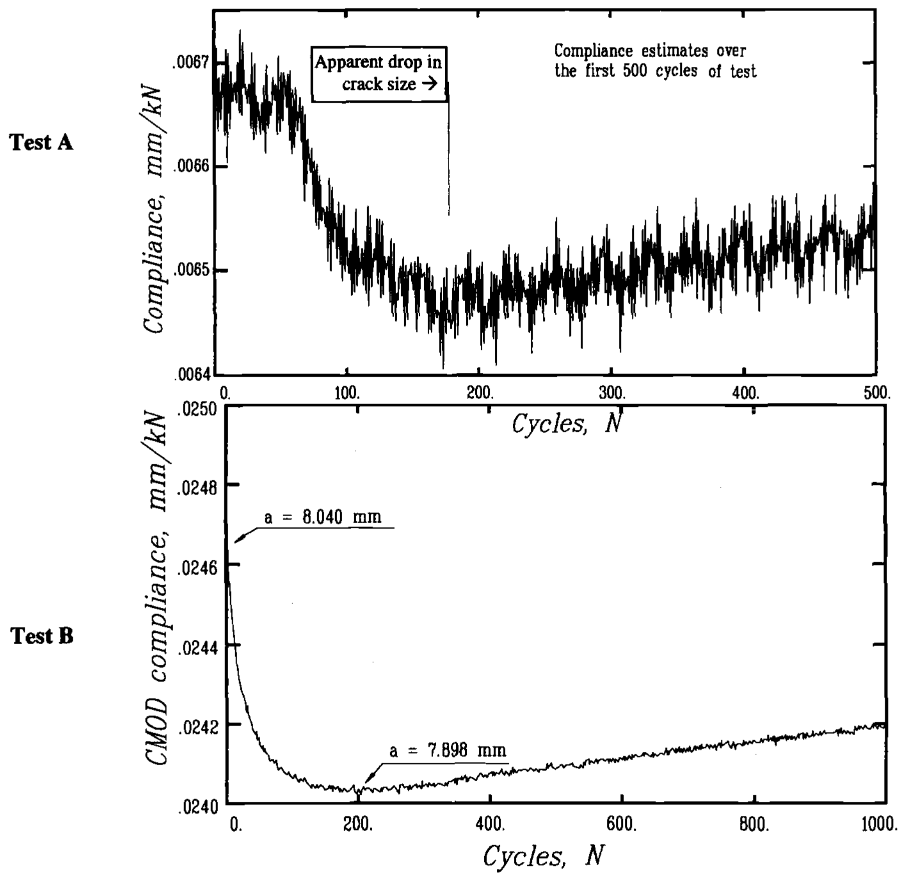

FIG. 4—*Compliance at the commencement of cycling at higher load level appears to initially drop before increase, associated with crack extension.*

earlier. However, after the initial settling period, compliance readings registered a steady growth over the entire interval of measurement. In both tests, precracking had been performed at about half the load level used in subsequent cycling. The drop-in measured compliance is attributed to the development of a rougher crack front due to enhanced shear mode cracking at the higher stress intensity. The associated difference in estimated crack size appears to be of the order of 0.15 mm. The drop in compliance is gradual and appears to require crack extension. Therefore, effect of larger plastic zone and crack tip blunting may be ruled out as these would have caused an immediate reduction in measured compliance.

Overall, crack length estimates in both tests meet resolution requirements of ASTM E 647. However, the compliance estimates from Test A show much greater scatter than those in Test B. In Test A, load range over which compliance was measured was under 15% of load cell range, while COD data in the compliance window covered just 3% of full transducer range. This effectively reduced resolution of compliance measurements to about nine bits. In contrast, load range in the compliance window for Test B was almost 30% of load cell range, while COD data variation exceeded 25% of transducer range. This adds up to an effective compliance resolution exceeding 13 bits.

In Test A, the largest peak to peak variation in compliance is of the order of ±0.6%, corresponding to about ±0.08 mm variation in crack size. A wavy pattern is observed in cycle-by-cycle compliance variation in Test A, with a periodicity of 20 to 30 cycles. This adds up to a real time frequency of under 0.01 Hz and may not be attributed to beat frequency effects in data acquisition. A periodic variation in COD gage output of under one micron over the compliance window would be adequate to cause the observed wavy pattern. This may be caused by cycle-to-cycle jogging of one of the cantilevers on the COD gage across a specimen knife edge due to minor misalignment. By smoothing compliance estimates with a 40-point incremental polynomial, cycle-to-cycle scatter is considerably reduced, leaving only the wavy pattern and the associated variation in crack length estimates of about ±0.02 mm. The pattern was seen throughout the test as seen in a sample of intermediate data in Fig. 5.

In contrast to Test A, the results from Test B do not show any systematic compliance variations apart from the small amount of random scatter. Extreme peak-to-peak variation in com-

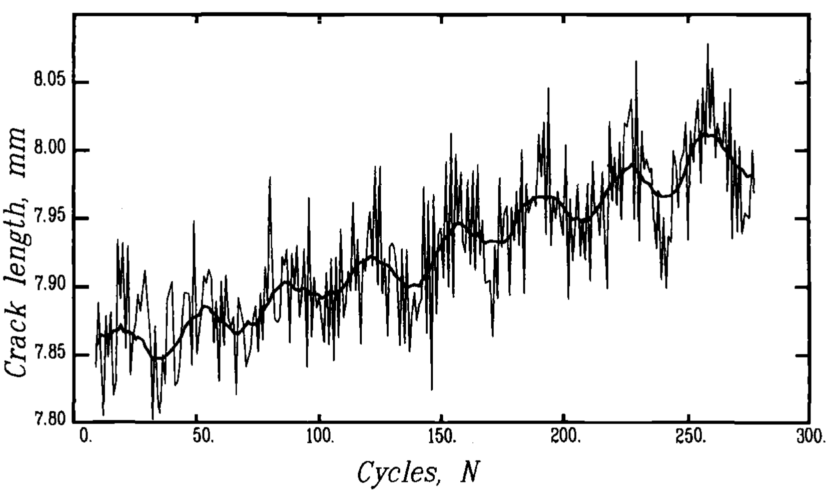

FIG. 5—*Crack length estimates after approximation of compliance data by a 40-point incremental polynomial. Data from cycle interval shown in Fig. 2 for Test A.*

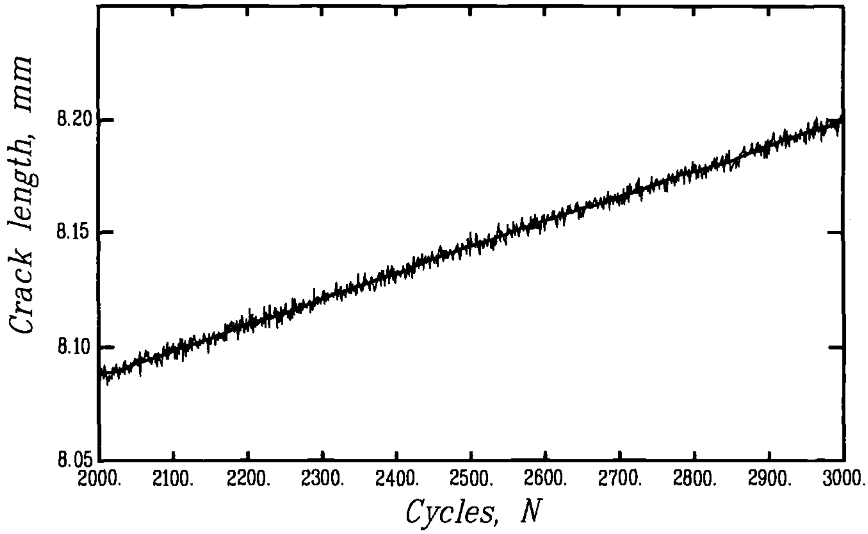

FIG. 6—*Test B: Cycle-by-cycle estimates of crack length over 1000 cycles. Line in middle represents 15-point incremental polynomial approximation.*

pliance is under ±0.05% in successive cycles, corresponding to under ±0.01 mm and to better than 12-bit resolution in compliance estimates. Figure 6 shows crack length estimates over one thousand cycles. Also shown is an approximating line obtained from a 15-point incremental polynomial.

Figure 7 shows crack length estimates from individual compliance measurements over 100

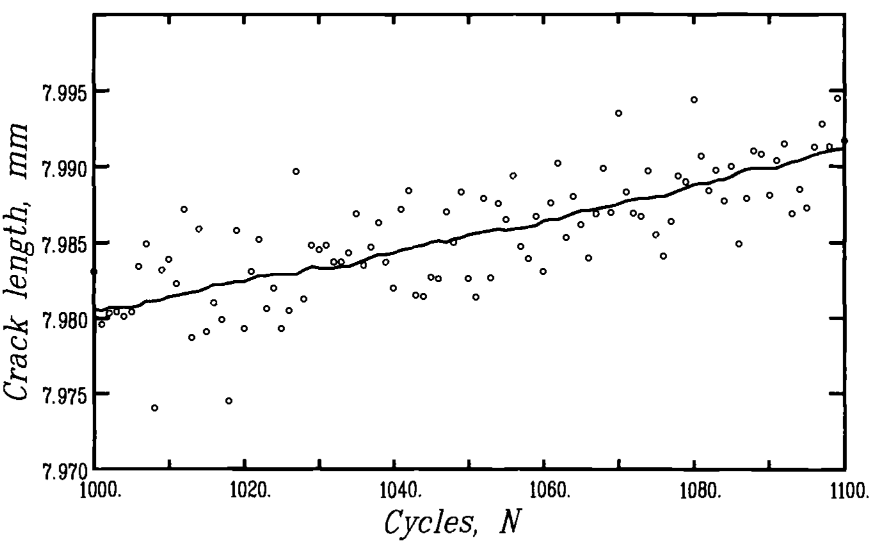

FIG. 7—*Test B: Cycle-by-cycle estimates of crack length over 100 cycles. Line in middle represents 15-point incremental polynomial approximation. The slope of this line represents crack growth rate,* da/dN ~ *10^{-4} mm/cycle.*

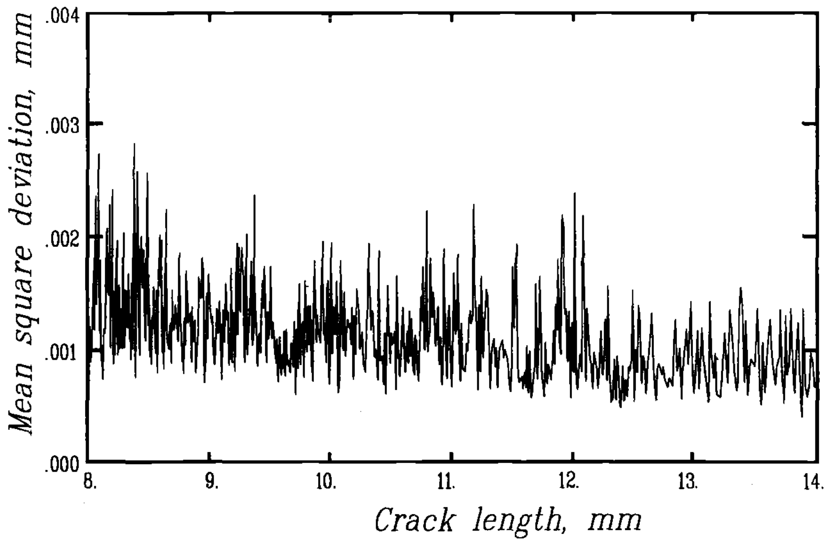

FIG. 8—*Test B: Mean square deviation of crack length estimates from approximating line. 15-point incremental polynomial was used to fit data from over 30 000 cycles.*

cycles. Note that extreme data points are restricted to a random variation in crack size of under ±0.01 mm, which are largely smoothed out by the 15-point incremental polynomial, i.e., an incremental polynomial stretching across 15 successive load cycles.

ASTM E 647 recommends crack growth rate estimation over crack extension interval not less than ten times the resolution of crack length estimation. The standard deviation from a set of successive measurements serves as an indication of this interval. As the crack may also extend during such a set of measurements, standard deviation may be computed using the distance of individual points from the approximating line. The results from such a calculation for Test B appear in Fig. 8. The mean square deviation of incremental data sets of 15 points from the approximating polynomial never exceeded 0.003 mm. As expected, this number falls with increase in a/W and may in fact drop below 0.001 mm at a/W exceeding 0.5. Assuming even the worst case of 0.003 mm and ASTM E 647 requirements, it would follow that crack growth rate can be estimated from as little as 0.03 mm of crack extension.

Figure 9 provides a summary of how crack growth rate estimates vary, depending on the procedure and parameters used in data processing. The dots in the figure are crack growth estimates using the simple secant method covering 150 cycle intervals, which corresponds to between 0.015 and 0.045 mm of crack extension. The continuous line going through these points represents growth rate calculations using a 150-point incremental polynomial. The line at the top was obtained using a 1 000-point incremental polynomial. It has been offset to avoid clutter. The 150-point incremental polynomial data indicate less scatter than the points from secant method. Point-to-point variation in growth rate in case of the 1 000-point approximation is less than half of that in case of the 150-point approximation.

The data in Fig. 9 suggest, that provided resolution of compliance estimates is better than 12-bits, consistent estimates of crack growth rate can be obtained from crack extension intervals as low as 0.02 to 0.05 mm. The deviations observed in case of the 1 000-point approximation appear to be persistent and unlikely to diminish noticeably even with more smoothing of raw data. Their source appears to be an interesting subject for further work.

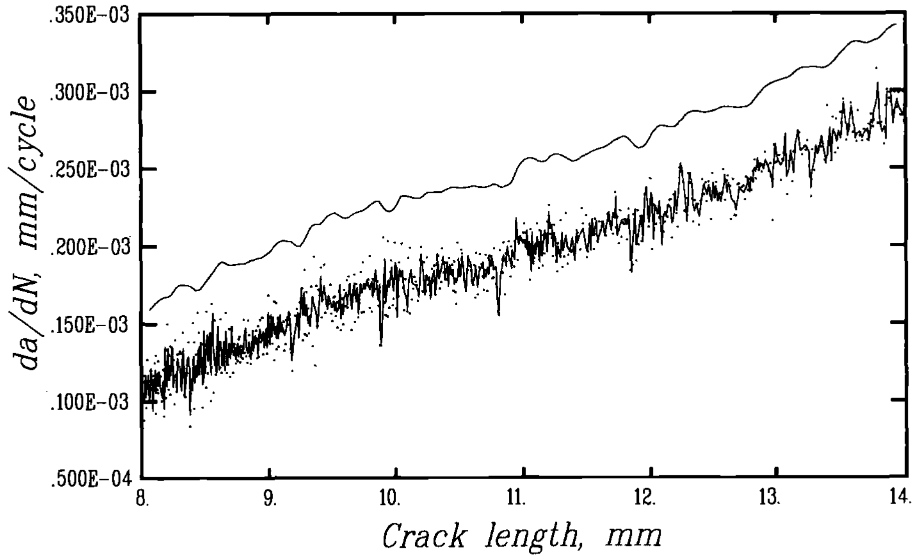

FIG. 9—*Test B: Estimated crack growth rate versus crack length. Dots represent* da/dN *calculated using secant method over 150-cycle interval. Lower continuous line shows* da/dN *estimates using 150-point incremental polynomial. Line at top shows results from 1000-point incremental polynomial. This line was offset to avoid clutter.*

Concluding Remarks

Advances in data acquisition technology permit continuous logging of transducer output which can be processed to resolve smaller extent of crack extension in a consistent manner. Higher resolution data acquisition using both hardware capability as well as data averaging make this possible. At the same time, it is extremely important to ensure that transducer outputs in the course of the test will vary over a reasonable fraction of total range. Noise in transducer output signal, signal sweep during test, resolution of data conversion and data filtering on the two channels being logged, all together control resolution of compliance measurements.

As crack length resolution is enhanced to 0.001 mm and beyond, the interval of crack growth required for consistent crack growth rate estimates reduces. This may offer advantages in studying thresholds, local microstructure related transients, where *da/dN* can be reliably determined from a smaller interval of crack growth and also in studies of growth rate exceeding 10^{-3} mm/cycle, where crack extension can be tracked on a cycle-by-cycle basis. It must be noted however, that the enhancements described in this paper relate to resolution, rather than to precision of crack length estimates. Improvements in resolution of crack length estimation are adequate to increase precision of crack growth rate as systematic errors if any, are lost in the derivative. Precision of crack length estimates will determine the quality of stress intensity estimates. However, one may assume the influence to be diminished by the square root relationship between K and a. The possibility of systematic error was underlined by "reduced" estimates of crack length after an incremental increase in load level that indicate an effect on measured compliance of crack extension mode.

The present study involved continuous data acquisition at about 3 kHz, which restricted the maximum frequency of testing to about 1 Hz. The performance of data acquisition and analysis requires substantial improvements to enable such testing at higher frequencies.

Acknowledgment

One of the experiments described in the paper was performed at Wright Research and Development Center, Wright-Patterson AFB, Ohio. The support of Andy Lackey and Dave Maxwell, University of Dayton Research Institute in organizing the experiment is gratefully acknowledged.

References

[*1*] *Use of Computers in the Fatigue Laboratory, ASTM STP 613,* H. Mindlin and R. W. Landgraf, Eds., American Society for Testing and Materials, 1976.

[*2*] Braun, A. A., "A Historical Overview and Discussion of Computer-Aided Materials Testing," *Automation in Fatigue and Fracture: Testing and Analysis, ASTM STP 1231,* C. Amzallag, Ed., American Society for Testing and Materials, 1994, pp. 5–17.

[*3*] Edwards, P. R., "Control and Monitoring of Servo Hydraulic Fatigue Machines Using a Computer Network, with Adaptive Control of Amplitude and Frequency," *Measurement and Fatigue—EIS '86,* J. M. Tunna, Ed., EMAS, 1986, pp. 3–17.

[*4*] AD771x series Data Sheets, Analog Devices, Norwood, MA, USA.

[*5*] Donald, J. K., "Sampling Rate Effects in Automated Fatigue Crack Growth Rate Testing," *Automation in Fatigue and Fracture: Testing and Analysis, ASTM STP 1231,* C. Amzallag, Ed., American Society for Testing and Materials, 1994, pp. 124–145.

[*6*] Holland, M., "Interference Reduction in Analogue Data Collection," *Meaurement and Fatigue—EIS '86,* J. M. Tunna, Ed., EMAS, 1986, pp. 135–152.

[*7*] Sunder, R. and Venkatesh, C. S., "Dedicated Microprocessor-Based Controller for Fatigue Testing," *Applications of Automation Technology to Fatigue and Fracture Testing, ASTM STP 1092,* A. A. Braun, N. E. Ashbaugh, and F. M. Smith, Eds., American Society for Testing and Materials, 1990, pp. 36–64.

Robert L. Tregoning[1]

Feasibility Study of Alternating Current Potential Drop Techniques for Elastic-Plastic Fracture Toughness Testing

REFERENCE: Tregoning, R. L., "**Feasibility Study of Alternating Current Potential Drop Techniques for Elastic-Plastic Fracture Toughness Testing,**" *Applications of Automation Technology to Fatigue and Fracture Testing and Analysis: Third Volume, ASTM STP 1303,* A. A. Braun and L. N. Gilbertson, Eds., American Society for Testing and Materials, 1997, pp. 43–65.

ABSTRACT: A prototype alternating-current potential drop (ACPD) measurement technique has been developed for quasistatic and dynamic *J-R* curve testing. This well-known technique has classically been used in fatigue crack growth testing, but may find its niche in dynamic testing of conducting materials when more classical compliance and direct current potential drop methods are unsuitable. The system was first optimized and a calibration curve was generated to relate a/W and ACPD output using fatigue crack growth testing for $0.47 < a/W$ 0.85. Calibration using quasistatic, unloading compliance, elastic-plastic crack resistance (*J-R*) testing where the higher stress level matches the proposed usage was also conducted for $a/W > 0.6$. These various calibrations relationships were applied to ACPD output in quasistatic and dynamic *J-R* curve tests. Preliminary results indicate that calibration relationships must be based on the higher stress, *J-R* testing to accurately predict the final crack extension in these tests. The quasistatic *J-R* curves developed from the ACPD technique generally agree well with unloading compliance results. Dynamic *J-R* curves calculated directly from ACPD also concur with key-curve results although further system development is necessary for system optimization at these high testing rates.

KEYWORDS: potential drop, ACPD, toughness testing, dynamic fracture testing, J-R curve, HY-130 steel

Crack length measurement is required for both quasistatic and dynamic elastic-plastic toughness testing to determine J-integral cracking resistance (*J-R*) material behavior. The compliance technique is most often utilized in single-specimen, quasistatic testing [*1*,*2*]. This method is acceptable for standard testing, but is limited for high-temperature (>175°C) and corrosive or aqueous environments. Further, for dynamic ($\dot{K} = 10^3 - 10^5$ MPA$\sqrt{\text{m}}$/s) *J-R* curve determination, the compliance technique is unsuitable since it requires repeated unloadings at regular crack growth intervals. Historically, dynamic testing has been conducted using either multi-specimen testing or normalization techniques to infer crack length from the load (P) versus plastic load-line (Δ_{pl}) behavior [*3–5*]. Multispecimen testing suffers because it provides only the initiation toughness (J_{Id}) and it can be expensive (and time-consuming) due to the amount of testing required. It is also nontrivial to accurately perform as accurate J_{Id} determination requires that the crack growth be arrested at specified intervals (ASTM Standard Test Method for J_{IC}, A Measure of Fracture Toughness, E813-89) in successive test specimens. This required accuracy is difficult to obtain dynamically as small changes in load-line displacement (Δ) can

[1] Mechanical engineer, Naval Surface Warfare Center, Code 614, 3A Leggett Circle, Annapolis, MD 21402-5067.

lead to large crack growth increments (Δa). Normalization techniques have been developed based on assumptions of contained ligament and deformation J plasticity that may be too severe for generalized testing requirements [5–7].

Clearly it would be advantageous to possess a technique that can be utilized quasistatically in severe environments and dynamically for physical crack extension measurement. One potential system is the direct current potential drop method (DCPD) that relates the bulk change in specimen electrical resistance to crack length. This technique is popular and well-established for fatigue crack growth testing (ASTM Standard Test Method for Measurement of Fatigue Crack Growth Rates, E647-95), has seen application in quasistatic *J-R* curve measurement [8–10], and been employed in dynamic *J-R* curve testing [11]. A drawback of this technique in quasistatic testing is its poor resolution. Bulk resistance changes are often less than the measurement system sensitivity near crack initiation that can significantly alter the computed *J-R* material response [8]. Dynamically, this technique also suffers from contributions to the measured potential from the magnetoelastic effect [11]. This effect contributes to specimen impedance through changes in the relative permeability (μ_r) as a function of the stress rate ($\dot{\sigma}$). This contribution masks the impedance variation that is proportional to crack growth during the short duration of the dynamic loading event.

A derivative of DCPD is the alternating current potential drop (ACPD) technique and its feasibility for quasistatic and dynamic fracture toughness testing is studied here. It has primarily been utilized for fatigue crack growth testing [12,13] although there is limited experience with it in quasistatic elastic-plastic fracture toughness testing [14]. Advantages of the method in this testing, the principals of the technique, and the ACPD measurement system developed for this testing are subsequently detailed. Also described are initial system tests to evaluate reference probe location and verify the accuracy of the compliance measurements. System calibration to determine crack length as a function of the normalized ACPD signal output was conducted using fatigue crack growth rate (FCGR) and quasistatic *J-R* curve testing. These calibration relationships are discussed as is their application to quasistatic *J-R* and dynamic drop tower *J-R* curve experiments. Finally, the current strengths and weaknesses of this prototype system are illuminated.

ACPD Technique

Principal of Operation

Consider a point, alternating current source (I_{ac}) on a plane that is large compared to the signal propagation depth (t, $h \gg \delta$ in Fig. 1) and containing a crack with uniform depth (a). The potential drop between two points (V_{pd}) in the field is described by

$$V_{pd} = I_{ac}Z = I_{ac}(R + i\omega l) \tag{1}$$

where R is the circuit resistance, ω is the signal frequency ($2\pi f_c$), and l is the circuit inductance. If edge effects are ignored in this simplified case, the equipotential lines become uniform and parallel to the crack face after a suitable distance from the source. Further, R and l can be idealized by the following expressions,

$$R = \frac{L\rho}{t\delta} \tag{2}$$

$$l = \frac{\mu_o \mu_r L}{8\pi} \tag{3}$$

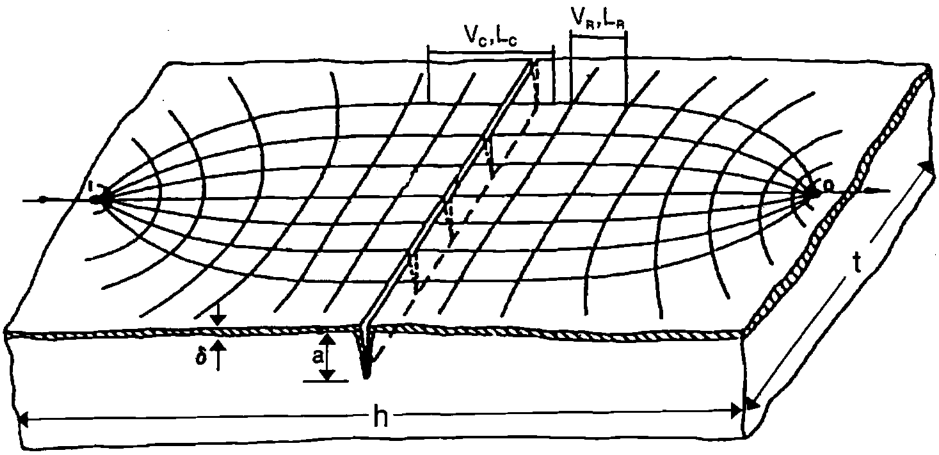

FIG. 1—*Idealized AC field for two-dimensional crack in a plane.*

where

δ = signal penetration depth (Fig. 1),
t = width of plane (Fig. 1) or specimen thickness,
μ_o = free space permeability = $4\pi \times 10^{-7}$ H/m,
ρ = material resistivity, and
L = measurement length.

For steel specimens, at frequencies of ≈20 kHz, it can be shown that the inductance contribution to the impedance is roughly equivalent to the resistive contribution to impedance [*11*]. More importantly, however, both terms are linearly proportional to the measurement length, L. Assuming μ_r, μ_o, ρ, δ, and t are all constant, the ratio between the potential difference measured across the growing crack (V_C in Fig. 1) to that of a reference state measured away from the crack (V_R in Fig. 1) is given simply by

$$\frac{V_C}{V_R} = \frac{2a + L_C}{L_R} \tag{4}$$

where L_C and L_R are the distances between the crack and reference probes respectively (Fig. 1).

Normalization of Eq 4 is useful to account for changes in the measured potential drop that can occur during testing of a single specimen and also for potential variations measured initially among different specimens and tests at a given crack length. Initial differences among specimens can result from a number of factors. Variability in probe placement, temperature, probe contact point integrity, specimen geometry, and external sensor requirements are several sources that affect the measured, baseline potential. With this in mind, a potential drop (PD) ratio can be defined as

$$PD \equiv \frac{(V_c - V_{ci})}{V_r} \times \frac{V_{ri}}{V_{ci}} \tag{5}$$

where lower case subscripts for c and r represent the measured crack and reference state, not the actual state; and the subscript i refers to the initial state. Initial potential differences are simply calibrated through the ratio of V_{ci}/V_{ri}. Further, if the measured potentials are linearly proportional to the actual potentials ($V_c = nV_C$ and $V_r = mV_R$), Eq 5 provides the same *PD* value for measured and actual potential drop regardless of system gain. Using this definition of *PD*, Eq 4 can be rearranged to provide a theoretical relationship between crack growth (Δa) and PD:

$$\Delta a = \frac{2a_i + L_c}{2} \times PD \tag{6}$$

where a_i is the initial crack length. Now, if a normalized *PD* (PD_n) is defined as $PD \times (2a_i + L_{ci})/(2a_1 + L_{c1})$ where a_1 and L_{c1} represent values for the first test specimen, Eq 6 leads to the following constant, proportional relationship:

$$\Delta a = \frac{2a_1 + L_{c1}}{2} PD_n \tag{7}$$

For a conventional test specimen, the accuracy of Eqs 2–7 is a function of the uniformity of the potential field and also the measurement system integrity. Establishing and measuring a uniform field depends on input current placement, reference and crack probe placement, specimen geometry (notably *t* and *h* in Fig. 2) and δ. Obviously, when δ/t, $\delta/h \ll 1$, the actual

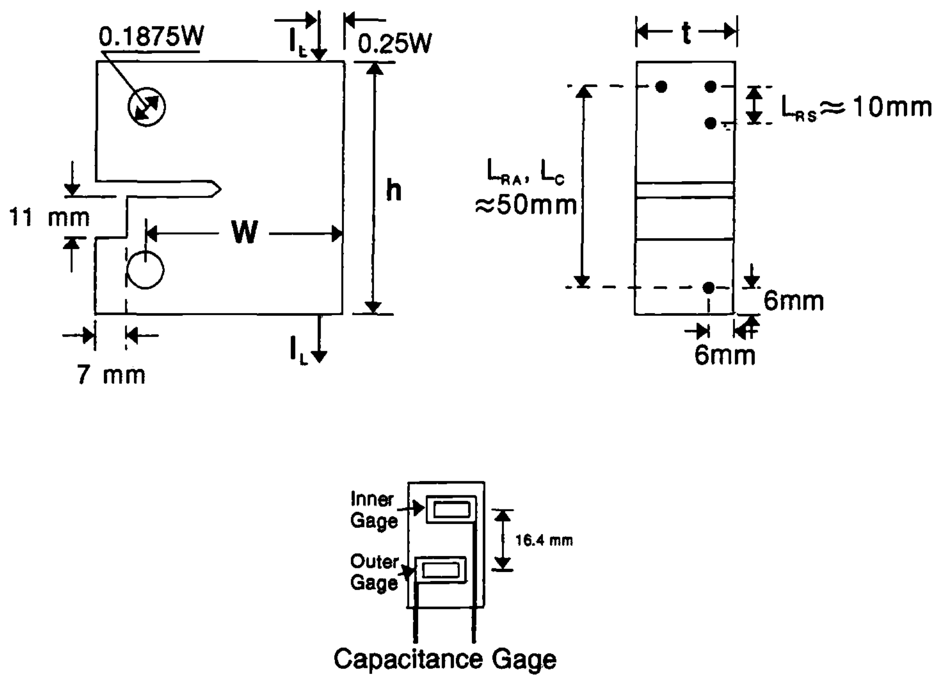

FIG. 2—*Modified 1T C(T) specimen geometry.*

field will more closely represent the one-dimensional assumptions inherent within the formulation. The penetration depth is described by the following expression [12],

$$\delta = \sqrt{\frac{\rho}{\mu_r \mu_o \pi f_c}} \tag{18}$$

Consequently, for a given material, as the input signal frequency increases, δ decreases and the accuracy of the one-dimensional assumptions increases.

Decreasing δ has the added benefit of increasing the sensitivity of the measurement system. In typical steel specimens, $\mu_r \approx 500$ and $\rho \approx 5.8 \times 10^6$ S/m. Choosing $f_c = 20$ kHz results in $\delta \approx 0.07$ mm. In a C(T) specimen geometry (Fig. 2), this depth results in an effective conducting area which is approximately 100 times smaller than in DCPD. Therefore, the current necessary for ACPD measurement drops proportionally and much more sensitivity is possible in ACPD for similar current magnitudes. Penetration depth is also influenced by the stress magnitude. Increasing the stress, decreases μ_r, which subsequently increases δ [12]. This effect implies that the relationship between Δa and PD_n may be dependent on the stress state within the specimen and consequently on the type of test performed (such as high-cycle fatigue, low-cycle fatigue, *J-R*). Further, the relationship may also be sensitive to crack growth within a single test. These possible dependencies will be addressed.

ACPD Measurement System

The ACPD system developed for this study consisted primarily of an input current circuit and the potential monitoring system (Fig. 3). The HP 3325 function generator was used to generate a 1 V peak-to-peak, 20 KHz signal that passed through a HP 6524A power supply/amplifier wired for constant current output. Amplifier gain was set between 0.45–0.5 A, near the system's maximum power output for the frequency chosen. The signal then passed through the specimen, on to an ammeter for current monitoring, and was then terminated back at the constant current amplifier. For tests where the reference potential drop was measured on the test specimen location (L_{RS} in Fig. 2), only one specimen was placed in the circuit. When the reference potential was measured on an adjacent specimen, it was placed in series with the test specimen (Fig. 3) using the identical current attachment points.

The input current leads were located on the C(T) specimen's top and bottom faces, at 0.25W from the back edge (Fig. 2). This location was chosen to minimize interference between input and measurement leads, and to ease specimen placement within the various clevis arrangements utilized in this testing. Shielded coaxial cables were utilized for both current input and potential monitoring leads. The cables were terminated at closed lugs at the specimen attachment end. The lugs were connected between two tightened nuts on a flathead 6-32 screw which was tightened into the specimen. The cable shielding from each lead was attached to a common ground.

The potential monitoring leads were attached across the crack face as illustrated in Fig. 2. Their location was dictated by the space required for the various crack mouth opening displacement gages utilized in subsequent testing. V_c was measured diagonally across the specimen thickness in an attempt to average potential variations due to crack curvature. Test specimen reference (L_{RS}) and adjacent specimen reference (L_{RA}) locations are also indicated on this figure. Either or both of these reference locations were used in this testing.

Each potential signal sampled was initially amplified using an Ithaco 565 preamplifier (floating ground transformer) powered by a HP 62236B supply. The amplified signal was then linked to a Tektronics AF501 bandpass filter for filtering and further signal amplification (×100). The AF501 output was recorded by one of three methods depending on the type of test. Manual

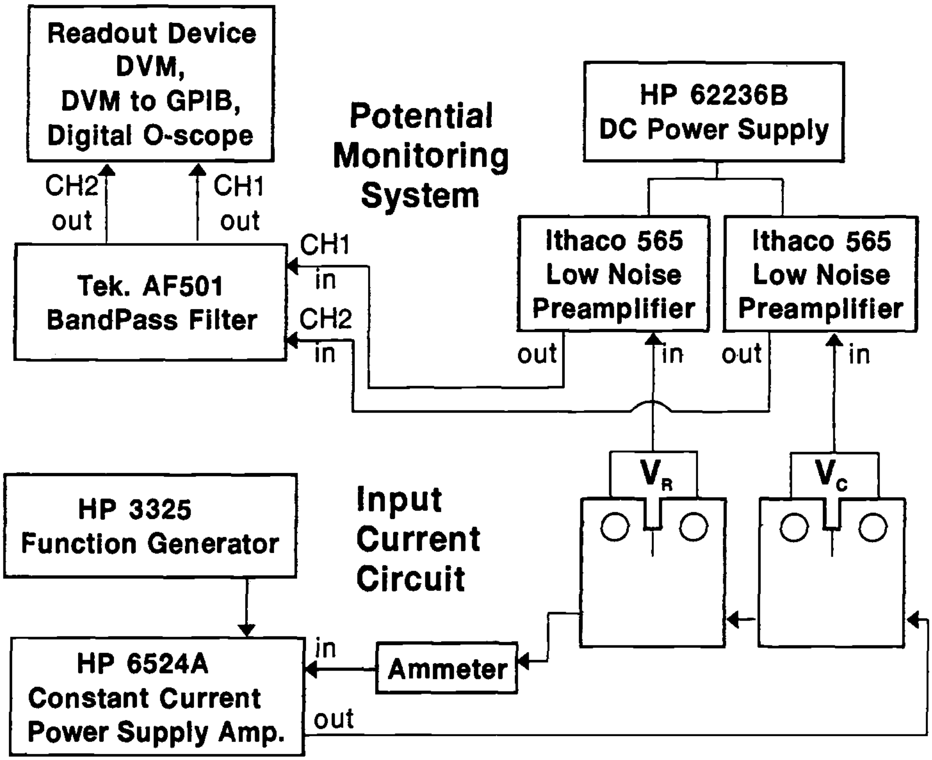

FIG. 3—*ACPD Measurement System Schematic.*

recording of the digital voltage meter (DVM), automatic recording and digital storage of the DVM signal via a GPIB interface, and digital storage on a Nicolet 4094 oscilloscope were all utilized.

Approach

Three different crack growth tests were conducted to study ACPD measurement system performance: fatigue crack growth testing using relatively low applied stress levels; quasistatic; and dynamic *J-R* curve testing. Both *J-R* tests have much higher applied stress levels. Fatigue crack growth rate (FCGR) testing was conducted initially between $0.47 < a/W < 0.85$ to develop a baseline calibration relationship between a/W and PD_n. Beachmarking was employed so that crack length could be visually measured after each test. The visual measurements were compared to compliance crack length measurements to verify system integrity. This step was useful because beachmarking was not possible for visual measurement in subsequent *J-R* curve testing.

The fatigue crack growth testing was also utilized to determine which reference probe location (test or adjacent specimen) led to the best normalized potential measurement. In one sense, it was advantageous to use the specimen reference location because the measurement system was self-contained and could more accurately monitor specimen temperature fluctuations. However, concerns existed from many conceivable problems with this location including leadwire interference between the crack and reference leads, the uniformity of the potential field at the specimen edge, and effects of changing stress state on this potential due to the proximity to the loading pin hole (Fig. 2).

Single specimen, quasistatic *J-R* curve testing was performed next using the unloading compliance method for in-situ crack length determination. The ACPD potential drop was simultaneously measured and used to develop a calibration relationship between a and PD_n for comparison with the fatigue crack growth testing curve. Calibration curve differences could conceivably result from both specimen geometry and stress state differences. Specimen geometry differences were present since the *J-R* test specimens were side-grooved to ensure straight crack growth during testing. Stress state differences occurred due to the higher applied loading in the quasistatic *J-R* testing. This stress state more closely simulates the fields in dynamic, as well as subsequent quasistatic, *J-R* test specimens. A mean a versus PD_n calibration curve determined from the unloading portions of the *J-R* test and the FCGR testing was used to relate the ACPD signals measured during the *J-R* test monotonic loading regions of individual tests to instantaneous crack growth. This instantaneous crack growth was used to predict the final, post-test crack extension (Δa_f) and to develop *J-R* curves for comparison with those developed using the standard unloading compliance technique.

Lastly, dynamic *J-R* curve testing was conducted using drop weight loading. Prediction of instantaneous Δa and post-test Δa_f was accomplished using calibration results based on the fatigue crack growth, unloading *J-R*, and precracking a versus PD_n relationships. The instantaneous Δa measurements were then used to formulate the dynamic *J-R* curve using standard equations. This result was then compared with *J-R* curves developed using the "key-curve" technique.

Material and Specimen Geometry

A high-strength Naval structural steel (HY-130) was tested. This low-carbon, high-nickel steel is constituted by the following nominal mix of major alloying elements: 0.12% C, 0.75% Mn, 0.25% Si, 5% Ni, 0.55% Cr, 0.45% Mo, and 0.25% Cu. Typical mechanical properties for this steel are as follows: yield strength (σ_{ys}) $\approx$ 900 MPa; ultimate strength (σ_{ult}) $\approx$ 920 MPa; elongation $\approx$ 15%; and reduction of area $\approx$ 50%. The most notable, pertinent characteristic of this material is its limited ability to strain harden. This limitation promotes poor cracking resistance behavior by providing little inherent restraint to net section yielding and void formation.

A modified 1*T* (t = 25.4 mm, W = 50.8 mm) *C(T)* specimen was utilized for this testing (Fig. 2). Modifications to the crack starter notch face were required to employ a dual capacitance gage (Fig. 2) for both crack mouth opening displacement (CMOD) and a displacement measurement inside the specimen load-line. This gage attaches rigidly to the flat face of the starter notch using screws (top side in Fig. 2). The bottom surface has a cutout section for attaching a target that extends just past the specimen edge for the CMOD capacitance sensor. The specimens also were modified for potential and input current lead attachment using $\approx$4 mm deep, 6-32 screw holes. Fatigue crack growth test specimens were not side-grooved while quasistatic and dynamic *J-R* specimens were side-grooved after precracking to ensure straight crack growth during testing. V-shaped side grooves reduced specimen thickness 20% using a 0.13 mm tip radius and a 60° flank angle.

Experimental Procedures

Fatigue Crack Growth Testing

Standard fatigue crack growth testing was conducted in a servohydraulic testing machine between $0.47 < a/W < 0.85$. A constant ΔK of 27 MPa$\sqrt{m}$ was used to grow the crack at a

$\sigma_{min}/\sigma_{max}$ (R) ratio of 0.1 and a cycling frequency (f_c) of 10 Hz while compliance measurements served to monitor the crack length. At a/W increments ($\Delta a/W$) of 0.025, the specimen was beachmarked using $\Delta K = 18$ MPa$\sqrt{m}$, $R = 0.1$, and $f_c = 10$ Hz for an additional $\Delta a/W = 0.005$. Cycling was resumed at the higher ΔK levels after each beachmarking cycle. Prior to resuming cycling at each ΔK change, the crack was fully opened to at least 90% of σ_{max} from the previous cycle. Then the reference and crack potential drop were recorded manually from the DVM. The specimen was unloaded and then cycling was resumed.

Four specimens were tested in this manner in air at room temperature. Only the reference signal V_{RS} was monitored for the first two specimens, FTF-1 and 2 while both V_{RS} and V_{RA} were monitored for the final two specimens (FTF-3, 5). After testing to $a/W = 0.85$, the specimens were broken open and the crack faces were photographed. The precrack, final crack, and the beginning and end of each beachmark was then measured from the digitized photograph using the ASTM standard 9 point average (ASTM Standard Test Method for Determining J-R Curves, E1152-87). The reference and crack potential readings were converted to PD_n for each beachmark location using Eq 5 for the measured a_i.

Quasistatic J-R Curve Testing

The *J-R* curve test specimens were first precracked from $0.47 < a/W < 0.6$ using the same procedure carried out in the fatigue crack growth testing. Precracking was again conducted using $\Delta K = 27$ MPa$\sqrt{m}$, $R = 0.1$, and $f_c = 10$ Hz. At $\Delta a/W$ increments of 0.025, cycling was halted, the crack was opened, and the reference and crack ACPD output from the DVM was manually recorded. Then beachmarking was conducted for $\Delta a/W = 0.005$ using $\Delta K = 18$ MPa$\sqrt{m}$, $R = 0.1$, and $f_c = 10$ Hz. After beachmarking, ACPD measurements were again recorded. The specimens were side-grooved following this precracking procedure.

J-R curve testing was performed on three specimens in air and at room temperature with a screw-driven universal testing machine. Unloading compliance using a clip gage at the crack mouth opening position was utilized for crack growth measurement. Unloading compliance using load-line displacement is the standard method for crack length measurement during *J-R* curve testing, but this was not feasible due to the unique specimen geometry required for subsequent dynamic testing. Therefore, the compliance expressions developed in ASTM E647 for the CMOD measurement location were employed for crack length determination. A suitable rotation correction factor based on the CMOD was developed along with a conversion between CMOD and Δ so that standard expressions for J-integral determination [*15*] could be employed. Testing has revealed that J_{Ic} values developed with the CMOD method are typically within 8% while J values at larger Δa values (3 mm) are within 5% of the standard load-line procedure [*15*].

The ACPD readings in this testing were recorded during both loading and unloading portions of the testing. The signals were stored digitally via GPIB interface from the DVM along with load, and COD measurements. After testing, the specimens were heat-tinted at 260°C for 30 to 60 min, broken, and the precrack, final crack, and beachmarks photographed and measured as in the fatigue crack growth testing.

ACPD signals recorded during loading portions were smoothed using a 5-point weighted average while those recorded during unloading portions were averaged to obtain one median voltage for each unloading. The ACPD signals from the loading portions of the *J-R* test were then converted to crack length using a/W versus PD_n calibration curves developed from the fatigue crack growth testing and the unloading compliance portion of the *J-R* curve testing. The *J-R* curve was then developed using equations in ASTM E 1152 for $0.001W\Delta a$ spacing. The accuracy of the ACPD system was assessed for these tests by comparing both the predicted Δa_f to the measured Δa_f and the unloading compliance *J-R* curve to the ACPD *J-R* curve results.

Dynamic J-R Curve Testing

The three dynamic test specimens were precracked from $0.47 < a/W < 0.6$ as in earlier testing. Beachmarking was once again conducted and the ACPD output manually recorded at the end of each cycling interval. The specimens were side-grooved as in the quasistatic *J-R* testing after precracking was completed. Dynamic loading was applied using a falling weight

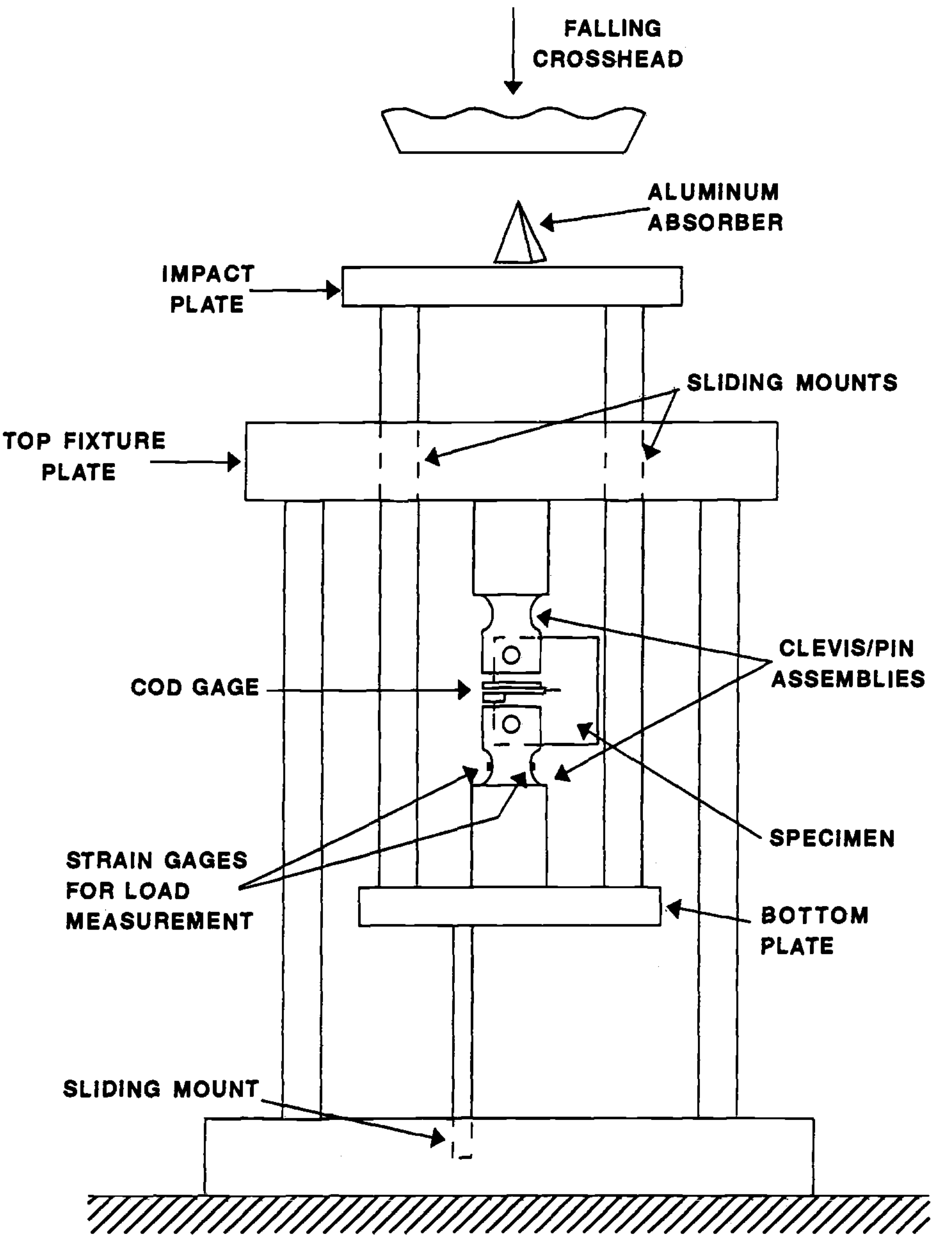

FIG. 4—*Drop tower testing rig.*

crosshead. The crosshead impact velocity and energy was roughly 3.5 m/s and 2300 *J* based on the weight and drop height. The compressive impact force was converted to tensile loading using a testing rig (Fig. 4). An O temper aluminum absorber was employed to smooth load transfer to the impact plate. The sliding mounts transfer load from the impact plate to the bottom clevis while also maintaining alignment (Fig. 4). Loading magnitude was adjusted using spacers of varying heights placed under the bottom plate to control the allowable displacement.

A full bridge strain gage assembly at the throat of the bottom clevis served as the load cell that was statically calibrated prior to testing over the expected loading range. As mentioned previously, a dual capacitance gage was used to measure both CMOD and Δ through linear interpolation between the inner and outer gages. Load, ACPD, and displacement data were stored in two Nicolet 4094 oscilloscopes with a 5 us sampling period to faithfully capture the 20 kHz ACPD signals.

Three specimens were tested in air at room temperature. The first specimen was loaded to just before crack initiation to determine the dynamic stability of the ACPD system for no crack growth. This specimen was broken after testing to verify the lack of crack growth. Another specimen was tested initially for no crack growth, but then tested to failure using a subsequent loading pulse. The final specimen was tested to failure on the initial loading pulse. After testing, the specimens were broken and the precrack, final crack, and precrack beachmarks measured as in previous testing.

The dynamic ACPD output was converted to rms voltages computationally for each full cycle. Data were then smoothed using the following procedure. First, a low pass filter with a 14 kHz cutoff frequency with a 1 kHz window surrounding the cutoff was used. Then, nine of every ten data points were deleted from all traces and, finally, all data were smoothed using two 5-point weighted averages per trace. Initial signals were compared with smoothed signals to ensure that data peaks and crack growth regions were faithfully reproduced. The *P* versus Δ data was used to develop *J-R* curves using the "key-curve" technique [*5,8*]. The ACPD data were converted to crack growth using the calibration results developed using the FCGR, precracking, and *J-R* curve testing. The *J*-integral was then calculated using ASTM E1152 equations for $0.001W\,\Delta a$ spacing to directly determine the dynamic *J-R* curve. The accuracy of the ACPD results was assessed through assessment of both the measured final crack extension and the "key-curve" *J-R* results.

Results and Discussion

Fatigue Crack Growth Testing

The visual crack length measurements are compared to the compliance predictions for the four tests over the full a/W range tested (Fig. 5). As anticipated, the compliance method agrees well with the visual, nine-point averaged crack length measurement. The average of the least squares fitted slope for each individual test is 0.988. A perfect correlation would be a slope of 1.0 so that the combined error is approximately 1% over this range of a/W. Differences between visual and predicted crack lengths are fairly consistent over the entire a/W range although they increase slightly at low a/W. This trend likely results from the influence of the starter notch. Regardless, the integrity of the compliance system used in subsequent testing is verified by this result.

Reference signals were simultaneously recorded on the test specimen and an adjacent specimen using two specimens (FTF-3 and 5) so that the influence on the reference potential could be studied (Fig. 6). This figure shows that there is a proportional, nearly linear relationship between the two reference locations and that a positive slope exists between the two locations for both these tests. This indicates that potential changes were sensed simultaneously at both

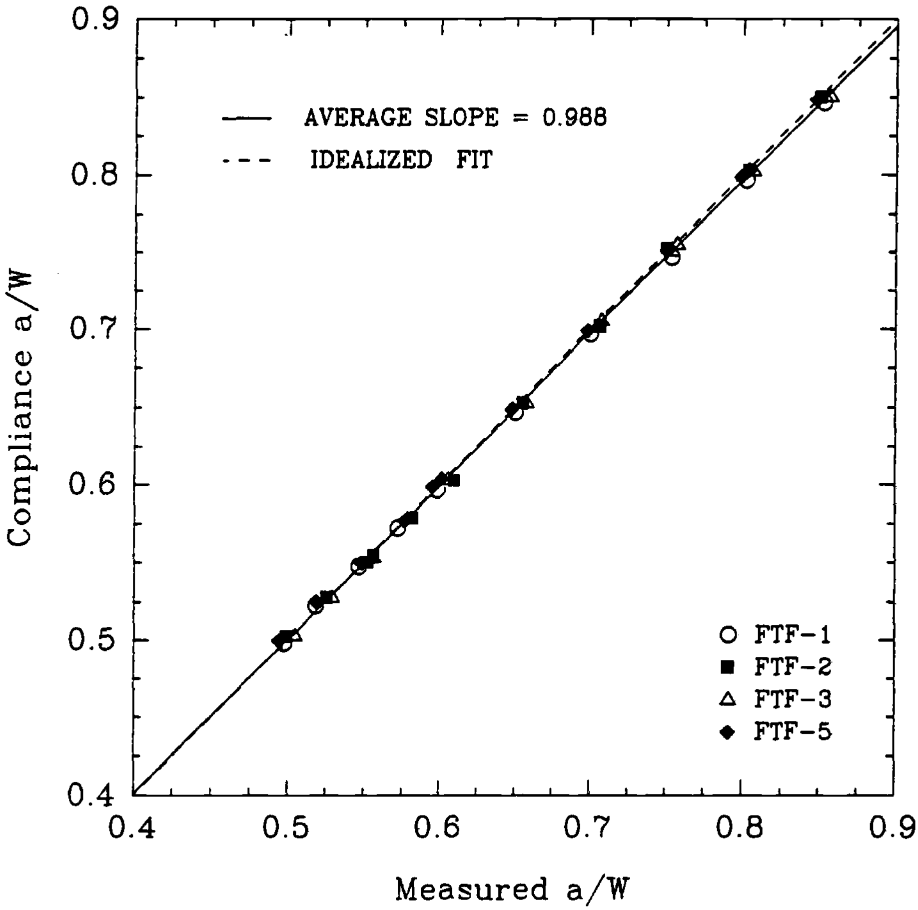

FIG. 5—*Compliance predictions in FCGR testing.*

the adjacent specimen and test specimen probes. Fig. 6 also indicates that there is not a repeatable variation in either reference signal potential as a function of crack growth. In one test, both potentials increased while in the other test, they both decreased. Since ΔK remains constant during crack growth, the load decreases along with the stress at the V_{RS} location. Decreasing stress levels increases path resistance (Eq 8), so that stress effects should be manifested by an increase in V_{RS} with crack growth assuming no other contributing factors. Therefore, V_{RS} does not appear to be affected by the decreasing stress state. However, front face stress will be greater in the *J-R* testing and V_{RS} may still exhibit a stress effect in these tests.

There is also a difference in potential sensitivity at V_{RS} that stems from the relatively short distance sampled by the test specimen reference (Fig. 2). Hence, the potential drop is less across this probe. This sensitivity likely contributes to the increased noise exhibited by the test specimen probe and the jumps apparent in the test specimen signal for both tests (Fig. 6). Noise could also be created through inductance effects from the input current and crack leads that are closely spaced during V_{RS} measurement. Therefore, as a result of the increased signal-to-noise ratio and the fact that stress effects at the test specimen probe could not be precluded without further testing, the adjacent specimen was chosen as the reference probe location for

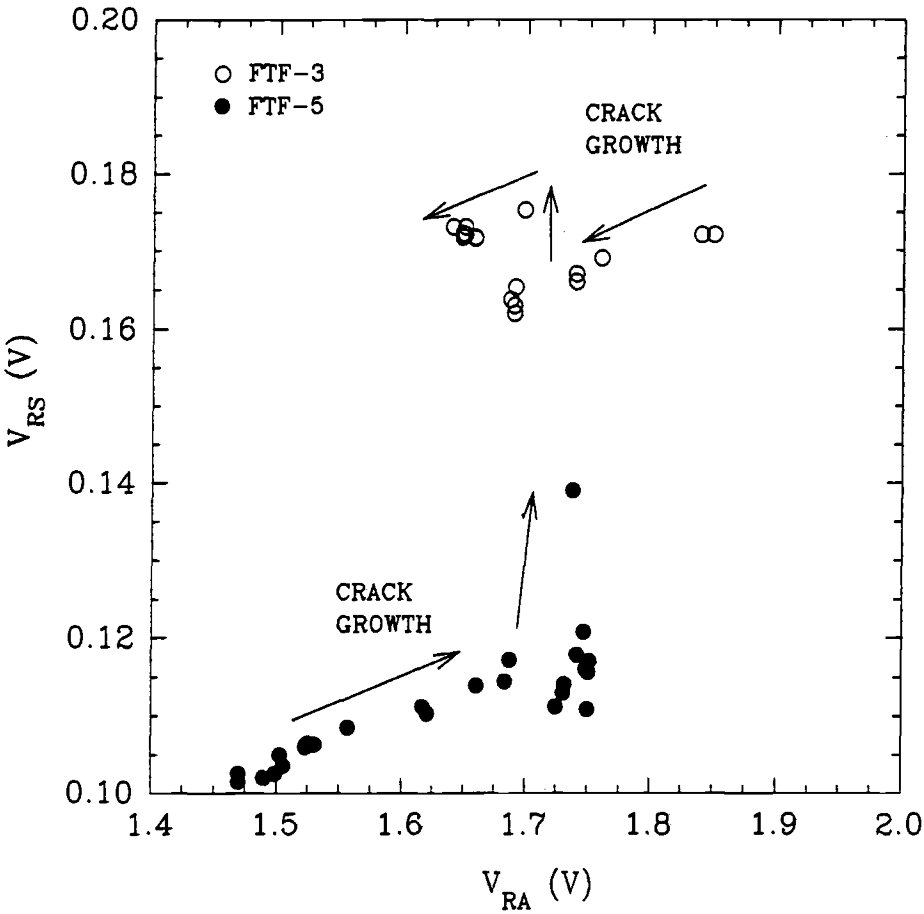

FIG. 6—*Reference location potential drop during testing.*

subsequent testing. Better isolation and further testing of the test specimen probe, however, could result in adequate performance and allow the superior temperature sensitivity and convenience of this location to be realized.

The calibration curves developed from the fatigue crack growth testing are illustrated in Fig. 7. Results for individual tests indicate if V_{RS} or V_{RA} was used for the reference signal. The calibration curves from the individual tests have been shifted slightly for agreement at a/W = 0.65 and clear indication of trends. The most noticeable feature of Fig. 7 is the nonlinear relationship that exists over the entire a/W range. Below $a/W \approx 0.6$, the PD_n values are less sensitive to crack length changes, while a more sensitive slope is apparent over $0.60 < a/W < 0.80$. There is also some limited indication that sensitivity will increase further for $a/W > 0.85$ (Fig. 7). For the purposes of this study, bilinear behavior was assumed with one slope representative of behavior for $a/W < 0.6$ and one for $0.60 < a/W < 0.80$. Data at $a/W > 0.8$ was neglected. The region $0.60 < a/W < 0.80$ corresponds to the region of interest in *J-R* testing. A least square linear fit over this range resulted in a mean $\Delta a/W$ versus ΔPD_n slope (m) of 0.484 with a standard deviation (Σ_m/m) of 7.8% (Table 1). This consistency reinforces the

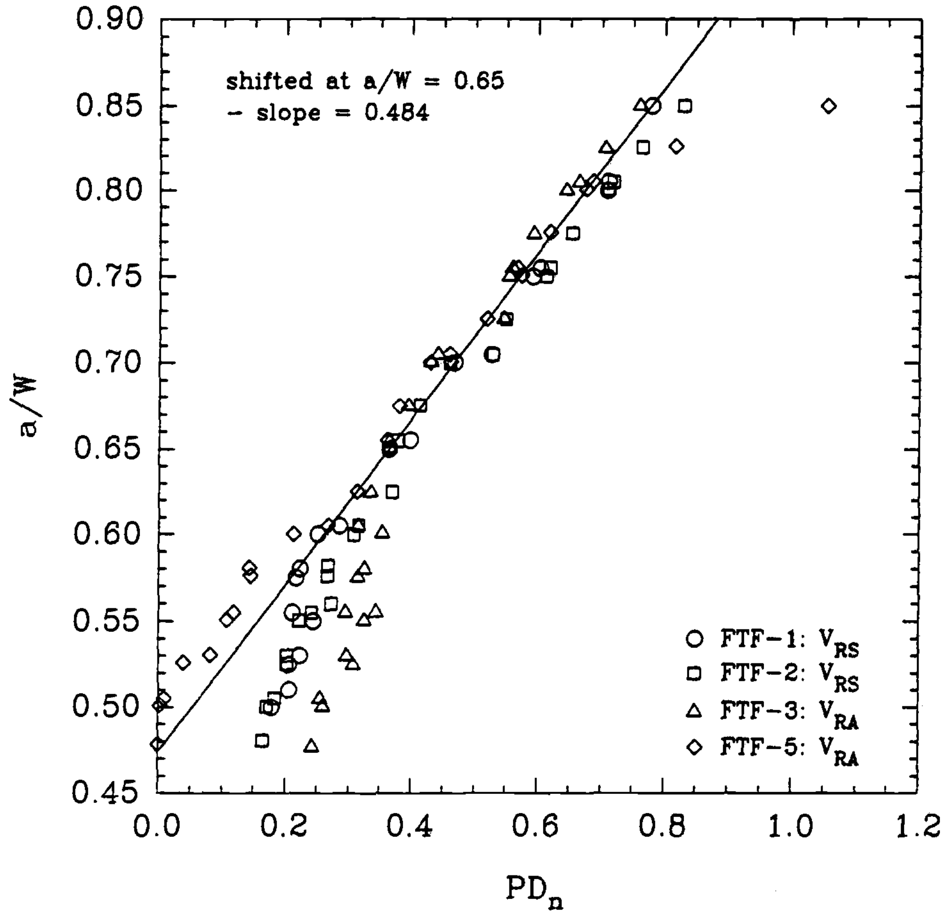

FIG. 7—*FCGR calibration relationship.*

generally good agreement and repeatability apparent in these tests (Fig. 7) and also reiterates the viability of the test specimen reference location for future testing.

However, there was a fairly low signal-to-noise ratio apparent during this testing. It was not uncommon to see signal fluctuations of 2–3% in the crack or adjacent specimen reference signals while the crack tip was held open near maximum load. For the test specimen reference probe signals, this noise level increased to 5 to 10%. This noise greatly contributes to the

TABLE 1—*Measured linear ACPD calibration relationships.*

Calibration Test	a/W Calibration Range	Slope: m	Σ_m/m, %
FCGR	$0.60 < a/W < 0.80$	0.484	7.8
Quasistatic *J-R*: Precracking	$a/W < 0.60$	0.900	20.0
Quasistatic *J-R*: Unloading Compliance	$0.60 < a/W < 0.80$	1.327	3.3

variability that does exist in Fig. 7. Signal averaging, as in compliance methods, should eliminate most of this random variability and will be part of future measurement systems.

Quasistatic and Dynamic J-R Curve Precracking

The ACPD signals were also monitored during precracking of the three quasistatic and three dynamic *J-R* curve specimens. Serendipitously, this region roughly corresponds with the transition ($a/W \approx 0.6$) between the low and high-sensitivity ACPD regions. The a/W versus PD_n relationship for a typical precrack specimen is overlaid onto the previous fatigue data (Fig. 8) to illustrate the general agreement with the earlier results. The ACPD variability in the precracking tests over this region is generally less than the FCGR results as the V_{RA} location was utilized. Therefore, a least squares linear fit was applied only to five out of six precrack specimens for $a/W < 0.6$. The mean slope of the individual results is 0.900 while the standard deviation is 21% (Table 1).

The high variability in this result stems from a number of factors. Most importantly, the behavior appears to be quite nonlinear in this region. Correlation coefficients from the linear

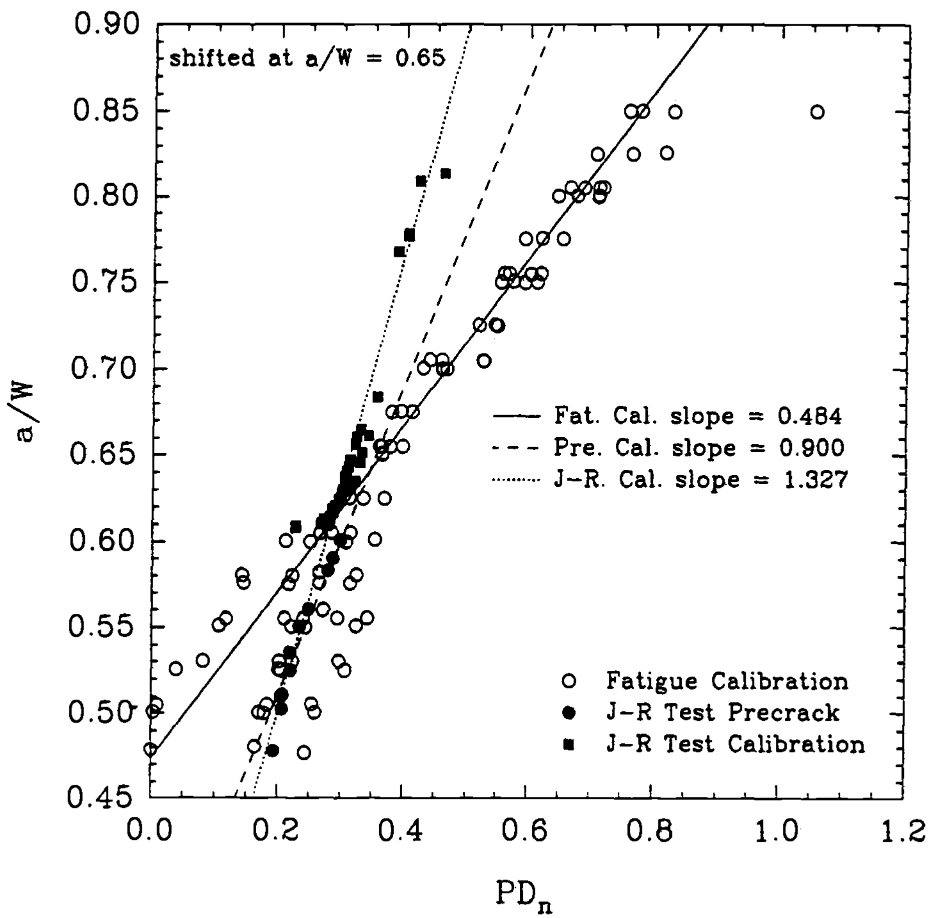

FIG. 8—*FCGR,* J-R *precracking, and unloading compliance* J-R *calibration relationships.*

fit for each data set were always well below 0.99. A second factor is attributed to the decreased sensitivity to crack growth in this region that increases the sensitivity of data in this region to signal noise. Finally, the relatively few points sampled during the precracking procedure also contributes to the high standard deviation.

Quasistatic J-R Curve Testing

Figure 9 illustrates the output for an unloading compliance quasistatic *J-R* curve test. This test is atypical in that relatively few unloadings were conducted; however, it more clearly illustrates the behavior of the ACPD system. In this figure, Load (P) normalized by the limit load (P_{LL}) as calculated as per ASTM E 1152 [*1*] and V_c/V_r are plotted as a function of Δ/W. These ACPD signals have been 5-point smoothed during loading, but the unloading portions have not been processed. During initial loading to P/P_{LL} = 0.8, the ACPD output remained steady: potential decrease due to increasing stress or potential increase from crack tip opening is not apparent. There is, however, clearly a rise in the potential just prior to maximum load. This rise may be due to either crack tip blunting or actual crack growth. It is doubtful that this

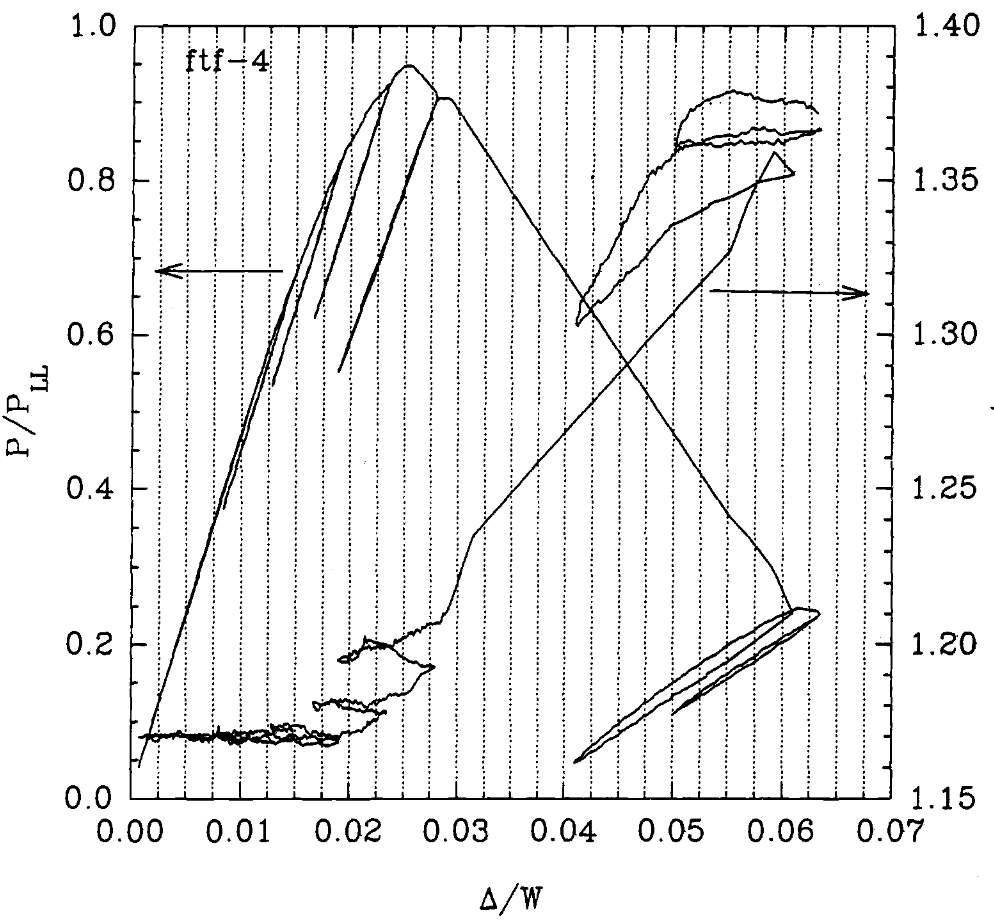

FIG. 9—*Unloading compliance P/Δ and ACPD behavior in* J-R *testing.*

increase results from crack tip opening as no closure at these high stresses. The next unloading after maximum load shows a clear increase in the potential that can only be attributed to crack growth. After this unloading, unstable tearing occurred that corresponds to the large potential rise. Two final unloadings were conducted after unstable tearing. Overall, the potential signals remained relatively constant during the unloading portions prior to crack instability after which the signal quality degraded immensely.

The calibration relationships for the three quasistatic *J-R* tests are overlaid on the fatigue crack growth and precrack calibration results in Fig. 8. The *J-R* calibration results have a much higher slope (less sensitivity) than both the fatigue crack growth testing over same a/W region and the precrack calibration results. The mean slope for the three *J-R* tests is 1.327. The mean correlation coefficient was 0.97—although two of three tests were greater than 0.98—which indicated the generally good linearity over this Δa range. Further, the variability in these results was much less: only 3% of the mean slope, which is at least partially a result of the increased signal averaging present during the unloading portions of the *J-R* test.

There are probably only two pertinent differences between the *J-R* and fatigue crack growth testing that could affect the crack growth sensitivity: specimen stress state and side grooving. Side grooving will not greatly affect the baseline specimen resistivity as only a small section of the specimen near the crack tip has reduced thickness. During growth however, the Δa to current area ratio is higher in a side groove specimen. Therefore, somewhat greater sensitivity to crack growth should exist. Since sensitivity is actually less in the *J-R* testing, the higher specimen stress likely dominates. Recall that increasing stress decreases specimen resistivity (Eq 8), which decreases crack growth sensitivity.

The precracking, fatigue, and *J-R* unloading compliance calibration results were applied to the monotonic portions of two quasistatic *J-R* tests (FTF-6 and FTF-9). The measured Δa_f for these tests are compared with the predicted Δa_f from the unloading compliance (Δa_f:JRUC), *J-R* specimen precracking (Δa_f:JRPC), and FCGR (Δa_f:FCGR) in Table 2. As indicated, the *J-R* unloading compliance calibration predictions are accurate while the other methods grossly underestimate Δa_f. This highlights the importance of using calibration relationships that closely correspond to the testing conditions of interest, especially the stress state, when using ACPD.

J-R curves developed using the *J-R* unloading compliance a/W versus PD_n calibration relation are presented in Fig. 10. Unloading compliance *J-R* curves are also illustrated for comparison. These results indicate that the ACPD performance was erratic. One test, FTF-9, provided accurate, yet noisy *J-R* curves. Again, noise should be minimized simply by further signal averaging. The other test, FTF-6, initially follows the blunting relationship, but then a sudden shift in potential at $J = 120$ kJ/m^2 resulted in a shift in the *J-R* curve. The tearing modulus after this shift, however, does match the unloading compliance resistance which implies that shifting the *J-R* curve at this point will align the ACPD and unloading compliance results for the remainder of this test. The reason for the shift in normalized potential is unknown, but may be remedied by using a slightly different signal normalization procedure. This topic is currently being pursued.

TABLE 2—*ACPD crack growth predictions.*

Test ID	Δa_f, mm	Δa_f: JRUC, mm	Δa_f: JRPC, mm	Δa_f: FCGR, mm
FTF-6	7.65	7.77	5.08	2.84
% Err	...	1.6	33.6	62.9
FTF-9	7.90	7.85	5.10	5.87
% Err	...	0.6	35.4	63.7

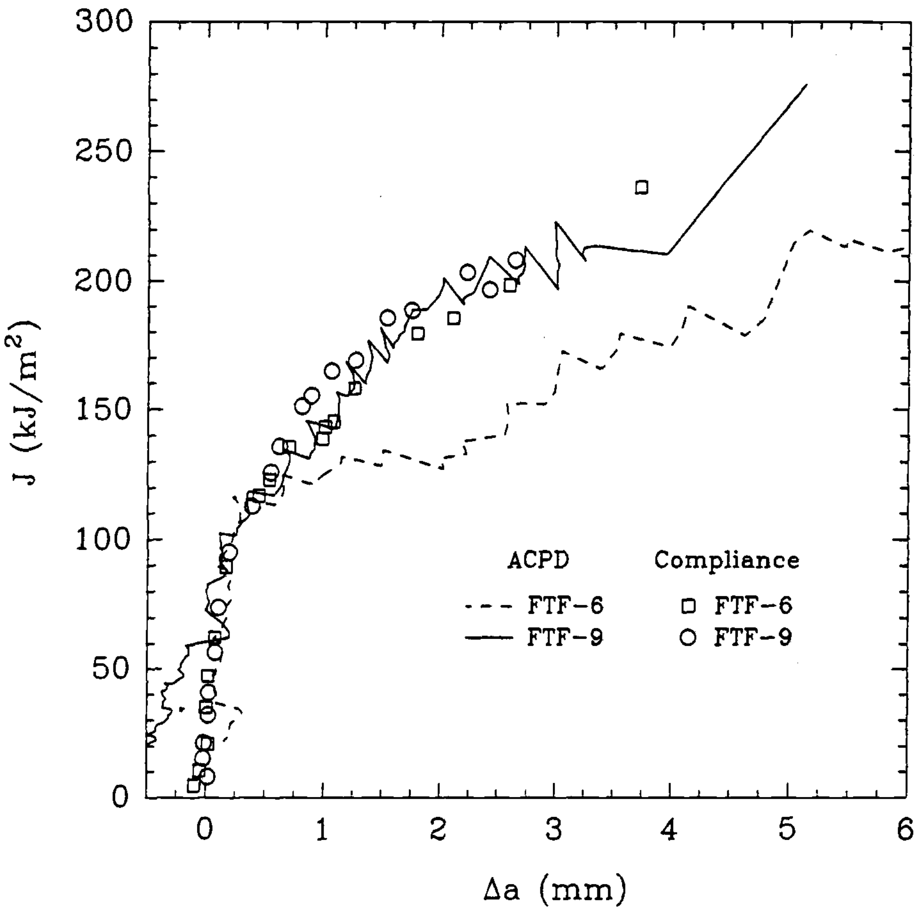

FIG. 10—*Unloading compliance and ACPD quasistatic* J-R *curves.*

Dynamic J-R *Curve Testing*

The first dynamic test examined ACPD signal behavior with no crack growth. The P, Δ, V_r, and V_c output as a function of time for two tests with no crack growth are presented (Fig. 11). Lack of crack growth in the upper test, FTF-11, was confirmed by post-test analysis of the fracture surface. Lack of crack growth in the second test was verified by the loading and unloading compliance and by the lack of plasticity in the P/CMOD response. The upper result (Fig. 11) is indicative of expected signal behavior. The crack signal increased during loading as the precrack opened. Then the potential decreased after the crack was fully open, likely due to the increase in crack tip stress. The crack signal was constant during the remainder of the test while the reference signal remained constant throughout the entire test.

The other test (FTF-12), however, exhibited some peculiarities. There are three places in the trace where both V_r and V_c recorded abrupt resistance changes. At the beginning and end of the test, the potential changes were primarily out-of-phase while the changes in the middle of the test were in-phase. The in-phase changes could be at least partially due to current fluctuation within both specimens. The out-of-phase fluctuations could not result from current fluctuations,

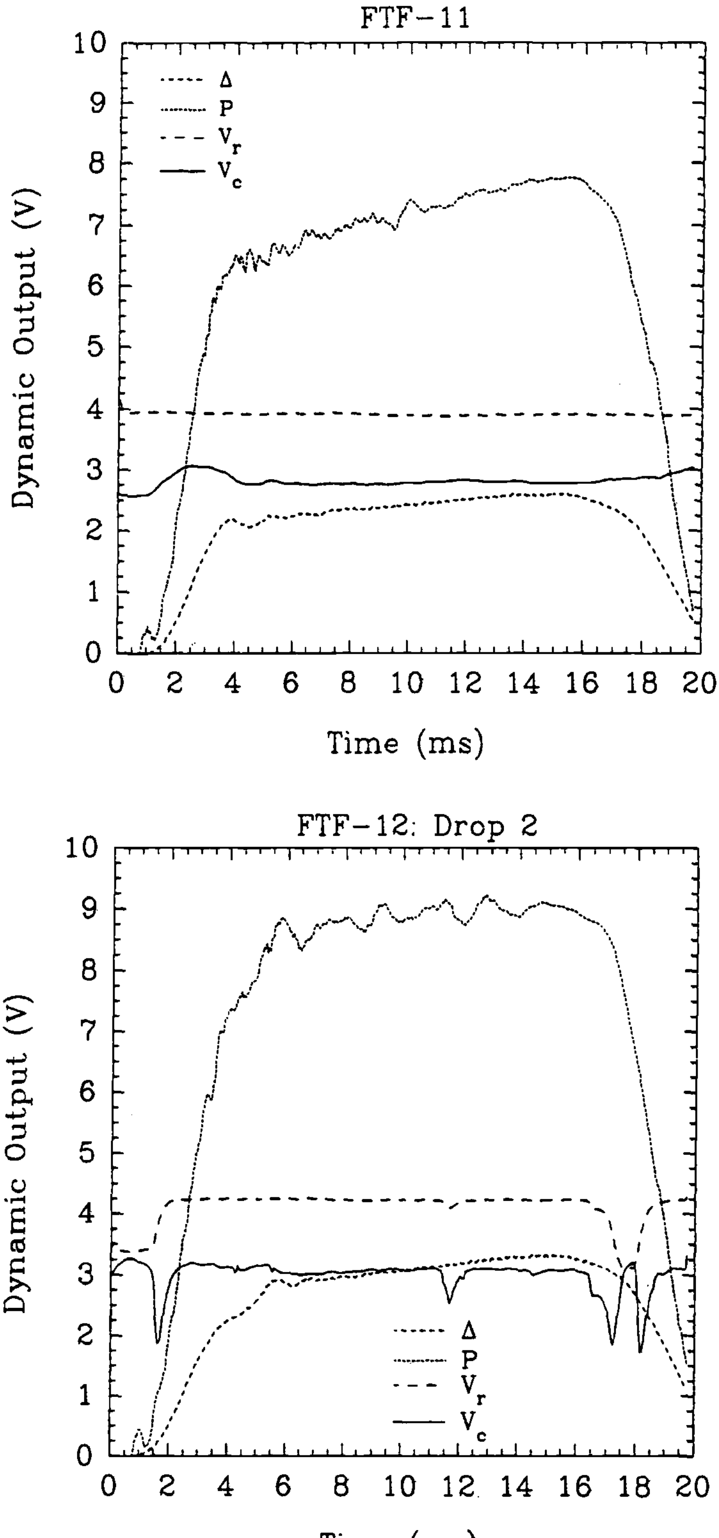

FIG. 11—*Dynamic signal output with no crack growth (FTF-11, 12).*

but may have resulted from inductance changes as leads moved during testing. It is interesting to note that the out-of-phase jumps occurred at the beginning of load application and during initial specimen unloading. These fluctuations were essentially replicated when this specimen was tested to failure and masked potential changes due to crack growth.

The other dynamic *J-R* test loaded to failure did produce useable ACPD output signals (Fig. 12). An enlargement of this signal (Fig. 12) illustrates the initial increase and then decrease in the crack signal as load was applied. After this portion, the signal remained steady until just past maximum load where the crack potential increased rapidly, briefly reached a plateau during unloading, and then greatly increased during the end of the unloading portion. The beginning of the unloading is marked on the figure. The small increase in the crack signal after unloading may be due to stress relaxation while the reason for the large increase (accompanied by a decrease in the reference potential) is unknown.

Steep load drop-off is a characteristic of HY-130 as ductile instability occurs with little resistance to tearing after crack initiation (Fig. 12). However, the crack probe was still able to track and monitor the crack growth within this time frame. This outcome is certainly promising. The ability of the technique to monitor rapid crack growth is a function of the ratio of crack speed to signal frequency since a complete wavelength was used to calculate rms voltage. Some measurement lag is conceivable at higher crack speeds, but this does not appear to be a factor in the current testing (Fig. 12).

The various calibration relationships established earlier were applied to the dynamic PD_n signal for prediction of the measured Δa_f. The signal was only analyzed up to the beginning of the unloading as indicated in Fig. 12. The actual Δa_f was 7.72 mm. The value of Δa_f predicted from the *J-R* unloading compliance was 7.7 mm. The predicted Δa_f using the fatigue crack growth and precrack calibration relationships were 2.8 and 5.0 mm, respectively. Therefore, once again, the other calibration expressions grossly underpredict Δa_f. The fact that the *J-R* calibration predicted Δa_f is so close to the measured Δa_f is somewhat serendipitous because the Δa between the processed dynamic ACPD data points was roughly 0.7 mm. Therefore picking the point just before or after the actual point chosen would result in roughly 9% error in Δa_f. However, system resolution can be greatly refined simply by not uniformly deleting points from the dynamic test results. This reduction procedure was employed only to aid subsequent *J-R* curve and key-curve analysis.

The dynamic *J-R* curve developed using the key-curve technique is compared to the *J-R* curve computed directly from the calibration ACPD output (Fig. 13). There are differences in the crack initiation *J* level, but post-initiation tearing is similar between the two methods. These initial differences are likely related to assumptions present in the key-curve analysis. First, blunting behavior ($J = 2\sigma_y \Delta a$) was assumed up to crack initiation ($J \approx 190$ kJ/m^2) at which point the key-curve analysis was initiated. This is why the key-curve data exhibit little noise prior to initiation. Further, crack initiation was assumed at maximum load although the accuracy of this assumption is unknown for HY-130. The load peak itself was relatively broad which led to some additional uncertainty in the true maximum load determination. It is therefore likely that the ACPD initiation *J* is more realistic since crack initiation was "assumed" in the key-curve analysis.

After initiation, both the ACPD and key-curve *J-R* curves possess little continued tearing resistance, even less than the quasistatic results (Fig. 10). The failure modes were ductile tearing in both tests so it would be surprising if the dynamic tearing resistance was actually less than the quasistatic. Further, both the ACPD and key-curve results exhibit a decrease in the *J*-integral for $\Delta a > 4$ mm. This decrease and the lack of tearing resistance are likely not physically realistic. Since the behavior occurs in both the key-curve and the ACPD results, problems with the crack measurement system are unlikely. However, the manufacturer of the capacitance sensor and amplifier has indicated that the amplifier-filtering characteristics introduce a

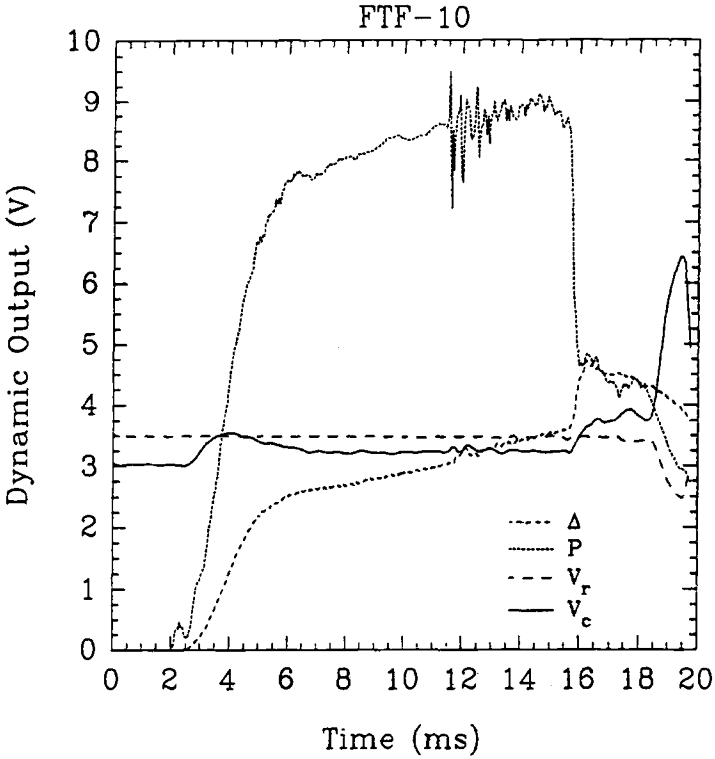

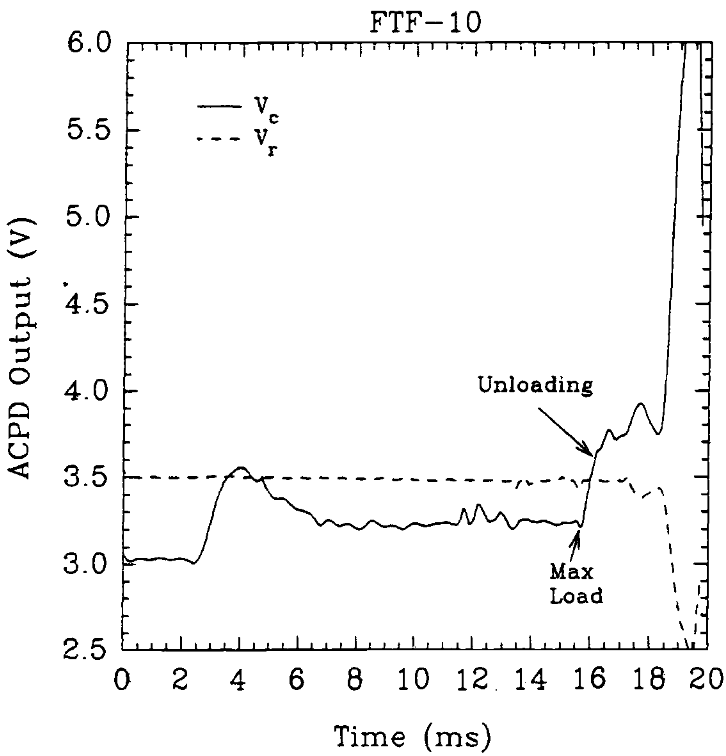

FIG. 12—*Dynamic signal output with crack growth (FTF-10).*

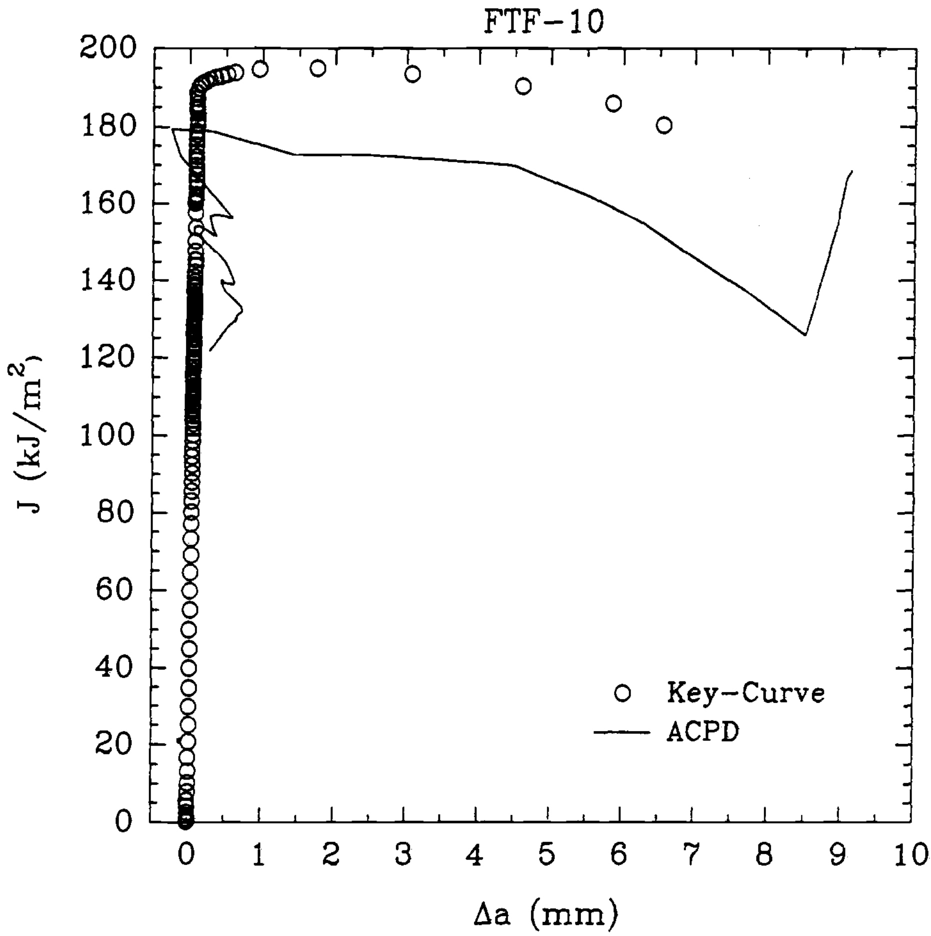

FIG. 13—*Key-curve and ACPD dynamic* J-R *curves.*

small-phase lag (≈100 us) in the beginning of the sensor output.[2] This small lag is not usually a problem unless crack growth is rapid, but it could account for these anomalous results. Further experimentation will be conducted on a material (lower strength steel or suitable nonferrous alloy) which does not exhibit such rapid, unstable tearing. Also, changes in the capacitance sensor filtering circuit will be explored in additional testing to eliminate this lag.

Conclusions

The following summary of ACPD system performance is possible based on the results of this study:

- The ACPD technique is feasible for quasistatic and dynamic *J-R* curve testing. The current system provides good sensitivity to crack initiation, dynamic response, and repeatability

[2] Personal communication between S. Graham of NSWC and J. Paduzzi of Capacitec.

as long as proper signal normalization is used. Signal processing can be used to improve the signal-to-noise ratio and increase the consistency of the technique.

- The ACPD FCGR calibration relationship between a/W and PD_n is nonlinear between $0.47 < a/W < 0.85$ for the modified C(T) specimen and input and probe lead positions studied. This result will also hold for *J-R* testing conducted over this range. Calibration must be conducted with crack tip stresses that closely simulate the intended testing application.
- For quasistatic *J-R* curve testing, final crack extension predictions are excellent and the *J-R* curve computed from the ACPD results generally reproduces unloading compliance results well. Some ACPD shifting is currently required when unexplained potential "jumps" occur.
- In dynamic *J-R* curve testing, ACPD output integrity is occasionally compromised, possibly due to leadwire inductance effects. However, excellent predictions of the final crack length is possible when these effects are nonexistent. The *J-R* curves calculated from the ACPD results are comparable to those determined using the key-curve method, although both curves possess anomalous tearing behavior compared to the quasistatic results for the failure mode present.

References

[1] Hudak, S. J., Jr. and Saxena, A., "Review and Extension of Compliance Information for Common Crack Growth Specimens," *International Journal of Fracture,* Vol. 14, No. 5, 1978, pp. 453–468.

[2] Baratta, F. I., Kapp, J. A., and Underwood, J. H., "More on Compliance of the Three-Point Bend Specimen," *International Journal of Fracture,* Vol. 28, 1985, pp. R41–R45.

[3] Landes, J. D., Zhou, Z., Lee, K., and Herrera, R., "Normalization Method for Developing J-R Curves with the LMN Function," *Journal of Testing and Evaluation,* JTEVA, Vol. 19, No. 4, July, 1991, pp. 305–311.

[4] Joyce, J. A. and Hackett, E. M., "An Advanced Procedure for J-R Curve Testing Using a Drop Tower," *Nonlinear Fracture Mechanics: Volume I—Time Dependent Fracture, ASTM STP 995,* A. Saxena, J. D. Landes, and J. L. Bassani, Eds., American Society for Testing and Materials, Philadelphia, 1989, pp. 298–317.

[5] Joyce, J. A. and Hackett, E. M., "Dyanmic J-R Curve Testing of a High Strength Steel Using the Multispecimen and Key Curve Technique," *Fracture Mechanics, ASTM STP 905,* 1984, pp. 741–774.

[6] Ernst, H., Parris, P. C., Rossow, M., and Hutchinson, J. W., "Analysis of Load Displacement Relationship to Determine J-R Curve and Tearing Instability Material Properties," *Fracture Mechanics, ASTM STP 677,* C. W. Smith, Ed., American Society for Testing and Materials, Philadelphia, 1979, pp. 581–599.

[7] Joyce, J. A., Ernst, H., and Paris, P. C., "Direct Evaluation of J Resistance Curves from Load Displacement Records," *Fracture Mechanics: Twelfth Conference, ASTM STP 700,* American Society for Testing and Materials, Philadelphia, 1980, pp. 222–236.

[8] Hackett, E. M., Kirk, M. T., and Hays, R. A., "An Evaluation of J-R Curve Testing of Nuclear Piping Materials Using the Direct Current Potential Drop Technique," NUREG/CR-4540, U.S. Nuclear Regulartory Commission, April 1986.

[9] Vassilaros, M. G. and Hackett, E. M., "J-Integral R-Curve Testing of High Strength Steels Utilizing the Direct Current Potential Drop Method," *15th National Symposium on Fracture Mechanics, ASTM STP 833,* 1984, pp. 535–552.

[10] Wilkowski, G. M., Wambaugh, J. O., and Prabhat, K., "Single-Specimen J-Resistance Curve Evaluations Using the Direct Current Potential Method and a Computerized Data Acquisition System," *15th National Symposium on Fracture Mechanics, ASTM STP 833,* 1984, pp. 553–576.

[11] Joyce, J. A. and Schneider, C. S., "Crack Length Measurement During Rapid Crack Growth Using an Alternating-Current Potential Difference Method," *Journal of Testing and Evaluation,* American Society for Testing and Materials, Philadelphia, 1988, pp. 257–270.

[12] Dover, W. D., Charlesworth, F. D. W., Taylor, K. A., Collins, R., and Michael, D. H., "A.C. Field Measurement—Theory and Practice," *The Measurement of Crack Length and Shape During Frac-*

ture and Fatigue, C. J. Beevers, Ed., Engineering Materials Advisiory Service, West Midland, U.K., 1980, pp. 222–260.

[*13*] Wei, R. P. and Brazill, R. L., "An Assessment of A-C and D-C Potential Systems for Monitoring Fatigue Crack Growth," *Fatigue Crack Growth Measurement and Data Analysis, ASTM STP 738,* S. J. Hudak, Jr. and R. J. Bucci, Eds., American Society for Testing and Materials, Philadelphia, 1981, pp. 103–109.

[*14*] Gibson, G. P., "The Use of Alternating Current Potential Drop for Determining J-Crack Resistance Curves," *Engineering Fracture Mechanics,* Vol. 26, No. 2, 1987, pp. 213–222.

[*15*] Tregoning, R. L. and Mercier, G., "Fracture Toughness Testing of C(T) Specimens Using Crack Mouth or Load Line Displacement Measurement," in preparation.

Simulation

Timothy E. Langlais,[1] *Jeffrey H. Vogel,*[2] *Darrell F. Socie,*[3] *and Thomas S. Cordes*[4]

Fatigue Life Contours from Elastic FEM Considering Multiaxial Plasticity

REFERENCE: Langlais, T. E., Vogel, J. H., Socie, D. F., and Cordes, T. S., "**Fatigue Life Contours from Elastic FEM Considering Multiaxial Plasticity,**" *Applications of Automation Technology to Fatigue and Fracture Testing Analysis: Third Volume, ASTM STP 1303,* A. A. Braun and L. N. Gilbertson, Eds., American Society for Testing and Materials, 1997, pp. 69–80.

ABSTRACT: Structures are subjected to a number of individual loads. These loads vary in amplitude and phase, resulting in multiaxial loading and fatigue. The fatigue analysis technique presented here is based on available models for multiaxial cyclic plasticity, notch correction, critical plane and rainflow counting, and damage estimation. Integration of these models with elastic finite-element analysis (FEA) is discussed, and an example of the fatigue design process from FEA to life prediction is presented.

Understanding the damaging nature of a multiaxial load history is difficult because it is not obvious how these loads combine to produce fatigue damage at a critical location. When joined with the aforementioned computational techniques, use of current visualization hardware and software tools can provide a designer or test engineer considerable insight into the damaging nature of a multiaxial load history. Visualization examples are presented to illustrate the capability and utility of this approach and show the potential options for visual output.

KEYWORDS: multiaxial fatigue, fatigue life visualization, notch correction, multiaxial cyclic plasticity

Nomenclature

s_{ij}, α_{ij}	Deviatoric stress tensor, deviatoric backstress tensor
ε_{ij}, e_{ij}	Strain tensor, deviatoric strain tensor
${}^{e}\varepsilon_{ij}$	Fictitious (elastically calculated) strain tensor
ε^{p}_{ij}, ${}^{e}\varepsilon^{p}_{ij}$	Plastic strain tensor, nonlinear part of the fictitious strain
$\bar{\sigma}$, ${}^{e}\bar{\sigma}$	Equivalent stress, equivalent fictitious stress
$\bar{\varepsilon}$, ${}^{e}\bar{\varepsilon}$	Equivalent strain, equivalent fictitious strain
$\bar{\varepsilon}^{p}$, ${}^{e}\bar{\varepsilon}^{p}$	Equivalent plastic strain, nonlinear part of the equivalent fictitious strain
C, ${}^{e}C$	Generalized plastic modulus, fictitious generalized plastic modulus
σ'_f, τ'_f	Tensile, shear fatigue strength coefficient
ε'_f, γ'_f	Tensile, shear fatigue ductility coefficient
σ_{max}	Maximum stress normal to the plane

[1] University of Minnesota, 111 Church St. SE, Minneapolis MN 55455.
[2] SciMed Life Systems, 2010 E. Center Circle, Plymouth MN 55411.
[3] University of Illinois-U.C., 1206 West Green, Urbana IL 61801.
[4] Deere&Co. Technical Center, 3300 River Dr., Moline IL 61265-1792.

Most engineers in the ground vehicle industries today rely on uniaxial analysis in the context of the local strain approach to predict fatigue life. These methods have proven effective in correlating fatigue life for many parts whose loading can be assumed to be uniaxial. However, the interest in multiaxial methods has grown as the ability to measure multiaxial loading histories and perform three-dimensional stress analysis becomes more routine. Designers frequently ask: why we do uniaxial fatigue analysis when we measure and compute multiaxial loads, stresses, and strains?

While researchers have demonstrated the ability of multiaxial methods to correlate crack nucleation life and direction [*1*], it still needs to be demonstrated that multiaxial methods, which come with a large computational price, are worth the added complexity. The strength of multiaxial methods lies in their ability to account for behavior that is otherwise ignored when one performs a uniaxial analysis. In particular, it becomes apparent that one cannot simply examine the loads or the geometry separately to get an idea of how a part becomes damaged. While many designers today use finite-element analysis to gage how fatigue damage is distributed, that analysis cannot tell the whole story. When a researcher uses finite-element methods alone (and thus considering geometry alone), it is difficult to judge the effects of variable amplitude and variable phasing with multiple load inputs.

A schematic of the multiaxial life prediction process is shown in Fig. 1. Both notch correction and plasticity are used to determine the local stress-strain state. Several notch correction models have been developed for multiaxial stress-strain states [*2–5*]. Likewise, many researchers have proposed successful plasticity models for use in fatigue [*6–8*]. Critical plane methods, first developed by Findley [*9*] and later extended to strain by Brown and Miller [*10*], are used to estimate the fatigue life. Note that the method requires three major inputs: loads, geometry information in the form of elastic FEA, and material properties. A homogeneous material is

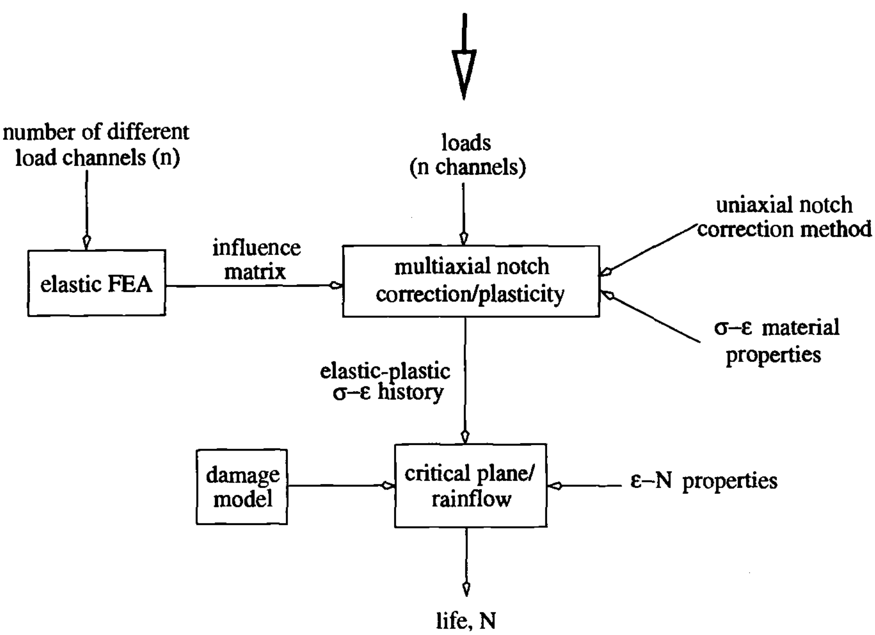

FIG. 1—*Multiaxial life prediction overview.*

assumed, and transient behaviors are neglected. Analysts can readily characterize the material properties using well-established uniaxial test procedures.

Methodology

Influence Matrix

In order to begin a fatigue life analysis, something must be known about a part's service history; most often, this information comes in the form of load histories measured during simulations or during actual use. Although it could be experimentally determined or analytically derived, an influence matrix relating loads to in-plane elastic strains in the notch is most often found using elastic FEA

$$^{e}\varepsilon_i = L_{ij}P_j \tag{1}$$

where P_j is the vector of loads, L_{ij} is the influence matrix, and $^{e}\varepsilon_i$ is a vector of elastically calculated in-plane notch strains. The influence matrix is akin to the notch concentration factor, K_t, used for uniaxial loading. The procedure for finding the influence matrix from elastic FEA follows.

1. Identify the number of different loads, usually corresponding to the number of load channels in a service history (e.g. $P = \{P_1, P_2, \ldots, P_n\}$).
2. Establish a suitable mesh in the elastic FEM software of choice.
3. For each load type (channel), apply a singular unit load ($P^1 = \{1, 0, \ldots, 0\}$, $P^2 = \{0, 1, 0, \ldots, 0\}, \ldots P^n = \{0, \ldots, 0, 1\}$).
4. Solve for the elastic stresses and strains in the area of interest; these are the components of the influence matrix. For load channel 1

$$^{e}\varepsilon_i = \begin{Bmatrix} \varepsilon^1_{xx} \\ \varepsilon^1_{yy} \\ \varepsilon^1_{xy} \end{Bmatrix} \tag{2}$$

5. By application of superposition, assemble the components into the final influence matrix

$$\begin{Bmatrix} ^{e}\varepsilon_{xx} \\ ^{e}\varepsilon_{yy} \\ ^{e}\varepsilon_{xy} \end{Bmatrix} = \begin{bmatrix} \varepsilon^1_{xx} & \varepsilon^2_{xx} & & \varepsilon^n_{xx} \\ \varepsilon^1_{yy} & \varepsilon^2_{yy} & \ddots & \varepsilon^n_{yy} \\ \varepsilon^1_{xy} & \varepsilon^2_{xy} & & \varepsilon^n_{xy} \end{bmatrix} \begin{Bmatrix} P_1 \\ P_2 \\ \vdots \\ P_n \end{Bmatrix} \tag{3}$$

Using the influence matrix, it is easy to find the elastically calculated notch strains for any loading combination.

Notch Correction/Plasticity

Once the elastically calculated strains are known, a notch correction/plasticity model is used to find the elastic-plastic stress-strain state. Our approach to plasticity and notch correction is based on the observations that continuous-surface Mróz models do a good job (errors less than 15%) estimating all but severe nonproportional loading [*11,12*] and that correction models used to find notch strains usually employ a plasticity model in stress control. For these reasons we use Chu's [*11,13*] Mróz-type plasticity model for kinematic hardening effects. Köttgen's ${}^{e}\varepsilon$ notch correction method [*4*] is embedded within the plasticity model, resulting in a single-pass algorithm for determining local stress and strain from a given load history. The algorithm is summarized below.

A: $d\,{}^{e}\varepsilon_{ij} \Rightarrow ds_{ij}$

use $d\,{}^{e}\varepsilon^{p}_{ij} = \dfrac{1}{{}^{e}C}\, g(s_{ij} - \alpha_{ij}),\ \Delta^{e}e_{ij} = \dfrac{s_{ij}}{2G},\ {}^{e}C = \dfrac{2}{3}\dfrac{d\bar{\sigma}}{d\,{}^{e}\bar{\varepsilon}^{p}}$

numerically integrate $ds_{ij} = f_{s}({}^{e}C, s_{ij}, \alpha_{ij})$

B: $ds_{ij} \Rightarrow d\varepsilon_{ij}$

use $d\varepsilon^{p}_{ij} = \dfrac{1}{C}\, g(s_{ij} - \alpha_{ij}),\ \Delta e_{ij} = \dfrac{s_{ij}}{2G},\ C = \dfrac{2}{3}\dfrac{d\bar{\sigma}}{d\bar{\varepsilon}^{p}}$

numerically integrate $d\varepsilon_{ij} = f_{e}(C, s_{ij}, \alpha_{ij})$

Note that the procedure summarized above amounts to simultaneous integration of the continuum mechanics equations, with $d\,{}^{e}\varepsilon_{ij}$ independent and ds_{ij} dependent in Step A, and ds_{ij} independent and $d\varepsilon_{ij}$ dependent for Step B.

Critical Plane Analysis

The critical plane approach tries to do analytically what the test engineer does experimentally. To analyze a failure, a test engineer finds the location of crack nucleation, places a strain gage in that location in a direction perpendicular to the observed crack and measures the strain history. Analytically, the location and direction are unknown and all possible ones must be evaluated by rainflow-counting cycles on each plane. It is assumed that the plane and direction having the most computed damage will be the first one to nucleate a crack.

As yet, there is no consensus among researchers as to which damage model is best. Nevertheless, we may observe that successful models have features that:

1. Account for plasticity using a strain-based parameter,
2. Account for nonproportional hardening using a stress range or maximum stress parameter,
3. Model mean stress affects with a mean stress or maximum stress parameter, and
4. Account for different failure modes by characterizing damage as tensile or shear related.

No single method meets all of these requirements, the most difficult being to distinguish between tensile and shear damage modes.

In this paper we have used a simple but effective strategy—compute shear and tensile damage on each plane and add the damage together to obtain a conservative estimate of component life, N:

$$\frac{1}{N} = \frac{1}{N_t} + \frac{1}{N_s} \tag{4}$$

where N_s and N_t are found from

$$\frac{\Delta\gamma}{2}\left(1 + k\frac{\sigma_{max}}{\sigma'_f}\right) = \frac{\tau'_f}{G}(2N_s)^b + \gamma'_f(2N_s)^c \tag{5}$$

$$\sigma_{max}\frac{\Delta\varepsilon}{2} = \frac{\Delta\sigma_r}{2}\left(\frac{\sigma'_f}{E}(2N_t)^b + \varepsilon'_f(2N_t)^c\right) \tag{6}$$

The shear model, Eq 5, was first proposed by Fatemi and Socie [*14*]. The tensile damage is computed from the Smith-Watson-Topper (SWT) model, Eq 6.

Comparison to Experiment

It is important to verify that the multiaxial stress-strain predictions agree with the uniaxial methods on which they are based. Shown in Table 1 are the results of simple uniaxial loading with notch correction. Note that the multiaxial method reduces to expected behavior in uniaxial tension. The comparison is made between a uniaxial Neuber's analysis and the integrated notch correction/plasticity model for SAE 1045 steel, hardened to Rockwell C 29.

Figure 2 shows computed and experimental data for a simple tension (S_{xx} = 296 MPa) and torsion (S_{xy} = 193 MPa) loading of a circumferential notched shaft. The nominal quantities are computed from the applied torque, T, and the applied axial load P as $S_{xx} = P/A$ and $S_{xy} = TR/J$, where A is the cross-sectional area, R is the nominal radius, and J is the rotational moment of inertia. Note that the coupling between the shear and axial loading is captured by the model. The notch shear strain increases during the tensile loading portion of the loading cycle even though the nominal shear stress is held constant during this loading segment.

Example: Plate with a Hole

Fatigue Analysis Process

A simple plate with a hole is shown in Fig. 3. The plate is fixed on one end and is loaded with an axial load and two corner loads. The step-by-step analysis procedure will be detailed here by example.

TABLE 1—*Comparison of uniaxial and multiaxial notch correction procedures.*

K_f	Nominal Strain, $\mu\varepsilon$	Fictitious Strain, $\mu\varepsilon$	Notch Strain, $\mu\varepsilon$	Notch Stress, MPa
$K_f = 1.0$				
Uniaxial	2690	2690	3190	467
Multiaxial	2690	2690	3130	476
$K_f = 2.0$				
Uniaxial	2690	5380	9030	660
Multiaxial	2690	5380	8945	697

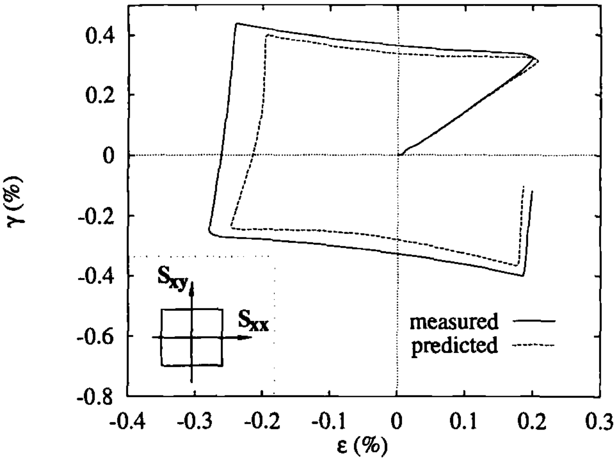

FIG. 2—*Box path, notch correction.*

Step 1: Identify the regions of interest and the inputs.

There are three load channels for this case: P_1, P_2, and P_3. A mesh is chosen with sufficient refinement to resolve strains in the area of the hole, where stress concentrations are likely to occur.

Step 2: Determine the influence matrices using elastic FEA.

We perform an elastic FEA to determine the strains for each node for each of three load cases (using ANSYS 8-noded brick elements): $P_1 = \{1000, 0, 0\}$, $P_2 = \{0, 1000, 0\}$, and $P_3 = \{0, 0, 1000\}$ (in Newtons). For a node on the top centerline of the plate located halfway between the hole and the loaded end,

$$\begin{Bmatrix}\varepsilon_{xx}^1\\ \varepsilon_{yy}^1\\ \varepsilon_{xy}^1\end{Bmatrix} = \begin{Bmatrix}-132\\ -100\\ 0\end{Bmatrix}\mu e \quad \begin{Bmatrix}\varepsilon_{xx}^2\\ \varepsilon_{yy}^2\\ \varepsilon_{xy}^2\end{Bmatrix} = \begin{Bmatrix}942\\ -376\\ -4543\end{Bmatrix}\mu e \quad \begin{Bmatrix}\varepsilon_{xx}^3\\ \varepsilon_{yy}^3\\ \varepsilon_{xy}^3\end{Bmatrix} = \begin{Bmatrix}942\\ -376\\ 4543\end{Bmatrix}\mu e$$

The influence matrix for a 1-N load can be assembled:

$$L_{ij} = \begin{bmatrix}-0.132 & 0.942 & 0.942\\ -0.100 & -0.376 & -0.376\\ 0.0 & -4.543 & 4.543\end{bmatrix}$$

Step 3: Given the loads and influence matrices, compute the stress-strain history.

For the load history shown in Fig. 5 with load levels of $P_1 = 9500$ N, $P_2 = 650$ N, and $P_3 = 650$ N, the stress-strain response is shown in Fig. 4. The above influence matrix was used for this computation.

Step 4 and Step 5: Perform a critical plane analysis; determine the final life.

The method estimates a fatigue life of 1325 blocks.

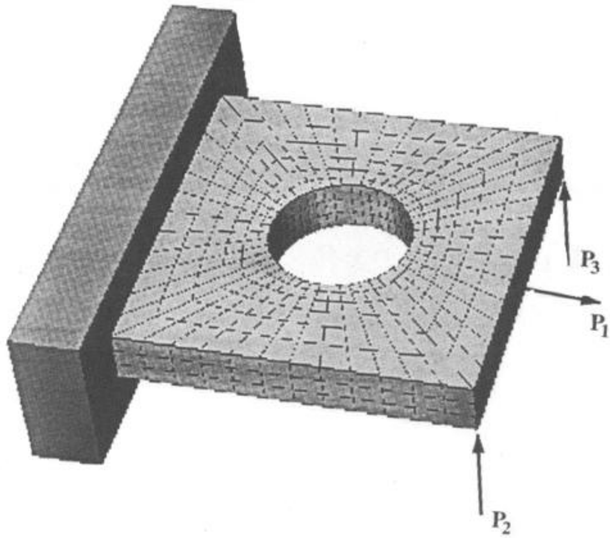

FIG. 3—*Plate with a hole.*

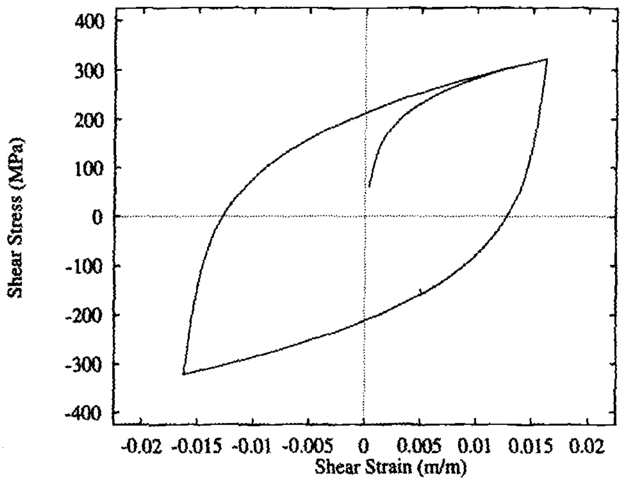

FIG. 4—*Stress-strain plot for proportional loading failure point.*

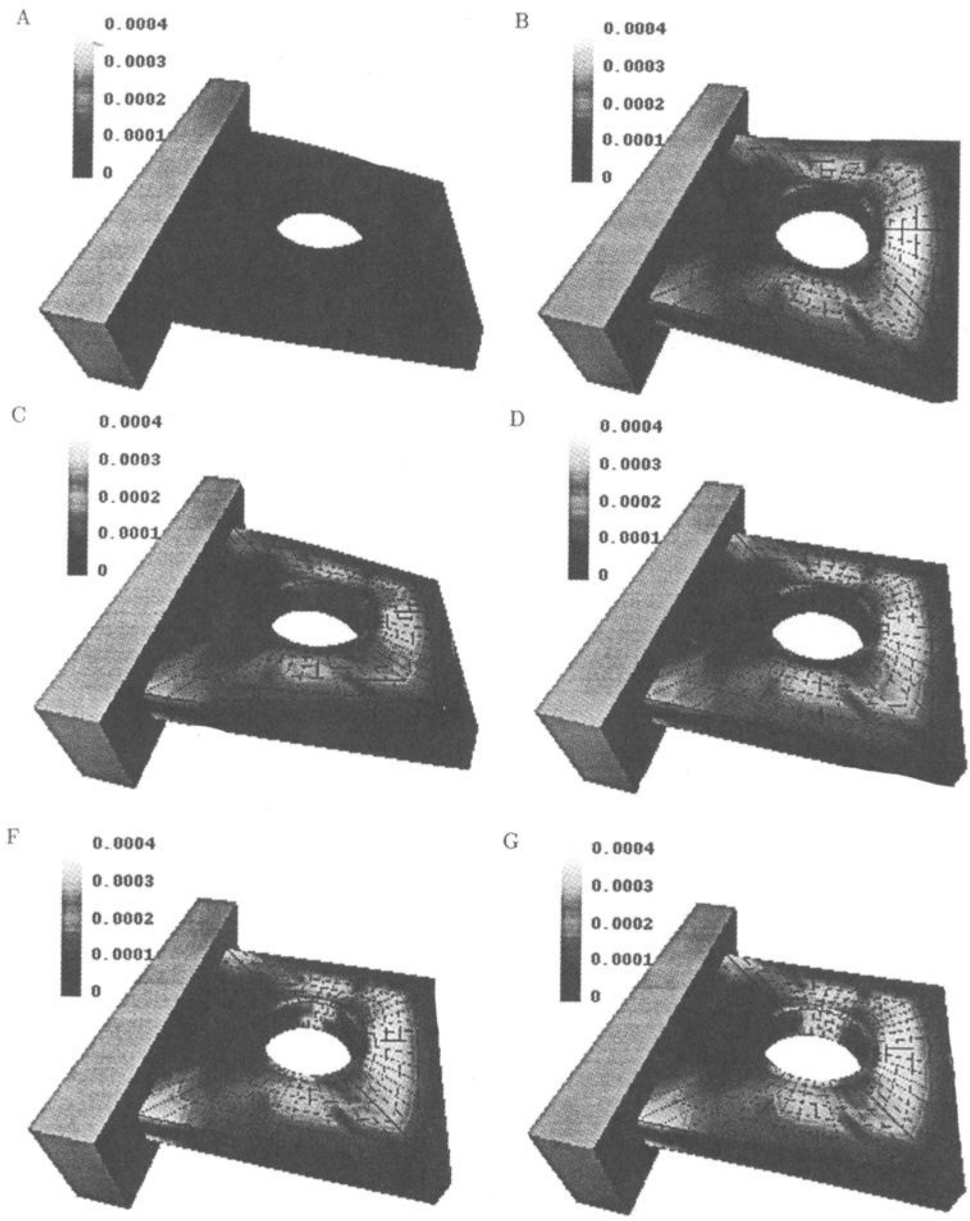

FIG. 5—*Plate example: proportional loading.*

Visualization

Visualizing damage contours on a part is a powerful tool for the assessment of fatigue damage. Figures 5 and 7 show a series of snapshots at different points in time of the accumulated damage for the two load histories shown in Figs. 6 and 8. Greyscale color denotes fatigue damage ($D = 1/N$), with lighter shades representing areas of greater fatigue damage. Displacements are exaggerated to emphasize the loading. Each snapshot represents the number of blocks required to nucleate a crack at any location on the surface, assuming the block history ended at that point.

The predicted damage distribution for proportional loading of the corners is shown in Fig. 5. Note that the calculated damage accumulates most rapidly near the side of the plate on which the loads are applied, and that damage in the hole only appears in the later part of the history when the axial load is applied. The damage also appears to be uniformly distributed over a significant area of the plate surface.

Figure 7 displays the predicted damage accumulation for the plate under nonproportional corner loading. Note that as P_3 is held constant the plate is damaged on the side of the hole corresponding to cycled load, P_2, shown in A', B', and C'. But as P_3 is brought back to zero, constituting the completion of a 0 to max cycle of P_3, the plate is damaged on the P_3 side of the hole, though less severely than the other side damaged by the nonproportional cycling of P_2. Finally, the axial load P_1 is cycled, adding to the damage on the top surface of the plate and damaging the inside of the hole as shown in G'.

Now compare the damage distribution in C' with that shown in C from Fig. 5 (carefully note the difference in damage scales shown on the legend). While the load levels are the same, the damage distribution is different because of the phasing of the loads. While the preponderance of fatigue damage is located between the hole and the loaded edge in C (Fig. 5), the plate in C' (Fig. 7) shows no damage in that region. The message that can be gleaned is that the distribution of fatigue damage is a strong function of geometry, load level, and phasing of the loads. In short, one needs to consider all three to correctly assess the damaging nature of a nonproportional multiaxial load history as applied to a specific part geometry.

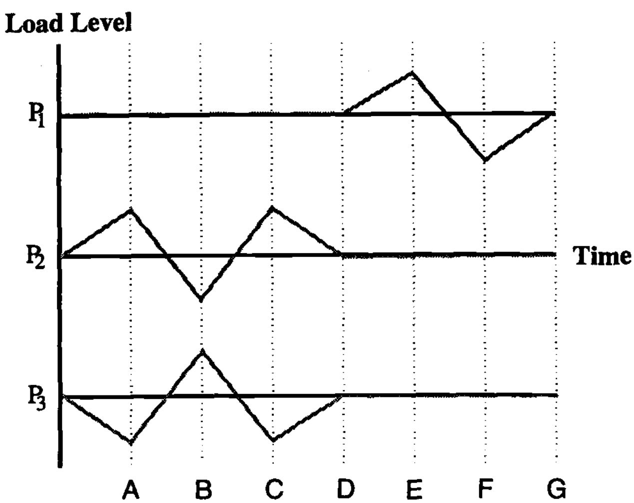

FIG. 6—*Plate example: proportional load path.*

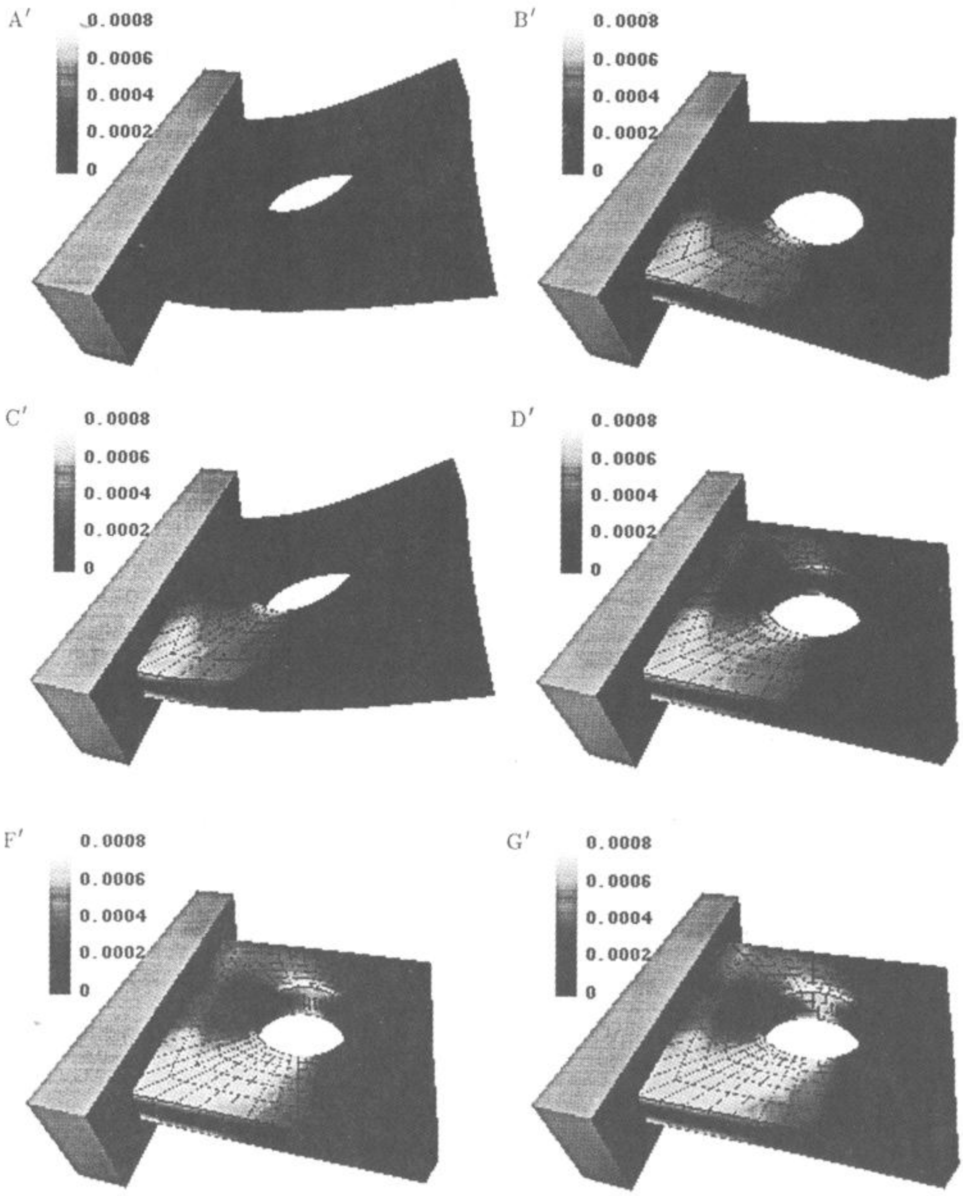

FIG. 7—*Plate example: nonproportional loading.*

Conclusions

An integrated procedure for multiaxial fatigue analysis has been outlined. The notch correction/plasticity model has been shown to qualitatively capture material behavior and the total process from input loads to final life estimation has been detailed. The results of a multiaxial

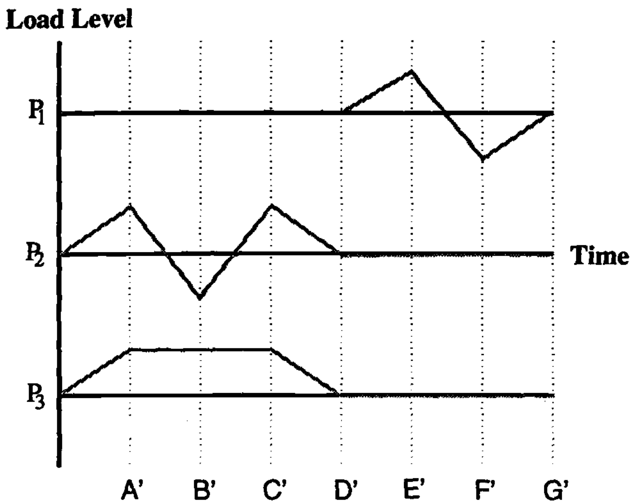

FIG. 8—*Plate example: nonproportional load path.*

analysis on a simple part were visualized using damage contours mapped to a model of a part. These visualizations of damage contours can provide insight into the damaging nature of multiaxial loads and their interaction with part geometry.

References

[1] Socie, S., "Critical Plane Approaches for Multiaxial Fatigue Damage Assessment," *Advances in Multiaxial Fatigue, ASTM STP 1191,* D. L. McDowell and R. Ellis, Eds., American Society for Testing and Materials, 1993, pp. 7–36.

[2] Hoffman, M. and Seeger, T., "Chapter 3: Stress-Strain Analysis and Life Predictions of a Notched Shaft Under Multiaxial Loading," *Multiaxial Fatigue: Analysis and Experiments, AE-14,* G. E. Leese and D. F. Socie, Eds., Society of Automotive Engineers, Warrendale, PA, 1989, pp. 81–99.

[3] Barkey, M. E., Socie, D. F., and Hsia, K. J., "A Yield Surface Approach to the Estimation of Notch Strains for Proportional and Nonproportional Cyclic Loading," *Journal of Engineering Materials and Technology,* Transactions ASME, Vol. 116, 1994, pp. 173–180.

[4] Köttgen, V. B., Barkey, M. E., and Socie, D. F., "$^e\sigma$ and $^e\varepsilon$ Based Approaches to Multiaxial Notch Analysis," submitted to *Fatigue and Fracture of Engineering Materials and Structures.*

[5] Singh, M. N. K., Glinka, G., and Dubey, R. N., "Elasto-Plastic Stress-Strain Calculation in Notched Bodies Subjected to Multiaxial Nonproportional Loading," submitted for publication in the *International Journal of Fracture,* March 1995.

[6] Mróz, Z., "On the Description of Anisotropic Workhardening," *Journal of the Mechanics and Physics of Solids,* Vol. 15, 1967, pp. 163–175.

[7] Dafalias, Y. F. and Popov, E. P., " A Model of Nonlinearly Hardening Materials for Complex Loading," *Acta Mechanica,* Vol. 23, 1975, pp. 173–192.

[8] McDowell, D. L., "A Two Surface Model for Transient Nonproportional Cyclic Plasticity," *Journal of Applied Mechanics,* Vol. 52, June 1985, pp. 298–308.

[9] Findley, W. N., Coleman, J. J., and Handley, B. C., "Theory for Combined Bending and Torsion Fatigue with Data for 4340 Steel," in *International Conference on Fatigue of Metals,* The Institution of Mechanical Engineers, New York, 1956, pp. 150–157.

[10] Brown, M. W. and Miller, K. J., "A Theory for Fatigue Failure Under Multiaxial Stress Strain Conditions," *Proceedings of the Institute of Mechanical Engineers,* Vol. 187, No. 65, 1973, pp. 745–755.

[11] Chu, C. C., "Programming of a Multiaxial Stress-strain Model for Fatigue Analysis," *SAE Technical Paper Series 920662,* Society of Automotive Engineers, Warrendale, PA, 1992.

[*12*] Langlais, T. E., "Computer Methods for Multiaxial Cyclic Plasticity," master's thesis, University of Minnesota, 1994.

[*13*] Chu, C. C., "A Three-Dimensional Model of Anisotropic Hardening in Metals and its Application to the Analysis of Sheet Metal Forming," *Journal of the Mechanics and Physics of Solids,* Vol. 32, No. 3, 1984, pp. 197–212.

[*14*] Fatemi, A. and Socie, D. F., "A Critical Plane Approach to Multiaxial Fatigue Damage Including Out-of-Phase Loading," *Fatigue and Fracture of Engineering Materials and Structures,* Vol. 11, 1988, pp. 149–165.

R. L. Hewitt[1] *and F. J. Albright*[2]

Computer Modeling and Simulation in a Full-Scale Aircraft Structural Test Laboratory

REFERENCE: Hewitt, R. L. and Albright, F. J., "**Computer Modeling and Simulation in a Full-Scale Aircraft Structural Test Laboratory,**" *Applications of Automation Technology to Fatigue and Fracture Testing and Analysis: Third Volume, ASTM STP 1303,* A. A. Braun and L. N. Gilbertson, Eds., American Society for Testing and Materials, 1997, pp. 81–95.

ABSTRACT: Full-scale aircraft structural fatigue tests are extremely complex, not only in terms of the test definition and implementation, but also from the control systems viewpoint. The load spectra that these tests are subjected to are also becoming more complex as manufacturers and certifying authorities strive for more realistic loading conditions. At the same time, there is pressure to complete the test more quickly or at least in the same time as previous tests that were simpler and contained fewer cycles. This can only be achieved by optimizing the test configuration and control system parameters or in some cases implementing new control strategies. This is difficult on a full-scale test because of all the complex interactions on these multi-channel tests. Methods that may work well on smaller tests can sometimes result in poorer performance. Thus there is a need for a greater understanding of the system and some predictive capability. This can be achieved with computer modeling.

This paper suggests an implementation scheme in terms of the introduction and acceptance of the concepts of modeling to a full-scale structural test laboratory and provides examples of the use of modeling at various stages in its implementation. Examples are presented from the very basic level of education, using models to understand sources of problems on simple tests, to evaluating new control strategies and predicting the impulse response of a test system (structure/actuators/control system). Finally, the possibility of predicting system behavior with sufficient accuracy to optimize the test for given test and control system hardware is discussed.

KEYWORDS: aircraft, control, fatigue, full-scale testing, modeling, servohydraulic, simulation

Full-scale aircraft structural fatigue tests are extremely complex, not only in terms of the test definition and implementation, but also from the control systems viewpoint. There are usually a large number of servohydraulic actuators connected to a complex structure through a variety of loading attachments. The response of any one actuator is a function of all of the other actuators, the structure, the loading attachments and the reaction system, as well as the actuator and servo valve characteristics, and the control system parameters. Starting up of one of these tests is very demanding for the test engineer because of the enormous economic implications (specimens alone are often worth millions of dollars and delays in the testing program can have even greater economic implications). Anything that can be done to predict the response of the total system before start-up and allow greater confidence in system stability will lessen risks and make the test engineer's life more bearable.

The load spectra that these tests are subjected to are also becoming more complex as manufacturers and certifying authorities strive for more realistic loading conditions. The result is

[1] Senior research officer, Institute for Aerospace Research, National Research Council of Canada, Montreal Rd., Ottawa, Ontario, K1A 0R6.

[2] Senior staff scientist, MTS Systems Corporation, 14000 Technology Drive, Eden Prairie, MN 55344-2290.

generally more independent load conditions that have to be applied and a larger total number of applied loads. At the same time, there is pressure to complete the test more quickly or at least in the same time as previous tests that contained fewer cycles. This can only be achieved by optimizing the test configuration and control system parameters. In many cases, even this is insufficient and new control strategies may be required. Determination of these optimum parameters and implementation of new control strategies on a full-scale aircraft structural fatigue test is difficult because of the complex interactions on these multi-channel tests. Methods that may work well on smaller tests can sometimes result in poorer performance. Thus again there is need for a greater understanding of the system and some predictive capability.

Computer modeling and simulation can provide a means for greater understanding and a predictive capability. Commercial packages are available that can model many of the individual components in a system such as the controller, servo valve and actuator. Furthermore, all modern aircraft are designed using finite element analysis, meaning that a structural model of the basic test structure exists. All the building blocks for modeling the complete structural test are therefore available. What is required is a scheme to integrate these various elements and, perhaps more importantly, a method of implementation within the laboratory that will provide sufficient confidence in the tools to allow their use on these multi-million dollar tests.

This paper suggests an implementation scheme in terms of the introduction and acceptance of the concepts of modeling to a full-scale structural test laboratory. This relies on the use of modeling concepts at all levels in the laboratory and the demonstration of their usefulness at the lowest level before implementation at the next level. Modeling can be introduced at a basic level with no risk for the education of inexperienced test personnel. Examples of the types of demonstrations that have proven useful are provided. At the next level, modeling should be used in a qualitative way to understand sources of problems, initially on very simple tests. Examples of where this has been achieved will be documented. As confidence in the techniques are gained, they can be used on more complex problems. At these levels, modeling can be achieved with existing model blocks, using simple springs and masses to qualitatively represent the structure.

As the structure becomes more complex, it will be necessary to model it more accurately. The paper provides an example of a simple cantilever beam using the output of a dynamic finite element model in the simulation. Again, this model can initially be used to qualitatively study various effects and provide understanding of general behavior and the impulse response of the beam with an actuator and control system is used as an example. At this level it may also be used to evaluate new control strategies or test devices that have shown promise on simpler systems.

At the final level, which may take some time to achieve, it may be possible to predict the system behavior with sufficient accuracy to optimize the test for given test and control system hardware. This would entail defining those control system parameters that allowed the fastest possible cycling with a defined loading accuracy and a suitable margin of stability. This would allow the test engineer to significantly reduce the time required to tune the system and obtain a much more accurate estimate of test time prior to test start.

Simulation Basics

The simulations described in this paper were all performed using Extend, an easy-to-use simulation software package developed by Imagine That, Inc.[3] with additional modules developed by MTS Systems Corporation, and all were run on a Macintosh Quadra 650. Simulation systems such as these that operate in a user-friendly, graphical user interface environment are essential to the acceptance of such systems within a full-scale test facility because they allow

[3] Imagine That, Inc., 6830 Via Del Oro, Suite 230, San Jose, CA 95119-1353.

direct use by personnel that are involved in the structural testing. This helps to develop confidence in the simulations.

The simulation model is assembled by connecting various element blocks such as a function generator, controller, servo valve, actuator, and a spring. The model can then be analyzed much as a test engineer would analyze a physical set-up. A simple sine wave command can be applied if the only requirement is to evaluate the sine wave response, or a step can be applied to evaluate the stability of the system as would be done for tuning a physical system. If more information on the frequency response of the system is required, an impulse can be applied and the feedback analyzed using a Fast Fourier Transform (FFT) plotter. The advantages of the simulation are that, besides being able to quickly change components and settings, these tests can all be performed very simply and the outputs can be displayed and manipulated all on the one machine. In addition, most element blocks have been written to allow them to run with or without dynamics: this allows the use of hardware that cannot be achieved in practice which is very useful when trying to determine which particular component in a system is causing an instability.

Simulation as an Education Tool

An immediate benefit from the initial implementation of a simulation system within a test facility is the ability to teach less-experienced test engineers about some of the more important variables in test and control system set-up. This is becoming increasingly important as many of the more experienced test engineers retire and because of the somewhat cyclical nature of structural testing, which often results in the dismantling of test teams between tests.

Effects of Mass and Moving Load Cells

Two of the most important distinctions between typical aircraft structural tests and material tests or many vehicle tests is the relatively low stiffness of the test specimen and the use of feedback from load cells mounted between the actuator and the structure rather than fixed load cells or displacement feedback. These "moving load cells" significantly reduce the amount of proportional gain that can be used in a given test situation, which drastically reduces the response of the system and hence test speed. This can be illustrated using a simulation model.

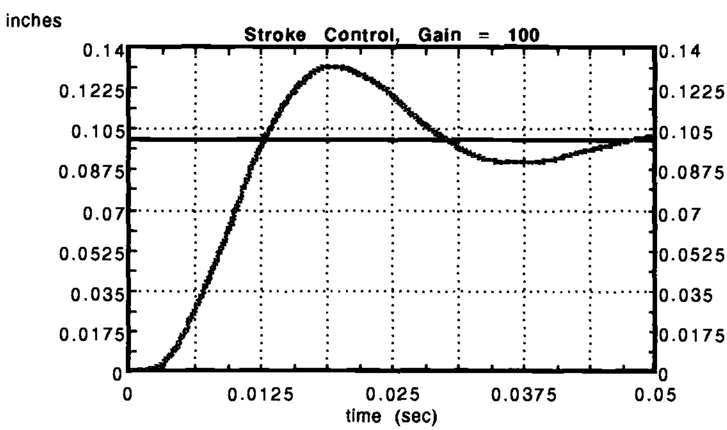

FIG. 1—*Step response under stroke control at gain = 100.*

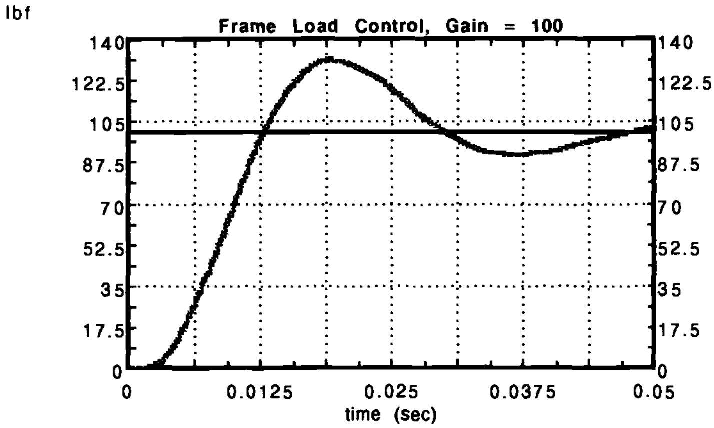

FIG. 2—*Step response under load control with load frame-mounted load cell at gain = 100.*

Consider a simple spring specimen with a stiffness of 1000 lbf/in. (0.175 MN/m) loaded by an 11 kip (48.9 kN) actuator with a 15 gpm (0.946 L/s) servo valve. For a 40 lb (18.14 kg) grip mass and a stroke transducer with 10 in. (25.4 cm) full scale, the response to an input step of 0.1 in. (2.5 cm) in stroke control at a gain of 100 is shown in Fig. 1. The system overshoots but is stable. A similar response for the same gain is obtained with a 100 lbf (0.445 kN) step input using load feedback from a frame-mounted (fixed) load cell with a full scale of 10 000 lbf (44.5 kN) as shown in Fig. 2. However, using feedback from a load cell mounted on the actuator rod (moving load cell), the response to an input step of 100 lbf (0.445 kN) at a gain of 100 is completely unstable. Even at a gain of 5, the system is unstable as shown in Fig. 3, as there is still considerable oscillation related to the inertia of the grip mass. The influence of grip mass is clearly shown in Fig. 4 where by reducing the grip mass to 4 lb (1.81 kg) the system is stable at a gain of 10. Reducing the grip mass entirely would allow similar gains to the fixed load cell case but this cannot be achieved in practice since, even with no fixturing, there is still the mass of that part of the load cell above the measuring section.

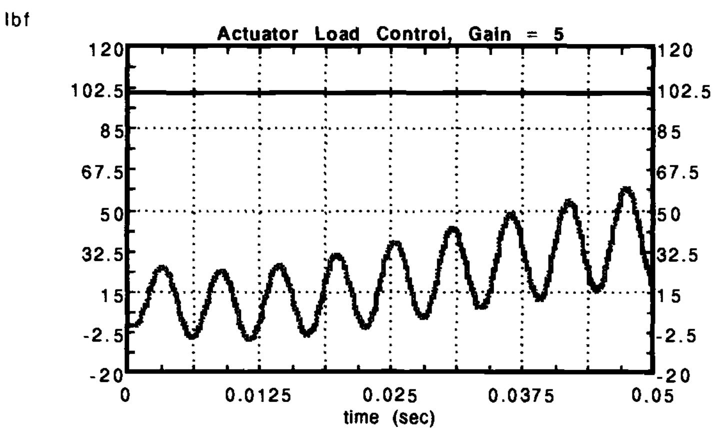

FIG. 3—*Step response under load control with actuator-mounted load cell at gain = 5.*

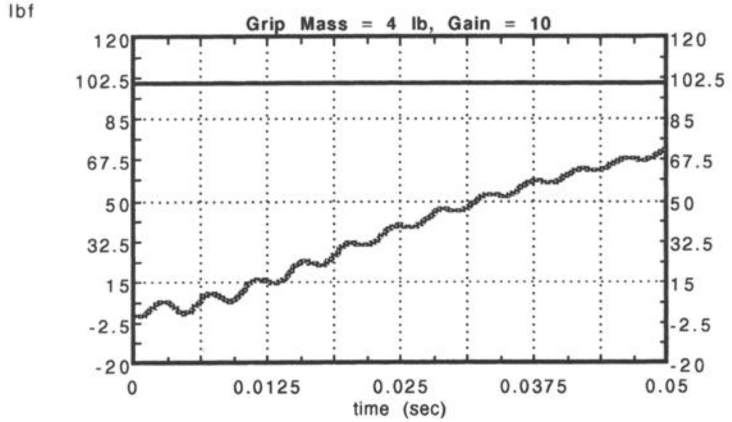

FIG. 4—*Step response under load control with actuator-mounted load cell at gain = 10 with grip mass reduced to 4 lb.*

Feed Forward Control in Structural Tests

These simulation tools can also be used to investigate the effects of choosing different components for a particular test. The new test engineer can quickly see the effects of changing actuator and valve sizes as well as those of changing load cell full-scale ranges. The interactions of the various control terms such as proportional, rate, and integral gain and feed forward can also be investigated very simply without the need for hardware. Such investigations by one of the authors (who has little control background per se) taught him that feed forward control, while useful in some situations, can be detrimental in some structural test situations as detailed below.

Figure 5 shows the response of a 6.6 kip (29.4 kN) double-ended actuator with a 2.5 gpm (0.158 L/s) servo valve and a 1000 lbf (4.45 kN) full-scale load cell attached to a simple spring of 1100 lbf/in. (0.193 MN/m) stiffness to a sine wave input. With a forward loop gain of 3.6 and a fixed crosshead, the feedback lags the command and the peaks are not achieved. Addition

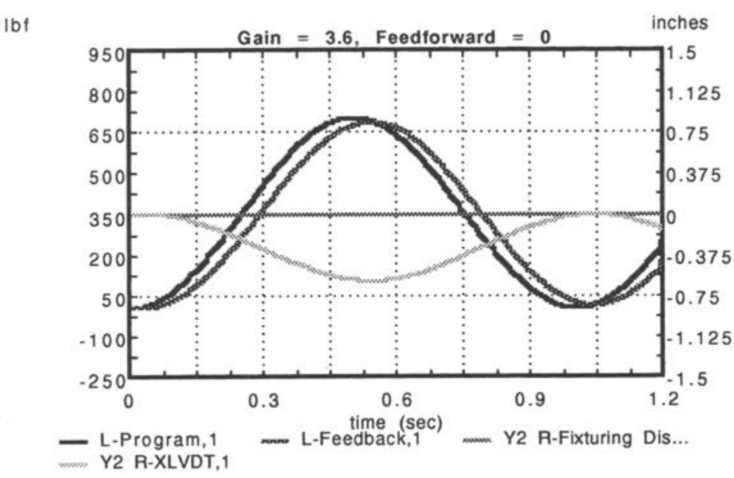

FIG. 5—*Response of actuator with fixed crosshead and no feed forward.*

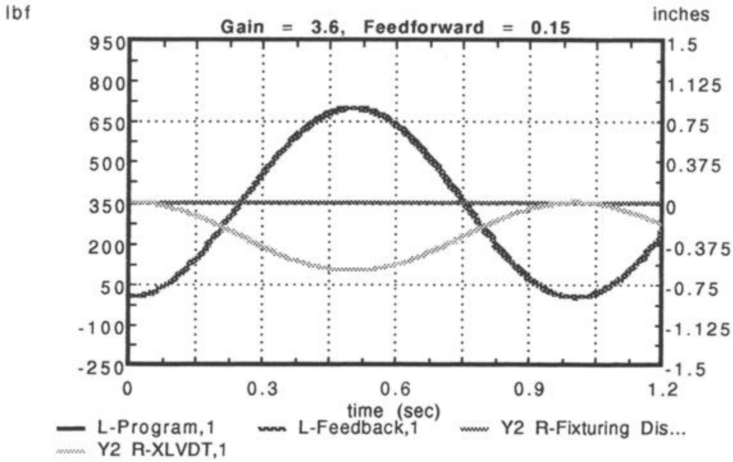

FIG. 6—*Response of actuator with fixed crosshead and feed forward = 0.15.*

of a feed forward gain of about 0.15 makes the feedback follow the command much more closely as can be seen in Fig. 6.

However, if a sinusoidal displacement of the same frequency as the command is added to the crosshead to simulate the overall motion of the structure, the effective stiffness changes. Figure 7 shows the resulting response for a displacement that is twice the magnitude and in the opposite direction to the natural displacement, which gives an actuator displacement of the same size as previously but in the opposite direction. Clearly, the feedback now leads the command and the peaks are exceeded. Addition of feed forward gain to this case increases rather than decreases the error as shown in Fig. 8. This situation can occur frequently in structural testing where an actuator is pulling down, for example, on a wing to introduce torque while the overall motion of the wing is up. Thus feed forward control can be detrimental in some structural testing cases.

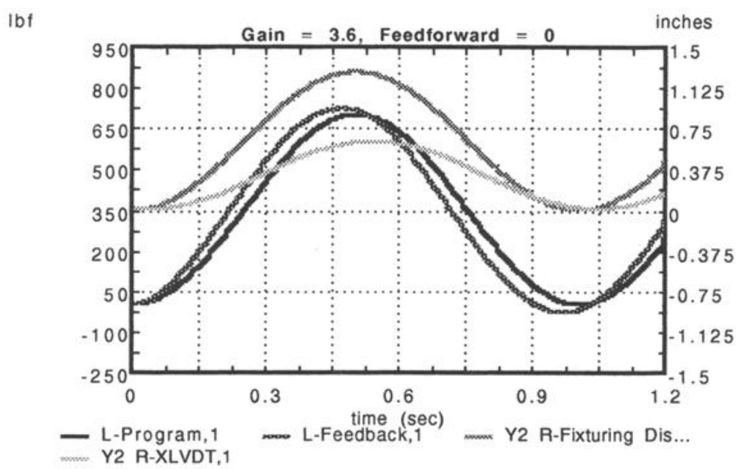

FIG. 7—*Response of actuator with crosshead displacement opposite to normal displacement and no feed forward.*

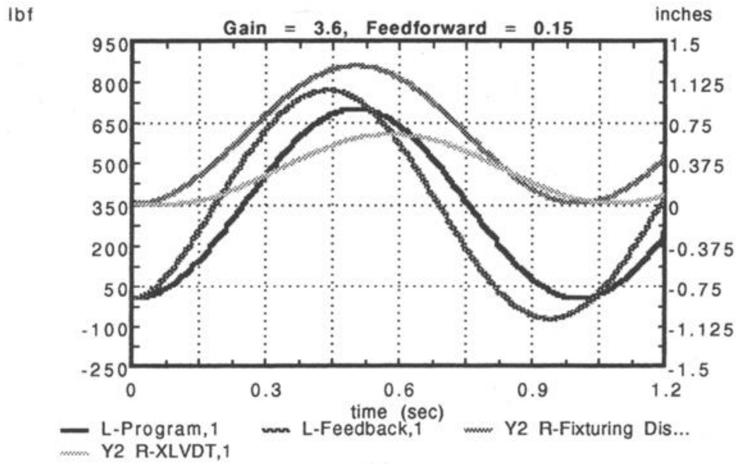

FIG. 8—*Response of actuator with crosshead displacement opposite to normal displacement and feed forward = 0.15.*

A key factor in the acceptance of simulation in the testing laboratory as an educational tool is the opportunity to examine a few of the variables discussed above using real hardware to confirm that the general trend of the simulations is correct.

Simulation for Problem Solving

Increasing Test Frequency by Reducing Servo Valve Size

The next stage in the implementation of simulation in the test laboratory is to be able to use it as a tool to understand sources of problems or to suggest better ways of testing. One example that occurred in one of the authors' laboratories involved a simple specimen test in a load frame. Because of limitations in the availability of testing machines, this particular test was being conducted in a machine that had a significantly larger actuator than required. In order to get as large a test frequency as possible with the oversize actuator, the operator had selected a large servo valve. However, test frequency was not sufficient and loading stability was poor. Since the allowable transition errors in this test were limited to 5% and the maximum proportional gain that could be used without causing stability problems was only about 1, only 5% of the valve flow was being used. Therefore a smaller servo valve was suggested that might allow a proportionately larger gain and hence larger real flows and test frequency. However, this was met with some skepticism. The existing test system was therefore modeled and the step response predicted with the maximum gain that could be used in the test. This is shown in Fig. 9 where it can be seen that there is some initial overshoot. If the valve characteristics of the smaller valve were identical to the larger one, substitution of a 2.5 gpm (0.158 L/s) valve in place of a 15 gpm (0.946 L/s) valve might be expected to allow a gain of 6 for the same total flow as before. The step response for this case is shown in Fig. 10 and it is clear that this case is much more stable. Increasing the gain to 9, as in Fig. 11, still produces a response that is more stable than Fig. 9. Thus a 50% increase in flow and test frequency appeared possible. The operator therefore tried the smaller valve and was able to realize a slightly larger increase in test speed. In addition, the load resolution was improved considerably by using the smaller servo valve since the valve hysteresis is effectively less. Valve hysteresis is usually about 1%

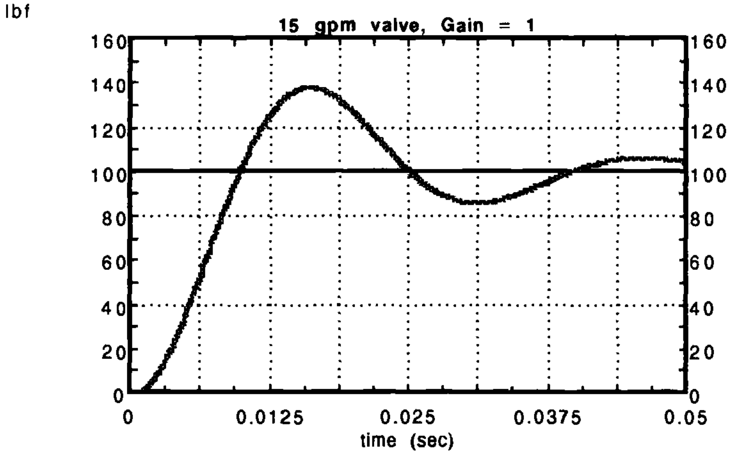

FIG. 9—*Step response of system with 15 gpm valve at a gain of 1.*

of rated flow which therefore requires a feedback error of about 1% of full-scale load for the 15 gpm (0.946 L/s) valve at a gain of 1, but only about 0.1% with the 2.5 gpm (0.158 L/s) valve because it could be operated at a gain of about 10.

Response Frequencies of Simple Systems

Simulations can also be used to understand the sources of problems. A typical problem in aircraft structural tests is to try and determine the source of noise or instability and to know what can be modified to alleviate the problem. This can be studied at a very basic level using a simple spring specimen with an attached mass between it and an actuator-mounted load cell by analyzing the impulse response of the system. Additional information, not available exper-

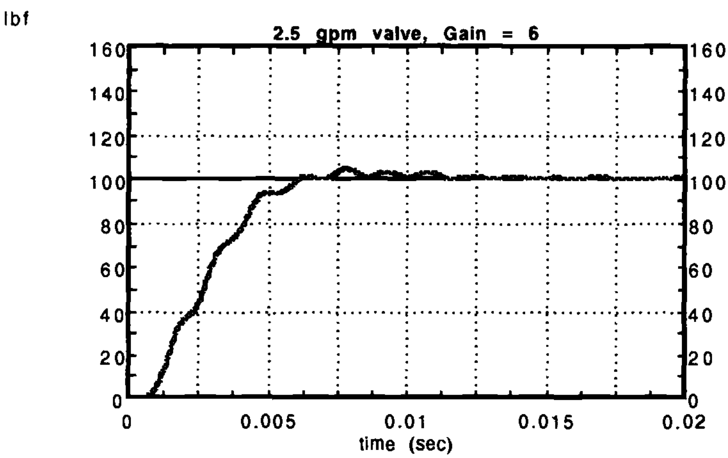

FIG. 10—*Step response of system with 2.5 gpm valve at a gain of 6.*

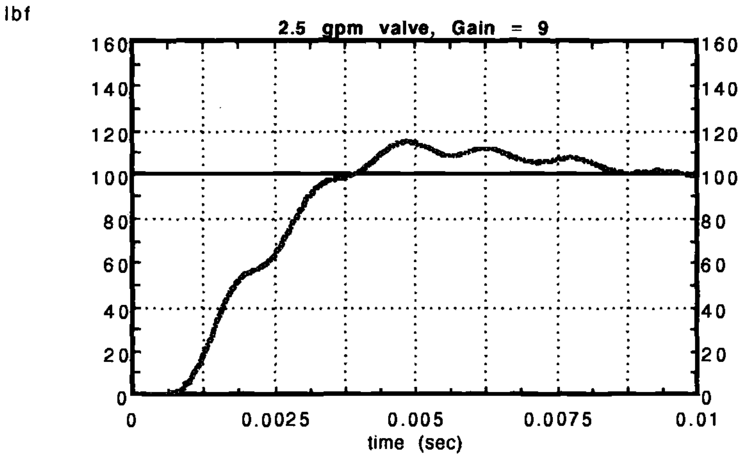

FIG. 11—*Step response of system with 2.5 gpm valve at a gain of 9.*

imentally, can be obtained with a simulation by selectively turning off dynamics in various elements of the model.

The model used in the example below consisted of a 2.5 gpm (0.158 L/s) servo valve, a 1.1 kip (4.89 kN) actuator with a 10-in. (25.4 cm) stroke and 10-lb (4.54 kg) grip mass and a spring with a stiffness of 835 lbf/in. (0.146 MN/m). The natural frequency of the actuator/mass combination (oil column frequency) was about 114 Hz. Full scale was set at 1200 lbf (5.34 kN) and feedback from an actuator-mounted load cell was selected. The proportional gain was initially set to 4 (the system became unstable for a gain >4.8) and the impulse response was analyzed using an FFT plotter to observe the predominant response frequencies. When all dynamics were turned on, the FFT plot of the impulse response shown in Fig. 12 was obtained,

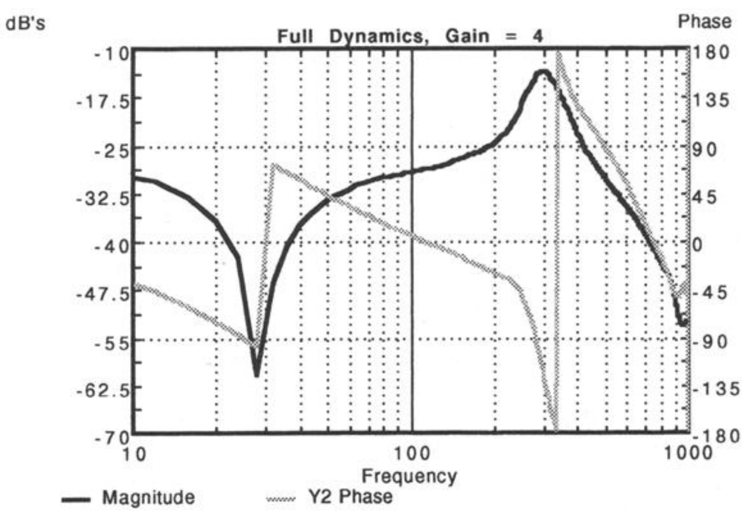

FIG. 12—*FFT of impulse response of spring/mass system using full dynamics and gain = 4.*

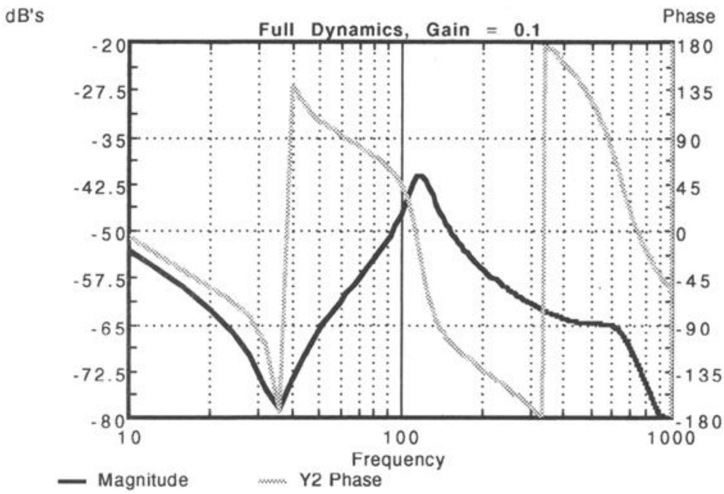

FIG. 13—*FFT of impulse response of spring/mass system with full dynamics and gain = 0.1.*

which indicates that the predominant frequency is at about 300 Hz, significantly higher than the oil column natural frequency. It also indicates a "hole" in the response at about 28 Hz, the natural frequency of the spring/grip mass system.

When the actuator dynamics or valve dynamics were turned off, the oscillation disappeared. This implies that both valve dynamics and actuator dynamics operate together to create the oscillations. If all dynamics are turned on and proportional gain is reduced to 0.1, the response frequency is reduced to about 115 Hz as shown in Fig. 13. The frequency of the hole is increased to about 36 Hz. Thus, as the gain is reduced, the response frequency appears to tend toward the oil column natural frequency while the frequency of the hole increases.

To clarify the effects of the various system parameters, such as grip mass, actuator rod mass, spring stiffness, and gain, a series of impulse simulations were performed and analyzed in terms of peaks and holes. These are summarized in Table 1, which also shows the calculated natural frequencies using various combinations of the springs and masses in the system.

The first simulation shown in Table 1 was for the standard case but with zero grip mass. The results clearly show that the frequency of the peak in the response is that of a simple spring/mass system where the spring stiffness is the combined stiffness of the oil column and specimen spring stiffnesses, and the mass is the combined mass of the grip and actuator rod. This appears independent of gain, so with zero grip mass the response is simply the overall response of the actuator and specimen.

As mass is added above the load cell (meaning grip mass), the change in response becomes a function of controller gain. For low gains (0.1), the frequency of the peak is again that of a simple spring mass system using the combined masses and stiffnesses of the system. Thus the case for a grip mass of 50 lb (22.68 kg) and an actuator rod mass of 4.7 lb (2.13 kg) gives the same peak frequency as a grip mass of 25 lb (11.34 kg) and an actuator rod of 29.7 lb (13.47 kg). The frequency of the hole is clearly related to the natural frequency of the grip mass/specimen spring system (the structure) but is always higher. This implies either some reduction in mass or increase in stiffness. Changing the actuator rod mass has no effect on this frequency, which suggests that the structure is being stiffened.

For a high gain (4.0), the frequency of the peak increases with grip mass rather than decreases, as with the low gain. It also increases with a decrease in specimen stiffness. However,

TABLE 1—*Effects of system parameters on frequencies of holes and peaks.*

Rod m_1	Actuator k_1	Grip m_2	Spring k_2	$\sqrt{\frac{k_1}{m_1}}$	$\sqrt{\frac{k_2}{m_2}}$	$\sqrt{\frac{k_1+k_2}{m_1+m_2}}$	Gain = 0.1 Hole	Gain = 0.1 Peak	Gain = 4 Hole	Gain = 4 Peak
4.738	19800	0	835	202	...	206	...	206	...	206
4.738	19800	2	835	202	64	173	83	175	66	225
4.738	19800	5	835	202	40	144	50	150	40	270
4.738	19800	10	835	202	28	117	36	115	28	300
4.738	19800	20	835	202	20	90	25	90	20	320
4.738	19800	50	835	202	13	60	15	60	12	370
14.738	19800	10	835	114	28	90	36	90	28	200
29.738	19800	25	835	81	18	61	21	60	20	216
4.738	19800	10	8350	202	90	136	91	137	91[a]	140[a]
4.738	1980	10	8350	64	90	83	92	84	...	82
4.738	1980	10	835	64	28	43	28	46	32	44
valve dynamics removed										
4.738	19800	10	835	202	28	117	...	...	28	125
4.738	19800	50	835	202	13	60	...	...	12	60

[a] gain = 1, system unstable at gain = 4.

it does decrease with increasing actuator rod mass and decreasing stiffness of the oil column. Thus it appears that the frequency of the peak results from the interaction of the specimen dynamics and the control system/valve dynamics. This was confirmed by running the 10-lb (4.54 kg) and 50-lb (22.68 kg) grip mass cases without valve dynamics at a gain of 4: the frequency of the peaks were then close to those predicted for the combined system. The hole in the response for the high gain case always occurs at the natural frequency of the specimen spring/grip mass system.

These results can be rationalized as follows. While the load feedback in the simulation comes from a point between the grip mass and the actuator rod, the two are directly coupled. The system must therefore respond in terms of displacement as a completely coupled system. Any disturbance will cause response peaks in displacement at the natural frequencies of the total system (including the control system). For low gains, these will be the basic mechanical natural frequencies of the full system (structure plus actuator). These displacement disturbances will generate acceleration disturbances which result in load disturbances at the load cell because of the inertia of the grip mass. The disturbances in the load that the specimen itself experiences (L-Fspecimen) are significantly lower than those observed at the load cell (L-Feedback) as shown in the step response of the system in Fig. 14.

At high gains, the interaction of the grip mass and valve dynamics effectively increases the stiffness of the oil column and, hence, the natural frequency of the total system. The frequency of the oscillations in the feedback is therefore increased. The effective stiffening increases with grip mass.

No load would be required to drive the structure itself at its natural frequency. So if the structure were fully decoupled from the actuator, one would expect holes in the response plots at the natural frequencies of the structure. For high gains, the control system will be able to maintain the actuator load near the command level. Thus the control system effectively decouples the actuator and structure in terms of load and the holes are observed at the natural frequencies. For lower gains, the decoupling is not complete and the structure will have some added stiffness due to the actuator restraint. The frequency of the hole in the response is therefore higher than the natural frequency of the structure.

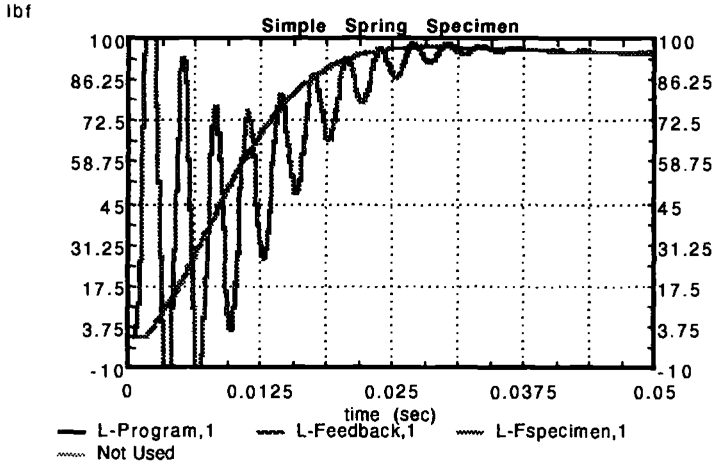

FIG. 14—*Response of simple spring/mass system to a step input using full dynamics and gain = 4.*

Simulation of Complex Structures

The examples above used simple representations of the specimens using springs and masses that are often available within simulation programs or are easily built. However, as the test structure becomes more complex, modeling the structure in terms of simple springs and masses becomes increasingly difficult and a more formal modeling of the structure is required. Fortunately, the test engineer is not required to do this since most modern airframe components have already been modeled using finite elements during their designs. All that is required is a model block that can take the appropriate model output from a finite element model and use it in the simulation.

A general structural element has been developed by the authors for use in the Extend simulation package based on modal concepts. A simple preprocessing program has also been developed that can extract the relevant information from a standard NISA finite element eigen value analysis. The output from the preprocessing program is then used as a direct input to the structural element.

Response Frequencies of Cantilever Beam

To illustrate the use of this structural element, the case of a cantilever beam with an actuator at the free end is considered. The first four natural frequencies and mode shapes for the cantilever beam by itself were the only inputs required for the structural element. The beam parameters were chosen such that the beam stiffness was the same as the spring considered earlier and the first natural frequency was the same as the simple spring/mass system. All other system parameters were as used in the previous example. If the rationalization given for the simple spring/mass system is correct, one would expect peaks in the feedback response at the natural frequencies of the combined beam/actuator system at low gains and holes in the response at the natural frequencies of the cantilever beam in the fixed-free condition at high gains. The frequencies of the holes should increase as the gain is reduced while the frequencies of the peaks should increase as the gain is increased due to the effective increase in stiffness of the oil column.

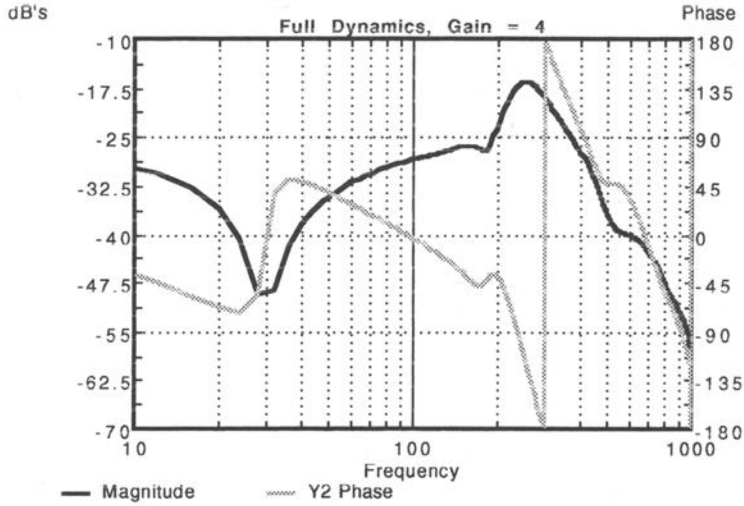

FIG. 15—*FFT of impulse response of cantilever beam using full dynamics and gain = 4.*

Calculation of the natural frequencies of the cantilever beam in the fixed-free mode is straightforward and for the beam used in this example they are 30, 187, and 523 Hz for the first three modes. Calculation of the natural frequencies of the beam/actuator system was accomplished using a finite element (FE) analysis of the beam with a point mass added at the free end to represent the mass of the actuator rod and a spring attached between it and ground added to represent the oil column stiffness. The first three natural frequencies calculated using the FE model are 100, 191, and 465 Hz.

The FFT plots of the impulse responses for the high and low gain cases are shown in Figs. 15 and 16. At low gain, the peaks are at about 100, 195, and 440 Hz and the holes are at about 36, 175, and 550 Hz. For the high gain case, the peaks are at about 170, 250, and 420 Hz while the holes are at about 30, 190, and 550 Hz. Thus the peaks and the first hole are exactly where expected from the previous rationalization while the second and third holes are at a slightly lower frequency than expected for the low gain case.

Simulation for Test Optimization

The ultimate aim of simulation, from a test engineer's viewpoint, is to be able to model a complete test system (test article, actuators, rigging, and control system) and use it to determine both the optimum configuration and the optimum tuning parameters. The test engineer would then be able to determine how fast the test will run long before the test is assembled and would be able to run at the optimum speed right from start-up rather than go through the long, manual tuning process that is currently necessary. The building blocks for this total simulation are now available but there are significant obstacles to full implementation.

The first obstacle is to proceed from a simulation that provides good qualitative results to one that can accurately duplicate experimental results. This is underway but will take time as the various model blocks are refined and their individual parameters determined for specific hardware. For example, there are more than 20 parameters that must be set in the servo valve block. But once they have been determined for a specific valve model they would not require any input. As simulations become more complex, it may also be necessary to add effects that

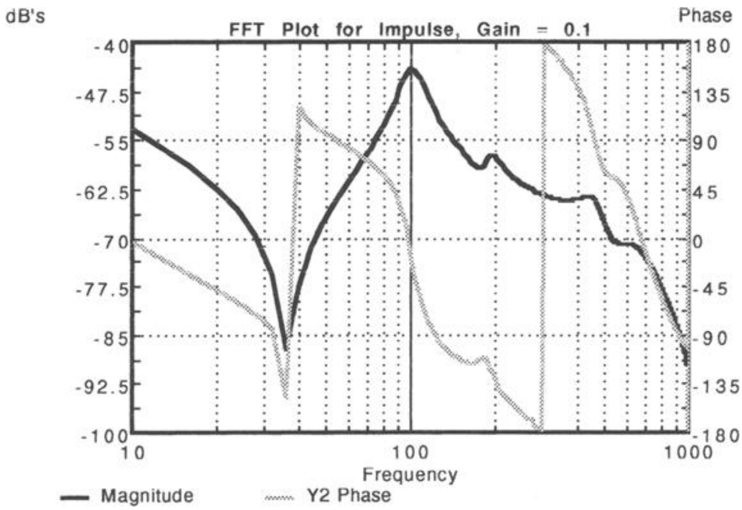

FIG. 16—*FFT of impulse response of cantilever beam with full dynamics and gain = 0.1.*

have been assumed to be negligible. This process will obviously require significant experimental evaluations at all stages as model blocks are added to the total model.

The second obstacle will be the acceptance of the simulation tools by the full-scale testing community. This will require incremental introduction of the techniques. If test operators and engineers have the opportunity to use simulations themselves, initially in the education mode and then as a tool to understand and solve problems, even in small component tests, acceptance will follow. However, the quantitative aspects of simulation must not be promoted before they have been thoroughly examined for the hardware they are to be used with. When so much time and money is involved in an aircraft structural test, one bad simulation could destroy any confidence that has been built up in the simulation system.

Another impediment at the present is the availability of easy-to-use software on a platform with sufficient power to run these large-scale simulations. However, once the concept is accepted, more restricted versions of the software, tailored for this particular use, can be developed for the more powerful platforms. The systems must retain their ease of use so that they can be used as a tool by the test engineer rather than simply providing the results of a simulation to the test engineer.

Conclusions

The concepts of modeling a complete full-scale aircraft structural test have been introduced and suggestions were made for a method of implementation in a full-scale test laboratory that will aid in their acceptance and consequent use.

It has been suggested that simulation systems initially be introduced as an educational tool for new operators and test engineers. Examples of where this has previously been of benefit have been provided. The models can then be used in a qualitative manner to understand sources of problems in specific test arrangements and to suggest improved ways of performing tests. An example of using a smaller valve to improve test speed has been provided together with an example of how simulations can be used to explore the dynamic interactions in a simple spring/mass test system.

An example of a simple cantilever beam with a single actuator at the free end was used to demonstrate how a simulation can be used to understand the dynamic interactions in a test with a complex structure using model data obtained from a finite element eigenvalue analysis.

Finally, the possibilities of using simulations to optimize a complete structural test have been discussed. It has been suggested that this will only be possible if simulation techniques are introduced incrementally and are accessible to the test operators and engineers as development tools rather than as a separate service.

Acknowledgments

This work was funded by MTS Systems Corporation under a research contract with the National Research Council of Canada.

Test Control

C. S. Venkatesh,[1] *Raghu V. Prakash,*[1] *and R. Sunder*[2]

Computer-Controlled High Strain Rate Compression Test System

REFERENCE: Venkatesh, C. S., Prakash, R. V., and Sunder, R., "**Computer-Controlled High Strain Rate Compression Test System,**" *Applications of Automation Technology to Fatigue and Fracture Testing and Analysis: Third Volume, ASTM STP 1303,* A. A. Braun and L. N. Gilbertson, Eds., American Society for Testing and Materials, 1997, pp. 99–110.

ABSTRACT: A computer-controlled 100 kN high strain rate compression test system was developed for hot deformation experiments at up to 1300 °C under controlled strain rates between 0.01 s^{-1} and 200 s^{-1}. The design implements a number of schemes tailored for high strain rate testing. These relate to the servo-hydraulics, mechanical fixtures, and controls. It incorporates "green" features such as low power pump, air-cooled heat exchanger, and a mechanical fuse to protect the load frame assembly and transducers from overloads.

KEYWORDS: workability, metals, high temperature, strain rate, servo-hydraulic testing machine, hydraulic power-pack, servo-valves, servo-controller, mechanical fixtures, compression testing

Metals are worked to achieve the desired shape through two routes: (1) moderate mechanical forces after heating the material to high temperatures, or (2) high rates of working [*1*]. The former considers that metals in general exhibit high ductility and low resistance to deformation at temperatures greater than one-half of the melting temperature. However, this poses operational problems of heating the parts to high temperatures and maintaining them until the mechanical working is complete. High rates of working, which are preferable for economic considerations and heat transfer conditions, could result in increased resistance to deformation and as a consequence decreased ductility of the material being worked [*2*]. Thus, an optimum combination of heating and mechanical working can provide better results for hot working of materials.

Flow stress (σ), the stress required for plastic deformation at a constant temperature and strain (ε) is related to strain rate ($\dot{\varepsilon}$) by a power law relationship:

$$\sigma = (C\dot{\varepsilon})^{m}$$

where m is the strain sensitivity of the material.

Workability is evaluated under constant strain rate. Compression tests conducted under constant actuator speed result in increasing rate of strain, as the instantaneous gage length of the specimen decreases during the test. To maintain constant strain rate during testing, it is essential to vary the speed of the actuator in accordance with changing gage length. Required instantaneous actuator speed is determined by strain rate and instantaneous gage length. Instantaneous

[1] Structural Integrity Division, National Aerospace Laboratories, Bangalore, 560 017, India.
[2] BiSS Research, 99, 14A Cross, Malleswaram, Bangalore 560 003, India.

speed of the actuator at high strain rate can be of the order of a few meters per second. This paper describes the design of a high strain rate compression test system for testing materials over the strain rate range from 0.01 s^{-1} to 200 s^{-1} using standard compression test specimens conforming to the ASTM Method for Compression Testing of Metallic Materials at Room Temperature (ASTM E 9).

System Configuration

The basic system consists of a load frame, servo-hydraulic actuator, hydraulic power pack, controls, load and displacement transducers, and load fixtures. For testing at elevated temperatures, two furnaces are provided, one for heating up to 1000 °C and another for heating up to 1300 °C.

Load Frame

The 200 kN load frame is a conventional double column, self-reacting type with provision to mount the actuator either on the cross head or at the base platen. The distance between the columns is 625 mm, and vertical daylight is about 1.6 m. Hydraulic lifts and clamps assist in cross head movement and clamping.

Servo-actuator

A ± 100 kN double ended, double acting servo-actuator rated for 275 bar operating pressure, with a working stroke range of ± 80 mm is mounted on the base platen. An LVDT for stroke measurement is integrally mounted into the actuator centerline cavity. The system design called for testing at controlled constant strain rates ranging from 0.01 s^{-1} to 200 s^{-1}. This calls for low hydraulic flow requirement (of the order of a few litres per minute) for tests conducted at lower strain rate, while very high instantaneous flow rates (a few hundreds of liters per minute) are required for conducting tests at high strain rates. To make this possible on the same test system, a 900 litre per minute (L/min) as well as a 40 L/min servo-valve are mounted on the actuator manifold.

Figure 1 shows the servo-actuator manifold. To meet the instantaneous flow requirements as well as to compensate for the pressure losses during high strain rate testing, two 5-L bladder type accumulators are provided on the manifold close to the servo-actuator. The two accumulators shown on the photograph provide for an instantaneous flow rate of up to 1200 L/min and dead volume of 10 L. The volume requirement for a single test is of the order of 0.25 L. The manifold is connected to the actuator cylinder through three ports at either end. The side port connections visible at the top of the manifold are through rotatable connectors for relaxed tolerances on dimensions. The multi-port entry facilitates large flow rates without significant pressure loss. The small servo-valve seen at the top of the manifold is of 40 L/min capacity, while the large one at the bottom is rated for 900 L/min.

To avoid the need for manual switching of servovalves, the 900 L/min servo-valve was configured with a dead band, approximately equal to the flow rate of the smaller servo-valve. A schematic of the resultant response of the two servo-valves to drive current is shown in Fig. 2. Servo-amplifier gains were programmed through the test software to effectively shut-off the high flow rate valve during low speed actuator movement, thereby ensuring better system performance and stability over the entire range of strain rates. A 10-μm pressure line filter is provided on the manifold. To accommodate large flow rates at the end of high strain rate testing,

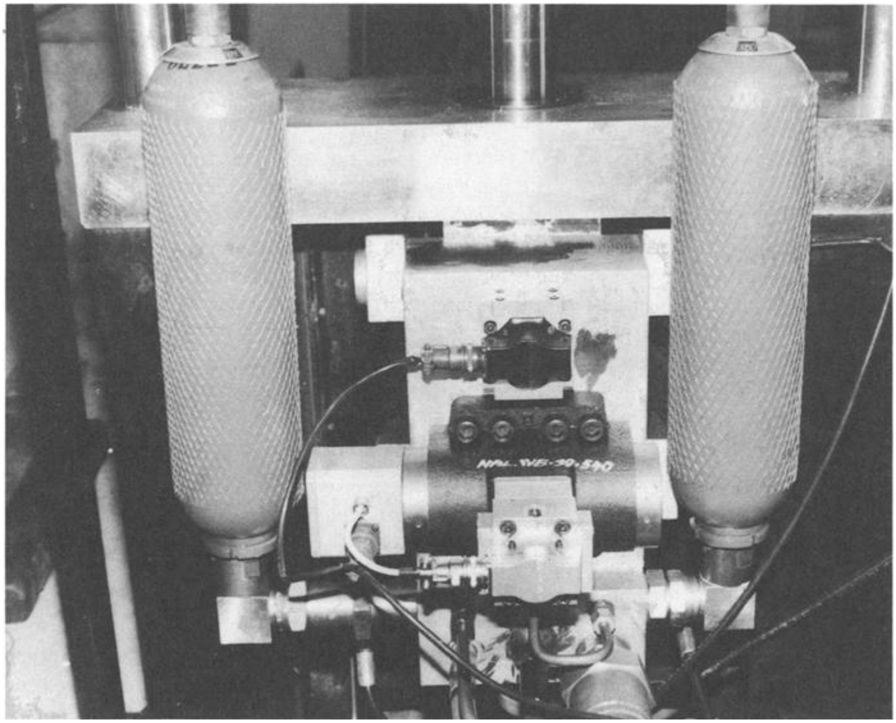

FIG. 1—*Servo-actuator manifold assembly. Two 5-L accumulators are shown vertically mounted on either side of manifold. Small black servo-valve at top of manifold is of 40 L/min capacity. The large one below it handles 900 L/min.*

a 2-in. diameter return line is provided in the system hydraulics. To avoid back pressure problems on the return line at high discharge rates, the return line is directly connected to the hydraulic reservoir without any components between the actuator manifold and the reservoir. An independent circulation pump is provided for filtration and cooling.

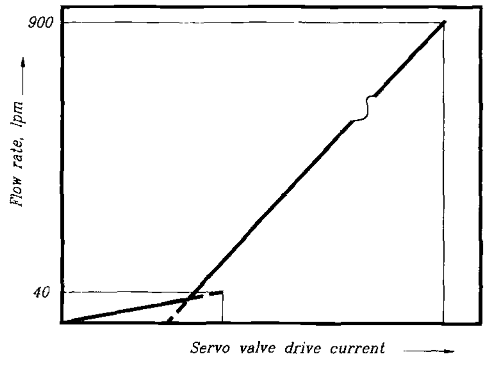

FIG. 2—*Flow rate versus drive current for the two servo-valves.*

The 900 L/min servo-valve consists of a high-flow, four-way spool valve which is positioned by a smaller pilot servo-valve. An LVDT internally positioned on the main stage of the servo-valve converts the main stage spool position to an output voltage. This voltage is used as feedback in the inner control loop to accurately position the main stage spool. Essentially, flow rate on this valve is controlled by the position of the four-way spool. The servo drive signal for the 900 L/min valve is fed to a servo-amplifier at the lower right of the accumulator seen on the left-hand side in Fig. 1. The drive signal is compared with the conditioned LVDT output, providing spool position feedback and the resultant error signal fed through the short white cable seen in the figure to the pilot servo-valve sitting piggy back on the large spool.

Given a null drive signal, the pilot valve will thus ensure zero position of the main stage spool. However, it may be noted that the pilot servo can actuate the main stage spool only when a certain minimum pressure is available on the system. This design feature effectively makes the high flow rate valve uncontrollable at low system pressure, typical of startup conditions. As a consequence, in the event the main stage spool position was in the open position (in either direction) at system startup, the actuator is likely to shoot to the extreme position when the pressure is turned high—even at zero signal on the servo-valve input. This can cause damage to the specimen and other fixtures on the load train and pose a hazard to the operator. In view of the inertia component at impact, the associated loading can be far in excess of loads estimated from current system pressure.

The possibility of inadvertent actuator movement was eliminated by ensuring that the spool is in the closed position at shut down and start up. The following procedure is used to achieve this: A cut-off switch is introduced on the high flow servo-valve circuit. Prior to system shutdown, the switch is put *Off* with the actuator at stationary position *before* hydraulic pressure is reduced. It is put back *On* at the next session *after* system pressure is switched Hi. The scheme appears to ensure that the high flow servo-valve is activated only when it can be controlled. As it is switched *On* and *Off* at zero flow conditions, there is no jerky movement and loss of control while switching. The dead band on the spool provides additional protection to these conditions. It may be noted that a returning spring installed within the spool would have ensured neutral position at zero pressure.

Hydraulic Power Pack

A fixed delivery hydraulic power pack with a discharge capacity of 16 L/min at a maximum delivery pressure of 275 bar was set up for this test system. The power pack manifold is shown in Fig. 3. As system idle time is long compared to the test duration due to the nature of testing and the time required for attaining the required test temperature on the furnace, an unloading valve (shown next to accumulator in Fig. 3) was provided to cut-off the pump output from the pressure line when the operating pressure is reached.

Figure 4 shows a schematic of system pressure versus time under idling conditions in the presence of an unloading valve. The rise time is due to accumulator charging with pump flow cut into the system. The fall time is due to internal leakages under idling conditions. As seen from this figure, the pump motor is loaded only for about 10% of the total operating time. The pressure settings for the cut-off are user-selectable and can be adjusted through a relief valve. It must be noted that the same goal could have been achieved by using a more expensive variable displacement pump with pressure compensation.

An independent low pressure circulation cooling circuit is provided on the system with an oil-air heat exchanger and a 3 μm filter. This feature allows the return line from the high strain rate machine to be free of components that may contribute to back pressure at high flow rates. This circuit maintains oil temperature under 45 °C at ambient temperature up to 30 °C.

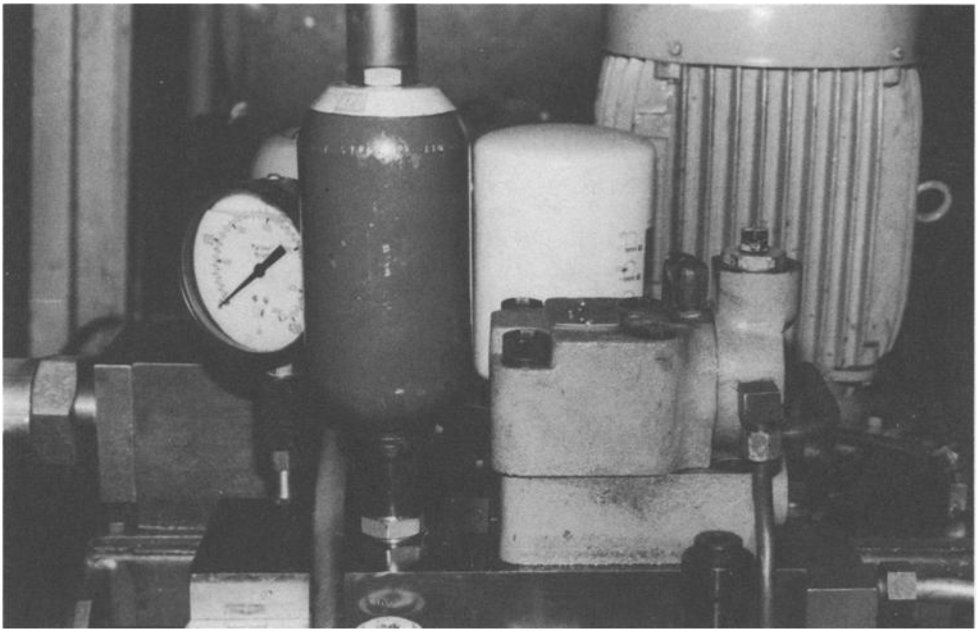

FIG. 3—*Hydraulic power pack manifold with accumulator and unloading valve.*

Mechanical Fixtures

Three basic types of fixtures were developed: test fixture for axial compression for solid as well as ring compression specimens, plate compression fixture for testing plate samples under plane-strain conditions, and quick changing tensile grips. These were made out of AISI 4340 hardened steel for room temperature testing applications, and out of an oxide dispersion strengthened alloy PM 2000 for testing at elevated temperature. Figure 5 shows the three different types of grip heads.

Under low rates of loading, the stall load on the actuator determines limit loading likely to

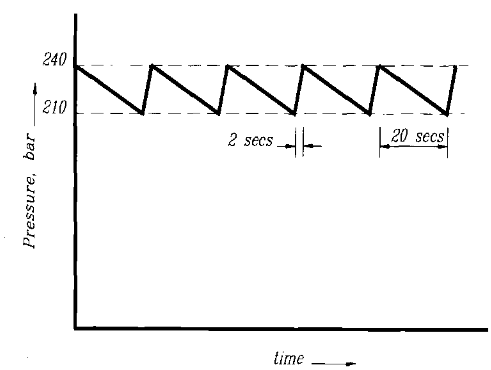

FIG. 4—*Power pack system pressure variation versus time under idling conditions.*

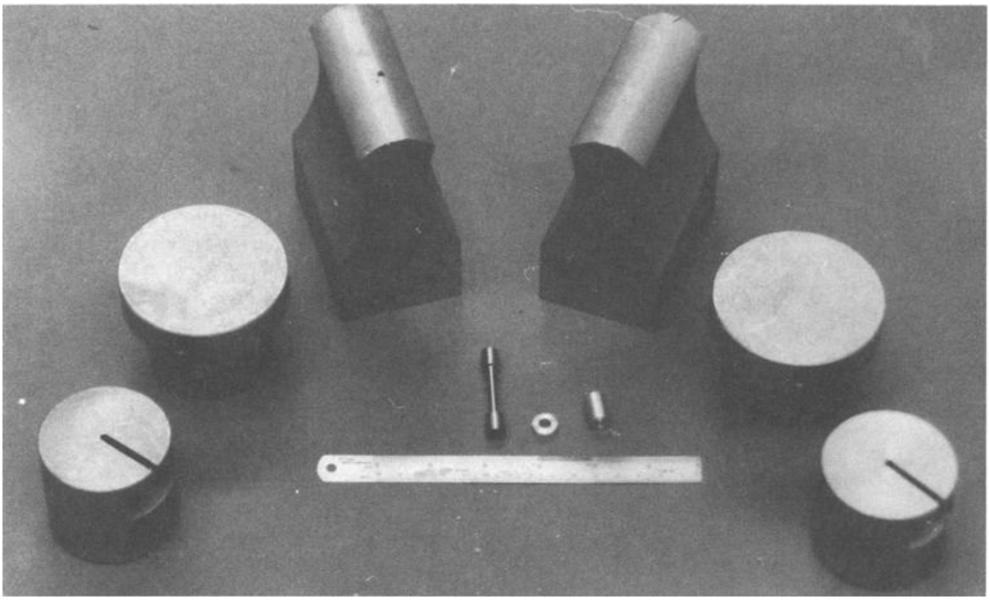

FIG. 5—*Grip heads for tension, compression platen and plane strain compression anvils. One set of fixtures were made from AISI 4340 steel for testing at room temperature, while another set of identical fixtures was fabricated from an oxide-dispersion strengthened alloy PM 2000.*

be seen on the testing machine. However, under high rates of compressive strain, the moving actuator and load train mass may develop inertia loads, that together with hydraulic loading, can exceed rated loading on the testing machine. In an attempt to reduce chances of damage due to such loading, a few protective features were introduced into the test system. All the load fixtures and load cell are designed to sustain a 50% axial compressive overload without damage. In addition, a mechanical fuse that would fail under shear load was designed to ensure load release in the event of a compressive overload. A drawing of the compression fuse assembly appears in Fig. 6. The assembly consists of the following: a base shaft having a central cavity, above which a circular metallic disk of known shear strength is placed. Above the metallic disk, a telescopic pull rod guided by an alignment ring (for alignment of load-line) is placed. In the event of compressive loads in excess of the shear failure load of the mechanical fuse, the fuse snaps and the telescopic rod sinks into the cavity of the base shaft. This ensures immediate release of compressive loads from the load train. The material and thickness of the fuse are user selectable. In case of tensile testing, it was assumed that the specimen sections used would preclude the possibility of sustaining loads exceeding nominal load cell capacity.

The mechanical fuse assembly, along with the rest of the load train and machine columns introduce a certain degree of compliance into the test setup. Therefore, in compression testing, specimen displacement is measured by an external LVDT mounted on the top platen which senses the movement of core fixed on the lower platen (Fig. 7). As this signal is used for strain measurement and forms part of the control loop, data are insensitive to load frame and load fixture deformation. The LVDT mounts extend out of the furnace assembly and the lower mount stiffness is adequate to withstand large accelerations without significant inertia induced load arm deflection.

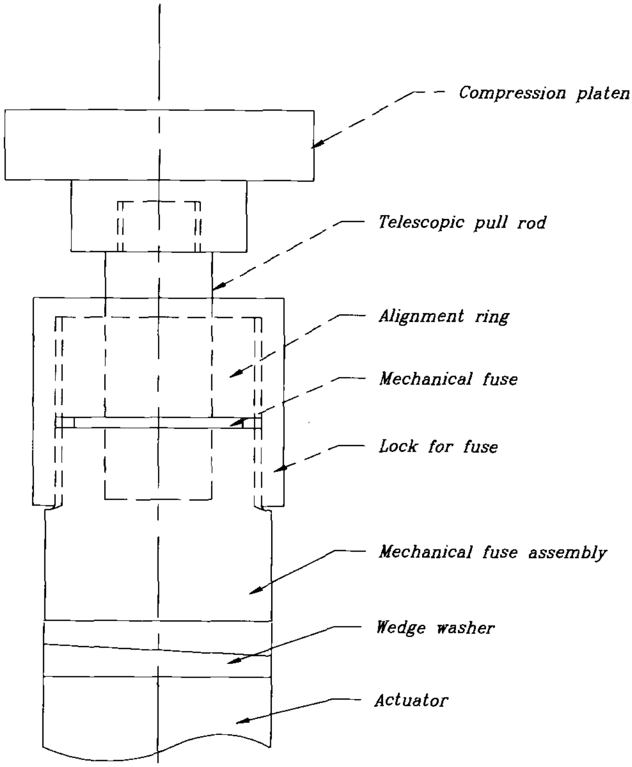

FIG. 6—*Mechanical fuse assembly. Thickness of shear fuse element is selected to suit desired limit load. As fuse element is punctured, telescopic pull rod can sink into cavity below fuse element, removing load on specimen.*

Controls

A dedicated microprocessor-based "Intelligent Mechanical Test Controller" (IMTC) is used with the test system. Reference *3* provides a detailed description of the IMTC. The IMTC is in-turn hooked on to an IBM PC-compatible host computer under Microsoft-Windows(TM) environment.

The IMTC contains all the components of a servo-hydraulic load frame controller: digital wave-form synthesizer, signal conditioners for LVDT and strain bridge transducers, servo-amplifier, data acquisition and interlock subsystems. Real time control and data acquisition firmware on the IMTC are driven by application software on the host computer. The operational parameters of all the IMTC components are software programmable. This includes gains and offsets on signal conditioners and the servo-amplifier.

The IMTC was originally designed to handle the more common mechanical tests including low rate tension and compression, fatigue, and fracture. The sine and ramp wave-forms required for these tests are built into firmware on the system and are invoked through the IMTC command set. Also, in conventional tests, servo-amplifier settings once selected, remain unchanged in the course of the test. As explained earlier, high constant strain rate testing requires an exponential variation of actuator displacement with time. Further, at high strain rates, actuator

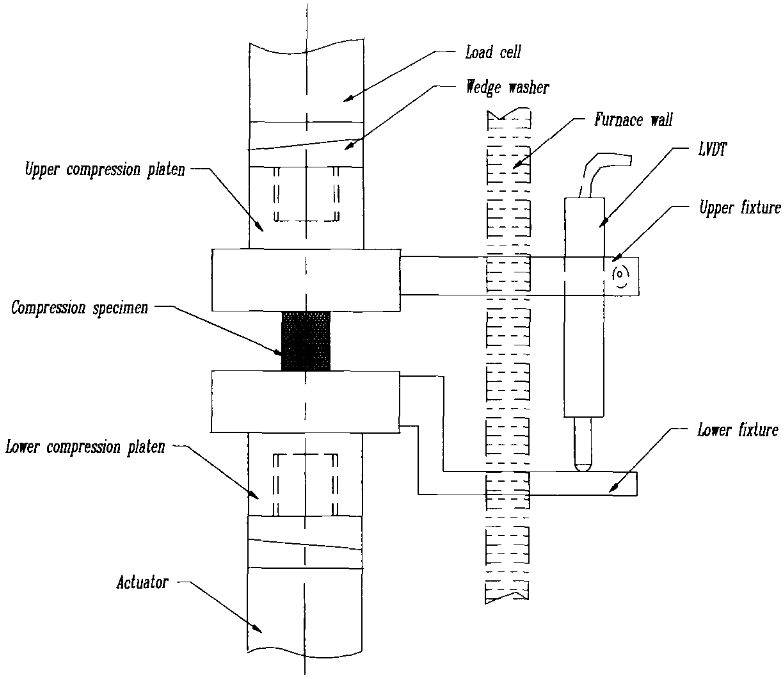

FIG. 7—*External LVDT transducer to measure specimen gage length displacement in compression testing.*

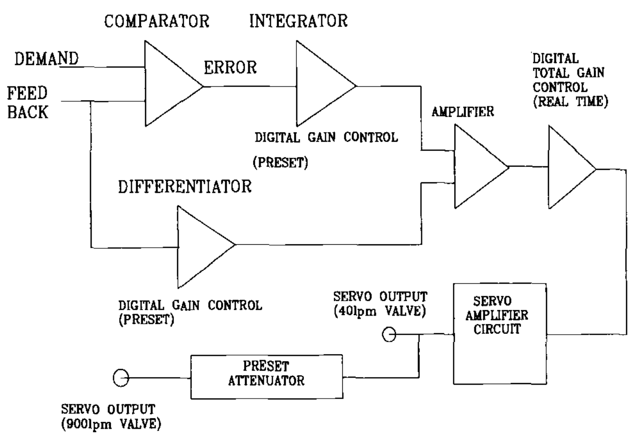

FIG. 8—*Pseudo-differential feedback (PDF) servo-amplifier circuit for dual valve operation [3]. The PDF circuit does not use the proportional gain element seen in conventional PID schemes. Integral, differential and total gain settings along with null and dither are software programmable. A trim potentiometer acts as preset attenuator on the high flow rate servo-valve drive signal to enable tuning of combined flow as shown in Fig. 3.*

acceleration at the commencement of a compression test can be very high, followed by deceleration as gage length reduces. This may call for variable servo-loop gain settings in the course of the test. To accommodate these new requirements, the IMTC firmware was modified to provide for a user programmable burst of control wave-form steps along with associated servo-loop overall gain settings.

The IMTC servo-amplifier circuit was modified to provide for independent attenuation of the drive signal for the high flow servo-valve (see Fig. 8). The attenuation is frozen during system set up and does not appear to require further modification. Proper balance of the two drive signals ensures that the two valves "work as one." This is demonstrated by the system response under low and high rate control wave-forms shown in Figs. 9 and 10. The results in Fig. 10 correspond to an actuator speed of about 1.75 m/s over a travel of 60 mm with 90 L/min servovalve.

The system was tuned to ensure sufficient gain reserve such that under pulse wave-form, the 900 L/min valve hits its dead band before the onset of overshoot conditions. As shown in Fig. 10 (bottom), the low flow rate valve "takes charge" as low speed conditions are approached. The response in Figs. 9 and 10 was obtained under preset constant servo gain settings. However,

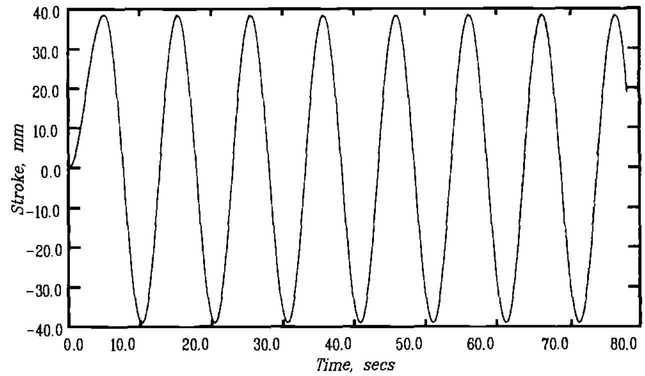

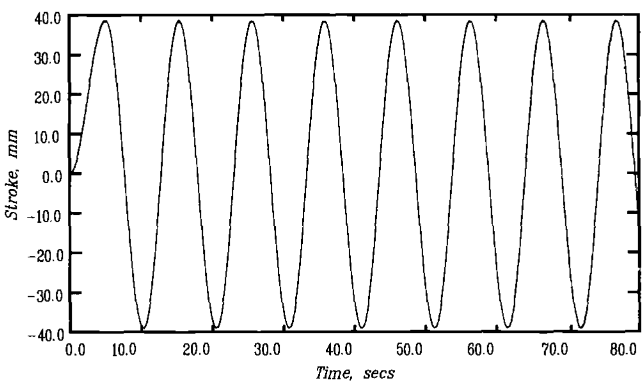

FIG. 9—*Control and feedback wave-forms appear to coincide at 0.1 Hz actuator oscillation over half span. The traces on the left were obtained with the high flow rate valve disabled. Switching in the 900 L/min valve did not appear to affect response (bottom), indicating that the attenuated drive signal was within the dead band.*

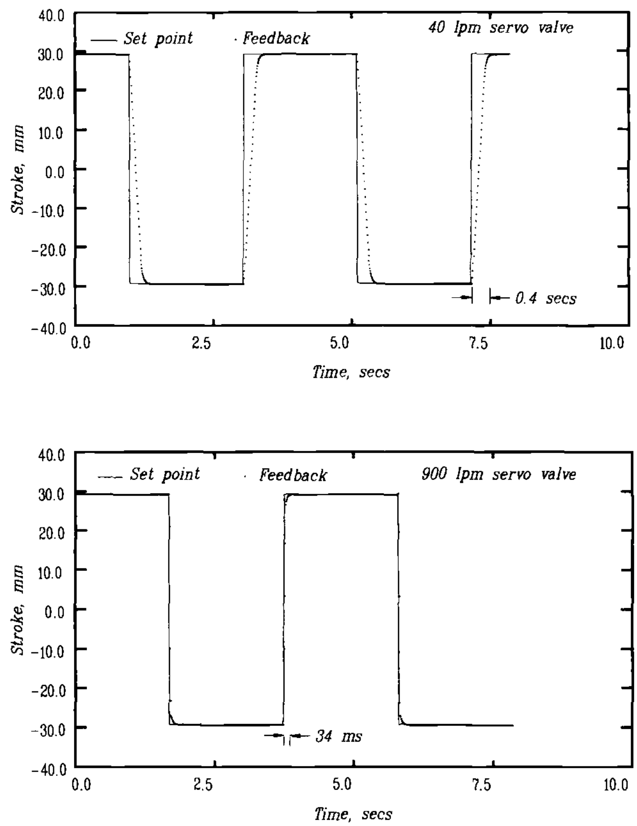

FIG. 10—*System high rate response without (top) and with (bottom) 900 L/min servo-valve switched into the servo drive circuit. Rise time on left is restricted by the 40 L/min flow rate on the smaller valve.*

provision was also made for dynamic, real time manipulation of servo gain, utilizing the gain reserve available on the system. The idea is to provide enhanced response during the transient associated with the test, with return to quasi-static settings as the test concludes.

An off-line test set up program is used for constant strain rate test set up. User inputs at start-up are specimen gage length, strain rate, and required percentage compression/tension. Up to three independent test stages can be specified, each with its own strain rate. Using these inputs, a real-time table of up to 1200 discrete control wave-form points is built up, with a constant programmable time step given in multiples of 50 μs. If required, the user may set a new total servo gain value for each of these wave-form points. A suitable combination of time step and number of steps is selected for a given gage length and strain rate. The second column in the table lists the servo-loop gain amplification against each discrete set point. These data are saved for use by the application program controlling the test. At the commencement of the test, the lookup table with control wave-form and servo-loop gain settings is loaded onto the IMTC's working memory. When the test is started, an Interrupt Service Routine (ISR) driven by a programmable real-time clock is triggered on the IMTC. On each call, the ISR loads the next control wave-form set point and the associated servo-loop gain setting. At this point, it also acquires data on selected feedback channels and builds up a table of specimen response that is read into the host computer at the end of the test.

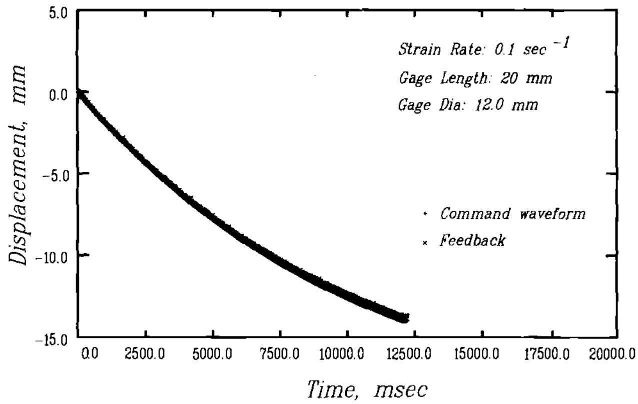

FIG. 11—*System response under constant strain displacement rate of 0.1* s^{-1}.

Figures 11 through 13 show actuator displacement response under three different constant strain rates for a specimen having a 20-mm gage length to be compressed down to 6 mm. These tests were done with free-moving actuator. It may be noted that there is a delay of about 25 ms between the demand and feedback signals even for tests conducted at 20 s^{-1} strain rate. However, the feedback signal matches the demand signal in shape just after the initial lag, suggesting the possibility of constant true strain rate over a large section of the test.

The response in Fig. 11 was obtained under constant gain settings. We find that after an initial delay associated with valve response and subsequent minor deviation, system response settles down to a steady offset from the required wave-form. The results in Fig. 12 are indicative of system response to variable gain settings.

In repeat tests, the off-line test set up program is used to examine previous test results and interactively modify servo-loop gain settings to achieve the desired system response. The time lag between demand and feedback is associated with gain settings as well as with the servo-valve response time and actuator dead volume. The time lag was about 5 ms on the machine and had to be accounted for while modifying gain settings to improve performance. By examining required and achieved performance, machine response is tuned for no-load conditions. At the next stage of testing, a dummy specimen is tested to verify machine and specimen

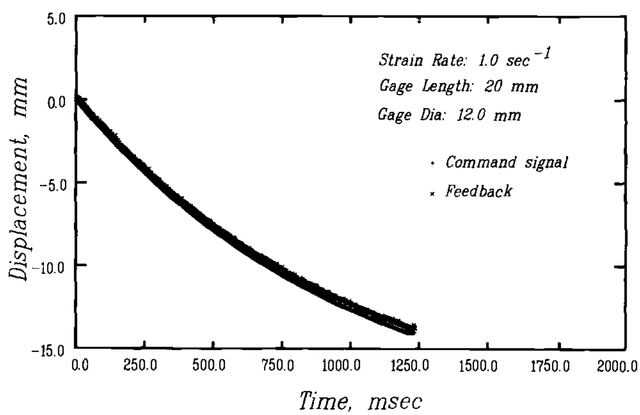

FIG. 12—*System response under constant strain displacement rate of 1.0* s^{-1}.

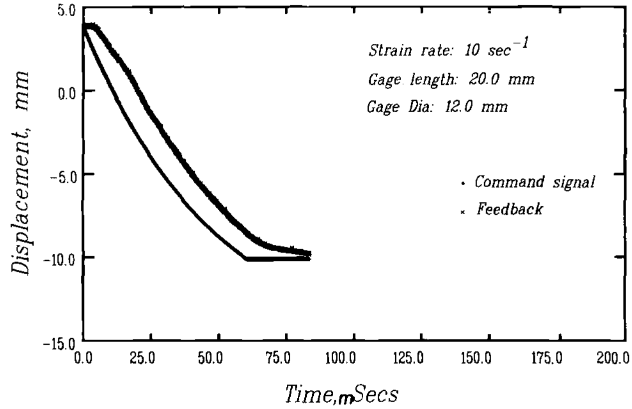

FIG. 13—*System response under constant strain displacement rate of 10 s^{-1}.*

response. In certain cases, further modification of gain settings may be required. This was particularly true of tests at strain rates in excess of 10 s^{-1}. On establishment of the best suited loop gain table for a given test, the settings are saved on disk for future reference.

Concluding Remarks

The design of the high strain rate test system addressed certain unique application specific requirements, which may find application in other test systems:

1. Use of large accumulator capacity with small delivery rate power pack and unloading relief valve ensured higher energy efficiency. The power pack delivery is less than 2% of servo-valve rating and was selected to just exceed internal leakages. This was possible because high strain rate testing is "single shot" in nature and the system can be still used for low-cycle fatigue testing. The associated energy saving combined with a simple air cooling option make the power pack a compact and fully autonomous unit.

2. The dual servo valve solution with provision of dead band on the high flow rate valve makes them work as a "single solution" to both high and low rate requirements. There is no need for mechanical or electrical switching of servo valves for a specific test.

3. User programmable of gain settings permit on-site manipulation of system response without the need for hardware trims. Further work is required to develop a more "intelligent" real time control software which may reduce or eliminate the requirement for iterative tuning of the system.

4. The design of the high flow rate valve imposes certain limitations on system performance and safety. As multiple stages are involved, response time is higher than single stage servo valves. Also, if the system is shut down with the valve in the open condition, damage to system components may occur at the next startup.

5. The mechanical fuse protects the test specimen and fixtures against overload damage. Its operation is restricted to compression testing.

References

[1] *Workability Testing Techniques,* G. E. Dieter, Ed., American Society of Metals, OH 1984.

[2] Adler, J. F. and Phillips, V. A., *Journal of the Institute of Metals,* Vol. 83, 1954–55, p. 80.

[3] Sunder, R. and Venkatesh, C. S., "Dedicated Microprocessor-Based Controller for Fatigue Testing," *Applications of Automation Technology to Fatigue and Fracture Testing, ASTM STP 1092,* A. A. Braun, N. E. Ashbaugh, and F. M. Smith, Eds., American Society for Testing and Materials, Philadelphia, 1990, pp. 36–64.

Christopher E. Hinton[1]

Adaptive PID Control of Dynamic Materials-Testing Machines Using Remembered Stiffness[2]

REFERENCE: Hinton, C. E., "**Adaptive PID Control of Dynamic Materials-Testing Machines Using Remembered Stiffness,**" *Applications of Automation Technology to Fatigue and Fracture Testing and Analysis: Third Volume, ASTM STP 1303,* A. A. Braun and L. N. Gilbertson, Eds., American Society for Testing and Materials, 1997, pp. 111–119.

ABSTRACT: The dynamic behavior of both servohydraulic and electromechanical materials-testing machines is affected by the stiffness of the test specimen. This sensitivity is different in load and strain control. In load control the controller gain has to be set higher for soft specimens than for stiff specimens. In strain control, the reverse is true; the controller gain has to be set lower for soft specimens. The machine controller therefore has to be tuned to suit each type of test specimen. Tuning until recently has been conducted manually. It requires a fair degree of skill and often is not done properly.

An incorrectly tuned controller can seriously affect the quality of the materials test. If the proportional gain is set too low the resulting bandwidth reduction impairs the ability of the machine to closely follow the demand signal. Too high a gain can result in closed-loop instability that can rapidly destroy the test specimen.

The tuning problem is compounded by the fact that, in the majority of materials tests, the stiffness of the test piece alters as the test proceeds. Stiffness decreases with the propagation of fatigue cracks or the onset of plasticity or can increase if the test material cyclic-hardens. Some components have an inherent nonlinear stiffness characteristic. They become more or less stiff as the component is strained. In some tests, stiffness changes gradually while in others it fluctuates rapidly during each loading cycle. Varying stiffness means that even if the machine controller is optimally tuned to start with, it is unlikely to remain so throughout the test.

This paper describes an adaptive control system that overcomes these difficulties. It removes sensitivity to stiffness by continually updating the PID controller terms according to real-time stiffness measurements. There is no longer any need to conduct a tuning experiment every time a different type of specimen is installed and stiffness changes during a test are automatically accommodated.

A particularly demanding problem occurs in tests like low-cycle fatigue where the test specimen is exercised beyond its elastic limit. Sudden and significant stiffness changes that occur at each strain reversal are difficult to detect accurately because rates of loading and straining are near zero. This can be overcome by remembering how stiffness changed during the last cycle and this is demonstrated in a real low-cycle fatigue test.

KEYWORDS: testing machines, servohydraulic, electromechanical, sensitivity to specimen stiffness, load control, strain control, autotuning, adaptive control, continually-updated PID control, remembered stiffness, low-cycle fatigue

[1] Principal engineer, Instron, Limited, Coronation Rd., High Wycombe, Buckinghamshire, HP12 3SY, U.K.

[2] The adaptive control of materials-testing machines using real-time stiffness estimates and the use of remembered stiffness are the subjects of several pending international patents.

Nomenclature

e	Servo error
f	Specimen load
s	Laplace operator
u	Drive signal
x_p	Actuator piston position
x_s	Specimen extension
x_v	Valve spool displacement
G	Controller proportional gain
G_L	Static gain of the actuator and specimen transfer function in load control
G_S	Static gain of the actuator and specimen transfer function in strain control
K_S	Specimen stiffness
K_{SF}	Combined specimen and frame stiffness
τ_d	Controller derivative time constant
τ_m	Time constant of the actuator and specimen transfer function
τ_i	Controller integral time constant
Δ	Increment operator

Introduction

The behavior of dynamic materials-testing machines and their ability to closely follow command signals are affected by the stiffness of the test specimen. In load control, bandwidth tends to reduce as stiffness decreases, making response sluggish. In strain control the reverse happens; gain increases as the specimen becomes less stiff, and this can make the control loop unstable. The next section presents real test results for load and strain control that show these effects.

Although the experimental results presented in this paper were collected on a servohydraulic machine, similar sensitivity to stiffness is observed on electromechanical machines. The reasons why dynamic testing machines are affected by stiffness and the factors that make some machines more sensitive than others are now well understood [*1*,*2*]. Stiffness sensitivity has two implications for machine use:

1. It makes it important to re-tune the controller every time a specimen of different stiffness is to be tested. This is usually done by manually adjusting the controller terms. It requires some control knowledge and as this is not the natural discipline of most machine users, it is not surprising that it is not always done properly. A poorly tuned controller can affect the validity of the materials test.
2. A machine, even if well tuned at the start of a test, is unlikely to remain optimally tuned if the specimen stiffness changes during the test. Such changes occur in many materials tests. They can be gradual, the result of long-term fatigue damage, or they can occur during each loading cycle due to some inherent nonlinearity or the result of transitions from elastic to nonelastic behavior.

Stiffness sensitivity is a consequence of using a *fixed-parameter* controller. Since specimen stiffness is the quantity that affects machine response, it seems appropriate to use real-time estimates of stiffness to continually update the controller. It has been demonstrated [*1*,*2*] that this form of adaptive control makes the testing machine essentially insensitive to stiffness. It removes the need for repeated re-tuning and is able to preserve waveform fidelity even when stiffness changes during the test. The method is described in the section on continually updated PID control. What is new here is an extension to the basic method that uses remembered stiffness from the previous cycle to overcome the difficulty of estimating real-time stiffness during load and strain reversals. The section on remembered stiffness that follows shows the benefits of this for low-cycle fatigue (LCF) testing.

Stiffness Sensitivity—Two Examples

Load Control

Figure 1 shows the difference between measured load control responses obtained for a stiff and a soft specimen. The command signal was a 20 Hz triangular waveform. This test was conducted on a servohydraulic machine capable of developing forces of ±50 kN with an actuator working stroke of ±50 mm. The specimen was a length of rectangular section mild-steel bar (44 mm by 12 mm) mounted on a three-point bend fixture. Stiffness was adjusted by altering the spacing between the rollers of the three-point bend fixture and measured by noting the change in load caused by a change in actuator position.

The controller was tuned with the stiffness set at 24 kN/mm and gave the response shown in the upper trace. The stiffness was then lowered to 6 kN/mm but the controller tuning was not readjusted. The resulting response shown in the lower trace has a peak-to-peak amplitude that is much less than the command value and the shape of the output load waveform is more sinusoidal than triangular. This deterioration in response is the result of an overall decrease in loop gain caused by the reduction in specimen stiffness. It demonstrates that in load control, response becomes more sluggish as specimen stiffness decreases.

Strain Control

Figure 2 is a load versus extension LCF loop. The command was a 0.5 Hz triangular waveform and its amplitude of ±0.05 mm (±0.5% strain) exceeded the elastic limit of the material. This test was conducted at ambient temperature using the same machine as the load control

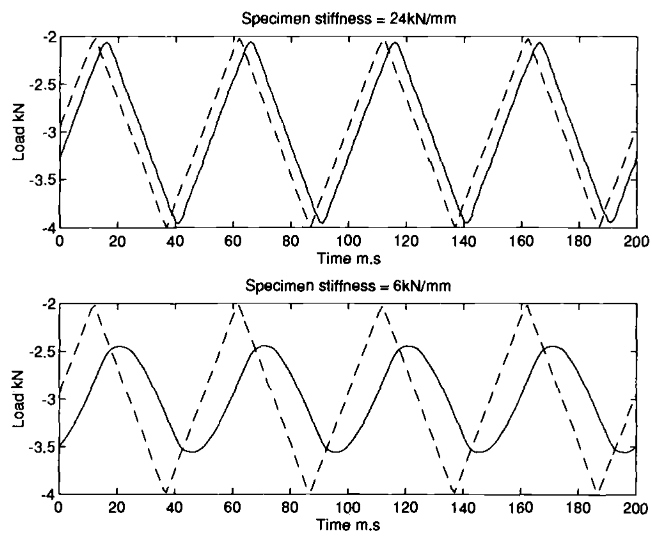

FIG. 1—*In load control, response becomes sluggish as specimen stiffness reduces (dashed line = 20 Hz triangular command, solid line = controlled load).*

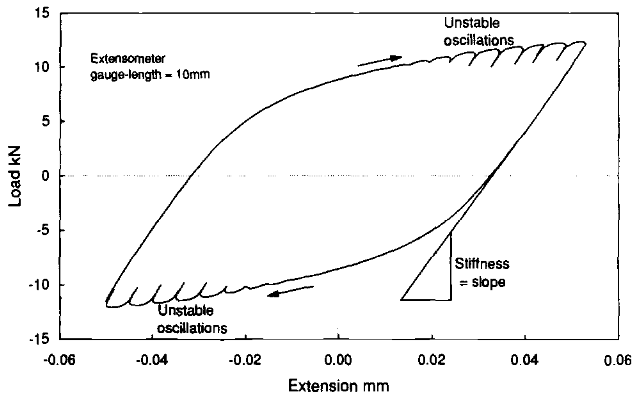

FIG. 2—*In strain control, gain increases as the specimen stiffness reduces. This is the reason for the unstable oscillations in the low-stiffness regions of this LCF loop.*

test of the previous section. A 10 mm gage-length extensometer with a working range of ± 1 mm provided the feedback signal for strain control. The specimen was martensitic stainless steel AISI 416. It had a diameter of 6 mm over a gage-length of 25 mm and was held in hydraulically pre-loaded, high-temperature, reverse-stress pull rods.

Since Fig. 2 is a plot of load versus extension, stiffness is equivalent to slope. The unstable oscillations in the low stiffness regions of the LCF loop are due to the fact that in strain control, the overall loop gain increases as stiffness reduces. The controller was tuned when the material was elastic but this setting is inappropriate once yield has been exceeded causing closed-loop instability.

Oscillations like this are often observed during LCF tests. They can be stopped by lowering the controller loop gain but at the expense of poor command following during the parts of the cycle where behavior is more elastic. Good following accuracy is particularly difficult during strain reversal when stiffness suddenly returns to the elastic value. The machine user is therefore forced to compromise between getting sharp reversals and adequate stability. Unfortunately, it is not uncommon for instability, once cured, to re-occur some time later on during the test as the overall stiffness is lowered by accumulated fatigue damage or cyclic softening.

Continually Updated PID Control

Figure 3 is a typical control loop for a servohydraulic machine. For an electromechanical machine simply replace the servovalve with a power amplifier.

All three feedback signals: actuator position, specimen load, and specimen extension, are available simultaneously. The mode selector chooses one of these to be the current feedback for closed-loop control. Despite the flexibility now offered by digital electronics, proportional + derivative + integral (PID) control is still popular because in the *interacting* form [*3*]:

$$\frac{u}{e} = G\frac{(1 + \tau_i s)(1 + \tau_d s)}{\tau_i s} \tag{1}$$

the integrator zero in the numerator can be used to exactly cancel the predominant pole of the actuator and specimen dynamics.

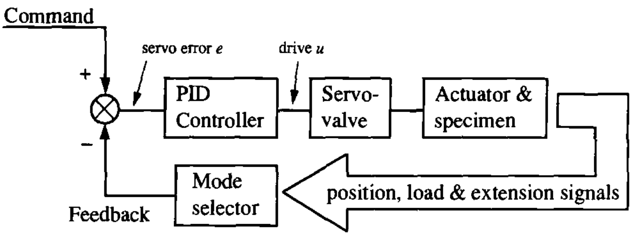

FIG. 3—*Servohydraulic machine control loop.*

Although the complete control loop is a high-order dynamic system, only the dynamics of the actuator and specimen are affected by specimen stiffness. It has been shown [1,2] that, providing the resonant frequency of the actuator is high enough, this block may be represented in load control and strain control by the following first-order continuous-time transfer functions:

$$\frac{f}{x_v} = \frac{G_L}{1 + \tau_m s} \tag{2}$$

and

$$\frac{x_s}{x_v} = \frac{G_S}{1 + \tau_m s} \tag{3}$$

where τ_m is a time constant and G_L and G_S are static gain terms.

Transfer functions (2) and (3) relate force and extension to the displacement of the servo-valve spool. They act in series with the controller so that if G_L, G_S, and τ_m are known it is possible to select a controller gain G and integrator time constant τ_i to cancel the combined actuator and specimen dynamics. This cancellation is conducted by the update algorithm in the block diagram of continually updated PID control (Fig. 4). Since the derivative time constant τ_d has no effect on stiffness sensitivity, there is no need to adjust it from its original auto-tuned value.

The parameters G_L, G_S and τ_m are functions of certain system constants and two variable

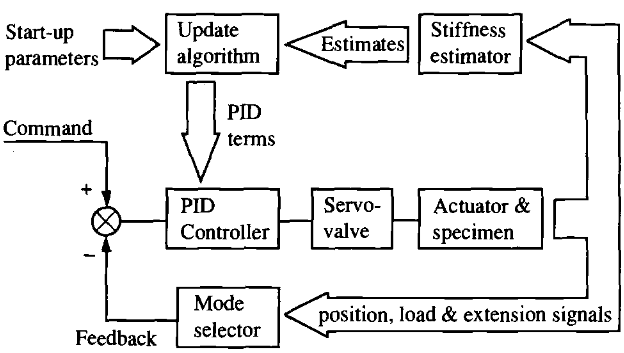

FIG. 4—*Continually updated PID control.*

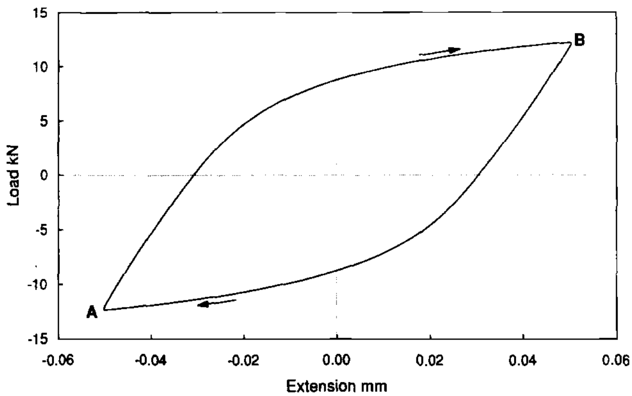

FIG. 5—*Unstable oscillations disappeared when continually updated PID control was switched on (compare this LCF loop with Fig. 2).*

stiffnesses: K_{SF} the combined specimen and frame stiffness and K_S the stiffness of the specimen over the extensometer gage-length. Real-time estimates of these stiffnesses can be obtained from the normal position, load and extension signals:

$$K_{SF} = \Delta f/\Delta x_p \tag{4}$$

$$K_S = \Delta f/\Delta x_s \tag{5}$$

The lower half of Fig. 4 is the standard control loop shown in Fig. 3. Adaptive control is achieved by continual updating of the PID terms based upon real-time estimates of K_{SF} and K_S.

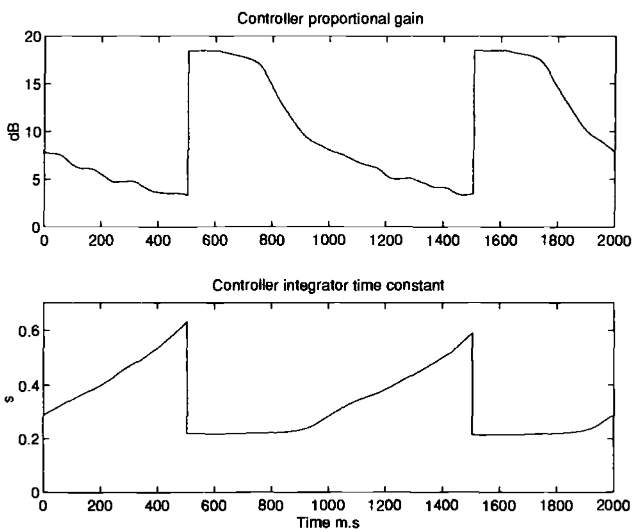

FIG. 6—*Controller proportional gain* G *and integrator time constant* τ_i *during the LCF test shown in Fig. 5. The sudden transitions correspond to strain reversal points A and B.*

It is not necessary to explicitly calculate values for G_L, G_S, and τ_m. Instead, the controller gain G and integrator time constant τ_i can be directly derived from the real time stiffness estimates and a previously determined optimum start-up set of parameters $G(0)$ and $\tau_i(0)$ corresponding to stiffnesses $K_{SF}(0)$ and $K_S(0)$. This direct approach has the considerable advantage of not requiring parameters of fixed dynamics such as those of the servovalve, load frame, and signal conditioning electronics to be identified or known beforehand. The start-up parameters are obtained during a once-only auto-tuning phase that resembles an automated version of manual tuning. Small-amplitude square waves are used to perturb the system and the PID terms are optimized by the maximum gain, minimum integral principal [*4*].

Figure 5 shows what happened when continually updated PID control was switched on during the LCF test described earlier. Oscillations in the low stiffness regions of the LCF loop completed disappeared. Figure 6 is a record of how the controller gain and integrator time constant were adjusted to achieve this. The sudden transitions coincide with the strain reversal points A and B.

Remembered Stiffness Overcomes the Estimation Problem at Strain Reversal

In bi-directional tests like LCF where the strain amplitude exceeds the material elastic limit, there are significant and sudden stiffness changes at each strain reversal. Continually updated PID control requires good real-time estimates of stiffnesses K_{SF} and K_S. The definitions of these stiffnesses given by Eqs 4 and 5 are close to their instantaneous values providing increments Δf, Δx_s and Δx_p are collected at sufficiently high frequency. Estimation, though, becomes difficult near strain reversal where these increments become zero or near zero. Just at the point where a most important stiffness change occurs, there is no information in the feedback signals to detect its magnitude.

Other factors near the extremes of strain produce apparent stiffness estimates that are not useful for control. Any load relaxation tendency of the specimen material can, according to the definitions of Eqs 4 and 5 produce high-magnitude stiffness estimates. There is also a potential aliasing problem due to the fact that the feedback signals are sampled rather than continuous.

The real-time stiffness estimator used for the tests presented in this paper is a recursive least-squares (RLS) design. It employs variable forgetting [*5*] to weigh out old data when stiffness is changing rapidly. Response can be slugged to reduce errors at strain reversal, but this impairs the ability to closely track the steady reduction in stiffness that follows yield. If closed-loop instability is to be avoided, this reduction must be followed accurately and this makes spurious estimates at strain reversal unavoidable (see Fig. 7*a*).

Some protection can be afforded by noting that, in an LCF test, stiffness cannot exceed the elastic value. This allows an upper bound to be set. Devising a lower bound is more difficult. Although stiffness can never be less than zero, a minimum finite value cannot be predicted. To prevent instability in strain control, the update algorithm reduces the gain when low stiffness is detected. Incorrect low estimates at reversal therefore tends to lengthen the time it takes to turn round.

The approach adopted here for overcoming this difficulty gets around the problem by using remembered stiffness from the previous cycle. Remembered values replace real-time estimates during the period that it takes for strain to reverse. Once the real-time estimator has recovered, its output is passed to the PID update algorithm in the normal way. The first estimate following recovery is stored so that it can be used for the reversal one cycle later. Since the stiffnesses immediately following reversals A and B (Fig. 5) are often slightly different, two stiffness values are remembered. A record of estimates processed this way is shown in Fig. 7*b*. The spurious values at reversal have been completely eliminated.

It is the absence of spurious estimates coupled with the considerable reduction in stiffness

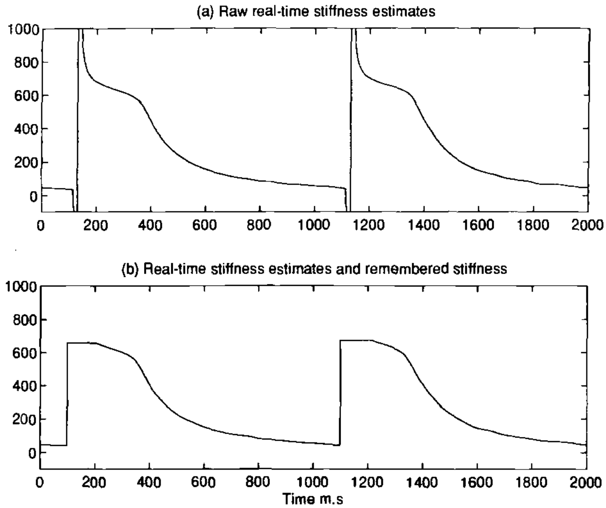

FIG. 7—*Remembered stiffness replaces spurious estimates during strain reversals.*

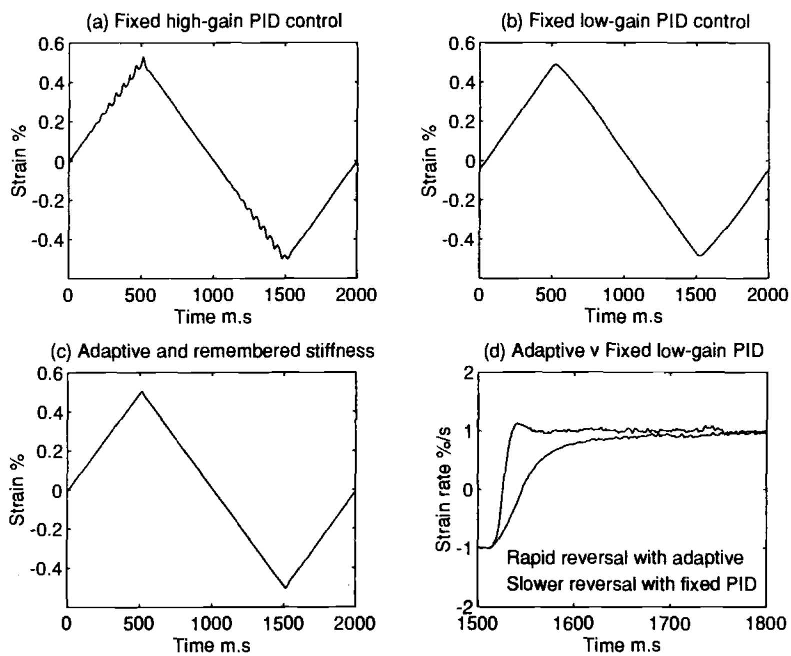

FIG. 8—*Comparisons of controlled strain during LCF testing:* (a) *Fixed PID control, tuned when the specimen was elastic. The oscillations correspond to those of Fig. 2;* (b) *Fixed PID with the controller gain reduced to eliminate unstable oscillations;* (c) *Continually updated PID control using remembered stiffness during strain reversal; and* (d) *Strain rate over the period of the lower reversal plotted in* (b) *and* (c).

sensitivity afforded by the update algorithm that makes crisp strain reversal possible during LCF testing. This is highlighted in the comparison of methods shown in Fig. 8. The command waveform for all traces is a $\pm 0.5\%$ triangle at 0.5 Hz.

Figure 8*a* is the recorded strain during the LCF loop plotted in Fig. 2. The oscillations in the low-stiffness parts of the LCF loop are clearly reflected in the strain record. Turning the controller gain down to the minimum indicated in Fig. 6 during continually updated PID control guarantees no oscillation, but the strain reversal and general following accuracy is not good (Fig. 8*b*). Without adaptive control, this is the best that can be achieved. Considerable improvement, though, was obtained (Fig. 8*c*) when continually updated PID control with remembered stiffness was switched on. This is the strain record corresponding to the LCF loop of Fig. 5. Evidence that strain reversal is much crisper with adaptive than is possible with low-gain fixed PID control can be seen in the comparison of the strain rate records (Fig. 8*d*). These show what happened during the negative-to-positive-going strain rate reversal. Ideal following would appear as a step change. Considering that strain is the controlled parameter and not strain rate, the more rapid change with continuously updated PID control shows how much better this mode of control is. Rapid reversal is also important if the specimen material is rate-sensitive.

Conclusions

Continually updated PID control makes the testing machine insensitive to specimen stiffness. This means that it is no longer necessary to manually retune the machine controller every time a different type of specimen is installed. The update algorithm automatically makes the necessary changes.

Stiffness changes that occur during the test are also compensated for. This has been demonstrated for LCF testing. During each LCF strain cycle there are significant and sudden stiffness changes that can cause closed loop instability with fixed PID control. Continually updated PID control stops this happening by continually sensing stiffness and appropriately adjusting the controller.

An extension to the basic algorithm uses remembered stiffness to overcome the problem of estimating stiffness during strain reversal. This is particularly useful in tests like LCF where stiffness changes abruptly at reversal. This enhancement considerably improves turn round performance and general strain following accuracy.

References

[1] Hinton, C. E. and Clarke, D. W., "Adaptive Control of Servo-Hydraulic Materials-Testing Machines," *Proceedings of the Joint Hungarian-British International Mechatronics Conference,* M. Acar, J. Makra, and E. Penney, Eds., 21–23 September 1994, Budapest, pp. 53–58.

[2] Hinton, C. E., "Continually-Updated PID Control of Servo-Hydraulic Materials-Testing Machines," *Seminar on Digital Control in Fluid Power Systems,* I. Mech. E., Birmingham, 22 June 1994.

[3] Clarke, D. W., "PID Algorithms and their Computer Implementation," *Transactions of Instrument Measurement and Control,* Vol. 6, No. 6, 1984, pp. 306–316.

[4] Hind, E. C., "Manual Tuning of Controllers Using Set Point Changes," *Transactions of Instrument Measurement and Control,* Vol. 3, No. 3, 1981.

[5] Fortescue, T. R., Kershenbaum, L. S., and Ydstie, B. E., "Implementation of Self-Tuning Regulators with Variable Forgetting Factors," *Automatica,* Vo. 17, No. 2, 1981, pp. 831–835.

K. Reifsnider,[1] *S. Case,*[1] *and L. Mosiman*[2]

Characteristics and Automated Control of a Dual-Frequency Servohydraulic Test System

REFERENCE: Reifsnider, K., Case, S., and Mosiman, L., "**Characteristics and Automated Control of a Dual-Frequency Servohydraulic Test System,**" *Applications of Automation Technology to Fatigue and Fracture Testing and Analysis: Third Volume, ASTM STP 1303,* A. A. Braun and L. N. Gilbertson, Eds., American Society for Testing and Materials, 1997, pp. 120–130.

ABSTRACT: The objective of the present research is to create a servohydraulic test system that can apply two independent excitations, simultaneously, to a specimen. The motivation for this objective is provided by a range of engineering situations in which such excitations are encountered, and the opportunity for monitoring specimen integrity by dynamic analysis during a "standard" fatigue test. In the first case, bi-frequency excitation is common to such engineering components as combustor buckets in jet engines that undergo low-frequency structural fatigue and high-frequency (low amplitude) fatigue loading having to do with the pulsation of the burning process. Other situations of that type include a variety of acoustic/structural excitations and other combinations typically encountered in transportation and propulsion systems.

The second opportunity, to use such a capability to monitor the integrity of a specimen that is being characterized under high-amplitude cyclic loading by conducting dynamic analysis on the same specimen with a low-amplitude high frequency (superimposed) excitation, is an idea that is related to the well-known "dynamic mechanical analysis" that is widely used for elastomeric material characterization.

The system described in the present paper was designed and built by a cooperative effort between the Materials Response Group at Virginia Tech and MTS Systems Corporation. The system consists of two separate actuators, in series, that are capable of applying high-frequency (up to about 1500 Hz) excitation with amplitudes up to about 2000 lb (8800N) beyond standard high-load, low frequency excitations. The secondary high-frequency actuator is isolated from the primary actuator *in a manner that makes the* control of the system by a computer interface possible. Other features of the system include a tube-testing grip arrangement, high-temperature capability, and internal pressurization capability for tube specimens.

The present paper will describe the attributes of the system, and present the characteristic response of the system under limiting conditions. Data will be presented to demonstrate the utility and capabilities of the system, using several types of specimens and materials. Control of the system will be discussed, especially as it is influenced by the stiffness of the specimen under test, and the nature of the superimposed test frequencies.

KEYWORDS: dual frequency, servohydraulic test machine, composites, tubes, high temperature

Purpose and Applications

We will refer to the present system as a Dual Excitation Mechanical Analysis Device, or the DEMAND system, for short. The DEMAND system was designed and built as a joint venture by the NSF Science and Technology Center for High Performance Polymeric Adhesives and Composites, the Materials Response Group at Virginia Tech, and the MTS Systems Corporation. The DEMAND system is believed to have a unique set of characterization capabilities

[1] Materials Response Group, Virginia Polytechnic Institute and State University, Blacksburg, VA.
[2] MTS Systems Corporation, Eden Prairie, MN 55344-2290.

that can be combined in a myriad of ways. For example, the system enables the following characterization methodologies.

High-Frequency Fatigue

There is currently a renewed interest in high-frequency fatigue and its effects on structural materials including metals, ceramic, polymers, and composites. Such excitations in structures are typically driven by rotating parts and noise, but other sources are possible. Previous characterization of such response has been done on shakers and resonance test systems, but these methods do not generally permit precise control of excitation amplitudes or the recovery of data that define the properties or response of the specimens during testing. Consequently, very little is known about the behavior of materials, per se, under high-frequency fatigue excitation. The DEMAND system can provide test frequencies up to 1500 Hz with load levels up to 2000 lb (8800N).

Moreover, the system is equipped with a furnace that can heat the specimen to about 2800°F. A single-zone resistive element furnace is used to achieve the elevated temperatures. A high-temperature extensometer may be used to measure axial strain on the test specimen at ambient and elevated temperatures, *up to the limits of the frequency response of the instrument.* The system is fitted with grips that can load either flat coupons or tubular specimens with an OD of 1.5 in. Tube testing is especially important for the purpose of determining the response of materials to multiaxial loading, since combinations of tension, compression, torsion, and internal pressurization can be applied.

Dual-Frequency Excitation

The DEMAND system has a primary and secondary actuator that act completely independent of each other. Keeping the *primary and secondary* control functions separate was a major design consideration. Since the mechanical actuators act in series, isolation of the secondary excitation required a special design that incorporates a reaction tube and strut arrangement that approximates the general compliance of the specimens. The resulting dual excitation is superior to single actuator systems.

Dual (or multiple) excitations are the rule, rather than the exception in the real world of fatigue loadings. It is hard to imagine a dynamic loading that has only one frequency component. Yet, virtually all data reported in the literature represent material response to single-frequency excitations. This is a more serious misrepresentation in some situations than in others. For engineering components such as the combustors and combustor liners in jet engines, for example, a combustion-related excitation (of typically 800 Hz or so) is superimposed on structural vibrations of a few tens of Hz. The high-frequency excitation occurs at very high temperatures, also. Finally, components such as these often have a tubular shape. The DEMAND system has a unique capability to simulate that type of test environment, with full control over the primary and secondary loading (amplitude and frequency), temperature, and multiaxial loading as a function of time and cycles. Figure 1 shows a block diagram of the control system.

Dynamic Analysis

The features of the DEMAND system can be combined to conduct Dynamic Mechanical Thermal Analysis (DMTA) on materials in the test frame. Since the temperature and the frequency can be scanned as a function of time, it is possible to measure the dynamic storage and loss modulus. The phase lag between the excitation and specimen response as a function of temperature and frequency, a widely used method of characterizing materials such as polymers

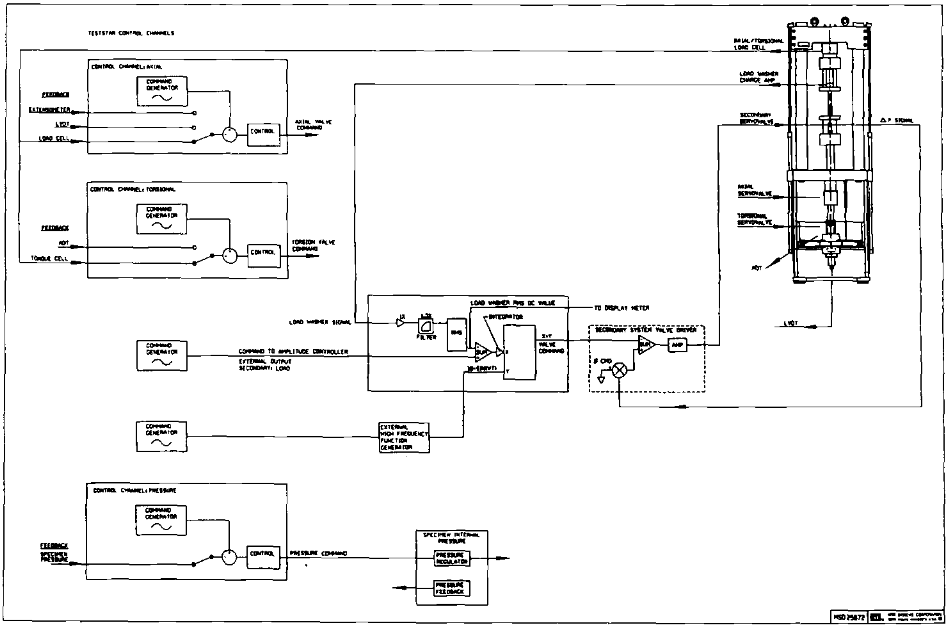

FIG. 1—*A block diagram of the complete control system.*

and polymer composites, can also be measured. Hysteresis loops (and dissipated energy) can also be measured at frequencies up to at least 1000 Hz. Also, waveform analysis *(Fast Fourier Transform Analysis, etc.)* can be performed to recover information and signatures in the frequency domain.

These dynamic analysis methods can be applied and interpreted in real time, while fatigue damage is being induced by the primary actuator system. Changes, for example, in the Tg of a polymer or polymer composites, *the transition temperature between glassy and viscous behavior*, can be measured as a function of a thermomechanical primary loading history.

This type of dynamic analysis of signals recovered from the test system is of special value for testing specimens at high temperature. The DMTA capabilities of the DEMAND system can be used, in that case, to follow damage development and to determine remaining strength and life [*1*]. This is especially valuable for the testing of high-temperature ceramics and ceramic composites.

A great variety of other combinations of the capabilities of the DEMAND system are possible *that we have yet to explore.* The system is ideally suited to the study of the rate dependence of the response of materials, as well as the effect of changing the sequence of countless combinations of thermal, mechanical, and dual-frequency excitations. It is possible to create heat in specimens that are highly dissipative, meaning that we can induce heating in specimens *and study the effect of internal heating on properties and performance, a topic of special interest to the acoustic fatigue community.*

Test System Description

Primary System Description

The primary actuation system is capable of applying an axial force of ±55 000 lbs (±250 kN) at frequencies up to 20 Hz and a torsional force of ±20 000 in.-lbs (±2500 N-M) up to 10 Hz.

An axial/torsional load transducer measures both axial and torsional load. The axial actuator uses an integral, hydrostatic bearing design for high lateral stiffness and greater system alignment capability. Axial displacement is measured using a linear variable displacement transducer (LVDT) and angular rotation is measured using an angular displacement transducer (ADT). The axial and torsional actuators are each controlled through independent control channels and are driven through independent servovalves.

Hydraulic collet grips, rated to 55 000 lbs axial/20 000 in.-lb torsional are used to directly clamp a test specimen for low-frequency testing or are used as the stationary point for the secondary system gripping subsystem.

Secondary System Description

The secondary actuation system uses a specially designed axial-torsional hydraulic gripping system with a high-frequency actuation and measurement subsystem. Figure 2 shows a picture of the secondary system actuator. The secondary system is capable of applying a peak-to-peak axial force of up to 4000 lb (18 kN) at frequencies from 200 Hz up to 1500 Hz. When combined with the primary system, the total load capacity of the system is $\pm$12000 lb primary system axial force, $\pm$4700 in.-lb primary system torsional force, and 4000 lb p-p secondary axial force. Figure 3 shows a chart of the combined primary and secondary axial waveforms.

The secondary system high-frequency force is applied to the specimen by a small single-ended actuator. The actuator is contained inside the piston of the grip. Hydraulic fluid is provided to the actuator through specially designed high-response servovalves. The servovalves are rated to 5 GPM of oil flow and utilize a special driver that provides significant oil flow at very high frequencies.

The high-frequency load is measured in the upper grip. A low mass collet assembly is preloaded to a piezo-electric load washer. The load washer is used to measure the dynamic load on the specimen.

Electronic Controller

Primary System Electronic Controller

A commercially-available digital materials testing workstation was used to control the primary test system. The controller has the ability to provide independent control of the axial, torsional, and internal pressurization channels. A general purpose test application software program is used to operate the system. These forces are combined with a high frequency secondary axial load.

A low pass filter is used to filter the axial load and displacement signals. The filter removes the high frequency waveform generated by the secondary loading system. This is necessary to allow the primary system to control in load or stroke control. The system may be operated in load or stroke control on both the axial and torsional channels.

Secondary System Electronic Controller

The secondary loading system applies a high frequency load to the specimen, superimposed on a low frequency axial/torsional primary load. Because the system controller is a digital device, its bandwidth of operation is limited by the sampling rate and the ability of the controller to calculate a valve-command within the sample period. The secondary system frequency range of 200 to 1500 Hz extends beyond the capability of the digital control system, which is limited to 1000 Hz. For this reason a non-standard *hardware* controller was implemented within the standard digital controller chassis. This controller will be referred to as the amplitude controller from here forward.

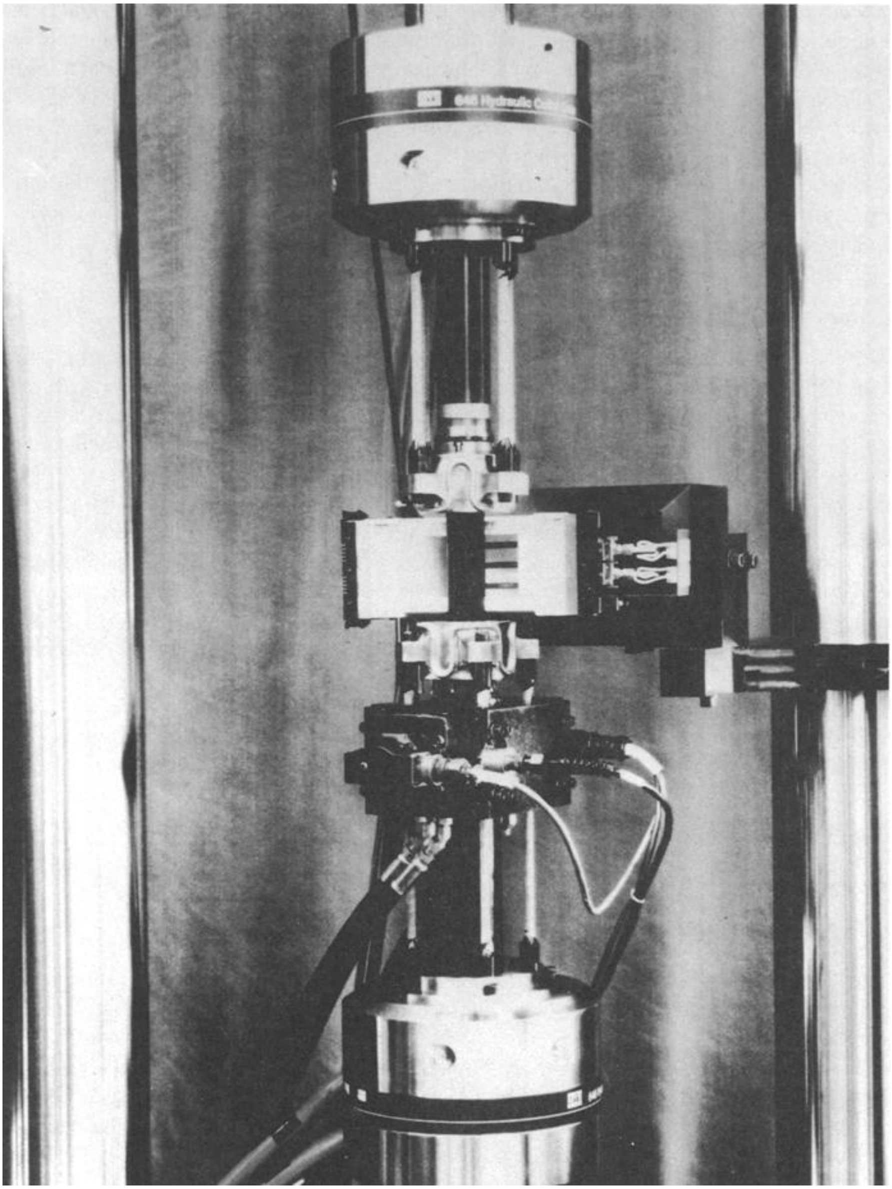

FIG. 2—*A picture of the secondary system actuator.*

Case 4. +/- 5000 lb @ 5 Hz primary, 4000 lb p-p @ 200 Hz secondary.

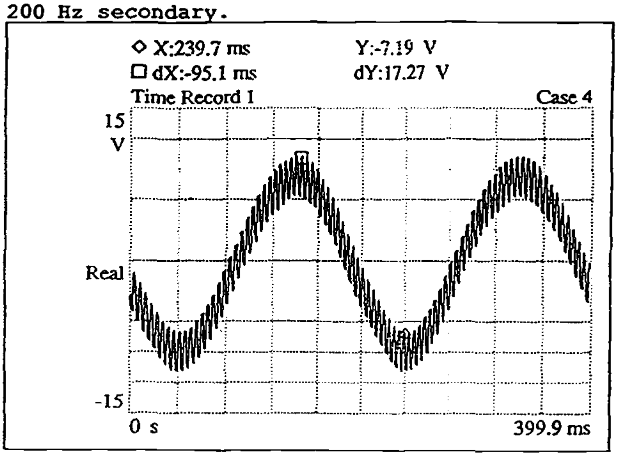

FIG. 3—*A chart of the combined primary and secondary axial waveforms.*

Like the primary system axial control channel, the amplitude controller requires a command and feedback signal that are summed to create an error signal. The controller operates on the error signal to produce a valve-command. The amplitude controller outputs a valve-command to a specially designed valve driver card.

The command signal to the amplitude controller comes from a control channel of the system's standard digital controller. By using a conventional control channel to produce the command signal, the operator is able to take full advantage of the controller segment generator and programming of the amplitude controller command signal.

The feedback to the amplitude controller comes directly from the system load washer (not the system load cell). Figure 4 shows a block diagram of the amplitude controller and its connections. The load washer range is switch selectable from a set of four switches under the console front panel. A piezo-electric transducer (load washer) was chosen to monitor the secondary loads because it offered a wide bandwidth of operation and a very long fatigue life. However, piezo-electric devices generally exhibit poor DC stability, and for this reason the load washer is calibrated dynamically. Another consequence of poor DC stability is the need to periodically "zero" the load washer. This is accomplished using the system digital controller.

On the amplitude control card, the load washer signal passes through a high pass filter with a 150 Hz cutoff frequency. This filter removes the low frequency load components attributable to the primary axial load system. The remaining high frequency signal represents the load due only to the secondary axial load system. This filter is in an active filter that amplifies the signal by approximately 1.3 times. The exact amplification is a function of frequency.

The load washer signal then enters a RMS converter. The converter produces a DC voltage output that is proportional to the time averaged RMS value of the input signal. The RMS load washer signal is routed into the system digital controller and is given the logical name "Load Washer." The secondary system control channel uses the Load Washer signal as its feedback signal.

The scaling of the feedback signal also controls the scaling of the control channel command signal because the two signals must have common units at the summing junction within the control channel. However, the scaling of Load Washer also depends on the range selection of the load washer amplifier.

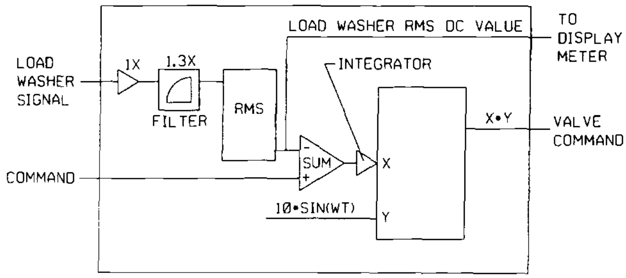

FIG. 4—*A block diagram of the amplitude controller and its connections.*

The Load Washer signal is displayed in one of the system's digital controller meter windows and is available for data acquisition. The signal has been scaled to display the peak-to-peak load washer amplitude. The load washer signal was filtered in the amplitude controller so the meter reading will NOT reflect any load applied by the primary system. Also, the signal is the DC RMS load washer value. The peak-to-peak meter display assumes an undistorted sinusoidal input. *The accuracy of this reading would be in question if the signal was not sinusoidal.*

Back inside the amplitude controller, the DC load washer RMS signal is summed with the command signal to produce an error signal. This error signal is integrated by an analog integrator and passed on to an XY chip. The integrator is necessary to reduce steady state error. Without an integrator the achieved secondary load would droop well below the commanded secondary load. The XY chip multiplies the error signal with a constant 10 volt amplitude sine wave from an external function generator thereby producing a modulated sine wave valve-command signal.

An external function generator is used to provide the high-frequency command signal (up to 1500 Hz), as the system digital controller is limited to 1000 Hz command generation. An additional control channel in the system digital controller provides a frequency command signal to this function generator. This implementation allows the operator to take advantage of the system digital controller's command generation and programming capabilities. As a result, the system has the ability for sweeping or using a constant frequency. The function generator produces a 10 volt constant amplitude sine wave output with a frequency that is proportional to its command signal.

The secondary system valve driver was originally designed to drive a three-stage servo valve. Three stage servovalves utilize a pilot servo valve to drive a slave spool. A position transducer connected to the slave spool provide feedback for an ''inner control loop'' that stabilizes the slave spool position. This control scheme was readily adapted to the secondary axial load system. For the secondary system, a pair of high-performance two-stage servo valves act like a pilot valve driving the secondary piston which in this case may be thought of as the slave spool. Instead of a position transducer, a double-ended pressure cell (delta P) senses the pressure on both sides of the cylinder producing a feedback signal *that* is proportional to the difference in pressure across secondary piston. An analog pressure control loop on board the valve driver card compares this feedback signal to a command signal to produce an error signal. The error signal is operated upon to produce a valve-command signal. This valve-command signal is summed with the valve command signal from the amplitude controller. This composite valve-driven signal is then amplified to drive the servovalves. The delta-P inner loop control scheme is necessary to prevent the secondary axial load piston from drifting off center. Figure 5 shows a block diagram of the valve drive circuit.

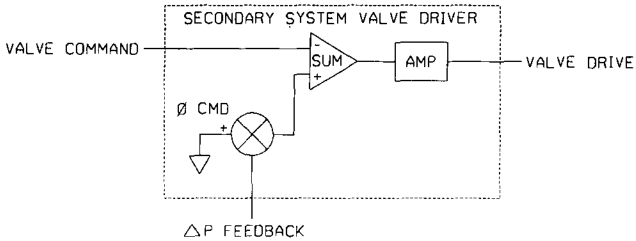

FIG. 5—*A block diagram of the valve drive circuit.*

Test System Performance

The DEMAND system has been in operation for only a short time. We will show only a few examples of data we have recorded to date, to illustrate some of the features of the system. Figure 6 shows a typical response of the secondary loading system for two materials with a

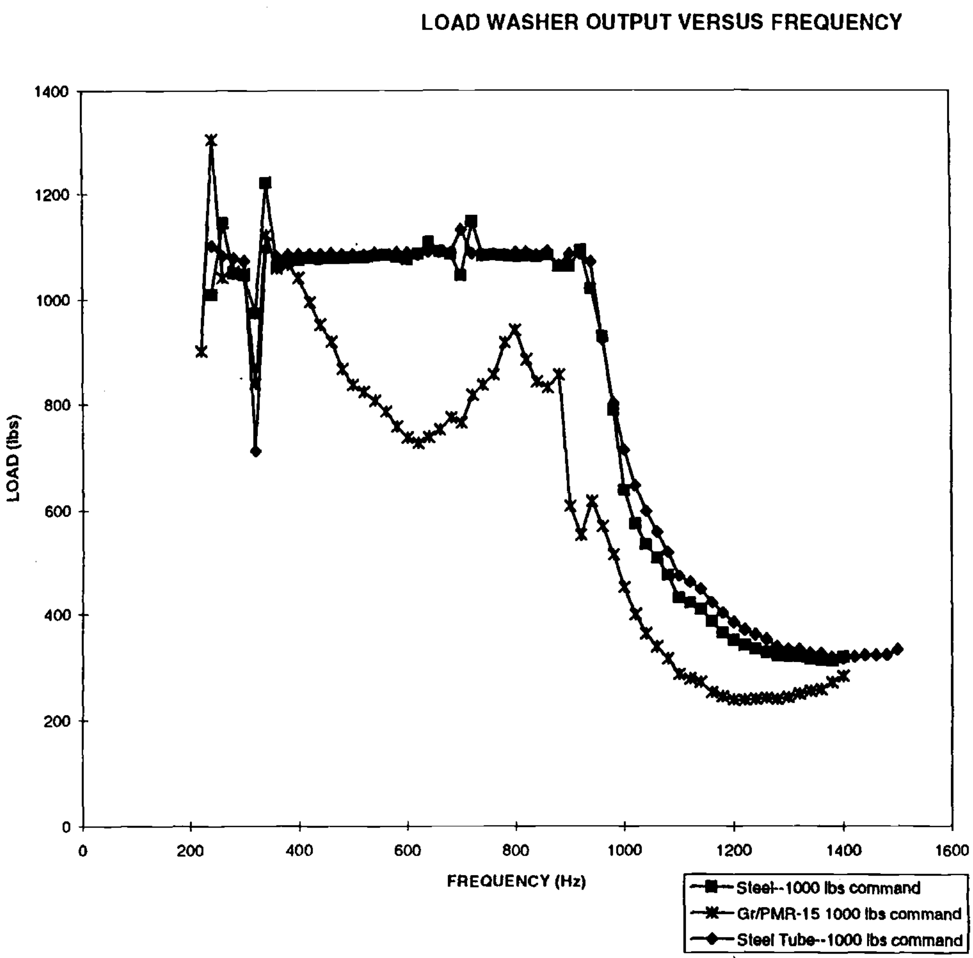

FIG. 6—*A typical response of the secondary loading system for two materials.*

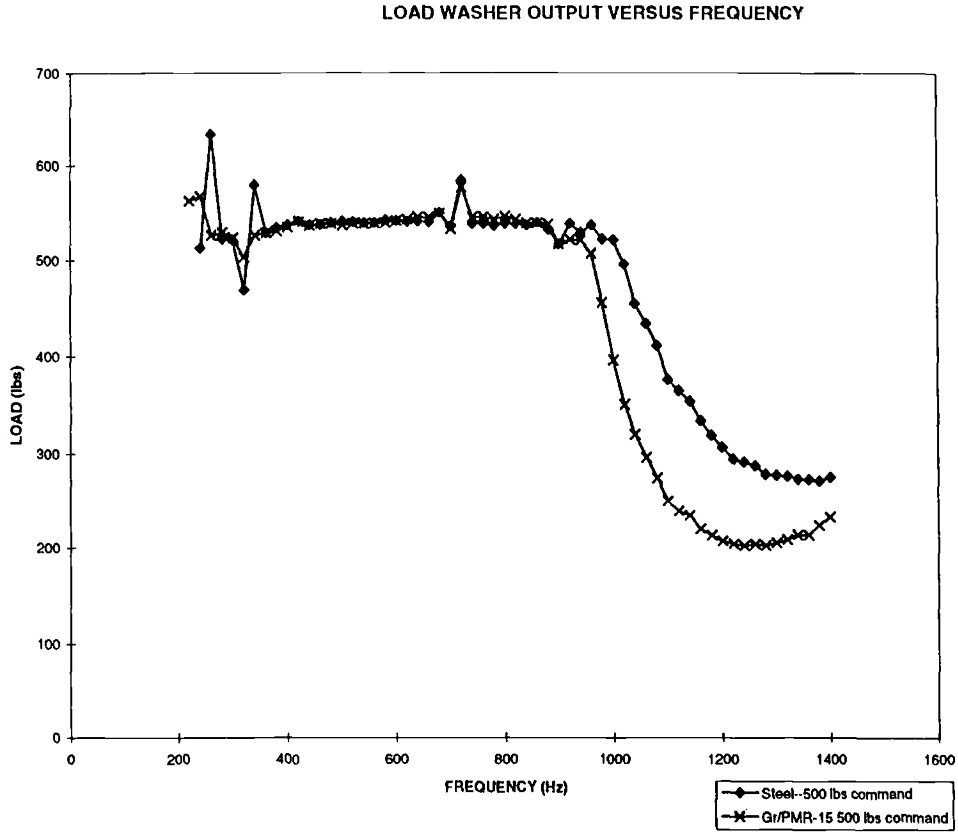

FIG. 7—*Peak load data for the same coupon specimens compared to the response of a steel tube.*

gage length of about 100 mm and a load-control command of 2200 N. *The gage section cross section was 0.25 thick and 1.0 wide.* The response of the secondary system is seen to be essentially flat out to about 1000 Hz, except for several resonance peaks. The resonance peaks are well-defined, consistent, stable, and do not result in loss of control of the machine or servo-system. The applied peak load decreases with increasing frequency above about 1000 Hz, and drops to about 50% of the command signal at about 1200 Hz. The response for the steel specimen (with a modulus of about 207 GPa) and the graphite epoxy specimen (with a modulus of about 68 GPa) is quite similar. The specimens were nominally 25-mm wide and 6-mm thick.

Figure 7 shows peak load data for the same coupon specimens compared to the response of a steel tube that has a 37.5-mm outside diameter and is nominally 3-mm thick. The effective spring constant of the tube is less than the solid coupon specimens, and the applied force of the secondary system drops off somewhat in the mid-frequency range. The command load level for the data is 4400 N. As the data show, it is possible to exert sufficient force at high frequencies to introduce damage into the specimens under test, an important feature. *However, the present system power limitations are demonstrated by the data. The maximum load at a given frequency for other situations will be determined by the spring rate of the specimen.* The system is fitted with grips that can accept tubular specimens 37.5 mm in diameter, and fittings are also available

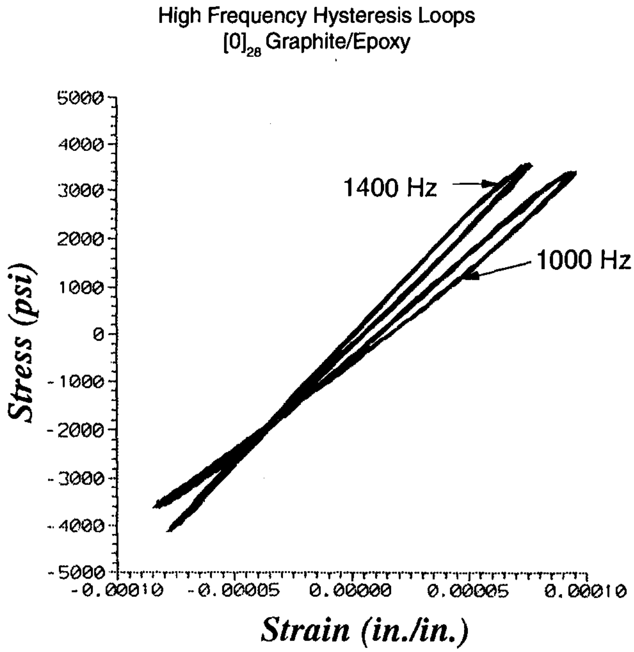

FIG. 8—*Hysteresis loops recorded at two different frequencies.*

that allow for internal pressurization of the tubes to achieve fully three-dimensional applied stress states.

Figure 8 shows hysteresis loops recorded at two different frequencies using unidirectional graphite epoxy specimens with fully reversed loading. At these loading frequencies, the material shows some rate dependence in the stiffness of the material, as we expect. The slope of the loading curve is greater at the higher frequency. Also, the tensile part of the loops is open, while the loops close down in compression. One can speculate that the internal dissipation mechanisms that produce relative motion in tension are not active under compressive stress, suggesting that they may involve opening cracks, broken fibers, etc. *Although we have not completed our characterization of the DEMAND system, tests on steel specimens at this frequency and load level showed no energy loss. This suggests that the inherent phase lag in the machine itself is making an insignificant contribution to the results shown in Figure 8.*

Summary

This paper has described a Dual Excitation Mechanical Analysis Device (DEMAND system) that has independent primary and secondary servohydraulic activated and controlled actuation systems. The primary system is designed to provide high-amplitude, low-frequency axial and torsional forces to the test specimens, while the secondary system is designed to provide high-frequency, low-amplitude superimposed loading. The system is fitted with grips that receive tubular specimens and with a furnace that can provide elevated temperatures for testing up to about 2800°F. The system, thought to be unique, opens several new avenues of investigation into the effects of high frequency excitation, dynamic mechanical analysis, frictional heating, rate effects, and superimposed loading. The system is fully operational and commissioned, and is being used for exploratory research in several technical areas.

Acknowledgements

The authors acknowledge, with thanks, the support of the MTS Systems Corporation, the NSF support under grant number NAG-1-343, and the Air Force Office of Scientific Research under grant number FA9620-95-1-0217.

Reference

[*1*] Elahi, M., Razvan, K., and Reifsnider, K. L., "Characterization of Composite Materials Dynamic Response Using Load/Stroke Frequency Response Measurements," *Composite Materials Fatigue and Fracture, ASTM STP 1156,* W. W. Stinchcomb and N. Ashbaugh, Eds., American Society for Testing and Materials, Philadelphia, 1993, pp. 575–590.

John Christiansen,[1] Roger L. T. Oehmke,[1] and Erik A. Schwarzkopf[1]

Materials Characterization Using Calculated Control

REFERENCE: Christiansen, J., Oehmke, R. L. T., and Schwarzkopf, E. A., "**Materials Characterization Using Calculated Control,**" *Applications of Automation Technology to Fatigue and Fracture Testing and Analysis: Third Volume, ASTM STP 1303,* A. A. Braun and L. N. Gilbertson, Eds., American Society for Testing and Materials, 1997, pp. 131–146.

ABSTRACT: This paper discusses new solutions to a variety of materials tests that were previously difficult and time-consuming to perform. Digital controllers now give the researcher or test engineer tremendous versatility in test control. The ability of the digital controller to perform user-defined, real-time control calculations using physical inputs from the test system gives previously unequaled performance in a variety of testing applications. Furthermore, software that allows these calculations to be quickly and easily defined improves system friendliness. This capability is applicable to a wide variety of tests, including thermal-mechanical fatigue, true stress control, inelastic and true strain control, and geomechanics applications. The authors will discuss some specific uses of this capability.

KEYWORDS: materials tests, digital controller, calculated variable control, thermal mechanical fatigue

New calculated variable controller technology makes it easier to perform many advanced materials tests. This paper discusses the relative advantages and disadvantages of the newer technologies over older, better known technologies, and presents some specific examples where the use of real-time calculated variable control makes the test easier to perform.

The term "calculated variable control test" is broadly used to describe any test where some type of calculation or manipulation must be performed on either the test system feedback or the command to the test system to enable the test to be performed properly. A wide variety of materials tests fit this definition of a calculated variable control test. These tests, and the various implementations used to perform these tests, are detailed in the literature [*1–4*]. A partial listing of these tests includes:

- Plastic strain control,
- Thermal mechanical fatigue,
- Fatigue crack growth,
- True stress control, and
- Strain rate or stress rate control.

Traditionally, most materials tests have been run with a PID or PIDF (Proportional, Integral, Derivative, Feed Forward) closed-loop servocontroller using direct feedback from the load, position, or strain transducer on the test frame. The servocontroller acts to drive the servovalve to minimize the error between the program input (from the function generator) and the feedback

[1] Applications engineers and software lead, respectively, MTS Systems Corp., 14000 Technology Drive, Eden Prairie, MN 55434-2290.

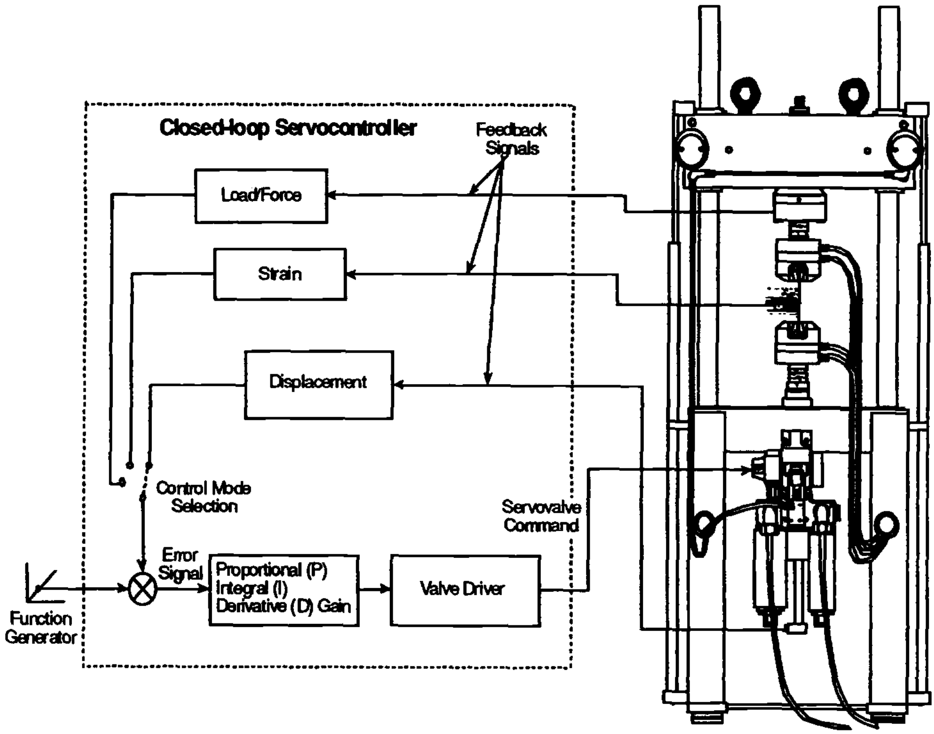

FIG. 1—*Typical closed-loop servocontroller block diagram.*

from the test system. This type of controller is shown in Fig. 1. In many testing applications, an additional supervisory system of some type is used to monitor the system and change the program input to the test controller. This outer-loop supervisory system monitors the test progression, determines the required program changes, and adjusts the program input to the PID controller (also referred to as the inner-loop controller) to obtain the desired result in the test system. A variety of implementations for inner/outer-loop control exist, using everything from dedicated electronics to microcomputers to perform the required test control calculations [*5,6*]. Figure 2 shows a block diagram of this type of controller.

Advances in microprocessor technology over the last decade enable digital control systems to perform arithmetic calculations within the real time control loop. These calculated variable control loops operate fast enough to control a servohydraulic test system in many advanced applications [*7*]. Figure 3 shows a block diagram of this type of controller. The advantages of the digital approach are reviewed in the next section.

Calculated Variable Control Systems—Historical Review

Analog Calculated Variable Control Systems

Before the widespread use of computer automation with materials testing systems, some calculated variable control tests were performed using analog circuits. These circuits were designed to calculate specific parameters of interest using feedback from the analog system controller. The analog devices had the advantage of operating in real time, but were fixed

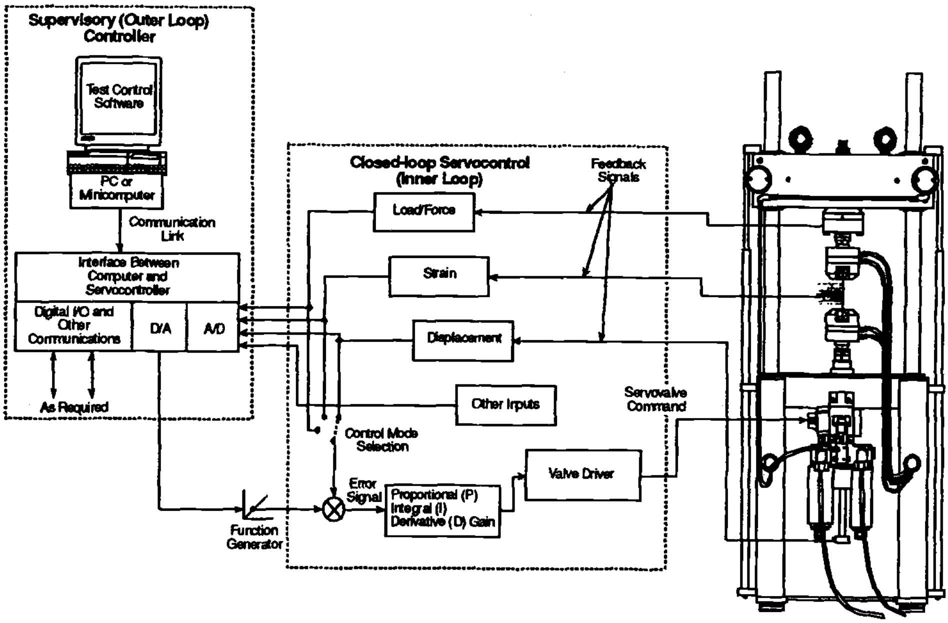

FIG. 2—*Typical supervisory (outer loop) calculated variable controller block diagram.*

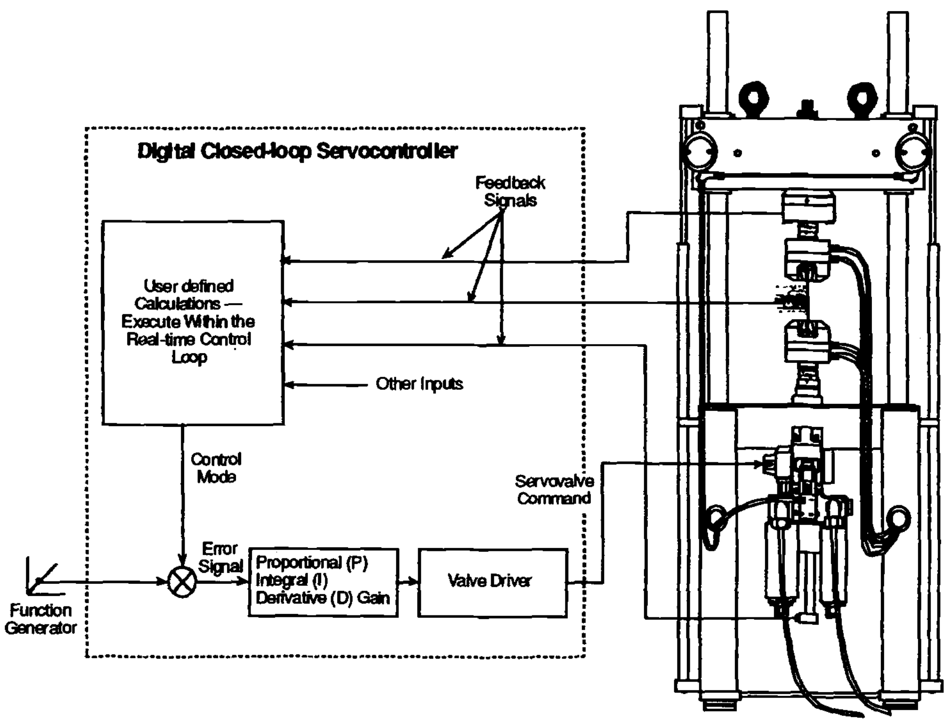

FIG. 3—*Digital control system with real-time calculated variable control block diagram.*

function arrangements designed to perform a specific calculation. Adjustment, calibration, and integration of the device to the test system controller were time-consuming and expensive. Accuracies were acceptable, but the specialized nature of the circuit and the care needed to set up the system correctly made this solution unacceptable for many general purpose laboratories. Examples of these devices include:

- An analog strain computer module [8]. This module could calculate axial strain based on a diametral strain input, or plastic strain based on a total strain input and load input. Analog potentiometers on the module provided scaling for other material parameters such as elastic modulus and Poisson's ratio.
- An analog crack length and stress intensity correlator module [9]. This module converts clip-gage (COD) input and load input into crack length and stress intensity values. The module uses the compliance based crack length measurement technique and thus requires elastic modulus, specimen thickness, and specimen width scaling inputs. Each specimen geometry needs different potentiometers settings in the fit function circuit.

Supervisory (Outer Loop) Calculated Variable Control Systems

The most common testing control strategy employed in the last two decades has been to use a computer operating in a supervisory mode to calculate and adjust the command to the inner loop PID servocontroller operating in load, strain, or position control (Fig. 2). This approach has been used in systems using either analog or digital servocontrollers to perform the inner loop PID control.

Generally speaking, this type of automation technique has been very successful. The advancements in the fields of Fracture Mechanics and Thermal Mechanical Fatigue are two examples where the use of outer loop calculated variable control has advanced the state of the art in materials research.

This inner/outer-loop implementation has a number of advantages. Typically, the supervisory system is a stand-alone system that is separate from the inner loop controller. This enables the supervisory system to be used with many different types of servocontrollers. Because the system utilizes an inner loop PID controller running directly in load, position, or strain control mode, system setup and loop tuning are straightforward.

Historically, one of the main difficulties with this type of approach has been in the speed at which the outer-loop controller can adjust the program input. Depending on the system architecture, the outer loop update rate can vary from several updates per second to several seconds per update (typical values are 0.5 to 5 Hz outer loop update rate). This slow response means that tests requiring the results from calculations in real time are difficult to perform with these systems. The update rate is a function of the microprocessor performance, and as faster computers become available, the update rate will increase.

Direct Digital (Inner Loop) Calculated Variable Control Systems

As microprocessor processing power has improved, a new type of calculated variable control testing system has become technically viable. This type of system can perform calculated variable control by executing both the required calculation(s) and PID control within the inner-loop in real time (Fig. 3). This gives the system the ability to directly control a calculated parameter using physical feedback(s) from the test system and the required calculation(s) to create the desired inner-loop control variable.

One specific implementation of this approach enables the user to enter the required calculation in a setup window, and reconfigure the controller by downloading the new inner-loop control variable calculation(s) and control parameters to the inner-loop controller [*7*]. This system has a number of advantages for the researcher. These include:

- The process of defining and configuring the calculated variable controller is simple and can be executed quickly. No programming, compiling, or other effort is required. It also enables the researcher to stop the test, redefine the required calculation, and restart the test very quickly.
- The speed at which the calculated control channel loop can operate, typically 1000 Hz to 5000 Hz, enables the calculated variable controller to be used in real-time servohydraulic control applications.
- The system has great flexibility in the types of calculations that can be used and the number of variables (which can be both physical inputs and calculated parameters) that can be used within the calculation. Figure 4 [*10*] shows a list of the calculations that can be utilized within the control loop calculation.
- Some experiments can be performed more easily and accurately than with previously available methods. One example of this is the Thermalmechanical fatigue experiment detailed in the section below. Both mechanical strain and actual gage length can be calculated in real time while the test progresses.
- Event detection and limit checking may be performed on both physical and calculated parameter(s) in real time. In addition, predefined actions may be taken upon detection of a specific level or event.
- The system also has the ability to run in a unique cascade control mode. In this mode, both the inner and outer-loop control modes can be configured in a manner similar to the supervisory system approach discussed earlier. However, in the digital control system being discussed, both the inner and outer loops actually operate together in real time, and real-time calculations are possible in both the inner or outer loops. Figure 5 shows a typical block diagram for this control scheme. The main advantage of this approach is that it enables a stable inner loop control mode to be chosen, and allows a more difficult parameter to be controlled using the outer loop. The result is a more stable test system that is more immune to external disturbances and noisy feedback signals.
- Direct digital control has the ability to functionally differentiate a physical signal or calculated signal in real time. The system does this by specifying the feedback (physical or calculated) value at a specific point in time for use within the calculation. This is discussed in the velocity control example in the next section.

When using the calculated variable control capability, a couple of things must be considered to ensure proper system operation. Since the loop is not a traditional load, position, or strain control loop, care must be taken in choosing proper tuning parameters. Some trial and error may be necessary to optimize the calculated variable control-loop tuning. In addition, it is possible to write control equations that are discontinuous or become asymptotic at some points. Care must be taken in the experimental design to ensure the system calculated variable feedback does not cross these points, or a system instability may result.

Specific Test Examples

True Stress Control LCF Test

True stress control can be advantageous under certain testing conditions. Specifically, true stress control can be beneficial when studying creep/fatigue interactions or when operating in the very large strain range. In creep/fatigue studies, it is important that tertiary creep not be attributed to a decreasing cross-sectional area. In this case, the load needs to be reduced as the engineering strain increases to maintain a constant true stress. True stress control can also be advantageous in materials where the stress rate can affect the results. It is also sometimes advantageous to execute tests in stress control when information is desired at certain stress amplitudes.

Function	Description	
avg(y,x)	Returns the last x samples of input signal. Y can be any input signal (including calculated inputs) or variable constant. X can be 1 to 100. This cannot be used with other functions.	
{constants}	Constants should be defined with the Edit Calculation Constants window. A constant is always entered with curly braces {constant name}.	
cos(x)	Returns the cosine of x; x is in radians.	
	Domain: -12868.0, 12868.0.	Range: -1.0, 1.0.
exp(x)	Returns e^x.	
	Domain: -_, +88.72.	Range: 0.0, +_.
ln(x)	Returns the natural log ln(x)	
	Domain: 0.0, 3.4^{38}.	Range: -103.28, 88.72.
log(x)	Returns $\log_{10}(x)$	
	Domain: 0.0, 3.4^{38}.	Range: -44.85, 38.53.
power(x,y)	Returns x^y.	
	Domain:x[>0.0, +_], y[-_, +_].	Range: -_, +_.
prev(x)	A special function that returns the input x (input signal) and stores the last 100 samples of that signal in a circular buffer. The stored samples may be accessed in an indexed mode using braces "[x]" (where x is the sample to be indexed). This cannot be used with other functions.	
{Input Signal Name}	The signal name defined in the Input Signals Definition window. A signal name is always entered with curly braces {signal name}.	
round(x)	Rounds off the value of x.	
sin(x)	Returns the sine of x; x is in radians.	
	Domain: -12868.0, 12868.0.	Range: -1.0, 1.0.
tan(x)	Returns the tangent of x; x is in radians.	
	Domain: -6434.0, 6434.0.	Range: -_, +_.
time	Increments at the servo loop update rate. Time is always entered with curly braces {time}. The clock is reset when the Function Generator or TestWare-SX program is started. A command to reset the clock is available for those who program.	
trunc(x)	Truncates the value of x.	
[x]	Brackets identify a variable array.	

FIG. 4—*Available calculation functions for real-time control formula definition.*

This example lends itself nicely to this discussion since true stress is dependent on both engineering stress and engineering strain. True stress control requires real-time data from both the load cell and the extensometer for calculated control. In this example, a steel specimen was cycled at 0.33 Hz, triangular waveform in true stress control. The true stress range is 773 MPa with R = 0. The test was run at room temperature. Two hundred data points were taken in each cycle.

For cyclic endlevels below the ultimate yield, a true stress control channel was created in the digital controller with the following formula:

$$\sigma = S(1 + e) \tag{1}$$

When rewritten using controller specific language, the control equation is:

$$= \{LOAD\}/\{AREA\} * (1 + \{STRAIN\}) \tag{2}$$

where

σ = true stress,
S = engineering stress,
e = engineering strain,
LOAD is the real-time data taken from the load cell,
AREA is the specimen cross-sectional area, assumed to be constant, and
STRAIN is the real-time data signal from the extensometer.

In this example, true stress is calculated in real time using instantaneous values from both the load cell and strain gage signals to calculate instantaneous true stress for control purposes.

Figure 6*b* shows the entire test from start to failure at cycle 24. As is easily seen, the strain ratchets out to approximately 8% before the specimen fails.

These graphs all show raw data taken during the test. The data are acquired from the transducers, calculated, and stored to a disk file during the test. Figure 6*a* shows the engineering stress and strain data.

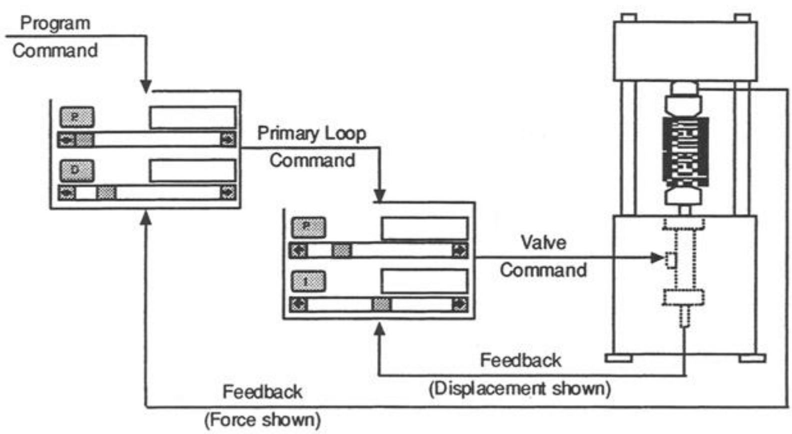

FIG. 5—*Cascade control strategy block diagram.*

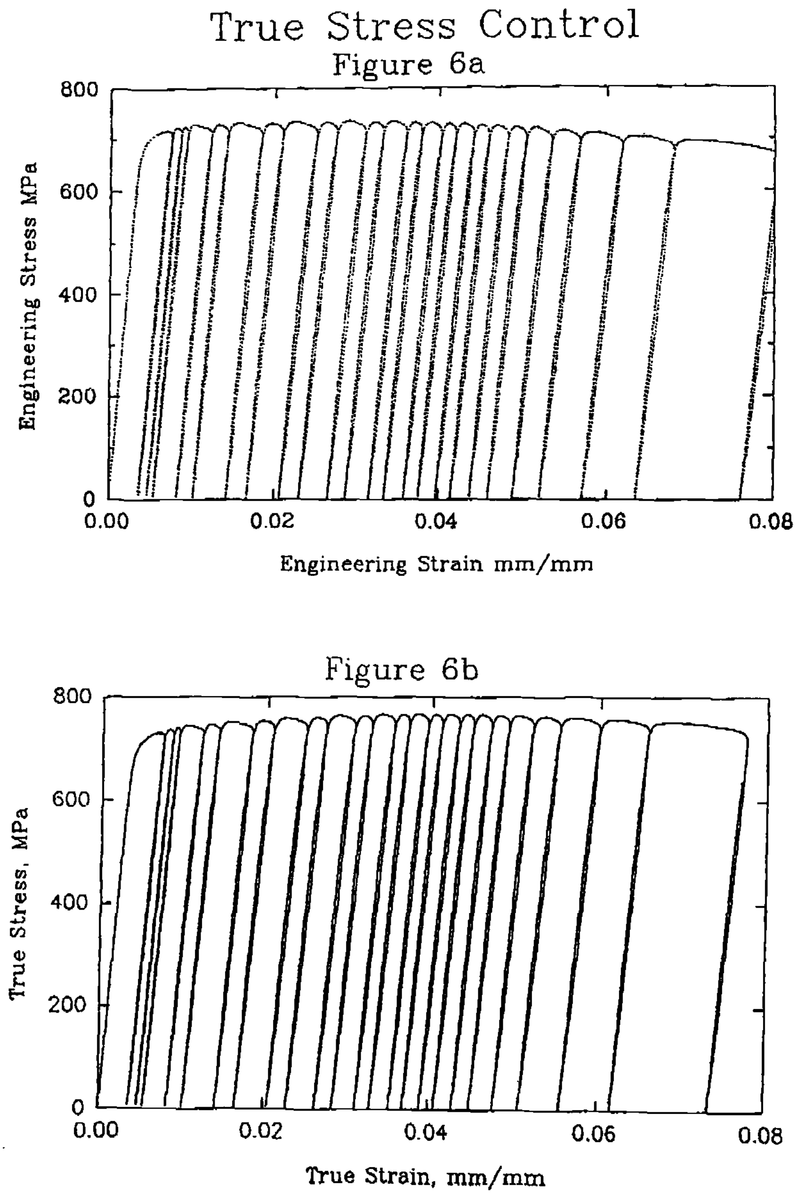

FIG. 6—*True stress control LCF test data.*

Plastic Strain Control LCF Test

Plastic strain control can be very important when examining plasticity-related processes. In deformation models, the plastic strain rate is often the dominant strain rate, especially for very high strains. The ability to test in plastic strain control, and therefore constant plastic strain rate, can mean the difference between good or bad correlation between computational models and experimental results.

Figures 7*a* through 7*d* are data taken during a plastic strain-controlled low-cycle fatigue test on a steel specimen. Figure 7*a* shows both the total strain versus time data and the plastic strain versus time data. Note that the plastic strain data were calculated in real time and written to

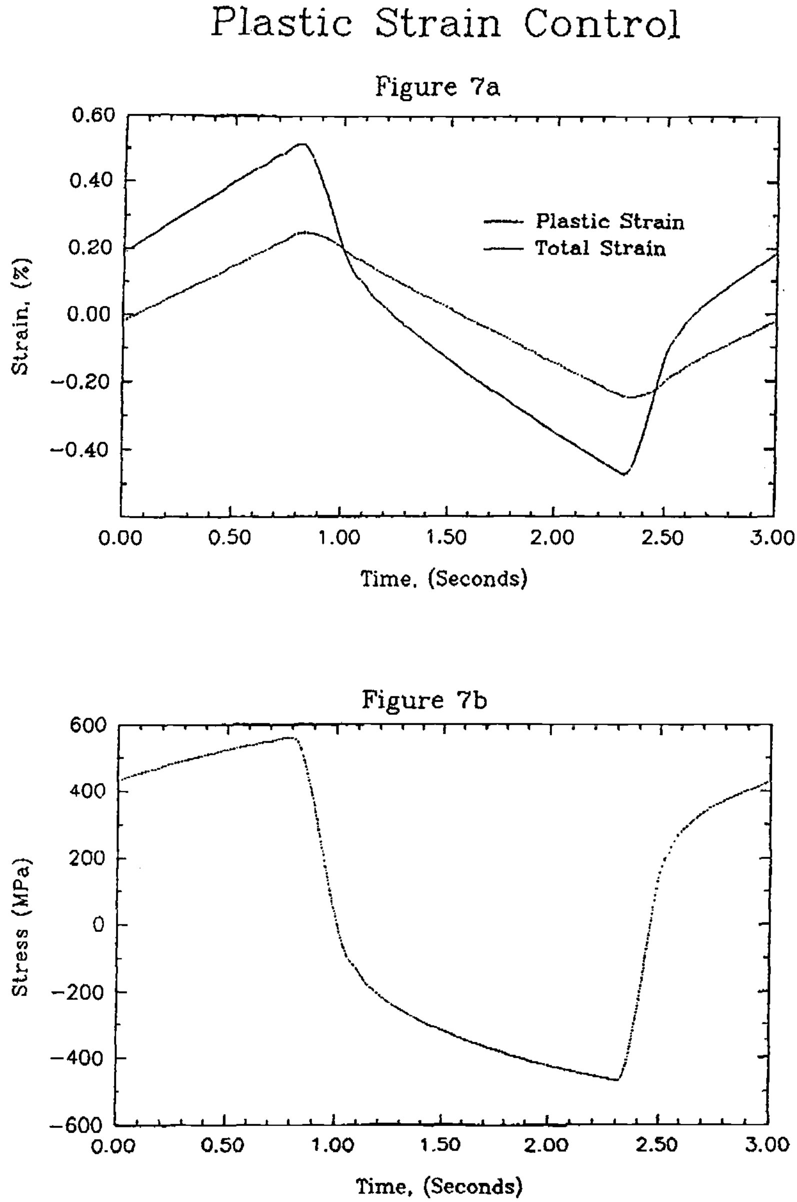

FIG. 7—*Plastic strain control LCF test data.*

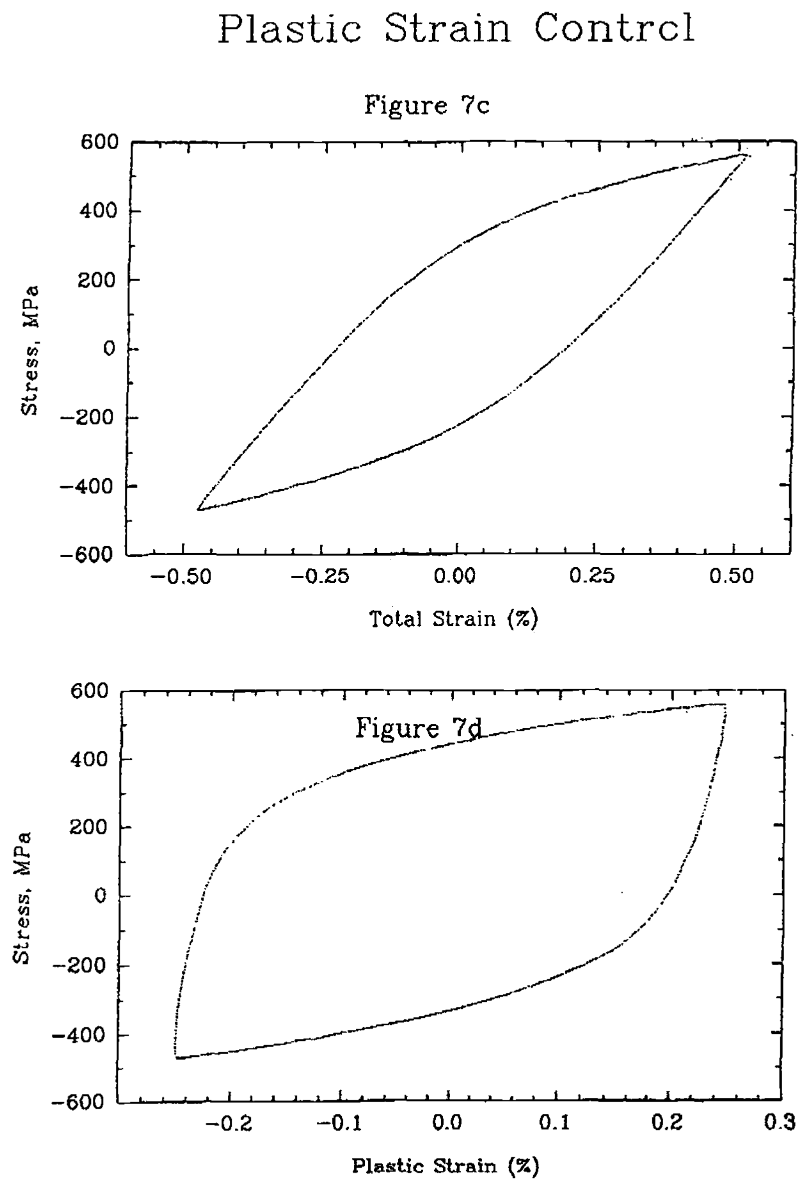

FIG. 7—*Continued.*

the computer hard disk simultaneously with time, load, and total strain data. Plastic strain for ambient temperature tests is calculated in the control loop as:

$$\varepsilon_{\text{plastic}} = \varepsilon_{\text{total}} - LOAD/AREA/E \tag{3}$$

where

$\varepsilon_{\text{plastic}}$ is the plastic strain,
$\varepsilon_{\text{total}}$ is the total strain from the extensometer,

AREA is the initial cross sectional area of the specimen,
LOAD is the instantaneous load from the load cell, and
E is Young's modulus for the material.

The control waveform was specified to be triangular with a plastic strain range of 0.005 in./in. and 0.33 Hz (plastic strain rate of 0.003/second). The data collected during the test were plastic strain, total strain, time, and load at 200 points per hysteresis loop. Calculation constants for the plastic strain control included the specimen area, 0.049 sq in., and Young's modulus at 30,000 ksi.

The stress response is seen in Fig. *7b*. This and Fig. *7c*, shown with the typical LCF hysteresis loop, are not out of the ordinary. Figure *7d* shows stress versus plastic strain and reveals the steep slopes wherein the specimen goes through the elastic region. This is also easily seen in Fig. *7a*, total strain plot, where the total strain changes very quickly at the reversals to quickly achieve the necessary plastic strain.

Thermalmechanical Fatigue Testing

Thermalmechanical fatigue testing is an area where real-time calculated control modes are immediately useful. Thermalmechanical fatigue testing (TMF) is used to simulate service conditions where mechanical loading and thermal loading are observed as in the service conditions often found in the aerospace and power generation industries.

The most common TMF test involves cycling strain and cycling temperature. In order to maintain temperature equilibrium throughout the specimen, the period of each cycle is on the order of minutes to hours.

TMF testing becomes complicated from an operational viewpoint when the operator tries to determine what strain value to use for strain feedback. Most TMF investigators would like to define a constant amplitude mechanical strain waveform and a constant amplitude temperature waveform, but extensometers only measure total strain. In TMF, total strain is considered a combination of mechanical strain and thermal strain. If the mechanical test system is using total strain as the inner loop feedback, then the program command for mechanical loading must be a combination of the desired mechanical strain and the thermal strain resulting from the temperature waveform. There are a number of ways to generate this combination command. Among the methods are look up tables for temperature, look-up tables for phase of the waveform, or calculation of thermal strain from temperature. Subtracting the thermal strain from the total strain before closing the loop in the controller allows direct control of mechanical strain.

Modern digital controllers with calculated inputs not only make this direct control possible; they make it easy. Thermal strain can be defined as:

$$\varepsilon_{\text{thermal}} = \text{Æ}T * \alpha \tag{4}$$

where $\varepsilon_{\text{thermal}}$ is the calculated thermal strain, $\text{Æ}T$ is the instantaneous feedback temperature minus the temperature where strain was zeroed, and α is the material's thermal expansion coefficient for the temperature range in question. (For wide temperature-range testing the control Eq 4 can be modified so that $\alpha = \alpha[T]$ for improved accuracy.) Mechanical strain can then be defined as:

$$\varepsilon_{\text{mech}} = \varepsilon_{\text{total}} - \varepsilon_{\text{thermal}} \tag{5}$$

where $\varepsilon_{\text{mech}}$ is the calculated mechanical strain, $\varepsilon_{\text{total}}$ is the measured strain from the extensometer, and $\varepsilon_{\text{thermal}}$ is the calculated thermal strain from Eq 4.

The ISO standards committee is currently working on a TMF standard. One of the areas under discussion is determining what gage length should be used to calculate strain. Although the recommendation is to use the gage length at the mean temperature, a number of TMF investigators are dissatisfied with this approach and instead calculate the instantaneous gage length during the temperature cycle.

Modern digital controllers make this gage length recalculation trivial. The instantaneous gage length can be calculated as:

$$G.L. = G.L._{RT} + (T - RT) * \alpha \tag{6}$$

where $G.L.$ is the instantaneous gage length, $G.L._{RT}$ is the gage length measured at room temperature, T is the temperature feedback, RT is the room temperature at which the gage length was measured, and α is as above.

Most elevated temperature extensometers are calibrated in terms of displacement rather than strain. Thus Eqs 5 and 6 become:

$$\varepsilon_{mech} = ([ÆL + G.L._{RT} - G.L.]/G.L.) \tag{7}$$

where $ÆL$ is the feedback from the extensometer and $G.L._{RT}$, $G.L.$ and ε_{mech} are as above.

Once mechanical strain is calculated, it can be used as a control feedback just like any other physical feedback. The complications of a TMF test collapse to those of any other test with two channels (temperature and strain) of phased control.

The software associated with modern digital controllers makes it easy to enter the calculation equations used within the real-time control loop. Figure 8*a* shows a typical screen for entering the thermal expansion constant, α, used in Eqs 4 and 6. Other constants, such as RT, or $G.L._{RT}$ could be entered using similar screens. Calculated feedbacks usually reference the calculation constants and often reference each other. Figure 8*b* shows a typical screen for defining the calculated feedback for control from Eq 5.

Mean Principle Stress Test

In the field of geomechanics, the ability to simulate the various conditions existing underground is important for a variety of reasons, including the development of underground space and understanding earthquakes. Test systems are used that simulate a number of parameters, including the three normal stress vectors on an underground element, σ_1, σ_2, and σ_3, as well as any possible fluid pressure, called pore pressure. In the case of a cylindrical specimen in a "tri-axial cell" (typically a vessel designed to apply axial load and lateral pressure to the specimen), pressurized fluid, typically called confining pressure, is used to simulate the lateral stresses, so that $\sigma_2 = \sigma_3$. Axial load is used to simulate the vertical stress on the cylinder.

Rock materials often exhibit deformation behavior that is dependent on the rate and sequence of the applied stress. This has led to research on the influence of this stress path on the material behavior. To study stress path dependence in the laboratory triaxial cell, the "mean principle stress test" is performed. During this test, the mean principle stress on the specimen, $(\sigma_1 + \sigma_2 + \sigma_3)/3$ is held constant.

Similar to TMF testing, the test is performed using two servocontrol channels. The axial actuator is operated in axial strain control, and the confining pressure channel is operated in a mean principle stress control mode where both load feedback and pressure feedbacks are used as inputs to the calculation of mean principle stress (Fig. 9). The test is conducted by ramping the axial strain control channel at a constant rate. The program input to the confining pressure

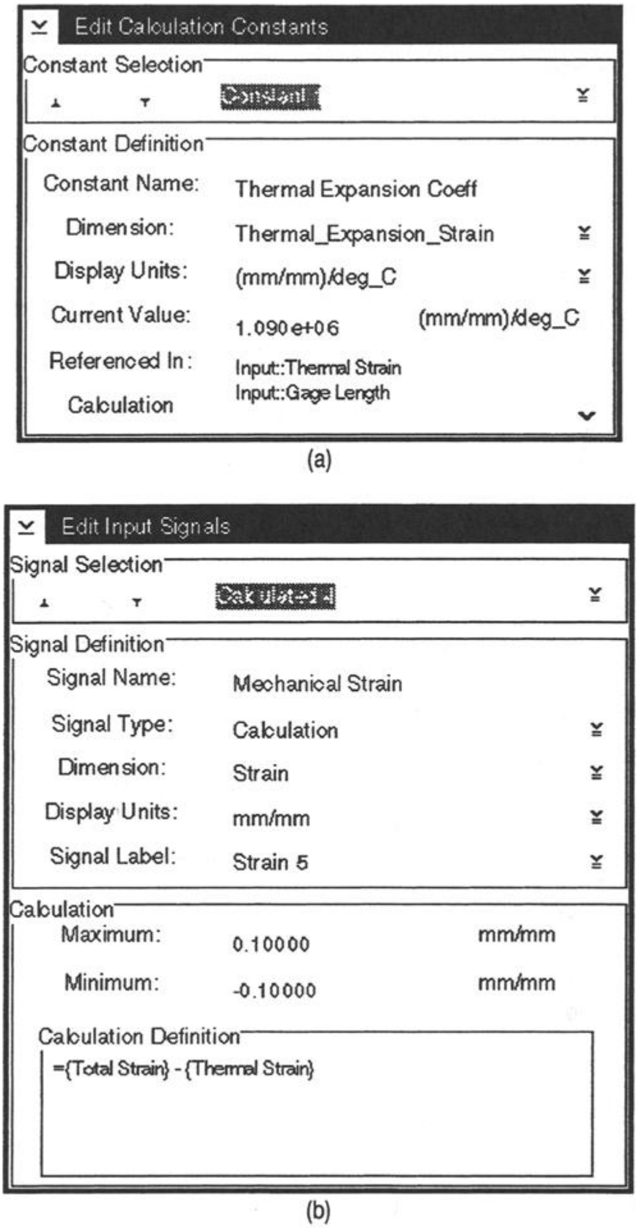

FIG. 8—(a) *Typical input screen for calculation constants used in various feedback calculations. This screen shows the coefficient of thermal expansion constant;* (b) *typical input screen for calculated control mode feedbacks. This screen shows the calculation defined by Eq 5 for mechanical strain.*

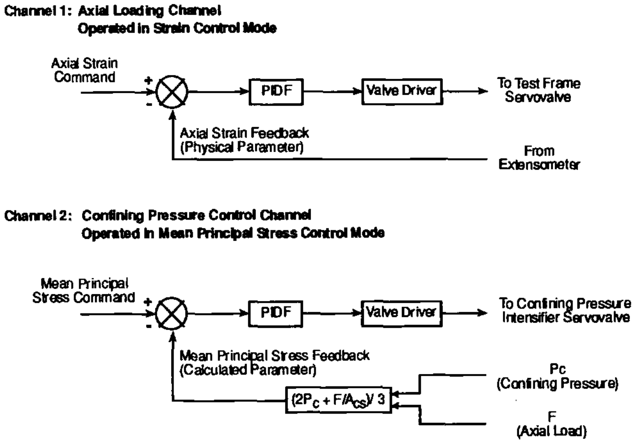

FIG. 9—*Mean principle stress test control strategy.*

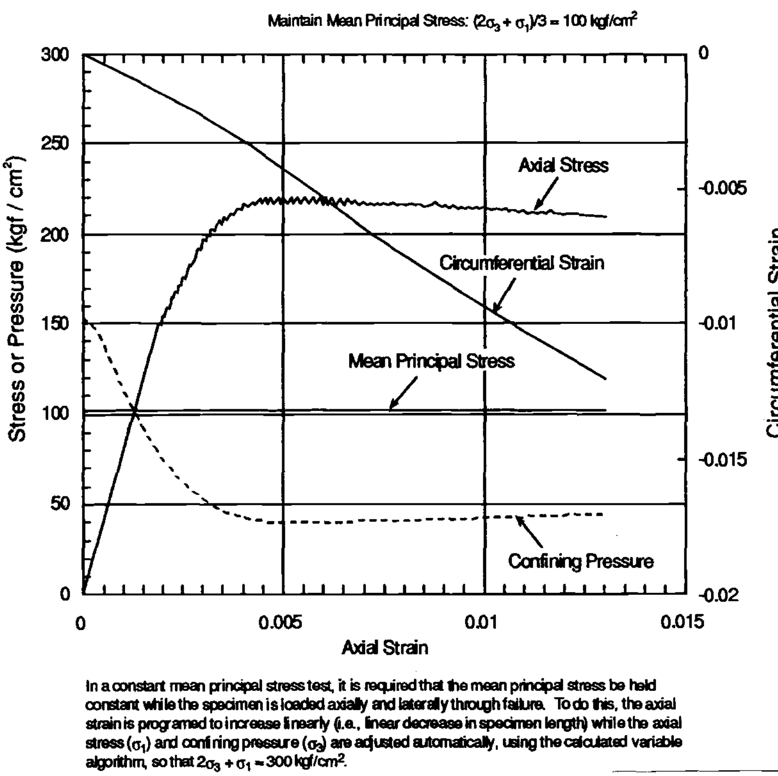

FIG. 10—*Mean principle stress data plot.*

channel, operating in mean principle stress mode, is set to the desired static level. As the axial strain increases, the axial stress also increases. The confining pressure channel reacts to this change and causes the confining pressure to decrease accordingly to maintain the desired mean principle stress. Data from a typical mean principle stress test are shown in Fig. 10.

Velocity Control Example

Although not specifically used in the field of materials research, other types of calculated variable control are of academic interest. Velocity control is included because it highlights two unique capabilities of the digital control system under discussion. These capabilities are:

- The digital control system has the ability to functionally differentiate a feedback (a physical or calculated feedback) in real time.
- The digital control loop has the ability to operate in cascade control mode (Fig. 5), using inner control loop and outer control loop, with both loops operating in real time.

The example we will use to demonstrate these capabilities is the direct control of actuator velocity. The system is set up to operate in cascade control mode with the inner loop in displacement control and the outer loop in velocity control mode. Alternatively, the system could be configured to run directly with the inner loop in velocity control mode. Cascade mode is chosen because it enables the intrinsically stable position control mode to be used for the inner loop. In addition, the position control loop is easy to tune. Because the outer loop control mode is also operational in real time, the cascade control mode can be used for control of velocity.

The calculation of velocity is made through a functional differentiation of the displacement feedback channel with respect to time. The system is able to calculate the difference in the feedback variable at different clock points, and divide this difference by the time difference. The exact formula used is:

$$Velocity = (\{Displ\ prev\}[0] - \{Displ\ prev\}[5])/(\{Time\ prev\}[0] - \{Time\ prev\}[5]) \quad (9)$$

where *Displ prev* and *Time prev* are the values of each of these parameters at the clock point referenced.

Conclusion

The ability to perform real-time calculated variable control has applicability to many different types of materials tests. Recent advances in microprocessor technology have improved direct digital control by enabling a simplified interface and faster control loop to be utilized. Test operators can now control materials tests in ways previously possible only through dedicated hardware or dedicated software programs designed for each application. With the modern calculated control variable systems, a simple controller allows improved versatility since control schemes are defined within the software and easily saved as an equation. To change the test control scheme, a new control equation is simply entered into the appropriate software window.

Some applications of interest not specifically addressed in this paper which merit further review are: (1) yield surface studies performed on multi-axial test systems; (2) direct shear tests on rocks conducted in normal stiffness control using a calculated channel of axial (normal) displacement and axial (normal) load; (3) centroid control in planar bi-axial testing; and (4) forging simulation.

References

[1] Nanstad, R. K., Alexander, D. J., Swain, R. L., Hutton, J. T., and Thomas, D. L., "A Computer-Controlled Automated Test System for Fatigue and Fracture Testing," *Applications of Automation Technology to Fatigue and Fracture Testing,* American Society for Testing and Materials, Philadelphia, 1990.

[2] Jones, W. B., Schmale, D. T., and Bourcier, R. J., "A Test System for Computer-Controlled Thermal-Mechanical Fatigue Testing," *Applications of Automation Technology to Fatigue and Fracture Testing,* American Society for Testing and Materials, Philadelphia, 1990.

[3] McKeighan, P. C., Evans, R. D., and Hillberry, B. M., "Fatigue and Fracture Testing Using a Multitasking Minicomputer Workstation," *Applications of Automation Technology to Fatigue and Fracture Testing,* American Society for Testing and Materials, Philadelphia, 1990.

[4] Hartman, G. A. and Ashbaugh, N. E., "A Fracture Mechanics Test Automation System for a Basic Research Laboratory," *Applications of Automation Technology to Fatigue and Fracture Testing,* American Society for Testing and Materials, Philadelphia, 1990.

[5] Braun, A. A., "A Historical Overview and Discussion of Computer-Aided Materials Testing," *Automation in Fatigue and Fracture Testing and Analysis,* American Society for Testing and Materials, Philadelphia, 1994.

[6] Hartman, G. A., Ashbaugh, N. E., and Buchanan, D. J., "A Sampling of Mechanical Test Automation Methodologies Used in a Basic Research Laboratory," *Automation in Fatigue and Fracture Testing and Analysis,* American Society for Testing and Materials, Philadelphia, 1994.

[7] Braun, A. A., "The Development of a Digital Control System Architecture for Materials Testing Applications," *Proceedings of the 17th International Symposium for Testing and Failure Analysis,* ASM International, Materials Park, OH, 1991.

[8] "Model 440.38 Axial Strain Computer Product Specification," MTS Systems Corporation, Eden Prairie, MN, 1974.

[9] "Model 438.11 Crack Correlator Product Specification," MTS Systems Corporation, Eden Prairie, MN, 1976.

[10] "MTS TestStar Reference Manual," MTS Systems Corporation, Eden Prairie, MN, 1994.

F. Joseph Albright[1] *and Luther E. Johnson*[1]

Control of a Biaxial Test Using Calculated Input Signals and Cascade Control

REFERENCE: Albright, F. J. and Johnson, L. E., "**Control of a Biaxial Test Using Calculated Input Signals and Cascade Control,**" *Applications of Automation Technology to Fatigue and Fracture Testing and Analysis: Third Volume, ASTM STP 1303,* A. A. Braun and L. N. Gilbertson, Eds., American Society for Testing and Materials, 1997, pp. 147–157.

ABSTRACT: Control of a single-channel material test is relatively straightforward with modern servocontrollers. During this type of test, the center of the specimen moves as the specimen length changes. Although normally not a problem, this motion is not acceptable for some tests, such as planar biaxial tests. Relative motion of the specimen center will introduce unwanted stresses in the test piece and make visual monitoring of the specimen difficult.

This paper describes a control technique to minimize specimen motion in the planar biaxial test application. It utilizes calculated input signals for the feedback. The control architecture is a cascade control loop. Description of the basic control method is provided and actual test results showing specimen motion with and without the control are presented.

KEYWORDS: planar biaxial control, matrix control, calculated input signal feedback, test method

Control of a single-channel material test is relatively straightforward with modern servocontrollers. The specimen is attached to a massive, rigid structure on one end. The other end is frequently attached to the piston rod of a hydraulic actuator. Motion of the piston rod stretches or compresses the specimen, generating forces in the part. Since one end is stationary and one end is fixed, the center of the specimen moves as the specimen length changes.

Although normally not a problem, this motion is not acceptable for some tests. Planar biaxial tests are one such type. In a planar biaxial test, the specimen is loaded along two orthogonal axes. The part is restrained at four points; typically two vertically opposed and two horizontally-opposed points. Relative motion of the specimen center along one axis will introduce unwanted stresses in the test piece. Additionally, the motion makes visual monitoring of the specimen difficult.

This paper describes a control technique to minimize specimen motion. Although the concepts presented are applicable to a wide variety of control actuators and controlled systems, this discussion will be limited to hydraulic actuators and simple, spring specimens.

Conceptual Overview

Biaxial control is a problem involving close coordination of four channels of servocontrol. Good matching of the servovalve and actuator characteristics enhances the quality of control. The key concepts are presented next.

[1] Senior staff scientist and senior project manager, respectively, MTS Systems Corp., 14000 Technology Drive, Eden Prairie, MN 55344.

Servocontrol

In a traditional material test, a hydraulic actuator is attached to a test specimen. Figure 1 shows a simplified example.

The actuator displacement and resulting specimen force is determined by the control method used. Material test systems are frequently closed loop machines. The actuator position is adjusted based on specimen and/or actuator measurements. The process of correcting the actuator's control signal based on the difference between desired feedback (program) and actual feedback is called servocontrol. Figure 2 shows a basic servocontroller added to the actuator and specimen of Fig. 1.

Closed loop control can be summarized in the following way: (1) Where are you? (2) Where do you want to be? and (3) Move!.

In Fig. 2, where are you is labeled as feedback. Where you want to be is labeled program. Comparison of the two is called error. It is simply the difference between program and feedback. Move! is the control signal. There are a variety of calculations that can be used to convert the error into a control signal. The most common is a direct multiplication of a constant G times the error. This method of control is called proportional control. Often this constant G is called P in a traditional PID (*proportional*, integral, derivative) controller.

Servocontrollers are often said to be operating in a specific control mode. That refers to the fact that what physical parameter is being controlled depends on the feedback being measured. Two very common control modes are stroke and load. Figure 2 is an example of stroke control. In stroke control the feedback is the position of the actuator piston rod. Its position is measured by a transducer, such as a linear variable differential transducer (LVDT), attached between the piston rod and actuator body.

In load control the force applied to the specimen is measured using a load cell. The load cell is mounted at one end of the specimen. If the specimen acts like a spring, then the force applied is proportional to the actuator displacement. In that case load control is quite similar to stroke control. Although an oversimplification of load control, it is adequate for the initial introduction of biaxial control techniques.

State of the Art

The simplest biaxial control approach would be individual load control of all four actuators. This would generally provide protection of unwanted bending in the specimen, at least statically. The greatest weaknesses to this approach are specimen installation and asymmetrical specimens.

When operating in load control, the actuators are free to move until they contact an object and generate a load. This is not a good situation when attempting to load a specimen into the test machine. The solution is usually to have a position-based, load-limited control mode for specimen loading.

The bigger limitation arises when the specimen stretches/compresses unequally from one side of center to the other. Now when a load is required, the two opposing actuators need

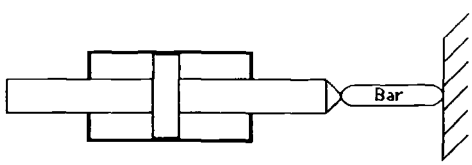

FIG. 1—*Hydraulic actuator with test specimen.*

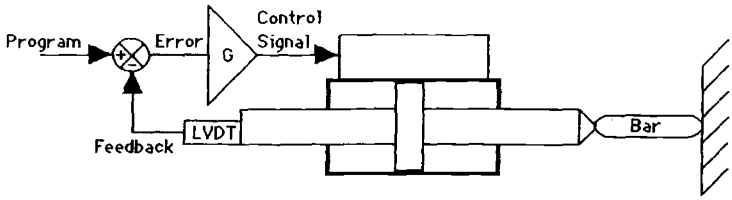

FIG. 2—*Basic servocontroller and actuator.*

different control signals so that they travel at different speeds. This is not readily achieved with individual load control loops.

Using individual displacement control loops is a method that would simplify specimen loading. Operating each actuator in independent-position control assures that each actuator will stay where you want it. It would also permit more direct control of the absolute motion of each actuator during the test, permitting control of the center of the specimen. However, without any use of load in the control loop as the stiffness of the part changes during the test, the load will wander. This, also, is not desirable.

What is desired conceptually is a single command to two actuators that causes them to do similar things. One technique that could be used is called master/slave control. In master/slave control the program for one actuator of a pair comes directly from the controller. The command to the other actuator is the actual position of the first. In this way, the second actuator is told to mimic the first. The biggest drawback to this approach is that the second actuator is not given a command until the first actuator has already moved. This guarantees that the second actuator cannot perfectly mimic the motion of the first, thus it is a limitation.

Matrix Control

Matrix control attempts to utilize the strengths of all of the above. It is a blend of load and stroke control. Load and stroke feedback from both actuators are used in the control algorithm. It gives each actuator roughly the same amount of anticipation for the desired motion.

In the section on servocontrol, the example shown in Figs. 1 and 2 is called *single degree of freedom.* That is, there is one control element; the actuator. It can only move in a single direction, horizontally, and it acts on only one point of the specimen; its left-hand end.

Planar biaxial tests attach four actuators to the specimen. They are attached as two sets of opposing actuators. This is called a multi-degree-of-freedom system. The impact of multiple actuators can best be understood by first considering the control of two opposing actuators.

A simple illustration is control of a bar attached between two opposing actuators. Figure 3 takes the basic system of Fig. 1 and replaces the fixed connection at the right end of the specimen with a second actuator.

In this example, the actuators are capable of controlling two characteristics of the bar: First is its position. As the right-hand actuator retracts, the bar moves only to the right *provided* the left-hand actuator also moves to the right. If, however, the left-hand actuator remains stationary, then one end of the bar moves to the right and a tensile force will also be imposed. Thus, force is the second characteristic of the bar that can be controlled by the two actuators.

For this example, then, matrix control is needed to develop a method of controlling both actuators. When the bar is to be displaced without applying forces, one actuator must extend while the other retracts. When the bar is to be stretched (or compressed) without displacing, both actuators need to extend (or retract) an equal amount. Matrix control provides this coordination.

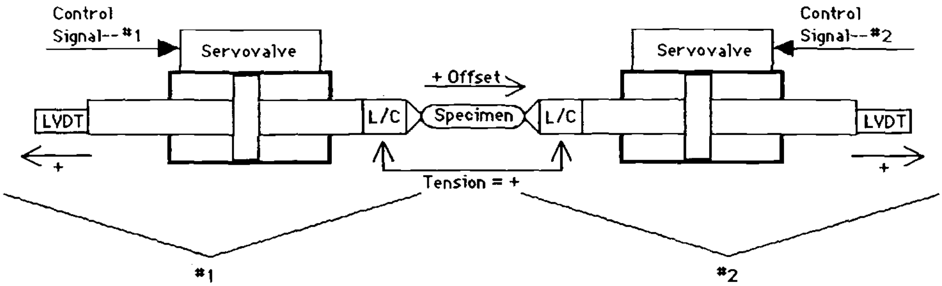

FIG. 3—*Two opposing actuators.*

Matrix control is a technique in which the control signal for an individual actuator is determined from the combination of multiple feedback signals and their respective commands. It is only applicable when multiple actuators are involved. Matrix control provides coordination of the multiple actuators to achieve a common goal. It is a well-proven technique that has been used extensively for many years with vehicle test systems [*1*].

Description of Matrix Control

The control signal for a control loop is typically based on the difference between the program and the measured feedback. In a single-degree-of-freedom system only one feedback is needed in the control loop. In a multi-degree-of-freedom system the measured feedback for each degree of freedom may be based on multiple measurements. Matrix control is accomplished by creating *logical control signals* based on the desired degrees of freedom instead of the individual transducers. The control signal for an individual actuator becomes the sum of logical control signals for all degrees of freedom that apply to that actuator.

Figure 4 shows a matrix controller for the two actuators example. To implement matrix

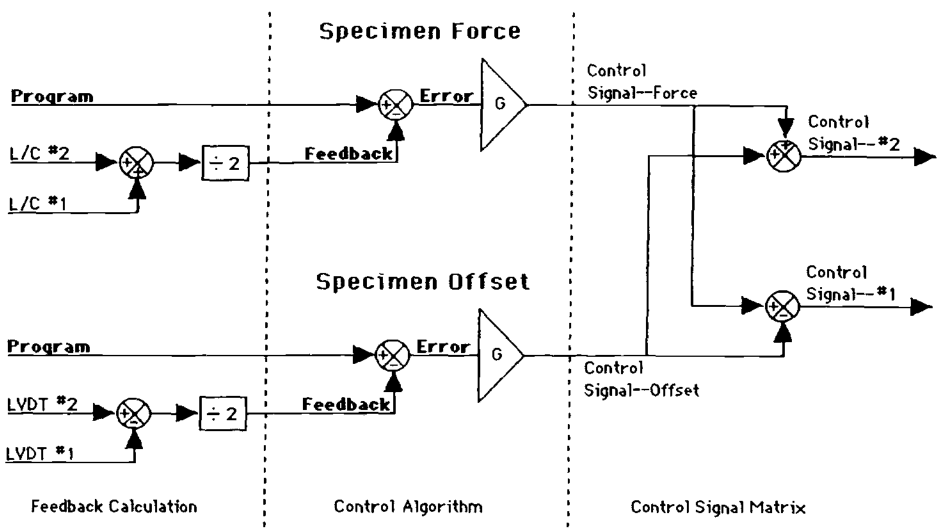

FIG. 4—*Two-channel matrix controller.*

control, two new control loops are created: specimen offset and specimen force. It was not particularly practical to measure specimen offset directly. We chose to estimate it by taking the difference of the two actuator displacements and dividing by two. Specimen force could be measured from either actuators' load cell in this case. However, to prepare for the four actuator case, specimen force will be estimated by taking the average of the forces as measured at each actuator.

With these two "new" feedback signals, two errors can be calculated, gains applied, resulting in two control signals. They are labeled "control signal—offset" and "control signal—force" for the specimen offset and specimen force loops, respectively. Those control signals are determined in the control algorithm section of Fig. 4.

Now what is needed is to appropriately sum those signals for the individual actuators. The load signal is the most straightforward. In Fig. 4, a + control signal to each servovalve causes its actuator to retract. Also, a positive force signal represents tension. Thus, whenever the specimen force loop has a + control signal, then that polarity of signal is appropriate for each servovalve and can be used directly as control signals 1 and 2.

Similar logic can be applied to the specimen offset loop. The conclusion is slightly different, though. For specimen offset, when control signal—offset is positive, the specimen is to move to the right. For Actuator #2 that is a retraction and requires a + control signal. Thus control signal—offset can be summed directly with control signal—force. For Actuator #1, however, the direction of motion requires a − control signal. Thus, for Actuator #1 control signal—offset must be subtracted from control signal—force. These calculations are represented in the control signal matrix portion of Fig. 4.

The previous example involved only two actuators. As mentioned, that meant that each actuator exerts the same force. The task of coordinating actuators grows more complex with more degrees of freedom. In Fig. 5, two additional actuators have been added.

The horizontal pair are as before, but the specimen has been replaced with a cruciform-style specimen. Now offset of the horizontal actuators will create bending in the vertical section of the specimen. Forces in the specimen for a single axis are now not necessarily the same at opposing actuators. This illustrates why the forces were averaged in the matrix controller described for two actuators. This is the hardware/specimen configuration of the planar biaxial test we conducted.

Theoretical Studies

A digital simulation of the system was performed in order to verify concepts well before hardware was built. The model was developed using the simulation product Extend™ [2]. This is an object-oriented modeling software package that runs on Macintosh™ and Windows™ platforms. We have used it extensively to model a wide variety of systems.

The initial modeling study was conducted by the same technician that would run the actual system. It was felt this would increase his understanding of any system idiosyncrasies. This goal was accomplished as the technician developed a very good understanding of how the system would behave before having hardware to use. This was probably most helpful in learning how to tune the various parameters. The authors were able to prototype some tuning procedures without the danger of specimen damage, or the pressures often associated with shipping the actual system.

Model use focused on the interaction between only two actuators. It utilized a very simplified servovalve model and actuator model. The cross-coupling effects were expected to be minimal. Of primary interest was learning how the various control terms behaved. There was even some doubt whether the system would be stable with a sufficiently high gain. The simulations showed the system to be more than adequate.

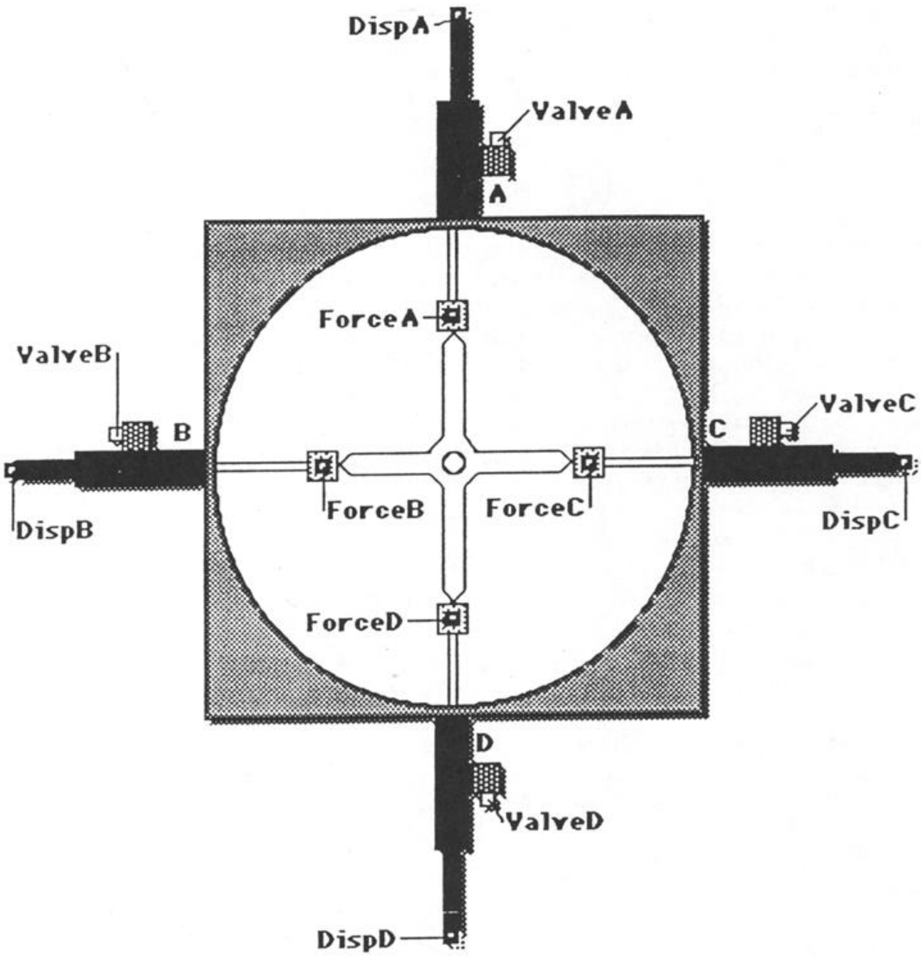

FIG. 5—*Biaxial frame and actuators.*

The initial modeling was kept fairly limited. Since this was a new area of investigation we did not want to put a lot of effort into the model until we had some actual test experience indicating the model was at least qualitatively correct. The actual system has been assembled and tested now and we have found the model to be qualitatively correct. Future work with the model will add additional characteristics.

In particular, we learned that the control system can be very sensitive to differences in actuator characteristics. Future studies may investigate differences in actuators and how they affect the behavior of the system. Different valve dynamics and frame dynamics are other areas of study that could be attempted.

Actual System Use

The concepts presented were actually put to use on a full system. This section briefly describes the system and presents test results from the project. We are pleased to report that the system worked very well.

Test Specification

The customer is interested in studying the low-cycle fatigue properties of 316 stainless steel as well as pressure vessel steels and nickel-based superalloys under in-plane biaxial stress states. The system is required to run strain-controlled fatigue tests at strain levels in each axis of up to 1%. Loading both in-phase and out-of-phase is required. The forces required to achieve these strain levels for the defined specimen are up to 100 kN. The centroid should be maintained within ± 3 micro meters during each test. Test temperatures are 300 to 1000 degrees C.

Specimen

The specimens are fabricated from 16-mm-thick plate. The specimen is fabricated into a cruciform shape. The specimen has a final thickness in the tab (gripped) area of 14 mm. It is reduced in thickness at the intersection to 8.75 mm, then reduced to 2.5 mm in the gage section. The gage section diameter is 15 mm. In a traditional uniaxial specimen, all force applied by the test system is reacted through the gage section. In the case of a planar biaxial test specimen, a significant portion of the force is carried by the area outside the gage section. It is important that the stress levels in this area be high enough to allow the gage section to continue into plastic strain, but not so high as to become the failure initiation site. Lack of balance between the design factors can also result in a poor stress distribution or buckling in the gage section, or buckling of the specimen as a whole.

Other specimens have been used for planar biaxial testing that utilize flexures intersecting the gage section. This style of specimen was not explored on this system.

System Description

The system consists of:

- Planar biaxial load frame,
- Four 250 kN hydraulic actuators (250 kN @21 MPa, 100 kN @8.4 MPa),
- Four-channel TestStar™ controller,
- Four 100 kN load cells,
- Four 100 kN hydraulic wedge grips,
- Alignment fixtures,
- Biaxial high-temperature extensometer,
- Induction heater,
- Hydraulic power supply.

Strain-controlled low-cycle fatigue tests to high plastic strain levels require careful attention to several design considerations. High lateral stiffness of the load frame and specimen design are keys to achieving compressive plastic strain without buckling. High axial stiffness of the load frame and a stable strain transducer are keys to allowing good strain control. These issues are exacerbated when extended to in-plane biaxial testing. Several key aspects of the biaxial system are described in the next section.

Load Frame and Actuators

The load frame was designed primarily for high stiffness. The static and dynamic capacities based upon stress levels were much higher than required.

The stiffness can be represented in two conditions: 1) deflection along one axis when both axes have equal forces (Force on X = Force on Y), Stiffness is 2.96×10^9 N/m; and 2) deflection along one axis when each axis has equal and opposite forces (Force on X = −Force on Y), Stiffness is 1.01×10^9 N/m.

The load frame is designed to be completely symmetric. In this way, all load frame deflection is symmetric along each axis with respect to the center of the specimen. The relative position of opposing actuators may be assumed to be representative of the motion of the specimen center.

The load frame was fabricated from carbon steel plates. It was welded, stress-relieved, and machined. Care was taken to ensure that the actuator mounting surfaces for each axis were parallel and perpendicular with respect to the other axis.

The actuators are ''oversized'' 250 kN capacity with 100-mm dynamic stroke. The extra-large diameter rods with large-area hydrostatic bearings yield high lateral stiffness. This is very important to achieve high plastic strain levels in compression without buckling.

The actuators were aligned in the load frame at assembly using a laser alignment system. Final alignment of the grips was achieved using the alignment fixtures and a specially designed strain gaged alignment specimen.

Controller

For the application described in this paper, matrix control was implemented using an MTS TestStar™ controller [*3*]. This is a four-channel digital servocontroller with analog signal conditioning and data acquisition. Signal conditioning for four LVDTs and four load cells was utilized. Dual valve drivers in the main controller chassis converted the control signals from voltages out of the digital controller into the current levels needed for the servo valves. Timed data was acquired using the software package TestWare SX™.

The features listed so far are available on many modern day servocontrollers. What made the TestStar™ controller particularly well-suited for a biaxial test were aspects of its digital controller section. As noted in the section on matrix control, a matrix controller has 3 main parts: control algorithm, feedback calculation, and control signal matrix.

Control Algorithm—The control algorithm portion of a matrix controller is a conventional PID controller. This algorithm is very common [*4*]. Once a test is running there is frequently little difference in performance between different manufacturers' PID controllers. The challenge, however, is how to get the specimen loaded, test started, and test stopped without breaking a specimen. This was an especially critical concern with this test, where we needed to bring four actuators into contact with the specimen.

This turned out to be a relatively straightforward task. The controller has bumpless mode switch on the individual channels. This feature essentially permits changing the control feedback and program at will without introducing unwanted load transients into the specimen.

Using the mode switch feature, the specimen can initially be held in position by some actuators in stroke control while the others are loaded. The actuators can then be switched to load or matrix control. Specimen loading and unloading proved to be a nonissue on this project.

Feedback Calculation—As previously mentioned, feedback for a control channel needs to be based on measurements made with the system being controlled. In a single-channel material test system it is frequently practical to measure the desired parameter directly with a single transducer. Actuator position is often measured with an LVDT mounted to the actuator piston rod. Specimen force is typically measured with a load cell attached to the piston rod or fixed end of the specimen.

Both LVDTs and load cells require signal conditioning to convert low-level analog signals into signals suitable for readout and control. After conditioning, the signals exist as analog voltages. Analog controllers would then determine the control loop error by combining that voltage with a voltage representing the program. The key issue to understand regarding an analog controller is that any manipulation of a signal typically required wires and discrete components. Thus implementing the feedback calculation required for matrix control involved considerable complexity. Signals needed to be routed together with wires and combined using amplifiers and resistors.

The arrival of digital controllers opens the door to much greater flexibility of signal manipulation after the analog signal is converted to a digital format within the digital controller. The TestStar™ calculated input feature is a powerful tool for performing such manipulations [5].

The calculated input feature permits mathematical manipulations of one or more conditioned signals in real time. The output of the calculation exists as a new signal that can be used further in calculations or as a control feedback. Although a wide range of mathematical operations are available, our needs were for simple addition, subtraction, and multiplication. Our biggest concern was the impact calculations may have on the update rate. Monitoring the controller's performance meter, we were pleased to see that there was no reduction in update rate when we added the calculations to the control algorithm.

Control Signal Matrix—Although the matrix control concept looks straightforward on paper, in practice we saw one major roadblock. Calculated input feedbacks addressed the matrix controller's need for determining specimen offset and average load. It did not seem to address the need for calculations on the control signals. What was needed for that portion of the controller was a means of summing two different control signals. Calculated input signals were only external signals, which seemed to rule out its utility for summing control signals. Or did it?

Figure 6 shows the matrix controller redrawn with some simplifications. It only shows the control signals for Actuator #2. Most important is the fact that the specimen offset was not intended to follow a program. Rather, it was simply to maintain a constant value. Therefore,

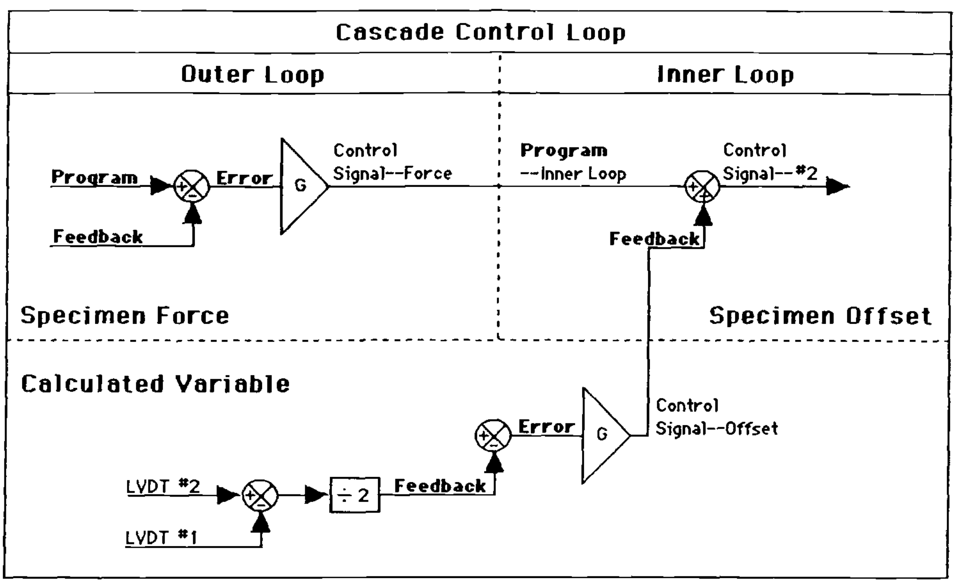

FIG. 6—*Cascade control loop.*

the specimen offset program line was eliminated from the figure. The other substantial elimination was the calculation for specimen force. That is still being done in order to compute the feedback for the specimen force loop, but was left off for clarity.

Along the top of the figure are three new key phrases: cascade control loop, outer loop, and inner loop.

Cascade control is a standard control architecture that we used in a nonstandard way to complete our matrix controller [6]. The concept of a cascade controller is that the control signal from a controller does not necessarily need to go directly to the servo valve. Rather, there are times where it is beneficial to use the control signal from one control loop as the program to a second control loop. The control signal from the second control loop is the one that finally goes to the actuator. Common terminology refers to the first control loop as the outer loop, and the second one as the inner loop.

This was exactly what we were looking to do. We wanted a means to sum two calculated signals: the control signal for the specimen force loop and the control signal for the offset loop. The conceptual leap that was necessary was the realization that the comparison between program and feedback in a controller as well as the multiplication by G could be done as a calculation using the controller's calculated input feature.

Refer to the calculated variable section of Fig. 6. Although we have discussed that portion of the control loop as a controller, the calculation needed is simply the combination of two feedback signals multiplied by a constant. Thus the control signal—offset can actually be calculated as if it were a system feedback, and then summed in at the feedback connection point of the inner loop. Since the offset program in the current application is always a constant, the error calculation just prior to the control signal—offset only requires the offset feedback. In a situation where the offset needed a program as well, it can simply be added in at the same point as the feedback.

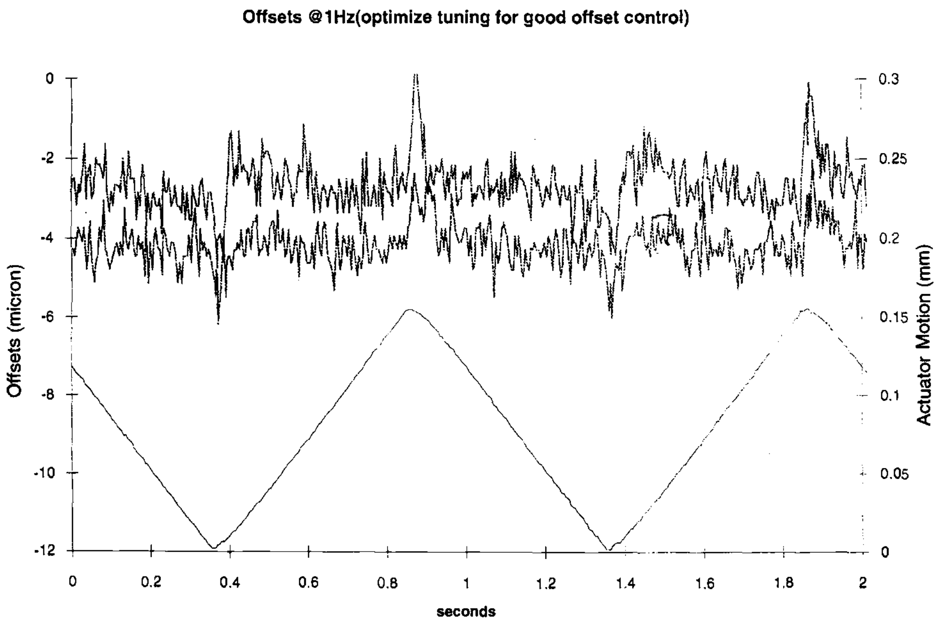

FIG. 7—*Test result—1 Hz test.*

This technique for building a matrix controller brought along an unexpected benefit. The G term for the specimen offset and specimen force loops has now become an independent term for each actuator. This allowed us to "trim" the gains for each actuator independently. We found this to be a very powerful tool for getting the most from the system. The next section shows just how good the control can be using matrix control.

Test Result

The final results were extremely satisfying. A variety of tests were conducted at different frequencies, amplitudes, and phasing of the two channels. Offset control was very good. Operation was straightforward. For some conditions, retuning the controllers improved the offset control.

Figure 7 shows a typical offset motion for the system during actual operation. The test was a 1 Hz, triangle wave, 0–50 kN test. The noisy signals are the offset motion of the vertical and horizontal channels during a 1 Hz, triangle wave test. They are plotted against the left-hand axis as microns. One actuator's actual displacement, in mm, is plotted against the right-hand axis. As can easily be seen, the offset motion is nominally 1% of the total motion of the actuator. The worst case excursions are only 3%, and are short transients. The system clearly recovers after each excursion.

Conclusions

(1) Coordinated motion of multiple actuators is important for some testing. It was shown how failure to control the relative position of all actuators in a planar biaxial test can lead to uneven loading of the test specimen. This was illustrated by developing the basic concept of servocontrol and how forces and motions are interrelated.
(2) Matrix control is an excellent method of providing coordinated motion. Various methods of coordinating control of actuators were discussed. Strengths and weaknesses were mentioned, leading up to the matrix control technique. It was shown how the matrix control method addressed the limitations of other means of coordinated actuator motion.
(3) Calculated input provides a powerful tool for creating a matrix control loop. A technique for creating a matrix control loop using calculated inputs was presented. It was accomplished in a somewhat nontraditional manner utilizing it in conjunction with a cascade control loop. Test results presented demonstrated that the technique does indeed work.

References

[1] *MTS Road Simulator Manuals,* MTS Systems Corp., Eden Prairie, MN, 1995.
[2] *Extend™ Reference Manual,* Imagine That, Inc., San Jose, CA, 1994.
[3] *TestStar™ Reference Manuals,* MTS Systems Corp., Eden Prairie, MN, 1995.
[4] Schwarzenbach, J. and Gill, K. F., "Design of Closed Loop Systems," *System Modeling and Control—2nd Edition,* Edward Arnold Ltd., Victoria, Australia. 1984, pp. 222–234.
[5] *TestStar™ Reference Manuals,* MTS Systems Corp., Eden Prairie, MN, 1995.
[6] McMillan, G. K., "Effect of Advanced Control Algorithms," *Tuning and Control Loop Performance,* Instrument Society of America, Research Triangle Park, NC, 1983, pp. 183–195.